Applications of new mass spectrometric technologies for the structural characterisation of synthetic polymers

MICHAEL JONATHAN PAUL SMITH

How to cite:

SMITH, MICHAEL JONATHAN PAUL (2013) Applications of new mass spectrometric technologies for the structural characterisation of synthetic polymers. Doctoral thesis, Durham University.

Durham University

Department of Chemistry

Application of new mass spectrometric technologies for the structural characterisation of synthetic polymers

A thesis submitted in partial fulfillment of the requirements for the degree of

Doctor of Philosophy

Michael Jonathan Paul Smith

2013

Abstract

The work detailed herein describes the developments made using new mass spectrometric techniques for the structural characterisation of synthetic polymers. Electron-based tandem mass spectrometry techniques including Electron Induced Dissociation (EID) and Hot Electron Capture Dissociation (HECD) have proven to be highly effective methods of characterising synthetic polymers. The product ion spectra obtained provided comparable structural information to Collision Induced Dissociation (CID), both in terms of the types of ion formed and the polymer sequence covered. The application of EID and HECD to copolymer analysis provided a facile method of differentiating copolymers with a variety of architectures, including identification of structural isomers.

Control of the charge carrier present demonstrated that electron-based tandem mass spectrometry results could be manipulated to maximise the amount of structural information obtained. For synthetic polymers, improved fragmentation efficiency using EID was achieved when the charge carrier present was a strong reducing agent. For small organic molecules, EID provided complementary information to vibrationally dissociative techniques in a manner that is more controllable through the choice of charge carrier. These experimental observations supported by molecular modelling both suggest that the complementary nature of the results is due to different locations of charge carrier attachment within the molecule.

The application of Atmospheric pressure Solids Analysis Probe (ASAP) mass spectrometry facilitated the analysis of common synthetic polymers directly from solids, circumventing issues regarding solubility. Key instrument parameters were identified that maximised the intensity of the molecular ion peaks whilst limiting in-source fragmentation. The synthetic polymers were ionised without the requirement for metal salts, forming protonated and radical cation molecular ions. CID tandem mass spectrometry of these precursor ions demonstrated that they fragmented readily, where analysis of radical cations resulted in product ions that are not observed during CID of even electron precursor ions. Following this extensive evaluation and optimisation, ASAP, for the first time, was successfully applied to the structural characterisation of an insoluble block copolymer. The product ions provided information about the individual components of the copolymer, which could not be obtained by any other analytical technique.

Contents

Abbreviations

AC	Alternating Current
APCI	Atmospheric Pressure Chemical Ionisation
API	Atmospheric Pressure Ionisation
ASAP	Atmospheric pressure Solids Analysis Probe
ATRP	Atom Transfer Radical Polymerisation
BD	Butadiene
CE	Capillary Electrophoresis
CI	Chemical Ionisation
CID	Collision Induced Dissociation
COSY	2 dimensional Correlation Spectroscopy
DART	Direct Analysis in Real Time
DC	Direct Current
DESI	Desorption Electrospray Ionisation
DLS	Dynamic Light Scattering
DP	Diphenyl ethylene
ECD	Electron Capture Dissociation
EDD	Electron Detachment Dissociation
EG	Ethylene Glycol
EI	Electron Ionisation
EID	Electron Induced Dissociation
EIEIO	Electron Induced Excitation from Organics
ESI	Electrospray Ionisation
ETD	Electron Transfer Dissociation
FAB	Fast Atom Bombardment
FTICR	Fourier Transform Ion Cyclotron Resonance
FWHM	Full Width at Half Maximum
HECD	Hot Electron Capture Dissociation
HMBC	Heteronuclear Multi-Bond correlation Spectroscopy
HSQC	Heteronuclear Single Quantum Coherence
IMS	Ion Mobility Spectrometry
IR	Infrared Spectroscopy
IRMPD	Infrared Multi-Photon Dissociation
LC	Liquid Chromatography
LDI	Laser Desorption/Ionisation
LSIMS	Liquid Secondary Ion Mass Spectrometry
LTQ	Linear ion Trap
MALDI	Matrix-Assisted Laser Desorption/Ionisation
MALS	Multi-Angle Light Scattering
Mat	Matrix

M_n	Number averaged molecular weight
MS	Mass Spectrometry
M_v	Viscosity averaged molecular weight
M_w	Weight averaged molecular weight
nESI	Nano-Electrospray Ionisation
niECD	Negative Ion Electron Capture Dissociation
NOESY	Nuclear Overhauser Effect Spectroscopy
NMP	Nitroxide Mediated Polymerisation
NMR	Nuclear Magnetic Resonance
PDI	Polydispersity Index
PEG	Poly(ethylene glycol)
PG	Propylene glycol
PMMA	Poly(methyl methacrylate)l
PPG	Poly(propylene glycol)
PS	Poly(styrene)
PSD	Pose-Source Decay
RAFT	Reversible Addition-Fragmentation chain Transfer
RF	Radio Frequency (voltage)
SEC	Size Exclusion Chromatography
S/N	Signal-to-Noise ratio
Tandem MS	Tandem Mass Spectrometry
ToF	Time-of -Flight
UV	Ultra-Violet Spectroscopy

Units

°C	Degree Celsius
A	Ampere
Å	Angstrom
Da	Dalton
eV	Electron Volt
hr	Hour
J	Joules
K	Kelvin
keV	Kilo Electron Volt
kV	Kilovolt
L	Litres
M	Molarity in Moles per Litre
min	Minute
mg	Milligram

mL	Millilitre
mM	Millimole
ms	Millisecond
m/z	Mass-to-Charge
ppm	Parts-Per-Million
s	Second
T	Tesla
µg	Microgram
µL	Microlitre
V	Volt

Declaration

The work presented herein was carried out in the Department of Chemistry at Durham University between October 2009 and March 2013. In May 2011, work was conducted at Astra Zeneca, Alderley Edge over two days. Unless otherwise stated all work is my own and has not been submitted for a qualification at this or any other university.

Statement of Copyright

Acknowledgements

There are a number of people I wish to acknowledge that have supported me in the completion of my doctorate.

Firstly, I must thank Dr. Jackie Mosely, whose commitment, guidance and support have been integral to the success of this project. Special thanks to the members of the Durham University Mass Spectrometry Group, in particular Dr. Mike Jones, Lara Turner, Dr. Dave Parker, Peter Stokes and Dr. Aruna Prakash, who have always been willing to listen to problems and offer advice.

Secondly, I am indebted to my co-supervisor Prof. Neil Cameron, who has always been on hand to provide direction and technical expertise. I must also thank all of the members of CY 235 (past and present) for their knowledge, ideas and collaborations and importantly for demonstrating the importance of a work-life balance.

Thirdly I am incredibly grateful to my family whose constant support and encouragement have kept me motivated in challenging times. I must also thank all of my friends for providing sources of distraction and inspiration, particularly in the final few months.

Finally, Gisela, whose unwavering support and patience has seen me through every aspect of my work from international presentations to thesis writing and viva preparation. Most importantly I am grateful to G for reminding me that there is a life outside of my PhD.

1. Characterisation of synthetic polymers

1.1. Introduction

Synthetic polymers at the most basic level are molecules that consist of hundreds, thousands or even millions of atoms, arranged in a variety of structures with an extended length at least an order of magnitude greater than its thickness.[1] Polymers represent a class of compounds that are integral to a wide variety of industrial processes and domestic applications. The variety of synthetic monomers and the different polymerisation processes provide a diverse range of chemical and physical properties, which allow polymers to be tailored to the desired application. It is therefore of critical importance to provide a reliable means of characterising such compounds. In addition to high molecular weight, polymers represent a considerable challenge for the analytical chemist due to their polydisperse nature with a vast number of different molecular species providing a molecular weight distribution. Further complications arise with the generation of polymers with different terminal groups which yield multiple species for molecules with the same degree of polymerisation, not to mention molecules with different polymer architectures. The diverse properties that make synthetic polymers such a widely used class of compounds have meant that no analytical technique is universally applicable. Consequently, numerous analytical techniques have been developed that investigate specific properties of synthetic polymers, where development is constantly sought to expand the range of synthetic polymers that can be analysed. A key parameter that is of interest to the synthetic polymer chemist is the molecular weight of a polymer sample. This value can be calculated in a number of ways as determined by the analytical technique used. Two statistically derived methods of calculating molecular weight are the number averaged molecular weight (M_n) and the weight averaged molecular weight (M_w), which can be calculated using the formulas in **Equations 1.1** and **1.2** respectively. The formulas are described in terms of $\mathbf{n_i}$ and $\mathbf{m_i}$, where $\mathbf{n_i}$ is the number of molecules of molecular weight $\mathbf{m_i}$.

$$M_n = \left(\frac{\sum m_i n_i}{\sum n_i}\right) \tag{1.1}$$

$$M_w = \left(\frac{\sum m_i^2 n_i}{\sum m_i n_i}\right) \tag{1.2}$$

Evaluation of M_n provides information regarding the thermodynamic and colligative properties of the synthetic polymer, whereas M_w affects macroscopic properties such as tensile strength and toughness. For M_n calculations, all molecules contribute equally regardless of molecular weight. In contrast, the larger molecules contribute proportionately more in the calculation of M_w than the smaller ones. It is for this reason that measured M_w values are larger than the respective M_n value. The ratio of the mathematically calculated values from **Equation 1.1** and **Equation 1.2** provide the polydispersity for the synthetic polymer using **Equation 1.3**, where a polymer of controlled and well-defined polydispersity (PDI) will have a value of <1.6.

$$PDI = \left(\frac{M_w}{M_n}\right) \tag{1.3}$$

1.2. Colligative methods

The colligative properties of dilute polymer solutions are examined through a number of different experiments, of which osmometry, freezing point depression and boiling point elevation are prominent examples. Analysis of polymers using these techniques derives results that are only dependent upon the concentration of the dissolved molecules, and not on the individual properties of the molecules such as molecular mass. Through determination of the number of molecules, **n** in a sample of known mass, **m** one can determine the average M_n using **Equation 1.1**. Due to the low sensitivity of freezing point depression and boiling point elevation, osmometry based techniques are almost exclusively used.[2]

Vapour phase osmometry and membrane osmometry rely upon changes in pressure to allow determination of molecular weight. Membrane osmometry utilises a membrane that separates a polymer solution from pure solvent, where the membrane is only permeable by the solvent as shown in Figure 1.1.

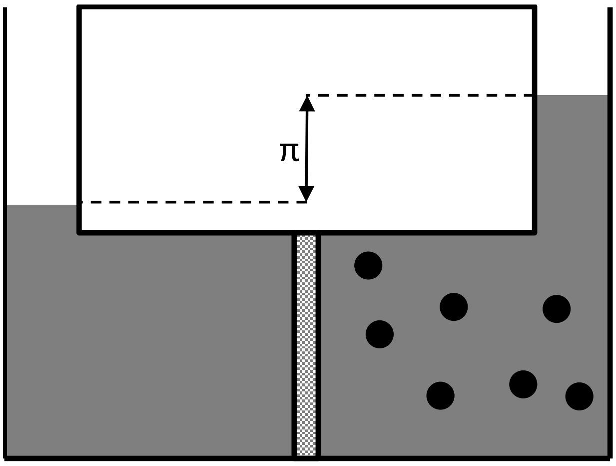

Figure 1.1 Principle of membrane osmometry for a pure solvent (left) and polymer solution (right).

At equilibrium, the solvent flow in each direction through the membrane is identical. The osmotic pressure (**π**) (Pa) can be calculated based on the difference in the fluid levels in the chambers at equilibrium. The osmotic pressure can be used to calculate M_n using **Equation 1.4**, where **c** is the concentration of the polymer in the solution (mol m^{-3}), **R** is the ideal gas constant (8.314 J K^{-1} mol^{-1}) and **T** is the temperature (K).

$$\frac{\pi}{c} = \frac{RT}{M_n} \qquad \textbf{(1.4)}$$

Measurements are made at a variety of concentrations, so that a plot of reduced osmotic pressure (**π/c**) vs. concentration (**c**) yields a linear correlation where M_n can be calculated through extrapolation to zero concentration. The selection of a suitable membrane is essential to the success of this experiment, where the membrane must be inert and compatible with the selected solvent. It must also have high solvent permeability, and strong mechanical properties to withstand the experimental conditions. A significant source of error in the calculation of M_n using this method is that each membrane has a low molecular weight cut off, below which molecules can pass through the membrane. This is a significant problem in the analysis of low molecular weight polymers, as molecules that diffuse through the membrane do not contribute to the calculated M_n leading to higher than expected values. In the analysis of high molecular weight polymers that are suspected of containing contaminants, a low mass cut off ensures that these contaminants do not contribute to the M_n value. A major disadvantage in the use of membrane osmometry for synthetic polymer analysis is the time required for an experiment to reach equilibrium, which can take from seconds to days.

Alternative methods where pressure is applied to the system to maintain fluid levels, known as dynamic equilibrium, has been shown to significantly reduce equilibrium times. Additionally, the rate at which equilibrium is reached can be increased through the addition of automatic pressure compensation, where flow cells have been developed for rapid measurements.

Vapour phase osmometry is a second technique that utilises the colligative properties of polymers in the determination of M_n values. A polymer solution of known concentration and a pure solvent standard are applied to a pair of matching thermistors, and placed within an environment saturated with solvent vapour. Condensation of solvent into the polymer solution increases the temperature of the droplet as measured by the thermistor, until the vapour pressures recorded at each thermistor are identical. The temperature difference required to heat the solution probe to the vapour pressure of the pure solvent can be related to the molality, and hence molecular weight, by **Equation 1.5**, where **R** is the ideal gas constant

(8.314 J K^{-1} mol^{-1}), **T** is the temperature (K), **λ** is the heat of vapourisation of the solvent and **M** is the molality (mol Kg^{-1}).[3]

$$\Delta T = \left(\frac{RT^2}{\lambda 100}\right) M \qquad \textbf{(1.5)}$$

Unlike membrane osmometry, vapour phase osmometry has no low mass cut off, and is therefore applicable to low molecular mass synthetic polymers that cannot be analysed by membrane osmometry. Despite facing increasing competition from mass spectrometry in the analysis of lower molecular mass polymers, vapour phase osmometry is still advantageous for synthetic polymers that readily fragment under MS conditions.

1.3. Viscometry

It has been well documented since the inception of polymer characterisation that the viscosity of a polymer solution is related to the molar mass of the solute. The measure of viscosity is not an absolute measure of M_v, so the equipment requires calibration with molecular weight standards determined by other means prior to analysis. Experimentally the viscosity of a dilute polymer solution is obtained through recording the time required for the meniscus of the solution to pass between two designated points. One of the major issues with the reporting of viscosity in publications is that there are a number of different ways of calculating viscosity. These methods are summarised in Table 1.1, where η and η_0 correspond to the viscosity of the polymer sample and pure solvent respectively, t and t_0 correspond to the recorded times for the sample and the solvent and c is the concentration (mol dm^{-3}).

Table 1.1 Methods of determining viscosity.

Viscosity Method	Definition
Relative Viscosity	$\eta_{rel} = \frac{\eta}{\eta_0} = \frac{t}{t_o}$
Specific Viscosity	$\eta_{sp} = \frac{\eta - \eta_0}{\eta_0} = \frac{t - t_0}{t_0} = \eta_{rel} - 1$
Inherent Viscosity	$\eta_{inh} = \frac{\ln \eta_{rel}}{c}$
Intrinsic Viscosity	$[\eta] = \left(\frac{\eta_{sp}}{c}\right)$

Intrinsic velocity is the most useful measurement, as it can be directly related to the molecular weight by the Mark-Houwink-Sakurada equation.[4] Viscosity averaged molecular weight (M_v) is a value that is exclusive to viscometry experiments, the value of which lies between the M_n and M_w. Factors such as chain branching, broad molecular weight distribution and the presence of copolymers can influence the accuracy of the relationship between intrinsic viscosity and M_v. Additionally, the requirement for a calibration to be performed, and the generation of a technique specific molecular weight, means that this technique is frequently used when a polymer is characterised routinely.[5]

1.4. Light Scattering Techniques

Light scattering represents a widely used method of calculating absolute values for (M_w) and also allows the determination of the radius of gyration of synthetic polymers.[2,6] Static light scattering can produces values for the radius of gyration (R_g) and consequently can be used to calculate M_w. In comparison dynamic light scattering (DLS), records the hydrodynamic radius of the polymer molecules (R_h) and cannot be used to determine M_w. In both instances, the relationship between the amplitude and intensity of the scattered light depends on a number of factors, including concentration, size and mass of the polymer and optical contrast of the polymer in the solvent. In static light scattering, a series of experiments are performed with solutions of different polymer concentrations, where the time averaged intensity is recorded at a series of scattering angles. Alongside measurements of the pure solvent, this information can be used to create a Zimm plot, from which extrapolation can yield a value inversely proportional to M_w and where the gradient of the slope is related to the radius of gyration. However, this method can be complex as the relationship plotted in the Zimm plot is not linear for all polymeric species. Issues also arise in the analysis of polymers that require binary solvent systems where only an apparent molecular weight (M_{app}) can be derived.[2] It is also noted that the analysis of copolymers by this method is time intensive and requires the sample to be dust free, which involves additional filtration steps and a sterile environment. Like static light scattering, DLS records the fluctuations in the intensity of the scattered light, but unlike static light scattering, which performs time averaged measurements, DLS records the intensity on a millisecond or nanosecond timescale.[2] Through the use of mathematical transformations that account for the Brownian motion of the dilute polymer solution, DLS can yield information regarding R_h with only a small quantity of sample required. As mentioned previously, dust particles must be removed from the solution prior to analysis, with air bubbles and charged impurities generating additional false results.[2] Light scattering is also not an applicable method to the analysis of low molecular weight polymers, due to the low scattering strength of such species.

1.5. Nuclear Magnetic Resonance (NMR)

The number average molecular weight (M_n) can be calculated based on the ratio of the end group protons to the number of backbone protons. Unfortunately, the calculation of molecular weight by this method is restricted to polymers with $M_n \leq 3 \times 10^4$ g mol^{-1}, as the number of end groups relative to the bulk reaches a level where quantitative determination becomes impractical.[2] This method also relies on the assumption that the polymer is linear, and that the end groups used to calculate M_n are the only end groups present. The main strength of NMR over other analytical techniques in synthetic polymer analysis is the ability to probe the microstructure, as the chemical shifts and coupling constants are incredibly sensitive to structural and stereochemical changes. NMR can be used to quantitatively probe the structural composition of polymers, providing fractions of different components in a mixture. For example, the polymerisation of poly(butadiene) monomers present from a 1,2 addition containing a pendant vinyl group can be easily distinguished from those monomers involving a 1,4 addition with no pendant groups.[7] The ability to provide information relating to adjacent functional groups has proven to be a significant benefit in the analysis of synthetic polymers, in particular in the determination of polymer tacticity. Vinyl based polymers that contain two different pendant groups, form pseudochiral centres that generate inequivalent hydrogen atoms on an adjacent CH_2. The splitting of this CH_2 in the proton NMR spectrum is representative of the stereochemistry of the adjacent monomer units. For isotactic polymers, a single CH_2 resonance will be observed, whereas syndiotactic will have exclusively two CH_2 resonances, and an atactic polymer would have a mixture of the two. In practice, given that the properties measured by NMR reflect those of the whole polymer sample, a mixture of resonances is observed where the different fractions of tacticities can be calculated. This information can also be obtained by ^{13}C NMR, where each chemically distinct carbon has a specific peak in the spectrum.[7] The analysis of copolymers by NMR allows for calculation of the fraction of each specific monomer unit, based on the relative intensities of the relevant backbone peaks in the NMR spectrum. The stereochemistry of adjacent groups to a monomer leads to the formation of location dependent peak splitting. The use of two dimensional NMR experiments have been shown to be effective at simplifying complex polymer spectra, establishing the interactions between homonuclear spin active species (COSY, NOESY) and heteronuclear spin active species (HSQC and HMBC). The relationships established by multi-dimensional experiments can be used to determine the chemical structures of synthetic polymers, and provide evidence of the molecular conformation. It has also been shown that three dimensional experiments can be performed, combining heteronuclear 2D experiments with a homonuclear 2D experiment providing additional clarity for complex spectra; a particularly useful experiment in the analysis of large molecules such as proteins and polymers. Like a number of other analytical techniques, solution phase NMR relies upon the sample being soluble in a limited range of deuterated solvents, which can restrict the application of this technique. Solid state NMR has been used in a limited number of applications, including the characterisation of poly(ethylene), however the long relaxation times required for the end groups leads to extremely long measurement times.[2]

1.6. Size Exclusion Chromatography (SEC)

Size exclusion chromatography is a liquid phase chromatographic technique, which achieves separation of mixtures based on the hydrodynamic radii of the molecules relative to the size of the pores present in the SEC column packing material. For synthetic polymer analysis, the size of the molecules in solution can be related to the chain length, and hence to the molecular weight. The hydrodynamic radius of a given molecule directly impacts the ability of the molecule to enter the pores of the column packing material. As shown in Figure 1.2, polymer chains with large hydrodynamic radii (i.e. high molecular weight) are able to enter fewer pores. Consequently these polymer chains proceed through the column with little interference and are eluted first (Figure 1.2(c)). At one extreme, known as the total exclusion limit, the molecules have a hydrodynamic radius such that they will not enter any pores, and passage through the column is only hindered by movement around and between particles of the packing material. At the other extreme, molecules that are small relative to the smallest pore size result in the co-elution of molecules, this is known as the total permeation limit. Between the total exclusion limit and the total permeation limit, molecules can be efficiently separated based on the individual hydrodynamic radius.

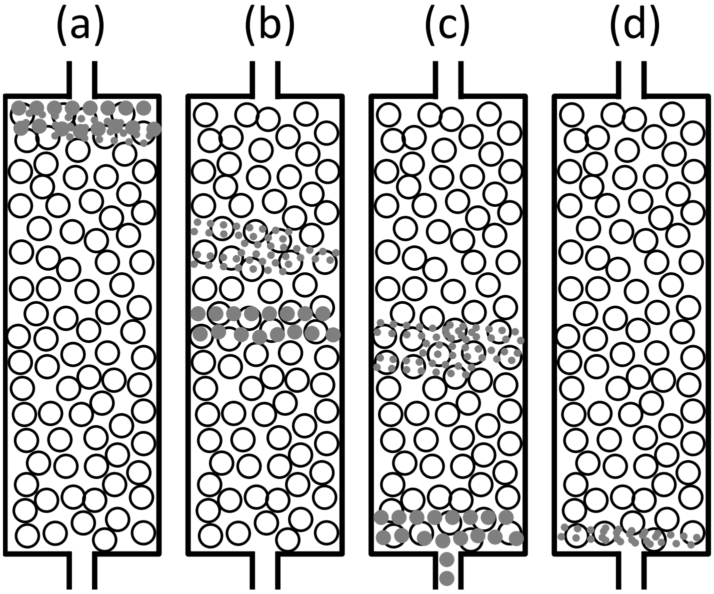

Figure 1.2 Principle of SEC, (a) sample injection, (b) size separation, (c) large molecule detection and (d) small molecule detection.

SEC measurements are dependent upon effective calibration of the instrumentation, as the obtained retention times for a specific polymer of unknown molecular weight will be evaluated relative to the applied calibration. Initial work in this area required that a calibration curve was generated with known standards related to the polymer of interest, a major issue as the availability of polymer standards with the low polydispersity is limited. This resulted in the generation of a universal calibration method, based on the observation that the product of the intrinsic viscosity and the molecular weight are independent of polymer type.[8] This value, denoted $[\eta]M$, is called the universal calibration parameter, and when log $[\eta]M$ vs. elution is plotted, a near linear trend is observed for a wide range of synthetic polymers. One further issue with calibration of the SEC column is that a given calibration is only valid for specific conditions, including temperature, stationary phase (column packing material) and selected mobile phase (solvent). A change in the solvent used as the mobile phase results in different degrees of swelling in the stationary phase, requiring a different calibration.

A key success in the application of SEC to synthetic polymers is the ability to interface the molecular separation with a number of analytical techniques that act as detectors, providing different parameters for synthetic polymers, as summarised in Table 1.2.

Table 1.2 Properties of polymers and detection modes.[9]

Macromolecular Distribution	Detection Mode
Mass	Static Light Scattering
Long Chain Branching	Multi-Angle Light Scattering (MALS)
Short Chain Branching	Infrared Spectroscopy (IR) and NMR
Architecture	MALS, Viscometry, IR and NMR
Chemical heterogeneity	UV, NMR, IR and Mass Spectrometry
Copolymer Sequence	NMR, IR and MS

For quantitative molecular weight interpretations, it is essential that a concentration type detector is used. Detectors that measure the refractive index are commonly used to determine concentration, as they can provide data for any polymer given the correct solvent choice. Optimal sensitivity occurs when the polymer and solvent have the maximum difference in refractive index. This parameter can also be influenced by temperature, which can result in an inconsistent baseline that restricts the observed resolution.[10] UV and IR detectors can also be utilised in concentration detection, where they are influenced less by temperature and maintain higher levels of sensitivity than refractive detectors. However, the application of such detectors is restricted to those polymers that contain a detectable chromophore, and are soluble in a solvent that is transparent to the incident light.[10] It has been demonstrated that the use of multiple SEC detectors can be a significant benefit in the analysis of synthetic polymers, particularly where no specific calibration can be applied. The most widely used configuration is the MALS and viscometry detectors, in conjunction with a differential refractometer concentration detector. This combination has been shown to not only provide average molecular weight values independent of calibration, but also physical attributes, including chain branching, macromolecular radii and thermodynamic states of the solutions.[11] The inclusion of chemical detectors such as NMR, MS and UV can provide additional information regarding chemical homogeneity of the polymer.

Synthetic polymers may contain multiple distributions within a single sample, including molar mass, chain branching, end group functionality, chemical composition and tacticity. To separate these components requires more than one type of chromatography. Two dimensional chromatography, combining SEC with conventional LC, has been shown to be an effective means of simplifying complex mixtures. Initially, LC can separate based on chemical composition and end group functionalities, where SEC allows further separation based on the hydrodynamic radii of the sample, separating molecules with different molar masses and branching.[11] Siewing *et al.* demonstrated the effectiveness of this technique in the separation of PMMA and poly(butadiene) (PB) homopolymers from a PMMA-PB graft copolymer, where a contour plot of chemical composition distribution against molecular mass distribution generates discrete regions for each type of polymeric species.[12]

A limiting factor in the separation of polymers by SEC is the time required to achieve effective separation, therefore development of faster separations is constantly sought. The use of faster flow rates on conventional columns leads to a significant decrease in the resolution, and can cause flow-induced degradation of the polymers.[11] One method that has shown some benefit for high-throughput analysis is the development of short length, wide bore columns, where the flow rate can be increased with no drop in resolution, and there is no evidence of degradation or peak broadening. Development of faster separations should be made with caution, as any inhomogeneity in the flow rate of the mobile phase can lead to poor accuracy in molecular weight determinations.[10]

1.7. Mass Spectrometry

Mass spectrometry (MS) is an attractive option for the characterisation of synthetic polymers, as direct analysis of individual oligomers allows for calculation of M_n and M_w from a single experiment. Separation of the individual polymer oligomers on the basis of the mass-to-charge ratio (*m/z*) allows identification of the repeat monomer unit of the polymer, as well as the assignment of the terminal groups. The observed molecular weight distribution, or distributions, permits the identification of functionality type distributions, as well as copolymers, additives and impurities.[6]

Initial analysis of synthetic polymers required thermal or chemical decomposition of the compounds for MS to be performed successfully, where only field desorption ionisation (FD) was shown to provide intact polymer molecular ions up to 10 kDa. The invention of Matrix-assisted Laser Desorption/Ionisation (MALDI)[13] and Electrospray Ionisation (ESI)[14] revolutionised the use of MS for the analysis of synthetic polymers, providing intact ions for synthetic polymers up to 1.5 MDa.[15] The importance of the development of these two techniques to the field of mass spectrometry saw Tanaka (MALDI) and Fenn (ESI) share the Nobel Prize in Chemistry in 2002.

1.7.1. MALDI MS

MALDI MS is an ionisation technique ideally suited to the analysis of synthetic polymers, as it provides singly charged quasi-molecular ions with little fragmentation.[16] This method combines the synthetic polymer sample with a matrix and a metal salt in a homogeneous layer, which is ionised through the absorption of laser light. Since the application of MALDI to synthetic polymers, MALDI represents the most widely used ionisation technique in terms of the number of publications regarding polymer characterisation. It has therefore been possible for regular review articles to be published, which provide a useful summary of recent work in the field.[5,16-24]

1.7.1.1. Matrix selection

One aspect that is essential to the success of MALDI is the preparation of the polymer sample, where the selection of matrix, solvent and metal salt are critical to effective ionisation. The selection of a matrix is not only important for ionisation, but has been shown to influence the molecular weight distribution and the degree of fragmentation observed.[25] One proposed strategy for matrix selection is to match the polymer and matrix based on polarity,[26] which has been shown to be effective in maximising signal intensity.[27] This represents a logical starting point, as matched polarities will allow effective mixing of the matrix and polymer in both solution and solid phases during sample deposition. However, where polymer end groups dictate polarity, the polydisperse nature of a sample will result in a change in polarity across the molecular weight distribution, which may influence the mass spectrum observed. Matrices typically incorporate features that aid in the MALDI process, such as the presence of a chromophore that absorbs energy at the frequency of the laser. Other useful features include high volatility, and the ability to readily donate a proton, which promotes analyte ionisation. The most common molecules that are used as MALDI matrices are small organic acids, for example 2, 5-dihydroxybenzoic acid (DHB) and α–cyano- 4-hydroxycinnamic acid (CHCA). Despite this, the range of matrices currently used in MALDI for synthetic polymer analysis remains limited, and consequently the investigation of new matrix molecules is continually sought. Meier *et al*. developed statistical approaches to identify new potential matrix molecules based on common characteristics of established matrices, providing an efficient selection method and a means of identifying functional groups that are important in the MALDI ionisation process, such as an extended π-system.[28] This logical approach allows for the identification of matrices similar to those already in use; it is therefore plausible that the newly identified matrices will have the same shortcomings as those currently in use limiting their impact in the analysis of new polymers by MALDI. For polymers such as poly(ester)s that have been shown to degrade under acidic conditions,[29] the use of the small organic acids will provide potentially misleading information from MALDI MS. Ionic Liquid Matrices (ILMs) have shown significant promise in the analysis of this class of polymer, since demonstrating successful ionisation where the presence of a quaternary ammonium cation allows soft protonation with minimal degradation.[30] The search for new potential matrices has not been restricted to purely organic compounds either, where Wallace *et al.* demonstrated that a molecular solid of fullerene intercalated with a cobalt cyclopentadienyl complex provided an ideal matrix for the analysis of poly(ethylene) and higher mass alkanes.[31] Depending on the functional groups of a synthetic polymer, it is also possible to perform laser desorption/ionisation without a matrix present (LDI). This was demonstrated to be an effective means of analysing thermally stable conjugated polymers that had energy transfer properties.[32] It was also found that direct LDI could be achieved when polymers were analysed on a series of nanostructures[33-36] that have shown potential in analysing polymers that readily fragment using traditional MALDI sample preparation.

1.7.1.2. Metal cation selection

A key difference in the analysis of synthetic polymers compared to biopolymers is that the final ionisation process of synthetic polymers predominantly involves cation attachment, rather than protonation. A metal salt is therefore a required component in sample preparation, where the selection of metal cation present is determined by the chemistry of the polymer. Polar polymers containing a large number of heteroatoms such as poly(ether)s, poly(acrylate)s and poly(ester)s have been shown to ionise effectively in the presence of small alkali metal cations, such as lithium, sodium and potassium.[16] Apolar polymers that do not contain heteroatoms such as poly(styrene)s, poly(butadiene)s and poly(isoprene)s, but do contain double bonds, have been shown to ionise well with silver and copper salts.[37-39] MALDI analysis of polymers that do not contain heteroatoms or double bonds such as poly(ethylene)s and poly(propylene)s remains challenging, where only silver has been shown to successfully ionise poly(ethylene).[40] The selection of cation is not only important for ionisation, but has direct implications for the observed molecular weight of a polymer. Low mass oligomers have been shown to favour smaller alkali metal cations, such as lithium and sodium, whereas larger cations work more efficiently with higher mass polymer chains. This resulted in higher M_n and M_w values for the same polymeric sample when larger alkali metal cations were added to the sample.[41,42] This is something that is necessary for the analytical chemist to consider when assessing the reliability of molecular weight information that is obtained by MALDI MS. The suitability of a metal cation as charge carrier with a specific polymer can be evaluated both experimentally and theoretically. Gidden *et al.* demonstrated the use of ion mobility separation as a means of calculating the collisional cross section for a series of polymers ionised with different metal cations.[43-45] The experimental findings, in combination with molecular modelling, allowed gas phase conformations to be postulated, and demonstrated that for polar polymers poly(ethylene glycol) (PEG) and poly(methyl methacrylate) (PMMA), small alkali metals provided the highest binding energies.[44,45] The authors also highlighted, however, the significant influence that the polymer terminal groups and chain branching have upon cation binding; an important consideration for future investigations.[44,45] Further investigations using this method found little difference for the binding of four different metal cations with poly(styrene) (PS), where the interaction involved stabilisation of the cation by two adjacent phenyl groups on the polymer backbone.[43] Despite this lack of specificity, the authors suggested that the success of silver and copper as cations for PS was due to superior overlap between the d-orbitals of the transition metals and the π-systems of the phenyl rings.[43] The cation-polymer interaction is not the only determining factor in the selection of the most effective cation for a given preparation, where the chemistry of the matrix present has also been shown to influence the most suitable cation. Rashidzadeh *et al.* demonstrated that for the same PEG sample, Li was a more effective cation in the presence of CHCA and dithranol, whereas Cs was a more effective cation in the presence of Indole Acrylic Acid (IAA) and DHB.[46] It has also been demonstrated that the chemistry of the anion present in the salt influences the mass spectra observed. Work by Hoberg *et al.* demonstrated that for alkali metal-halogen salts, decreasing the size of the anion resulted in a decrease in the intensity of PMMA molecular ion peaks.[47]

1.7.1.3. Sample preparation

As well as the components used in the MALDI sample preparation, the method of sample preparation can be a determining factor in analytical success.[48] The most widely used method remains the 'dried droplet' method, where polymer, matrix and salt are dissolved in a volatile solvent and applied to the target in a single droplet, which is allowed to dry. The correct ratio of matrix: polymer: salt is essential for the production of an accurate mass spectrum. Pasch and Schrepp suggested that a molar ratio of 1:100 to 1:1000 (polymer: matrix) was an optimal starting point in the analysis of polymers.[5] This is achieved through the preparation of a solution of matrix (20 gL^{-1}), a solution of polymer (1 to 10 gL^{-1}) and if required a salt solution (0.1 M), where the solutions are combined in a ratio of 10:10:1. This work was expanded on by Brandt *et al.*, who demonstrated that a statistical approach to the ratios could provide a better approximation for different polymer classes. This work demonstrated that a ratio of 5:5:1 and 5:5:10 for matrix (10 gL^{-1}): polymer (5 gL^{-1}):metal salt (0.1 M) were the optimal ratios for 70% of the samples analysed in their study.[49] This work also demonstrated that reduction of the salt concentration reduced the interference of cluster peaks, and increasing the ratio of matrix reduced the formation of multiply charged ions.[49] As precipitation from the solvent is a function of mass, the molecular weight distribution found in synthetic polymers produces an inhomogeneous layer that results in irreproducible data.[50] Issues regarding the solubility of all components in the same solvent can lead to the use of multiple solvent systems. Therefore, deposition of the different components becomes dependent on the relative volatility of the solvents used, where the composition of the mixture in the droplet changes with time, producing an inhomogeneous layer. For polymers, it is important to ensure that the sample is completely soluble in the selected solvent, as only soluble components will be observed in the mass spectrum. Yalcin *et al*. demonstrated this concept for PS in a range of solvents, where distinct differences in the observed molecular weight distribution could be observed.[51] There have been a number of approaches that have improved the reliability of sample preparation, for instance applying sequential layers of the separate components to the target, which demonstrated a significant increase in polymer peak area.[52,53] The use of spray based deposition from electrospray[52] or aerosol[50] was found to give superior shot-to-shot reproducibility for polymeric samples, through reduction in sample segregation compared to the dried droplet method.[54] Despite this, issues arose regarding the voltages applied to the electrospray probe during sample deposition, where increased voltages resulted in more extensive ion fragmentation, and consequently shifted the molecular weight distributions.[48]

In traditional MALDI sample preparation, it is essential that a polymer is soluble in a limited range of mass spectrometry appropriate solvents. Issues also arise when a polymer and matrix are not soluble in the same solvent, as binary solvent systems have been shown to produce spectra that suffer from mass discrimination.[55] However, the physical and chemical properties of a given polymer may inhibit solubility in any usable solvent, excluding the use of MALDI. One method that has been developed to circumvent this issue is solvent free sample preparation, where the polymer and matrix are manually combined in the solid state.[56,57] This not only eliminates the effect solvents may have upon sample deposition on a MALDI target, but has been shown to expand the range of polymers amenable to MALDI.[57] The efficiency of sample preparation was improved by Trimpin *et al*., who utilised a ball mill to mechanically combine matrix and polymer,[58,59] with a multi-sample method introduced in 2007.[60,61] Hanton *et al*. demonstrated that mechanical combination could be achieved in a glass vial with the addition of two ball bearings, expanding the range of polymers that could be analysed by this technique to include soft or waxy polymers, whilst reducing sample cross-contamination.[62] Solvent-free MALDI has not only proven to be a successful method for the analysis of insoluble polymers,[63-66] it has also demonstrated significant benefits in the analysis of partially soluble and soluble polymers, where the deposited solvent free mixture is more homogeneous, yielding more repeatable mass spectra.[65] This preparation method has been a distinct advantage when studying the gas phase affinities of metal cations and polymers, where no correction was required that accounted for solubility differences of the metal salts used.[67,68]

1.7.2. ESI MS

Electrospray ionisation (ESI) is another example of a soft ionisation technique that has proven to be a popular method by which to ionise synthetic polymers. The ionisation process involves solubilising the polymer in a polar solvent, which passes through a narrow capillary and is sprayed in the presence of a high electric field. The significant benefits of this technique are minimal fragmentation, high ionisation efficiency and the ability to multiply charge the polymer, allowing the analysis of high molecular weight polymers using mass analysers with a restricted mass range.[6,69] The formation of multiply charged ions is useful in principle, however mass spectra frequently contain multiple overlapping molecular weight distributions. This can result in a very complex spectrum where the ability to provide quantitative results is an issue.[70] This problem can be alleviated for low molecular weight polymers through deconvolution of the mass spectrum, or where they can be effectively resolved using a high resolution mass analyser such as the FTICR.[71] Critical to the success of ESI is firstly that a polymer is soluble, and secondly that it is soluble in a polar solvent. This requirement significantly restricts the scope for the application of ESI to predominantly polar polymeric species.[70] It has also been proven that solvent selection can affect the observed molecular weight distribution, where Latourte *et al.* demonstrated that increasing the solvent polarity influenced the molecular weight values for fluorinated phosphazine oligomers.[72] However, advances in sample preparation, including the use of binary solvent systems and the addition of inorganic salts, have permitted the analysis of a wider range of polymers.[73]

1.7.2.1. Chromatography-MS

Unlike MALDI, which has discrete packets of ions, ESI produces a continuous flow of sample entering the mass spectrometer. ESI therefore has a natural compatibility with solution phase separation techniques, where the most widely applicable technique for polymers is size exclusion chromatography or gel permeation chromatography (SEC/GPC).[74-76] The combination of the SEC with ESI MS is an attractive proposition, as it blends the quantitative powers of SEC with the absolute molecular weight determination of MS. Upfront chromatography can also simplify the material that is delivered to the mass spectrometer at a given time, limiting the influence of polydispersity on the mass spectrum and reducing spectral complexity. Aaserud *et* *al.* demonstrated the effectiveness of SEC-ESI-MS for the characterisation of a glycidyl methacrylate/butyl methacrylate copolymer with a wide polydispersity, where fractionation and the high resolving power of the mass analyser used were required for complete characterisation.[77] The combination of the two techniques has also proven to be a useful method for calibrating the SEC apparatus for compounds where no narrow molecular weight standards are available.[78] Automated SEC separation followed by MALDI has also been investigated,[79,80] however the collection and analysis of SEC fractions can be painstaking and time-consuming work.[81] Improvements to this technique have resulted in the development of an online SEC-MALDI method, where the eluent from SEC column is applied directly onto a MALDI target as an aerosol with a matrix.[82,83] Liu *et al.* demonstrated the shortcomings of SEC-MALDI in a comparison study with SEC-ESI-MS, where online SEC-ESI-MS achieved superior chromatographic resolution, particularly in the low mass range for poly(dimethylsiloxane) (PDMS).[84] SEC-ESI-MS has also been used to probe polymerisation processes, where Feldermann *et al.* employed the procedure to study the products of a RAFT polymerisation of acrylates.[85] In a related investigation Toy *et al.* used the hyphenated technique to probe the source of rate retardation in RAFT polymerisation, which allowed previously postulated causes to be rejected.[86]

1.7.2.2. Cation Selection

Like MALDI, ESI relies upon the addition of metal salts to promote ionisation in synthetic polymers, where the most favourable gas phase ions for PEG[87,88], PMMA[73] and PS[89] were identical to those observed for MALDI.[43-45] Greundling *et al.* also demonstrated the importance of the selected counter anions, where the substitution of a trifluoroacetate group with a tetrafluoroborate group resulted in enhanced ionisation for PS analysis using silver.[90] The presence of multiply charged species in ESI MS provides unique opportunities and challenges in the analysis of polymers. Despite establishing the most appropriate cations for PEG, the use of ESI can provide additional confirmation of the assignment through the generation of multiply charged ions. Bogan *et al.* utilised ESI to form doubly charged PEG molecular ions ionised with two different alkali metal cations, as this allowed the relative cation binding efficiencies to be directly investigated, where under activated conditions the most weakly bound cation was liberated.[91] One of the major issues with ESI is the formation of multiply charged species for higher molecular weight polymers, where the propensity for multiple charge formation increases with molecular mass, increasing spectral complexity. Numerous strategies have been proposed to control the charge state using charge reduction[92] and high resolution MS.[93] The addition of metal salts is common practice in MS of synthetic polymers to generate a favourable molecular ion, however Nasioudis *et al.* demonstrated that charge state control could be achieved for ESI of high molecular weight PEGs, through the addition of specific quaternary ammonium salts.[94] This control of the charge state and reduced fragmentation was proposed to result from the change in the solvent conditions through the addition of quaternary ammonium salts. These salts act as a surfactant, improving the surface tension of the droplets generated during ESI, and allowing the polymer to be more efficiently stabilised within the droplet.[94]

1.7.3. Ambient Ionisation MS

The constant desire to expand the range of compounds amenable to mass spectrometry has led to the development of a number of new ionisation methods. Desorption Electrospray Ionisation (DESI),[95] Direct Analysis in Real Time (DART)[96] and Atmospheric pressure Solids Analysis Probe (ASAP)[97] represent three ambient ionisation methods that have demonstrated significant promise in the field of synthetic polymers analysis. DESI, which is conducted under atmospheric conditions, involves exposure of a solid-phase sample (frozen solutions, solids and absorbed gases) to a pneumatically-assisted electrospray.[98] Charged solvent droplets impact the surface and transport desorbed sample into the mass spectrometer. This technique has demonstrated wide applicability to a range of compounds, including explosives,[95,99] biopolymers,[99,100] pharmaceutical molecules[101] and illegal drugs.[102] Nefliu *et al.* demonstrated that DESI could be applied to the characterisation of synthetic polymers, including PEG, poly(tetra-methylene glycol) (PTMG) and poly(acrylamide), up to a M_w of 3000 Da.[103] Given the close relationship to ESI, DESI of PEG leads to the generation of multiply charged polymers ions with a range of alkali metal cations, which produces a complex mass spectrum.[103] Jackson *et al.* expanded the range of synthetic polymers analysed by DESI to include PMMA, PS and PDMS. This work also demonstrated that doping the electrospray solution with metal salts provided cation specificity, generating molecular ions that were amenable to tandem MS experiments from which additional structural information could be obtained.[104] The authors also showcased the direct analysis capabilities of DESI, through the detection of a polymer used as an active ingredient in a pharmaceutical tablet.[104]

DART, a technique that creates a plasma from which charged ions, excited state neutrals, radicals and electrons are generated, that induce sample ionisation through ion-molecule reactions. Like DESI, DART has been successful in the analysis of a wide variety compounds, including explosives,[105] chemical warfare agents,[106] plasticisers[107] and counterfeit pharmaceuticals.[108] Despite PEG M_n = 600 being routinely used as a calibrant for DART,[103] the application of DART has been restricted to the analysis of low molecular weight polymers, including poly(ethyleneimine) and poly(caprolactam).[109] The novel ionisation method utilised in DART has permitted the analysis of some challenging synthetic polymers, including poly(ethylene) and poly(propylene), which both generate a methylene series when analysed with DART.[109]

ASAP is a method of performing direct ionisation of compounds as solids or solutions, where ionisation of the gaseous samples occurs via corona discharge similar to the mechanism used by the parent ionisation technique Atmospheric Pressure Chemical Ionisation (APCI).[97] The wide applicability of ASAP has seen the technique used in a diverse array of applications, including biological tissues,[97] drug molecules,[110] airborne particles[111] and nucleosides.[112] Synthetic polymers have been analysed from the first publication of the technique, where PEG M_n = 440 was used as a calibrant.[97] Trimpin *et al.* demonstrated that ASAP is a fast and efficient method of directly characterising a range of polymer additives and polymers, including poly(ethylene terephthalate) from a plastic bottle and nylon-6 from a carpet fibre.[64] Research discussed in detail in Chapter 8 describes further development where the application of ASAP to synthetic polymers was evaluated through the analysis of PEG and PS in the absence of metal cations, with the molecular ions observed being protonated adducts and radical cation respectively.[113] The investigation allowed important source conditions to be identified, allowing for optimisation of the intact molecular ions, from which additional structural information could be obtained through tandem MS experiments using Collision Induced Dissociation (CID).[113]

1.7.4. Tandem Mass Spectrometry (Tandem MS)

Mass spectrometry can be used to provide more detailed structural information for a specific polymer oligomer, through the use of tandem mass spectrometry. Tandem MS typically involves two stages of mass spectrometry measurements; the first involves mass selection of the precursor ion, and the second stage is ion activation and subsequent unimolecular dissociation followed by mass measurements of the resultant product ions. Tandem MS has shown significant benefit in the analysis of biopolymers,[114] however the application of tandem MS to synthetic polymers remains limited, due to the stability of the covalent bonds joining the individual monomers, and the fact that no approach is universally applicable.[115] In terms of synthetic polymers, tandem MS experiments can yield information for the individual polymer components, including monomer sequence and individual end groups, as well as how the components are connected to each other. In many cases, it may be the only analytical method that can differentiate between oligomeric species that are isobaric but with different architectures.[17] In trapping devices such as the linear ion trap, multiple stages of tandem mass spectrometry (MS^n) are possible where specific product ions are isolated and activated, leading to the formation of secondary product ions.[116] This concept is particularly useful in the elucidation of fragmentation pathways and characterisation of molecular structures.[117]

1.7.4.1. Product ion nomenclature

The application of a standard nomenclature has proven to be a significant benefit for compound classes such as proteins[118] and carbohydrates.[119] It has standardised spectral assignments, streamlining the comparisons of results as well as simplifying the reporting of product ions in publications.[120] This is a significant challenge in the analysis of synthetic polymers, where each polymer has unique backbone connectivity, chain end groups and chain architecture. This has resulted in publication-specific nomenclature where each polymer is classified individually. Wesdemiotis *et al.* recently proposed a standardised nomenclature for a range of linear synthetic polymers, where the following series of rules permit the assignment of product ions outlined in Figure 1.3.[120]

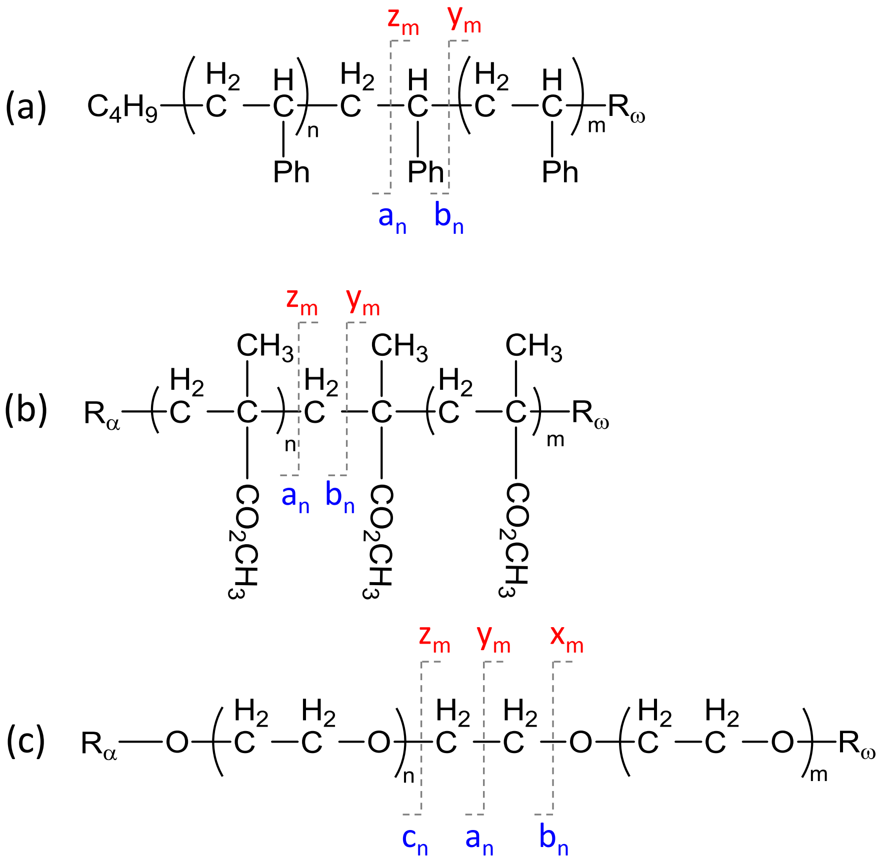

Figure 1.3 Structures and proposed ion assignments for (a) Poly(styrene), (b) Poly(methyl methacrylate) and (c) Poly(ethylene glycol).

For all linear polymers, the end groups are assigned as **α** for the initiating group and **ω** for the terminating group. Any product ion that is formed containing the initiating group (**α**) is labelled beginning with $\mathbf{a_n}$, and continuing with $\mathbf{b_n}$ and $\mathbf{c_n}$, depending upon the number of different backbone bonds present in the polymer. In each case, the subscript **n** denotes the number of intact monomers present in a given product ion. In a reciprocal manner, product ions containing the terminating group (**ω**) are labelled from $\mathbf{z_m}$, and continue backwards through the alphabet depending on the number of different backbone bonds, where subscript **m** denotes the number of intact monomer units in a specific product ion. The presence of additional symbols highlights differences in the types of product ions that could be theoretically generated through cleavage of a given bond. These rules are summarised below from Wesdemiotis *et al.*[120]:

- A product ion with an unpaired electron (radical ion, distonic ion) is designated by a superscript radical e.g. $\mathbf{b_n^{\bullet}}$.
- A product ion with an unsaturated terminal group (1 H atom less than the radical) is assigned with no further additions.
- A product ion with a saturated terminal group (1 H atom more than the radical) is designated with a superscript double prime, e.g. $\mathbf{b_n''}$.
- The presence of side chains can form an unsaturated terminal group through different side chain losses. To denote these different ions, subscript letters follow the assignment, where the loss of the smallest group is designated **a**, e.g. $\mathbf{b_{na}}$ and loss of the larger group is designated **b**, e.g. $\mathbf{b_{nb}}$.
- Consecutive backbone cleavages can lead to the formation of internal fragment ions, which do not contain either end groups. These species are denoted with capital letters, beginning with the centre of the alphabet, e.g. $\mathbf{J_n}$, $\mathbf{K_n}$ and $\mathbf{L_n}$.
- The presence of symmetrical end groups, as is the case for hydroxyl terminated PEG, generate product ions that have the same nominal mass in such a way that $\mathbf{a_n} = \mathbf{y_m}$, $\mathbf{b_n} = \mathbf{x_m}$ and $\mathbf{c_n} = \mathbf{z_m}$. In this instance, only the $\mathbf{a_n}$, $\mathbf{b_n}$ and $\mathbf{c_n}$ nomenclature is required to label the observed product ions.
- If a product ion is generated that no longer contains the original charge carrier, this is denoted by the presence of a superscripted exclamation point, e.g. $\mathbf{b_n^{!}}$.
- Multiply charged product ions are denoted with the appropriate charge assignment, e.g. $\mathbf{b_n^{2+}}$.
- For product ions generated from copolymers, the assignment contains the number of intact monomer units of each kind present in the product ion in superscript. For the

analysis of an ethylene glycol/propylene glycol copolymer, the presence of a $\mathbf{b_2}$ cleavage containing one monomer of each would be labelled $\mathbf{b_2^{E1P1}}$.

1.7.4.2. CID tandem MS of synthetic polymers

In tandem MS experiments, after isolation, the precursor ion is activated. Activation of an ion can be achieved in a number of ways, however the overall goal is to increase the internal energy of a precursor ion to a level that will induce unimolecular decomposition and the formation of product ions.[117] CID is the most common method of ion activation used in mass spectrometers that are capable of tandem MS experiments. This method of activation occurs through collision between the precursor ion and an inert neutral gas; typically helium, nitrogen or argon. Activation of the precursor ion through collision with a neutral gas results in a fraction of the translational energy of the precursor ion being converted to internal energy bringing the ion into an excited state. The resultant increase in internal energy induces fragmentation in the precursor ion through unimolecular decomposition. The amount of translation energy that can be converted to internal energy for a precursor ion can be defined in **Equation 1.6**, where **E** is the maximum internal energy. $\mathbf{E_k}$ is the kinetic energy of the precursor ion, and **N** and $\mathbf{m_p}$ are the masses of the collision gas and precursor ion respectively.[121]

$$E = \frac{N}{m_p + N} E_k \qquad \textbf{(1.6)}$$

The selection of the collision gas is important, as the cross section of the gas molecules used varies significantly. In a technique such as CID, which is reliant on collisions to activate ions, gas molecules with a larger cross section have a higher probability of being involved in collisions. It is also known from Quasi-Equilibrium Theory (QET) that gas molecules of increased mass result in a higher energy transfer than smaller gas molecules. Alongside the chemistry of the gas, it is important to consider the pressure of the gas, as higher pressure not only increase the number of ions undergoing collisions, but also improve the probability of an ion being involved in multiple collisions. However, for CID experiments in an FTICR mass analyser, which uses an ultra-high vacuum, the presence of a high pressure gas is not advantageous, as it increases the time taken to perform mass analysis, and has a negative effect upon mass resolution.

All CID processes can be divided into two categories dependent upon the initial translational energy of the precursor ion. CID involving collision energies in the range of 1-100 eV are considered low energy collisions, and typically occur in quadrupole and ion trap instruments.[117]

High energy collisions which occur in the keV range can be observed in sector and ToF/ToF instruments. Ions analysed by low energy CID experience internal energies of < 100 eV, which leads to vibrational excitation but not electronic excitation. This internal energy is consequently distributed over all available vibrational degrees of freedom (an ergodic process), and therefore results in cleavage of the most labile bonds. This can often restrict the amount of structural information that can be obtained from tandem MS spectra. Ion excitation in high energy CID is mainly an electronic process, where initial electron activation is followed by redistribution of energy through radiationless transitions.[117] The increased energy conversion in high energy CID creates activated ions, which result in a higher probability of direct bond cleavage than can be achieved with low energy CID. Regardless of energy level, CID has been the most widely applied activation technique to the analysis of synthetic homopolymers and copolymers, with regular reviews detailing recent publications (Table 1.3). Publications involving characterisation of monomer sequence and terminal groups for common synthetic polymers analysed by CID tandem MS are summarised below Table 1.3.

Table 1.3 Summary of homopolymers analysed using CID tandem MS.

Polymer	References
Poly(ethylene glycol)	87,88,91,104,122-132
Poly(methyl methacrylate)	104,122,133-136
Poly(ethylene terephthalate)	122
Poly(alkyl acrylate)s	73,137-139
Poly(styrene)	104,133,140-144
Poly(propylene glycol)	87,145
Poly(ester)s	146
Poly(dimethyl siloxane)	104
Poly(lactide)	147
Poly(ethylene imine)	148
Poly(sulfone)	149

As discussed previously, the role of the cation is essential to successful MS measurements of synthetic polymers. In CID tandem MS experiments, cation selection is of more significance, as the interaction between the polymer and the cation must be sufficiently strong to survive the CID process, where ineffective cation binding results in cation detachment. This effect is more pronounced in low energy CID, where the internal energy of the precursor ion is increased slowly, resulting in breaking of the weakest bond/interaction.[17] If cation detachment is the weakest interaction, then any fragments generated in the CID process will be neutral, and consequently not observed in the mass spectrum. Scrivens *et al.* demonstrated that increasing the size of the alkali metal cation resulted in increased cation detachment, as characterised by the presence of the raw metal cation in the mass spectrum in the analysis of PMMA.[133] The trend is related to the cation binding energy, and is supported by the observation that the trend for cation detachment is less pronounced with larger polymer chains, where the binding of larger cations is more effectively stabilised. A second polar polymer, PEG, exhibits similar behaviour to PMMA, where the analysis of PEG oligomers using low energy CID was optimal for precursor ions containing a lithium cation.[81,88,131,132] This observation has been investigated experimentally and theoretically, with both methods providing evidence for the importance of the cation binding. Bogan *et al.* utilised the ability of ESI to generate doubly charged PEG ions, ionised with two different alkali metal cations. Isolation and fragmentation with low energy CID resulted in simple cation detachment, where cation loss reflected the Lewis acidity of the cations, with caesium lost most easily.[91] This result is supported by theoretical calculations that modelled PEG with a range of alkali metals, and demonstrated that of all cation-polymer interactions, only lithium had sufficient binding energy to withstand the proposed low energy fragmentation pathway.[150] For non-polar polymers such as PS, cation selection was found to be less influential for transition metals, such as silver and copper cations, where differences between spectra were quantified by the presence of non-metal bound PS ions.[133,140] It has been demonstrated that CID tandem MS experiments can be performed on precursor ions that do not contain metal charge carriers. Chen *et al.* reported that formation of a protonated precursor ion, although unfavourable, would readily fragment to the extent that in-source fragmentation could not be avoided.[87] The major challenge for this method is that direct formation of protonated polymers is a significant challenge, with cation attachment being the dominant mechanism, even when metal salts are not added to the polymer.[87] However, Alhazmi *et al.* demonstrated a robust approach for the formation of protonated PMMA through initial complexation of the polymer with a short peptide chain, which permitted successful protonation of the polymer. Under activated conditions, this protonated precursor ion yielded complementary fragmentations to those observed for alkali metal cationised PMMA, with a preference for side chain loss.[136] Nasioudis *et al.* formed PEG precursor ions with a series of ammonium cation charge carriers, where the substituents of the ammonium ion were shown to influence the formation of a structurally significant CID tandem MS spectrum.[128] Quaternary and tertiary ammonium cations with bulky substituents had insufficient binding energy, where the only fragmentation mechanism observed was cation detachment. However, primary and tertiary ammonium cations with one long chain substituent led to extensive fragmentation of the polymer, with product ions either retaining the charge carrier or present as protonated adducts.[128]

A major advantage to the use of CID tandem MS experiments is the unambiguous identification and characterisation of polymer end groups. This has been shown to be an effective method of differentiating homopolymers with different end groups, generating end group specific spectra for PEG,[123,126] PMMA[134,137] and PS.[141] It was found in a number of publications that the presence of specific terminal groups influenced the signal-to-noise ratio of the product ions produced, demonstrating the importance of the end groups in cation binding.[124,129,137,151] Jackson *et al.* additionally found that the presence of terminal groups attached with ester bonds generated product ion series of internal fragments containing neither end group, highlighting the labile nature of these bonds.[129]

CID tandem MS has also been effectively used in the analysis of polymeric species with differing architectures, including the analysis of a range of synthetic copolymers. Work by Chaicharoen *et al.* demonstrated the first use of multi-stage CID tandem MS for the differentiation of linear and branched isobaric poly(acrylate)s, where the product ions generated were characteristic of the branch sizes.[138] The ability to characterise synthetic copolymers has been a significant challenge for the analytical chemist, as there are very few methods of differentiating block and random copolymers post-polymerisation. Jackson *et al.* introduced CID tandem MS as a successful method of characterising methyl methacrylate/butyl methacrylate block copolymers, permitting complete sequence characterisation for a specific copolymer oligomer.[152] This group also applied the CID tandem MS approach to the analysis of copolyethers, distinguishing block and random copolymers and allowing identification of the end groups present.[153] Terrier *et al.* expanded on this work on polyethers; applying CID tandem MS to the differentiation of triblock copolyethers that contain the same composition in repeat units but with different structures.[154] One of the major issues with the generation of the copolymers is the statistical nature in which they are formed, leading to a significant number of overlapping precursor ion peaks. Wesdemiotis *et al.* demonstrated that off-line SEC prior to MALDI-CID gave simplified mass spectra, allowing directional sequence information to be obtained for a block copolymer of poly(fluorooxetane-co-tetrahydrofuran).[155] *Weidner et al.* demonstrated that liquid adsorption chromatography (LAC) prior to MALDI-CID provided sufficient separation that species of the same nominal mass could be analysed individually, permitting the determination of the block lengths present.[156] As described previously, the application of liquid phase separation techniques is ideally suited to electrospray ionisation, where the analysis of copolymers by CID tandem MS is no exception. Girod *et al.* demonstrated in a series of publications focussed on the optimisation of PEG-b-PS block copolymer. The authors discovered that the combination of liquid chromatography at critical conditions (LCCC) prior to ESI-CID provided real time separation of the different copolymer species.[157] This work was optimised through the addition of lithium salts to promote ionisation, where the resultant precursor ion fragmented through sequential styrene losses, allowing for the end group and styrene block length to be accurately calculated.[158] Crecelius *et al*. performed work on a second PEG-b-PS copolymer, confirming that under activated conditions the bond most easily cleaved is that which joins the PEG and PS blocks together.[159] Miladinovic *et al.* recently published an extensive investigation into the analysis of copolymers by CID tandem MS. The authors demonstrated that random and block copolymers of methyl methacrylate/butyl methacrylate could be distinguished rapidly, based on characteristic patterns in the tandem MS spectra.[160] It was found that under activated conditions block copolymers have a tendency to fragment one block preferentially, leading to an intense series of product ion peaks, whereas random copolymers still have this preference, but due to the random distribution of peaks the resultant tandem MS spectrum is complex.[160]

1.7.4.3. CID tandem MS fragmentation mechanisms

Given that the structure of each type of polymer is unique, the fragmentation mechanism is specific to the precursor ion of interest. Despite this, the fragmentation mechanisms observed can be categorised as either: charge-induced fragmentations, charge-remote rearrangements or charge-remote fragmentations via radical intermediates.[120] Of the three methods, charge remote fragmentation processes dominate, where CID tandem MS of silver adducted PS is an example. Random homolytic cleavage of the backbone bonds of PS result in the preferential formation of $\mathbf{b_n}^{\bullet}$ and $\mathbf{z_m}^{\bullet}$ radical species at the secondary carbon atom. Radical stabilisation occurs by a 1,5 hydrogen shift, as shown in the first mechanism of Scheme 1.1.[142,143]

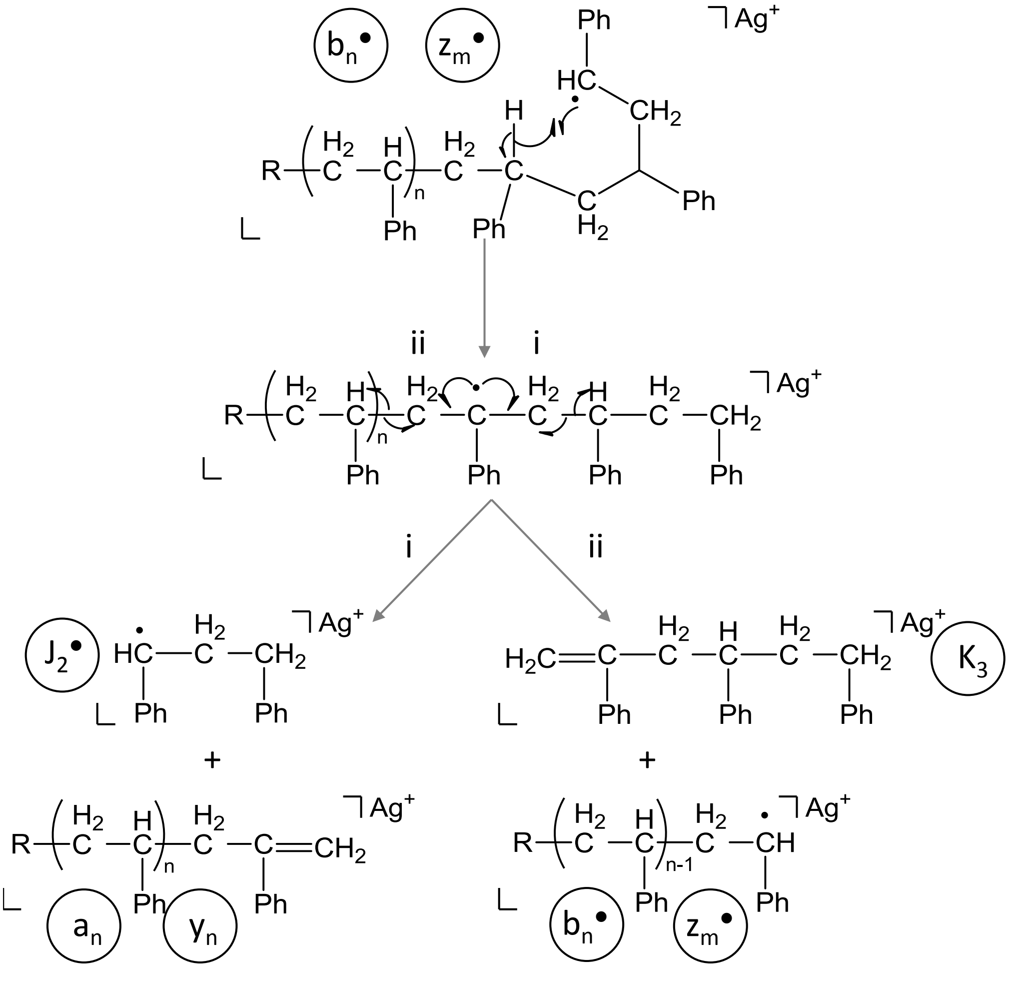

Scheme 1.1 Charge remote fragmentation of poly(styrene).

The resultant mid chain radical can dissociate via two competing fragmentation mechanisms, labelled **i** and **ii** in Scheme 1.1. The product ions observed provide evidence for both mechanisms occurring, where the product ion peaks with the largest signal to noise ratio are generated from route **i** and are low molecular weight species. However, the product ion peaks that provide most structural information, and whose repeat sequence of peaks covers the majority of the *m/z* range, are $\mathbf{b_n}$ and $\mathbf{y_m}$ ions, formed by the mechanism labelled **ii** in Scheme 1.1.

The fragmentation mechanism observed in CID tandem MS is dependent upon the amount of energy imparted in the process. It was found for lithium adducted PEG that low energy CID tandem MS in a quadrupole ion trap generated $\mathbf{c_n}''$ and $\mathbf{b_n}$ product ions, which are accounted for by the charge directed fragmentation mechanism shown in Scheme 1.2.[120]

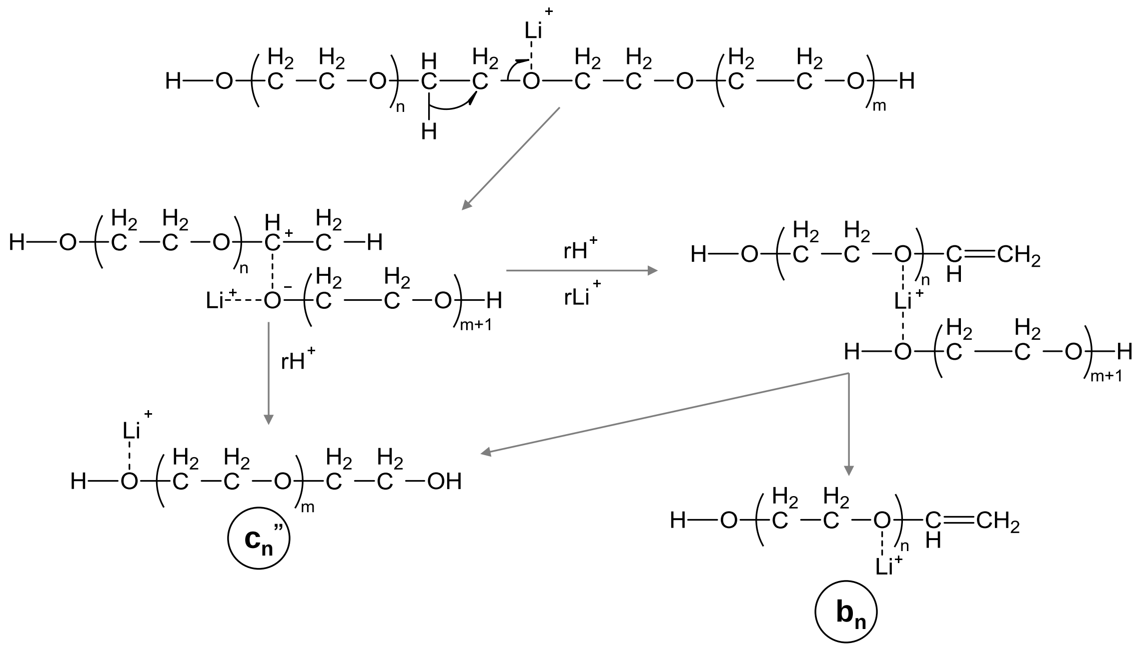

Scheme 1.2 Charge directed fragmentation of poly(ethylene glycol).

Coordination of the polymer to the lithium cation weakens the adjacent C-O bond, which results in bond cleavage, where a favourable 1,2 hydride shift generates a secondary carbocation, as shown in the first reaction of Scheme 1.2. As a result of this hydride shift, an ion-dipole complex is formed that has a stabilising effect upon the relative charged species. Subsequent proton transfer from the positively charged ethyl to the basic alkoxylate, results in direct formation of the **c_n”** product ion. Alternatively, proton transfer can be accompanied by rearrangement of the ligands, to form a lithium bound complex between ether oxygen atoms. This complex can dissociate to form both **c_n”** and **b_n** product ions. The fragmentation pathway is ultimately determined by the internal energy, and consequently the lifetime of the precursor ion. Highly excited, short lived species are likely to fragment with direct formation of the **c_n”** ion from the ion-dipole complex, whereas less excited and longer lived precursor ions favour ligand rearrangement and the formation of both **c_n”** and **b_n** product ions.

1.7.4.4. Electron- based tandem MS techniques

The introduction of electron-based fragmentation techniques has been limited in the application to the analysis of synthetic polymers. This is not the case for other classes of compounds, such as biopolymers, and other small molecules, where the number of publications relating to electron-based fragmentation techniques has grown significantly since their introduction (Figure 1.4). Electron Capture Dissociation (ECD), introduced to the MS community in 1998 by Zubarev *et al.*, is an activation method that causes fragmentation in multiply charged precursor ions through electron capture.[161] Performed in an FTICR mass analyser, this technique utilises low energy electrons, with typically 1 eV-5 eV of kinetic energy. These low energy electrons are captured by a multiply charged precursor ion, leading to the formation of an unstable hypervalent intermediate $[M + nH]^{(n-1)+\bullet}$. This intermediate state alters the bond energies with the ion, eventually resulting in fragmentation.

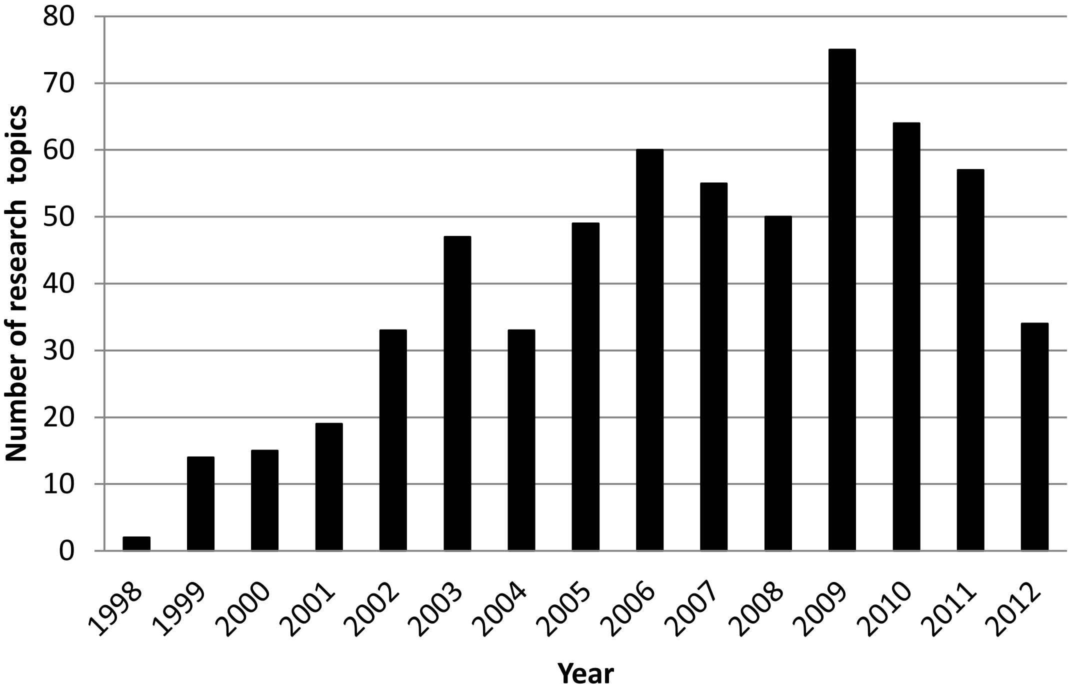

Figure 1.4 The number of SciFinder publications for "electron capture dissociation mass spectrometry" per year.

This activation method has been utilised extensively in the analysis of high molecular weight biomolecules, such as proteins and peptides, where electron capture has been shown to impart sufficient energy into the precursor ion to cause bond cleavage. Conventional activation using CID or IRMPD results in the formation of **b** and **y** type product ions, through cleavage of the peptide bond (Figure 1.5).[162] ECD has been shown to generate additional structural information through the formation of **c** and **z** type product ions, where the combined product ions of the different fragmentation techniques provide enhanced peptide sequence coverage.[163]. These differences in the fragmentation mechanism have been exploited particularly in the analysis of peptides containing labile modifications. [164,165]

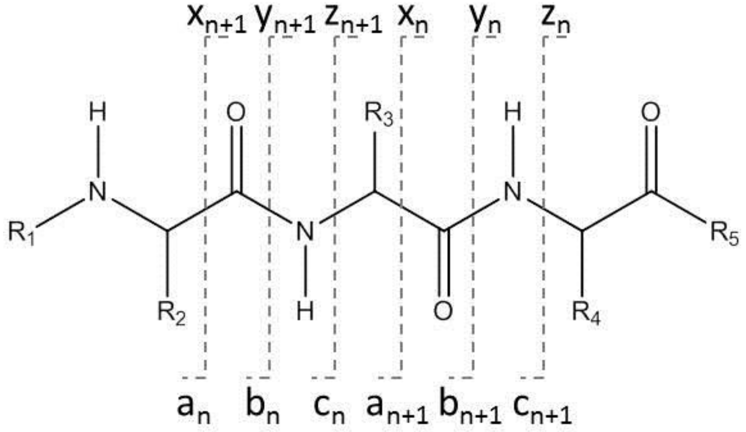

Figure 1.5 Common peptide backbone cleavages and associated nomenclature.

In spite of the success of ECD for the characterisation of a range of molecules, the mechanism by which fragmentation occurs remains a contentious issue. Two main strategies have been proposed based on the observed fragmentation in peptides; the first to be discussed is known as the "Hot hydrogen" or "Cornell" mechanism is outlined in Scheme 1.3. Initial electron capture neutralises the charge at a protonated amine unit, forming the hypervalent radical species. Stabilisation of this species is achieved through the ejection of a hydrogen radical ($H^{\bullet}$) that subsequently traverses the peptide backbone, interacting with carbonyl oxygen functionalities. As shown in Scheme 1.3, interaction of the hydrogen radical at the carbonyl oxygen results in cleavage of the N-C_α bond and radical migration to form a secondary carbon radical.[166,167] This strategy rationalises the preferential cleavage of the stronger N-C_α bond over the more fragile peptide bond, however recent experiments have cast doubt on this mechanism, due to the large distances that the hydrogen radical must travel from the site of protonation to the site of backbone bond cleavage.[168]

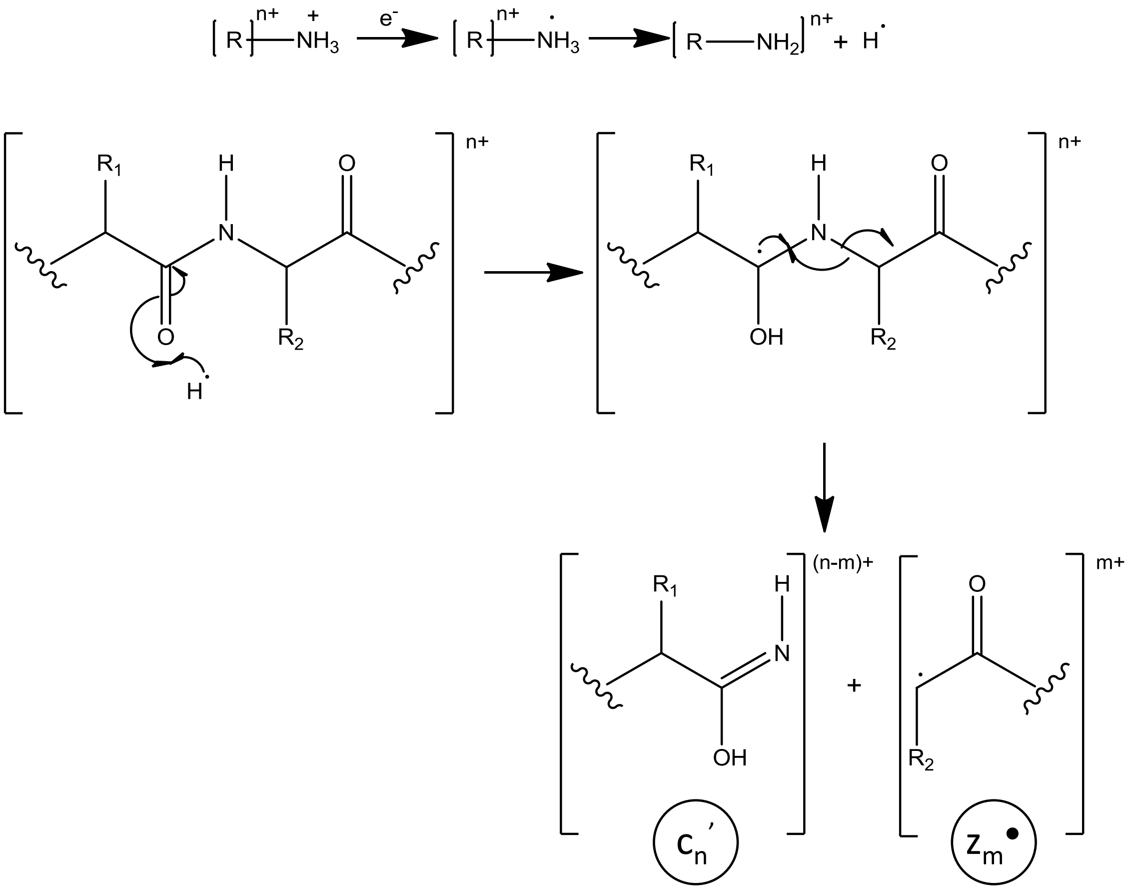

Scheme 1.3 Cornell "Hot hydrogen" ECD mechanism.

The initially generated hydrogen radical can also interact with disulphide bonds, resulting in bond cleavage as shown in Scheme 1.4, thus accounting for the disulphide bond cleavage observed in ECD of peptides.[169-171]

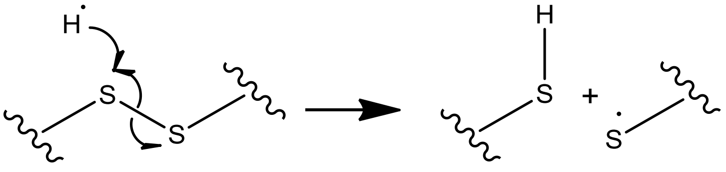

Scheme 1.4 Cornell "Hot hydrogen" disulphide bond cleavage.

The second mechanism, known as the "Superbase" or "Utah-Washington" is outlined in Scheme 1.5.[168,172] This mechanism proposes that the presence of a radical at the cleavage site is generated through radical migration from the initially formed hypervalent radical site, or by electron capture directly at the cleavage site. Fragmentation of the N-C_α bond occurs in a similar way to the Cornell mechanism; however a negative charge is generated, which is neutralised by a proximal proton.[168,173]

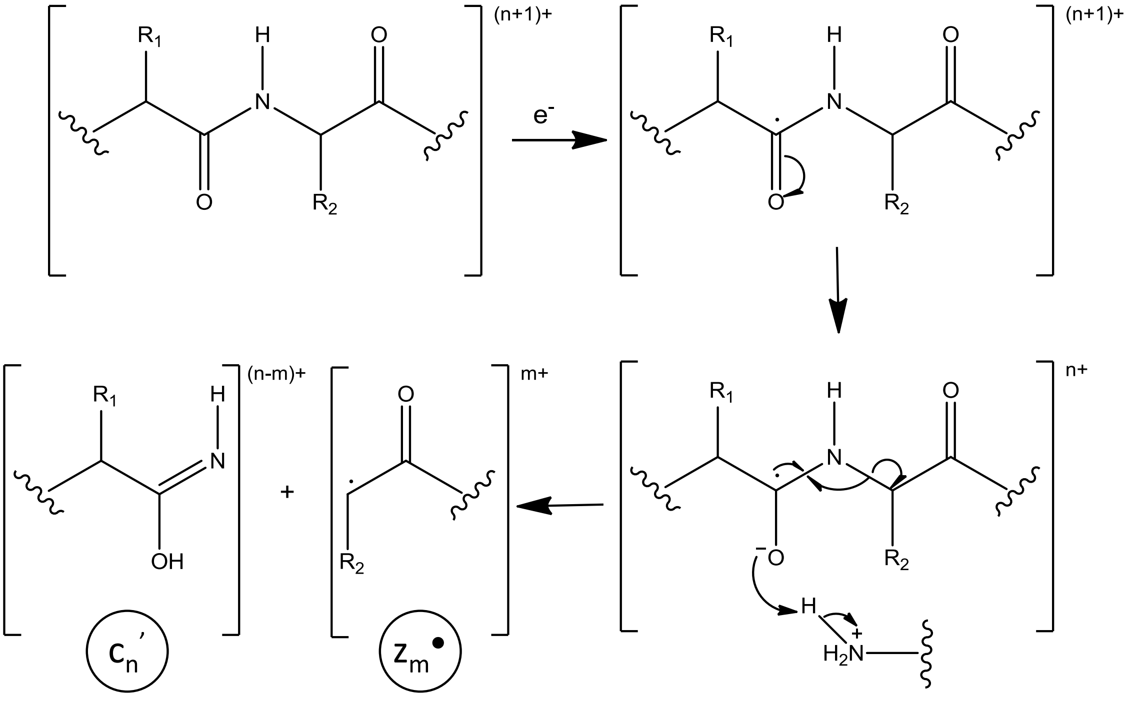

Scheme 1.5 Utah Washington "Superbase" ECD Mechanism.

Like the Cornell mechanism, a method of disulphide cleavage is proposed where initial electron capture at the S-S bond results in formation of an S radical containing fragment and a fragment containing S^- that reacts with a proximal proton, as shown in Scheme 1.5.

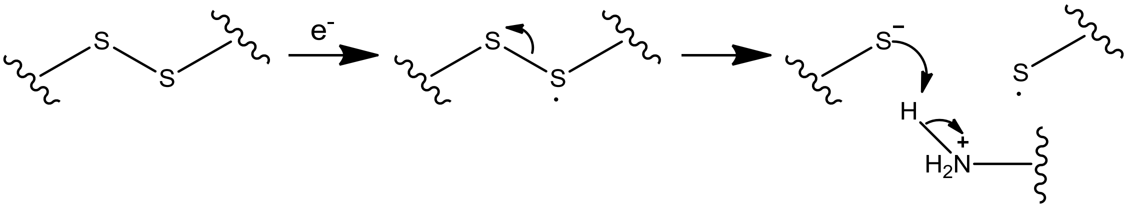

Scheme 1.6 Utah Washington "Superbase" disulphide bond cleavage.

The effort to determine the mechanism by which peptide backbone fragmentation occurs in ECD will continue. The focus upon the ECD of macromolecules has not been restricted to backbone fragmentation, as a number of publications highlight specific observations that relate to side-chain losses and other rearrangement reactions that occur during ECD. A more transparent understanding of how these reactions occur may provide support to the underlying backbone fragmentation mechanism. Leymarie *et al.* analysed a series of cyclic peptides that under ECD conditions generated losses of side chain and amino acid moieties, the formation of which could be accounted for by initial ring opening with the subsequent generation of an α-C$^{\bullet}$ that is involved in radical driven rearrangements.[174] Unfortunately, given the cyclic nature of these peptides, it is impossible to distinguish the product ions that result from primary cleavages or secondary fragmentations. Experiments to distinguish the mechanism of formation were performed by O'Connor *et al.,* who utilised two pairs of peptide sequences where one peptide contained ^{2}D labelled glycine residues that demonstrated deuterium scrambling under ECD conditions. The authors postulated that following rapid initial backbone cleavage long-lived radical intermediates were formed and stabilised through H/D abstraction from α-carbon atoms.[175] The lifetimes of such intermediates have been measured in the order of milliseconds through the analysis of peptides with a double resonance ECD experiment, thus accounting for the multiple radical rearrangements that can occur on this timescale.[176] The ECD spectra obtained for the analysis of peptides has been shown to reflect the conformations adopted by the molecules under experimental conditions. Work by Chakraborty *et al.* found for a series of peptides the degree of microsolvation and hydrogen bonding play an important role in the stability of the intact reduced ion species,[177] where the species could survive on the microsecond timescale. Mihalca *et al.* demonstrated that ECD of peptides under low temperature conditions generated fewer product ions than under ambient conditions, due to increased conformational homogeneity at low temperatures.[178] The low temperature conditions meant that the peptides were restrained in terms of conformation, and unable to form the normal degrees of hydrogen bonding due to the constrained formation, providing support for the observation and conclusions drawn by Chakraborty.

The success of ECD has led to the development of a number of related techniques that have extended the application of electron-based fragmentation techniques. Kjeldsen *et al.* pioneered the use of 'hot' electrons that had 10 eV of kinetic energy. Hot ECD (HECD) of polypeptides resulted in extensive fragmentation, including differentiation of leucine and isoleucine amino acids based on secondary fragmentation product ions.[179] The ability to differentiate two amino acids that have the same nominal mass is a significant benefit of HECD, and one that has been exploited by other research groups.[180]

The application of electron-based fragmentation techniques has not been restricted solely to multiply charged precursor ions. Electron-induced excitation of ions from organics (EIEIO),[181] probed the interaction of singly charged precursor ions with electrons whose energy was just below the second ionisation energy of the selected precursor ion. Irradiation of ions with electrons of this energy was shown to readily induce fragmentation.[181] The product ions generated by CID and EIEIO were similar, and therefore under EIEIO conditions it was believed that vibrational excitation was dominant. The term Electron Induced Dissociation (EID) has been used to refer to studies that utilise electrons with energies in the region of 10-25 eV. Lioe *et al.* demonstrated that, like other electron-based fragmentation techniques, EID provides complementary structural information to that obtained by CID in the analysis of singly charged short chain peptides.[182] In a comparison experiment with CID and IRMPD, EID generated extensive fragmentation regardless of size for a series of phosphate containing metabolites, whereas the fragmentation in CID and IRMPD was found to be dependent upon molecular weight.[183] EID has also been shown to be an effective means of characterising a range of compounds, including cationic[184] and zwitterionic clusters,[185] transition metal containing complexes,[186] pharmaceutical compounds[187] and metal bound amino acids,[188] demonstrating that EID is not limited to the analysis of protonated biomolecules. A major hurdle in the wider application of electron-based fragmentation techniques is the low fragmentation efficiency, which requires long irradiation times, however work by Prakash *et al.* demonstrated that EID was feasible on a timescale compatible with liquid chromatography for a pharmaceutical drug compound.[189] A major advantage of EID is the ability to analyse singly charged precursor ions, meaning that this technique could be used effectively with MALDI.

Electron Detachment Dissociation (EDD) is an electron-based fragmentation technique that, unlike the others discussed here, is used in the analysis of negatively charged precursor ions. Introduced in 2001, this technique relies on electron detachment to form an unstable odd electron intermediate that subsequently fragments. The energies of the electrons used in these types of experiments tend to be in the order of 10 eV.[190] Despite having a lower fragmentation efficiency that requires longer irradiation times than ECD or ETD, the rich fragmentation chemistry of EDD has provided extensive structural information for a range of polyanions.[191] The classes of compound that have been routinely examined using EDD include oligosaccharides,[192] peptides,[190] oligonucleotides[193] and gangliosides.[194] Activation of anions can also be achieved through electron capture, which initially appears problematic due to electrostatic repulsion, but has been shown to occur. Negative ion Electron Capture Dissociation (niECD) was demonstrated by Hakansson *et al.,* where singly charged peptides were shown to form dianions when irradiated with 3.5-6.5 eV electrons that resulted in fragmentation generating **c** and **z** product ions.[195]

The source of low energy electrons is not restricted to electron dispenser cathodes, where anions with suitably low electron affinities can be utilised. Electron Transfer Dissociation (ETD) was introduced by Syka *et al.* in 2006, where it was shown that electron transfer from anthracene anions could be utilised in the fragmentation of multiply charged phosphopeptides.[196] The use of anions has proven to be particularly advantageous, as electron transfer reactions can be performed in a wider range of mass analysers, including quadrupoles and ion traps. The superior cross sectional area of the anions dramatically improves the number of collisions that occur in ETD,[197] however the amount of energy transferred to the precursor ion tends to be lower than that observed in ECD, due to energy redistribution within the anion and the effect of collisional cooling.[198] Like ECD, however, ETD of peptides generates the characteristic **c** and **z** type products ions, and has been shown to preserve labile post-translational modifications.[199,200]

1.7.4.5. Electron-based tandem MS of synthetic polymers

Aside from CID, the application of other activation techniques to polymer tandem MS experiments has been limited. The generation of multiply charged ions, by ESI opened up the potential application of Electron Capture Dissociation (ECD) to the analysis of synthetic polymers. A successful technique for the analysis of biopolymers, ECD has been used to provide complementary results to those achieved by CID for peptides and proteins.[161,167] Cerda *et al.* demonstrated that ECD was an effective means of sequencing multiply charged PEGs ionised with protons, ammonium and alkali metal cations, where the product ions generated were identical to those formed by CID, suggesting a similarity in the fragmentation mechanism.[201] The authors suggested that the mechanism by which ECD is believed to act, involves initial neutralisation of a charge site where the distribution of product ions generated will reflect the likely points of charge carrier attachment.[202] The success of PEG analysis by ECD led to characterisation of an ethylene glycol/propylene glycol block copolymer. It was found that ECD was effective at eliminating sequence misleading rearrangements observed in CID, and demonstrated that a postulated tri-block copolymer was in fact a di-block copolymer.[203] The applicability of ECD to other synthetic polymers has not been successful, as highlighted by Miladinovic *et al.,* who demonstrated that ECD generated minimal fragmentation for the analysis of PMMA, where only product ions formed by small neutral losses were detected.[160]
The application of ETD to the analysis of synthetic polymers has yet to be published in the wider scientific literature, however preliminary results for polyethers[204] and polyesters[205] have been presented at recent conferences.

1.7.4.6. IRMPD of synthetic polymers

Mass spectrometrists have found alternative activation methods to CID that raise the internal energy of a precursor ion. One method is the use of photodissociation, where ions achieve an excited state through the absorption of one or more photons. In the case of Infrared Multi-Photon Dissociation (IRMPD), IR lasers create photons of quantifiable energy that are subsequently absorbed by the ions. The popularity of this activation method has increased with the demand for trapping mass analysers, as ions can be stored for extended time periods, with particular application to large biomolecules.[206] The mechanism of action is believed to involve absorption of IR radiation by IR active modes present in the ion, where the energy is redistributed over all the vibrational degrees of freedom, akin to CID. The activation is stepwise through a multiphoton process, followed by unimolecular dissociation following the lowest energy pathway.[117] It is important to consider that absorption of the photons by the precursor ion relies upon the ion being able to absorb energy in the form of photons that lead to excited states above the dissociation threshold. The technique has proven to be an effective means of analysing homopolymers, such as PEG, PMMA and PS. Despite no journal publications to date, McGrath and Glish have used the internet to report that IRMPD generated a larger number of product ions with a higher S/N ratio in a more facile way.[207] For IRMPD, there is no requirement for ion isolation for homopolymers, where activation of the entire ion cloud results in the formation of the same product ions as individual precursor ion analysis. It was also observed that continuous activation resulted in activation of first stage product ions, generating further product ions, and thus potentially increasing the amount of structural information that could be obtained.[207]

1.7.5. Ion Mobility Spectrometry (IMS)

It has already been demonstrated how effective liquid phase separation can be for the analysis of synthetic polymers. Research into gas phase ion separation has seen the development of ion mobility, a technique that separates ions based on the rotational cross section of a molecule in the gas phase. This approach has shown to be a valuable method of investigating the interactions of polymers with a metal charge carrier, adding significant mass to the structures proposed by theoretical calculations for PS,[43] PMMA[44] and PEG.[45] The calculation of gas phase structures can aid in the postulation of fragmentation mechanisms when tandem MS experiments are performed alongside ion mobility.[43,44] Jackson *et al.* utilised ion mobility to probe the gas phase conformations of ethylene glycol/propylene glycol copolymers, where change in molecular weight and increasing the ionic radii generated an ion with a larger collisional cross section, supporting the work performed previously on homopolymers. A more surprising conclusion from Jackson *et al.* was that oligomers of the same nominal mass with random or block structures represented no change in the conformation, demonstrating that the conformation adopted is independent of monomer sequence.[153] Trimpin *et al.* demonstrated that ion mobility allowed charge state families to be individually resolved for multiply charged PEGs with number averaged molecular weight ranging from 6000 to 14000 Da.[208] The authors demonstrated that an increase in charge state resulted in a larger rotational cross section for a given degree of polymerisation. This is the opposite of what is observed for biopolymers, and is found to result from increasing Coulomb energy through the addition of extra metal cations, indeed higher charge states were found to adopt a near linear conformation.[208] Trimpin *et al.* further extended the amount of information that could be obtained from an ion mobility experiment through the addition of a second ion mobility separation post ion activation (IMS/IMS-MS). This was found not only to improve the dynamic range and sensitivity of the instrument, but was also shown to provide subtle structural characteristics that were found to be polymer specific, including modified end groups and chain branching, allowing sample differentiation.[209] Further demonstration of the polymer specific nature of ion mobility technique was found in work by De Winter *et al.,* who discovered that doubly and triply charged ions of a poly(lactide) had a breaking point in the ion mobility distribution where the collisional cross section was temporarily independent of increasing monomer mass.[210]

2. Instrumentation

In all mass spectrometry systems, ions are separated based on their mass-to-charge ratios (*m/z*). However, each type of mass spectrometer has attributes that favour specific applications in such a way that MS and tandem MS spectra may vary significantly between instruments. Mass spectrometers have three distinct operations which permit the analysis of a compound:

- Ionisation - The conversion of neutral molecules into charged gas phase ions.
- Separation - Discrimination of ions based on the *m/z* values.
- Detection - Conversion of ions into an electrical signal which allows the abundance of ions to be calculated.

As there are a wide variety of ionisation techniques and mass-to-charge separators utilised in mass spectrometry, detail will be confined to those techniques used in the course of the research outlined in this thesis, as well as techniques that have produced results to which comparisons are made in this thesis. The instruments used in this research were:

- LTQ-FT (ThermoFinnigan Corp.), a mass spectrometer integrating linear ion trap (LTQ) and Fourier Transform Ion Cyclotron Resonance (FTICR) mass analysers in series, with ionisation achieved through an ESI source.
- Xevo QToF (Waters Corp.), a quadrupole mass analyser, collision cell and time-of-flight (ToF) mass analyser connected in series. This mass spectrometer has an interchangeable ion source housing permitting ionisation by ESCi, ASAP and Atmospheric Pressure Gas Chromatography (AP-GC).
- Autoflex II ToF/ToF (Bruker Daltonics Ltd), a time-of-flight (ToF) mass analyser fitted with a MALDI source.

2.1. Ion Sources

The formation of ions for mass analysis is preferable to neutral molecules as the application of electric or magnetic forces can manipulate the energy and velocity of ions, enabling their separation and detection. Effective ionisation of a sample can ultimately determine analytical success. Consequently a variety of ionisation methods can be utilised depending on the desired application as shown in Figure 2.1. It is noted that the list provided in Figure 2.1, do not represent all ionisation methods used over the years, however they are the most common and the most relevant to the work presented in this thesis. Soft ionisation techniques such as ESI and MALDI can form intact molecular ions via different ionisation mechanisms including protonation, deprotonation or cation or anion attachment. In comparison a technique such Electron Ionisation (EI) involves electron ejection and imparts significantly more internal energy into the analyte molecules and results in higher levels of in-source fragmentation. Such is the importance of ion generation John Fenn and Koichi Tanaka, the inventors of ESI and MALDI respectively were awarded the Nobel prize in Chemistry in 2002.[211]

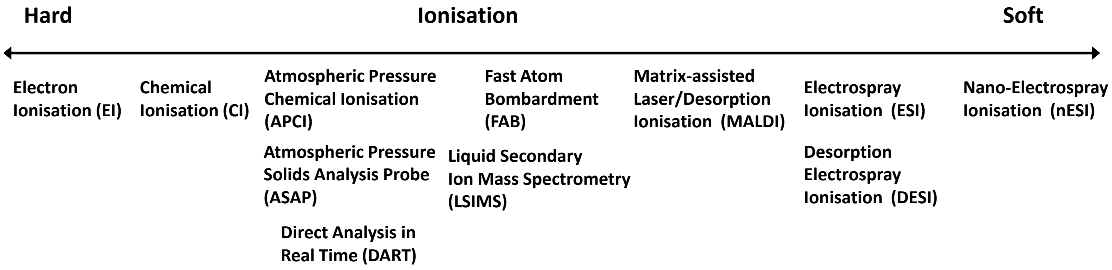

Figure 2.1 Comparison of ionisation techniques.

2.1.1. Matrix-Assisted Laser Desorption/Ionisation (MALDI)

2.1.1.1. Fundamentals of operation

MALDI was developed from laser desorption/ionisation (LDI) in 1988 by Karas and Hillenkamp[13] and later by Tanaka and co-workers[212] for use in the analysis of high molecular weight biomolecules and synthetic polymers. The analyte of interest is embedded in a host matrix to form a co-crystalline layer. The layer is subsequently irradiated with a short pulse from a laser beam at a wavelength that is strongly absorbed by the matrix. This leads to desorption of the matrix and analyte molecules into the gas phase, as shown in **Figure 2.2**. All charged species are initially accelerated by the potential difference that is established between the sample plate and the nearby grid electrode. Ionisation of a sample is thought to be a multi-step process with an initial ionisation event with secondary ion-molecule charge transfer reactions, where the most frequently proposed method is outlined in **Equations 2.1 – 2.4.**[5] (A more detailed discussion of the MALDI process can be found in recent publications by Garrison *et al.*[213,214]) Initially reactive matrix ionic (**Mat***) species collide with analyte molecules (**M**) leading to ion-molecule reactions that form analyte ions (**[M + H]$^+$**) in the desorption plume directly above the co-crystalline layer. Ionisation by MALDI generates predominantly singly charged molecular ions, which are formed by protonation/deprotonation or cation attachment.

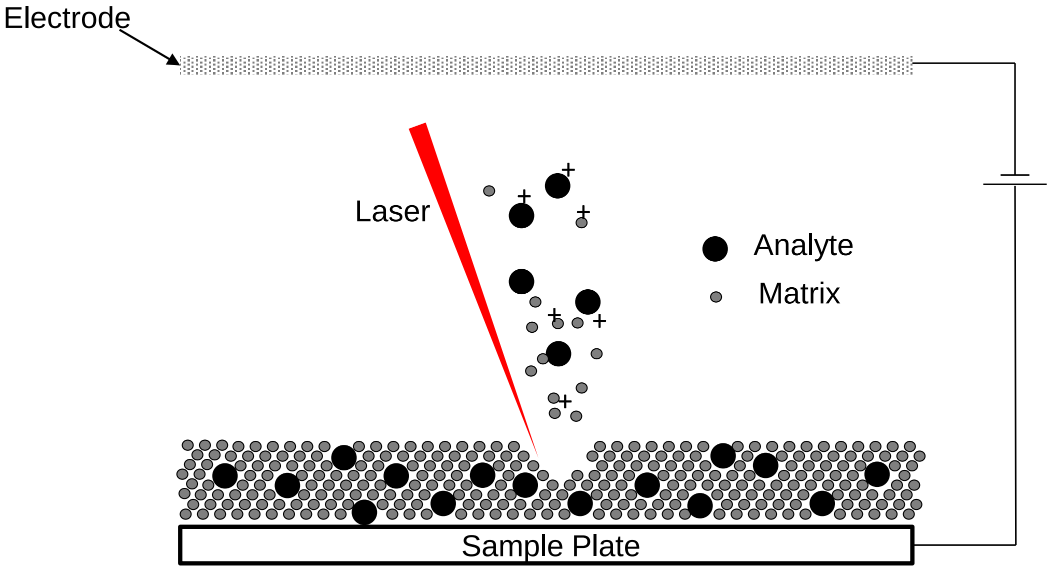

Figure 2.2 MALDI ionisation process.

$$Mat \overset{hv}{\rightarrow} Mat^* \qquad \textbf{(2.1)}$$

$$Mat^{*} + M \rightarrow (Mat - H)^{-} + [M + H]^{+} \qquad \textbf{(2.2)}$$

$$Mat^{*} + Mat \rightarrow (Mat - H)^{-} + MatH^{+} \qquad \textbf{(2.3)}$$

$$MatH^{+} + M \rightarrow Mat + [M + H]^{+} \qquad \textbf{(2.4)}$$

One of the most important aspects in MALDI mass spectrometry is preparation of the sample for analysis. It is desirable that a homogeneous layer is formed containing the analyte and matrix and where the application requires it, the addition of an additive such as a metal salt. The selection of the matrix is of critical importance as the matrix has numerous roles in MALDI including absorption of laser energy, a method of energy transfer to the analyte and as a medium to separate the analyte molecules preventing aggregation. Given these roles, there are a number of desired properties for a suitable matrix:

- Strong adsorption of radiation at the wavelength of the laser.
- Good solvent compatibility with the analyte and metal salt.
- Low sublimation temperature.
- Contribute to photochemical reactions allowing simple protonation/deprotonation.

The most commonly used matrices are low molecular weight organic acids which have all of the desired properties listed above.

It is important to consider the properties of the laser when preparing a sample for MALDI ionisation. Typically the lasers used in MALDI have wavelengths in the UV and IR regions of the electromagnetic spectrum. UV lasers, such as the N_2 (337 nm) are common in MALDI instruments where the emitted wavelength is close to the absorption maximum of a large number of matrices.[215] The major problems associated with N_2 lasers are the low repetition rate (< 100 Hz) and the relatively short lifetime of the laser ($\leq 10^8$ emissions). Due to these limitations, Nd:YAG lasers (355 nm) lasers can be used in high throughput UV-MALDI applications. IR lasers, such as the Er:YAG (2.94 µm) emit in the OH- and NH- stretch vibration range, therefore many of the matrices used for UV-MALDI are compatible.[215] A major disadvantage to IR lasers is the penetration depth of the laser, as it removes significantly more material than the UV lasers, reducing the number of repeat shots on a given spot. It is also known that the emission pulse length required for successful ionisation in IR-MALDI (5-100 ns) is significantly longer than for UV-MALDI (3-5 ns) and is believed to be a source of the lower resolution observed for IR-MALDI experiments.[16] The amount of energy required per pulse in MALDI is low, where UV-MALDI requires 10 µJ – 100 µJ per pulse and IR-MALDI requires 100 µJ

– 1 mJ. The major limitation for a laser in MALDI is the fluence (energy per unit area), where the energy required varies with the laser spot area.[215] As the laser is pulsed in MALDI, discrete packets of ions are generated; this matches up well with a number of mass analysers however (ToF) has been shown to be the most common.

2.1.1.2. Autoflex II MALDI

The ion source configuration adopted in the Autoflex II is shown in Figure 2.3. The target plate is axial to the ToF mass analyser creating a linear ion flight path. The laser system incorporates a 337 nm N_2 laser (3 ns pulse length and a pulse energy of 100 µJ), an attenuator which allows fine adjustments to the laser fluence and beam splitters that divert the laser light to the photodiode triggering the ToF measurement and to the target plate through a lens and mirror arrangement as outlined in Figure 2.3.[216]

The Autoflex II MALDI source uses Pulsed Ion Extraction (PIE) to enhance resolution and sensitivity. Following initial insertion of the target plate a positive or negative voltage is applied to the target plate (P1, typically 20 kV) that is equal to that applied voltage of the electrode (P2, 20 kV). Following laser ablation, the molecules and ions are set into motion, with a typical velocity of the order of 700 m s^{-1} from P1 towards P2, where the potentials of P1 and P2 remain equal.[216] This generates ions of the same *m/z* with a range of initial velocities and hence kinetic energies. After a delay period, the P2 potential is pulsed down (20 kV to 18 kV), so that the ions experience a potential difference in the region between P1 and P2. The amount of potential experienced by the ion is dependent upon the location of the ion within this region, where ions with lower initial kinetic energy that are close to P1 experience a larger potential than ions with higher kinetic energy that are close to P2. The result is that ions of the same *m/z* are exposed to sufficient potential, such that the arrival time at the detector is identical regardless of initial kinetic energy. The ground potential acceleration electrode and lens arrangement (held at 6 kV), accelerate and focus the ion beam before exiting the source.[216]

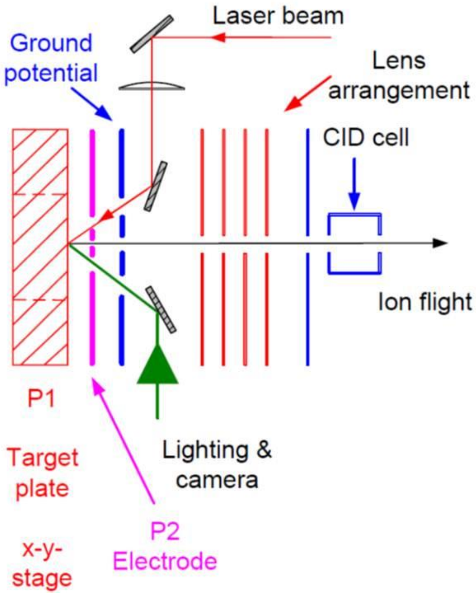

Figure 2.3 Autoflex II MALDI schematic.[216]

2.1.2. Electrospray Ionisation (ESI)

2.1.2.1. Fundamentals of operation

ESI is a soft ionisation method that allows the analysis of compounds that are soluble in polar solvents. As ESI produces a continuous flow of ions from a solvent, it has proven to be a popular method of interfacing separation systems such as liquid chromatography (LC), capillary electrophoresis (CE) and size exclusion chromatography (SEC) with mass spectrometry. ESI is an example of Atmospheric Pressure Ionisation (API), a collective term for related ionisation techniques where ionisation takes place in the atmospheric pressure region, outside of the mass spectrometer. The three major steps for ionisation by ESI include:

- Production of charged droplets at the ESI capillary tip.
- Shrinkage of the charge droplet through solvent evaporation.
- Ion desorption from small highly charged droplets.

In order to produce charged droplets, the sample is dissolved at a low concentration in a polar solvent, typically methanol or acetonitrile and is passed through a narrow conductive needle. A potential difference is established between the needle and the vacuum/atmospheric pressure interface of the instrument through the application of a high voltage as shown in Figure 2.4. This potential difference creates an electric field that penetrates the solution near the capillary tip, inducing polarisation of the solvent near the meniscus of the liquid. Polarisation causes positive charge to collect near the tip of the capillary and induces a distortion in the solution forming a cone as shown inset in Figure 2.4. The application of a large enough electric field forms a jet from the cone tip whose surface is coated with a positive charge.

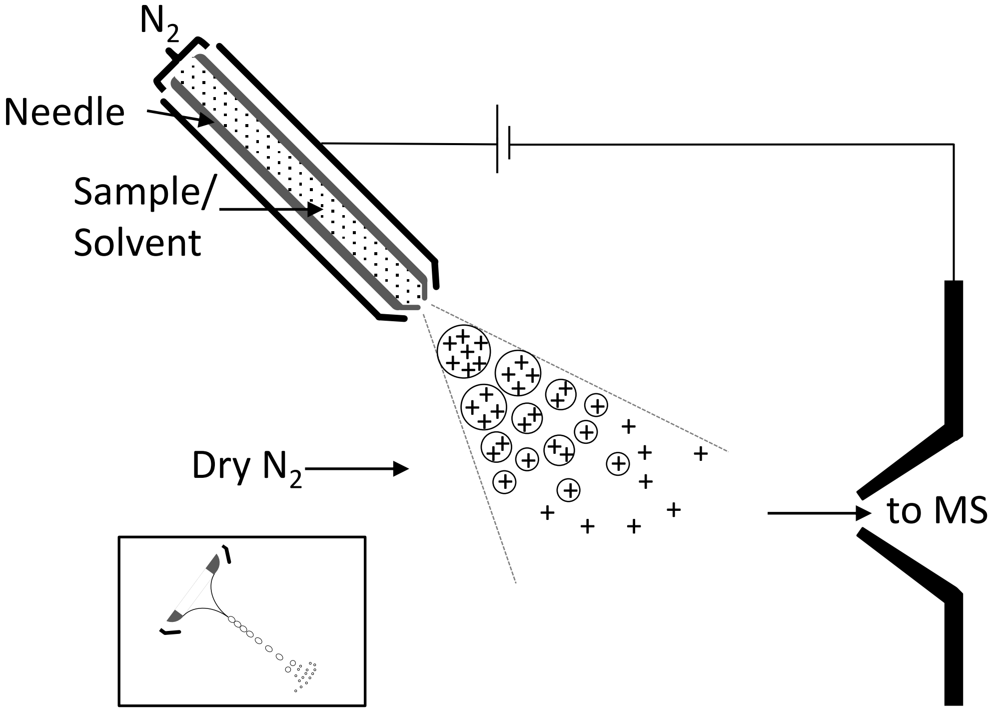

Figure 2.4 ESI source schematic, inset Taylor cone formation.

The presence of nitrogen gas flowing parallel to the needle disrupts the jet forming charged droplets. The positive charge present on the droplets leads to Coulombic repulsion that causes the jet to diverge. As shown in Figure 2.4, solvent evaporation in the presence of hot nitrogen gas causes droplet shrinkage that increases the charge density of the droplets. As the charge density increases, a point is reached, known as the Rayleigh limit (**Equation 2.5**), where the Coulombic forces within the droplet exceed the droplets surface tension, which causes fission of the droplet into smaller droplets.[14] This is a cascade process where further solvent evaporation results in subsequent droplet fission.

$$q_{Ry} = 8\pi^2(\varepsilon_0 \gamma R^3)^{1/2} \qquad \textbf{(2.5)}$$

Where $\mathbf{q_{Ry}}$ = charge, $\boldsymbol{\varepsilon_0}$ = permittivity of the vacuum (C^2 N^{-1} m^{-2}), $\boldsymbol{\gamma}$ = surface tension (N m^{-1}) and **R** = radius of the spherical droplet (m).

Two different mechanisms have been proposed for ion desorption. The charge residue model (CRM) suggests that droplet fission occurs until the droplet contains only one solute molecule, which following evaporation of the residual solvent yields the charged ion of interest.[217] The ion evaporation model (IEM) proposes that ions can be desorbed directly from the surface of intermediate size droplets whose Coulombic repulsive forces are high but do not exceed the surface tension.[218] Both mechanisms have been shown to be valid for different compounds with the CRM more reliable for hydrophilic molecules and the IEM for hydrophobic ones. ESI MS analysis of large molecules such as proteins or synthetic polymers can generate multiply charged ions, due to the presence of multiple ionisation sites. This allows high molecular weight compounds to be measured at a lower *m/z* value, a particularly useful feature when FTICR, quadrupole ion traps or quadrupole mass analysers are used which suffer from restricted *m/z* range.

2.1.2.2. LTQFT ESI

The LTQFT is fitted with an Ion-Max source (Thermo-Finnigan) as shown in Figure 2.5. In this particular instrument the high voltage of (±3 – ±5 kV) is applied to the ESI needle and the ion sweep cone is ground creating the required potential difference. In the Ion-Max source, the ESI probe includes the ESI needle, the ESI nozzle and the gas manifolds for the sheath and auxiliary gases. The ESI probe is mounted at an optimised angle of 120° from ion transfer capillary entrance, reducing the number of neutral species entering the mass spectrometer. The sheath and auxiliary gases are directed at the ESI droplets by the ESI nozzle, where the gases aid in aerosol formation and transportation of the ions towards the entrance of the mass spectrometer. The ion transfer capillary at the atmosphere-mass spectrometer interface transports ions towards the tube lens and subsequent ion optics through a reduced pressure gradient. Typically a low voltage (10 V) is applied to the capillary to repel ions from impacting the capillary surface. On leaving the capillary the ions enter the tube lens, the role of which is to focus the ions towards the ion optics. The voltage applied to the tube lens can be varied to maximise the sensitivity of the instrument, balancing desolvation and fragmentation.[219]

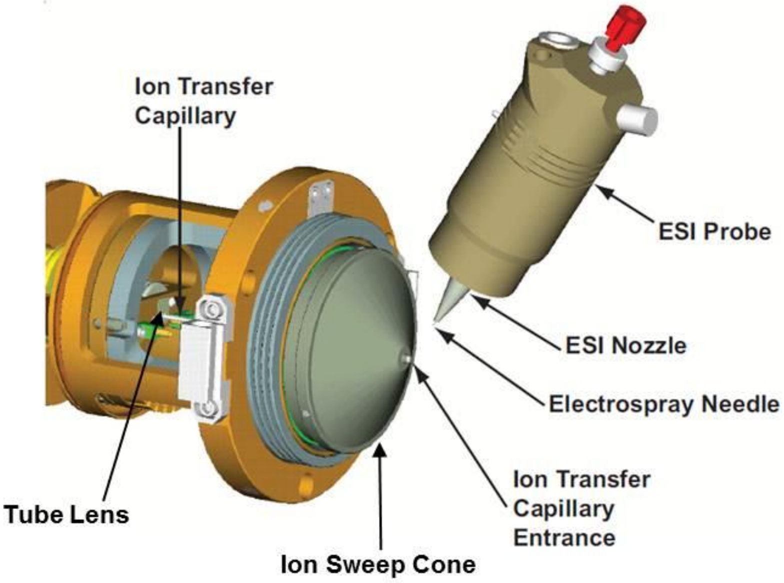

Figure 2.5 LTQFT Ion Max ESI source.[219]

2.1.2.3. Xevo QToF ESI

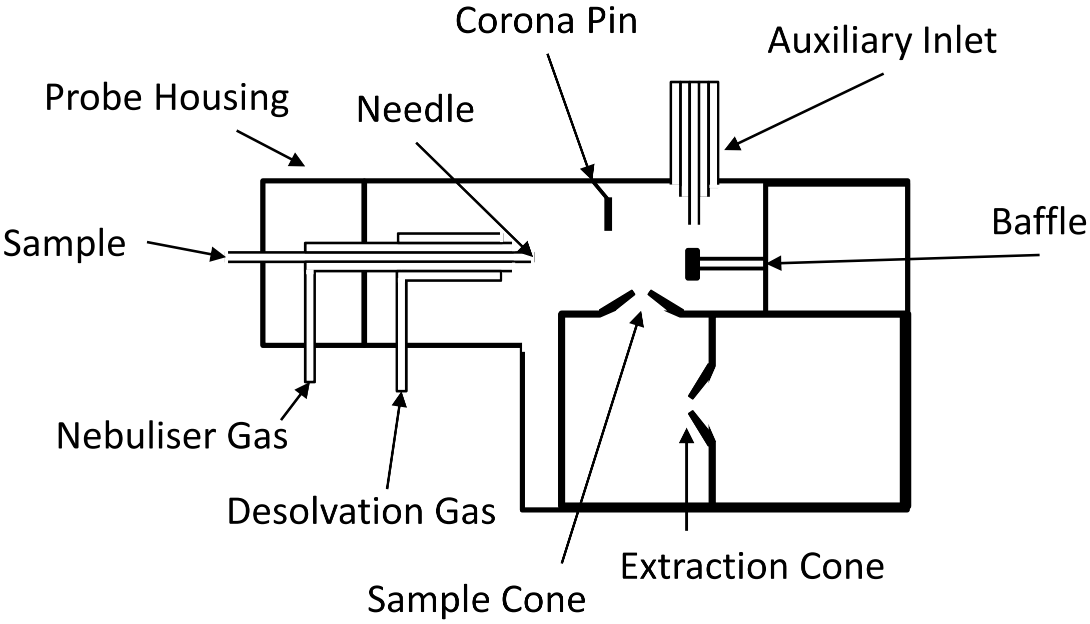

Figure 2.6 Xevo QToF Z-spray source.[220]

The Xevo QToF MS is fitted with a Z-spray ion source (Waters Corp.), where the high voltage is applied to the ESI needle which establishes a potential difference between the needle and the sample cone. The spray direction of the ESI probe in the Xevo is perpendicular to the entrance of the mass spectrometer, which limits the amount of non-ionised material entering the instrument. The voltage of the sample cone at the entrance to the mass spectrometer can be varied to achieve optimal levels of sensitivity for a specific sample. The role of the extraction cone in the Xevo QToF MS is to promote ion transmission to the mass analyser through small adjustments in the applied voltage.[220] This source is equipped with a corona pin that is used in Electrospray Chemical ionisation mode (ESCi). This multi-mode feature allows alternating acquisitions from ESI and APCI ionisation techniques in a single experiment. The presence of an auxiliary inlet in the Z-spray source allows samples to be co-sprayed into the source. This is particularly useful for infusing an external calibrant, providing real time data correction. The position of the oscillating baffle within the source inhibits the flow of ions of sample and calibrant towards the mass spectrometer providing clear separation of the data.

2.1.3. Atmospheric Pressure Chemical Ionisation (APCI)

APCI is another example of an ionisation technique that is performed under atmospheric pressure conditions. Akin to ESI, the solvent and analyte are sprayed into the ion source through the sample needle in the presence of a heated sheath gas that promotes aerosol formation. APCI differs from ESI in that there is no potential difference between the needle and the instrument. Instead, a high voltage, typically 2.5- 3 kV is applied to the corona discharge pin generating a potential difference between it and the instrument as shown in Figure 2.7. The voltage applied to the corona discharge pin is responsible for ionisation of the gas phase solvent and analyte molecules generated in the aerosol. Ionisation of the analyte is achieved through a series of collisions in proximity to the corona pin that involve charge transfer from the solvent and N_2 molecules to the analyte. This ionisation technique usually generates **$[M+H]^+$** and **$[M-H]^-$** molecular ions. APCI is often preferred to ESI in the analysis of low molecular weight analytes (<1000 Da), particularly in situations where the analytes are of medium or low polarity.[221]

.

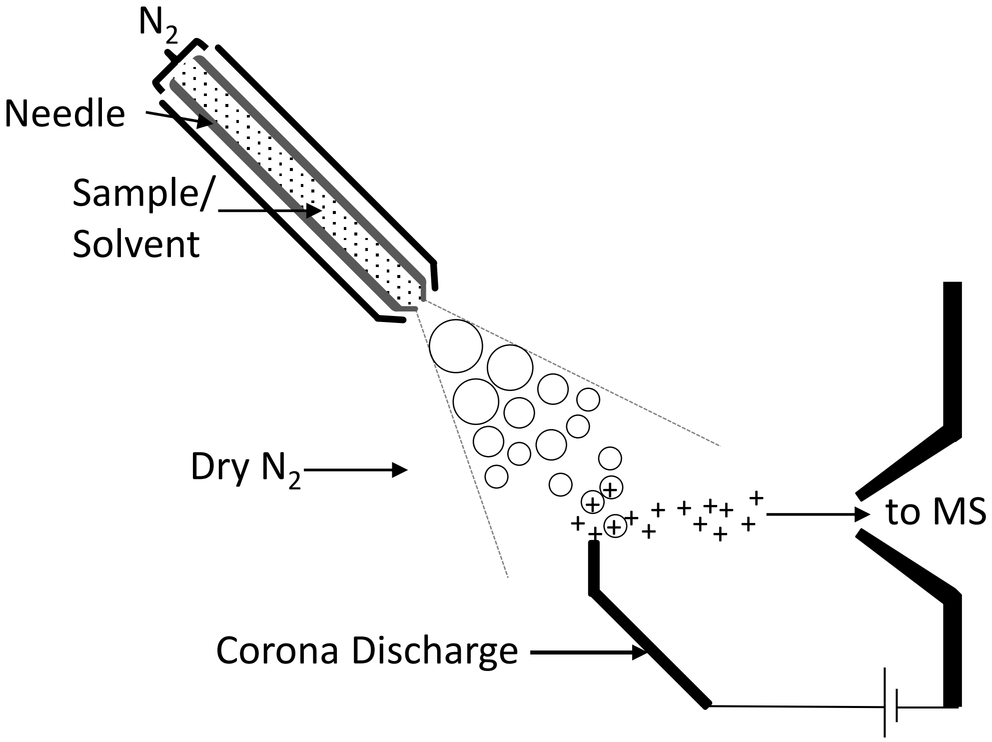

Figure 2.7 APCI source.

2.1.4. Atmospheric pressure Solids Analysis Probe (ASAP)

Ion source development has led to the emergence of new, ambient ionisation techniques, where ionisation occurs under atmospheric pressure outside of the mass spectrometer, akin to ESI and APCI. ASAP is an example of an ambient ionisation technique that has been shown to be an effective method of ionising volatile and semi-volatile samples as both solids and solutions.[97] Samples are applied directly to a disposable glass melting point tube, which minimises sample preparation. The use of a disposable melting point tube allows it to be discarded after analysis reducing sample carry over. As shown in Figure 2.8, the source has an off-axis configuration with the probe located 90° to the inlet of the mass spectrometer.

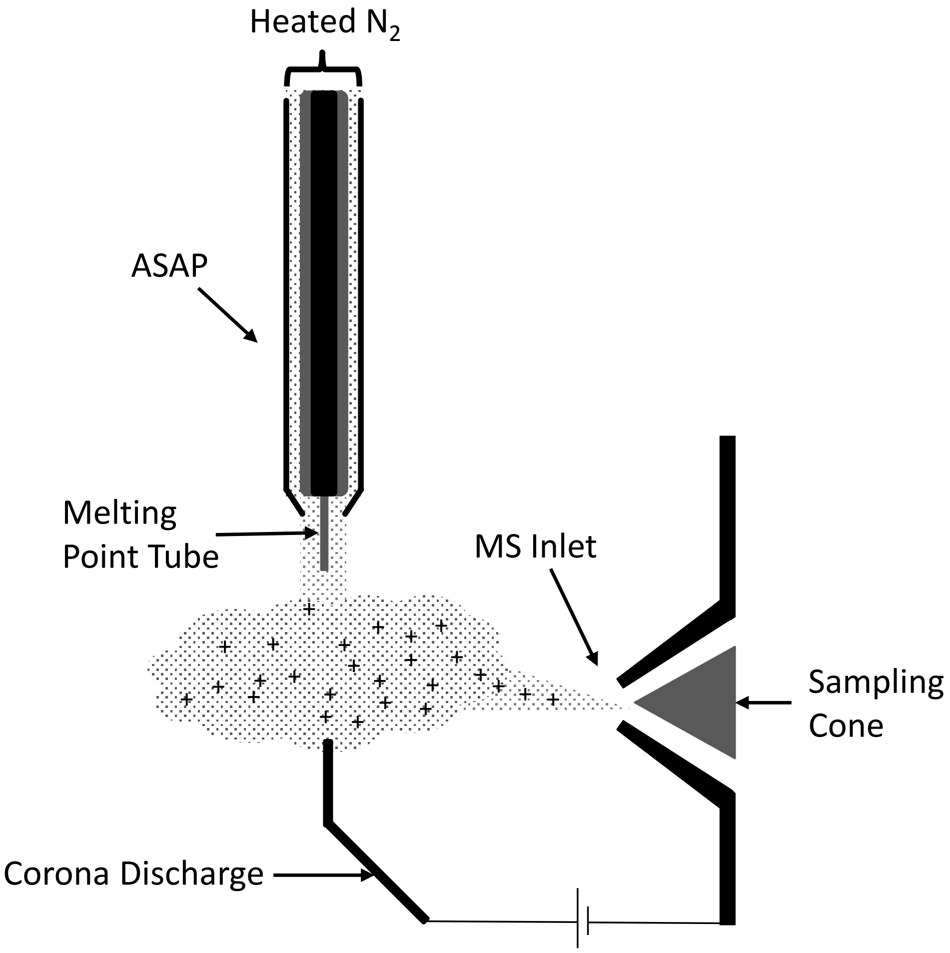

Figure 2.8 ASAP source.

The sample is vapourised by a stream of heated nitrogen desolvation gas that flows parallel to the melting point tube. The temperature of the desolvation gas can be controlled allowing for the analysis of a wide variety of compounds including those of low volatility. The gaseous molecules are subsequently ionised using a corona discharge pin in a method akin to APCI.[222-224] [72,225] Ionisation typically occurs via one of two established mechanisms, the first mechanism leading to the formation of molecular radical cations for the analyte (**M**) involves charge transfer from the nitrogen gas as shown in **Equations 2.6– 2.8**.[110]

$$N_2 + e^- \rightarrow N_2^{+\cdot} + 2e^- \tag{2.6}$$

$$N_2^{+\cdot} + 2N_2 \rightarrow N_4^{+\cdot} + N_2 \tag{2.7}$$

$$N_2^{+\cdot}/N_4^{+\cdot} + M \rightarrow M^{+\cdot} + xN_2 \tag{2.8}$$

The second mechanism involves the formation of protonated molecular ions created through proton transfer as shown in **Equations 2.9 – 2.11.[110]**

$$N_4^{+\cdot} + H_2O \rightarrow H_2O^{+\cdot} + 2N_2 \tag{2.9}$$

$$H_2O^{+\cdot} + H_2O \rightarrow H_3O^+ + OH^{\cdot} \tag{2.10}$$

$$H_3O^+ + M \rightarrow MH^+ + H_2O \tag{2.11}$$

The method by which ionisation occurs is influenced by the chemical properties of the analyte with polarity and proton affinity highlighted as determining factors.[226] Semi-polar and polar molecules are regularly observed as protonated molecular ions, where the degree of protonation is influenced by the proton affinity. Non-polar molecules and molecules with low proton affinity appear as radical cations. In general the competing mechanisms often result in the presence of both types of molecular ion. Ray *et al.* have demonstrated that the ionisation mechanism can also be influenced by conditions within the ion source. As shown in the proton transfer mechanism (**Equations 2.9 – 2.11**), H_2O is an integral component as a source of protons. It was found that addition of a methanol: water mixture via an auxiliary inlet created an environment within the source that favoured ionisation via proton transfer, where the use of a proton scavenger had the reverse effect.[97,226]

2.1.4.1. Xevo ASAP

The Z-spray source fitted to the Xevo QToF MS can be operated in ESCi which combines ESI and APCI where the normal ESI probe is used to vapourise the sample; however, ionisation is achieved using a corona discharge pin to which a high voltage applied. For ASAP, the ESI probe is replaced with the ASAP assembly as demonstrated in Figure 2.9. The corona discharge pin remains the source of high voltage in this configuration with an applied voltage of 3-5 kV. This causes ionisation of the nitrogen gas and the gas phase analyte molecules (**M**) as explained in the previous section. The voltage applied to the corona discharge pin establishes the potential difference with the rest of the instrument. The applied voltage creates a voltage gradient that promotes the movement of ions towards the mass spectrometer. The voltages applied to the sample and extraction cones are similar to those explained previously for the Xevo QToF ESI source in Section 2.1.2.3.

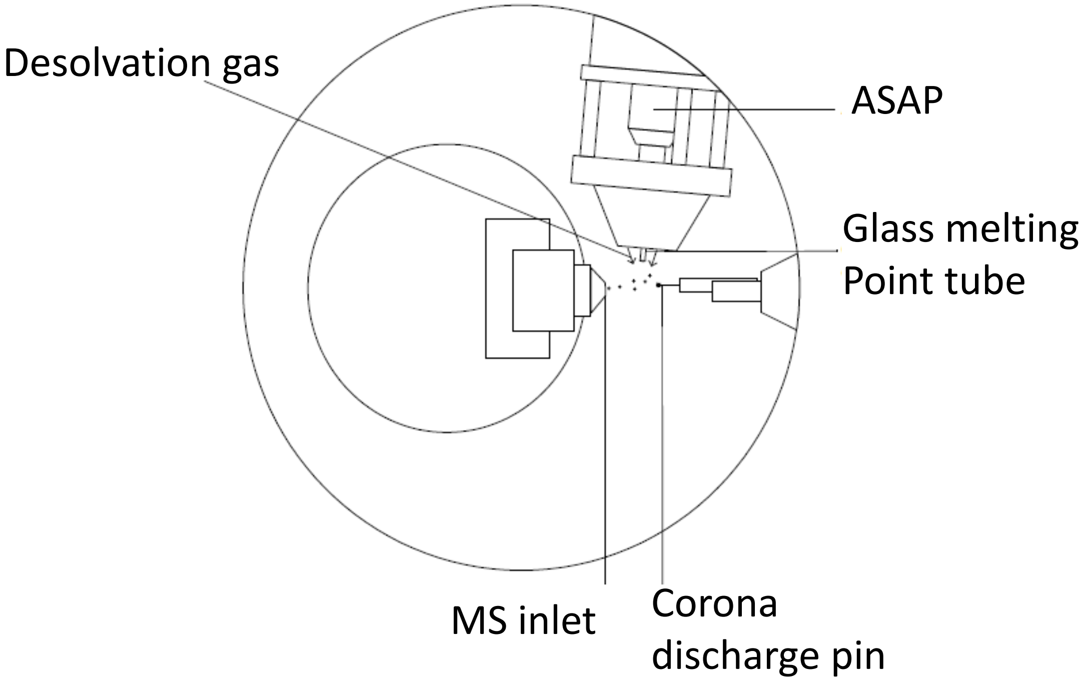

Figure 2.9 Xevo QToF ASAP assembly.

2.1.5. Direct Analysis in Real Time (DART)

Direct Analysis in Real Time (DART) is a second ambient ionisation technique that utilises the APCI ionisation principles to create a method of directly analysing compounds.[222]

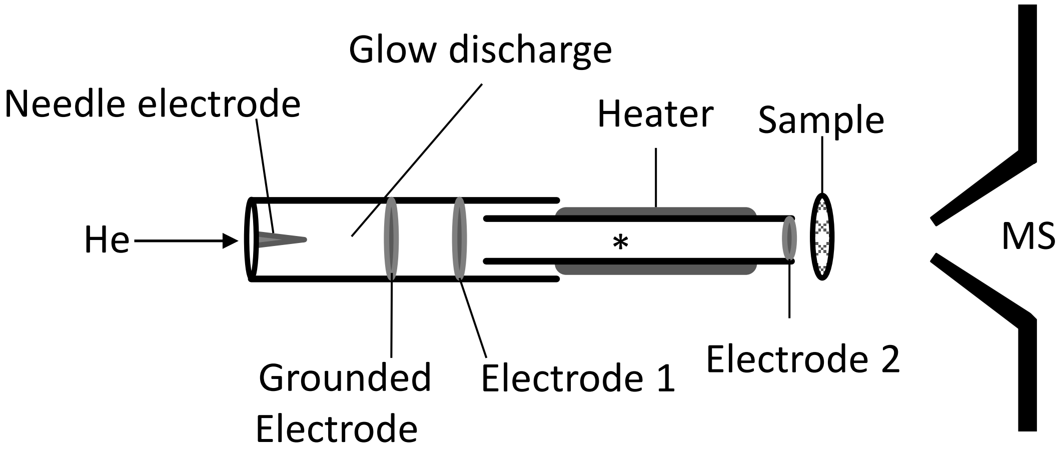

Figure 2.10 DART schematic.

Like other ambient ionisation techniques discussed here, DART is applicable to the analysis of solids, gases and solutions. The mechanism of ionisation involves the use of an inert gas, typically helium, which flows through the source as depicted in Figure 2.10. The gas is introduced to a chamber containing a needle electrode to which a high voltage is applied and a reciprocal grounded electrode where the potential difference between them is in the kV range. When the gas enters this environment it generates ions, electrons and excited state species in the form of a plasma. The electrodes allow for removal of unwanted ions within the flow which leads to the formation of metastable ions in the region labelled (*****) in Figure 2.10. The metastable species interact with other ambient molecules such as H_2O that lead to the formation of hydronium ions which ionise the sample by proton transfer. The sample in solid or solution form is placed in the atmospheric region between the exit of the DART source and the entrance to the mass spectrometer as shown in Figure 2.10.

2.1.6. Desorption Electrospray Ionisation (DESI)

As shown for MALDI (Section 2.1.1), desorption has proven to be an effective method of generating gas phase ions for MS analysis. Desorption Electrospray Ionisation (DESI) utilises a solvent spray, similar to ESI, to generate charged solvent ions that are sprayed onto the surface of a sample present as a solid or solution as shown in Figure 2.11.

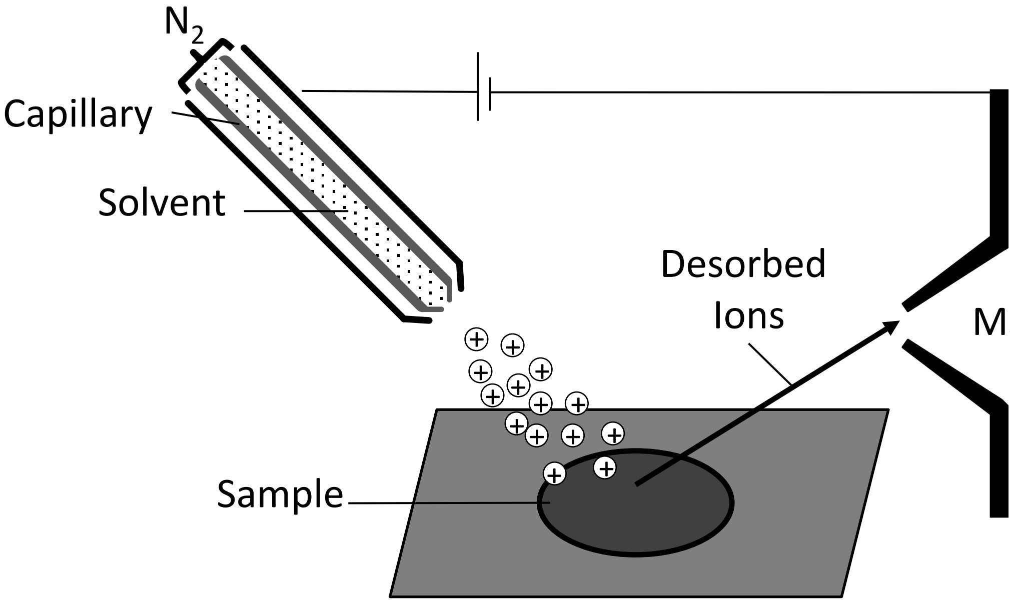

Figure 2.11 DESI source schematic.

The mechanism by which ionisation is believed to occur is a two-step process involving initial wetting of the sample surface allowing sample solvation, followed by the emission of secondary microdroplets through splashing of the sample area with subsequent solvent droplets.[227] The microdroplets generated lead to the formation of gas phase sample ions through solvent evaporation. DESI has been utilised in the ionisation of a wide variety of polar and non-polar compounds including small molecules such as amino acids and high molecular weight species including peptides and proteins. Like ESI, DESI can generate multiply charged ions permitting the analysis of high molecular weight species using mass analysers with a limited mass range. As the formation of the ions is the result of reflection from a surface, the geometry of the apparatus is essential to the detection of any ions generated. The DESI probe and sample table are consequently mounted on stages which have three dimensional linear motion allowing the optimal orientation to be achieved. Kertesz *et al.* demonstrated that manipulation of the geometry of the sprayer relative to the surface could generate a significant increase in resolution when performing chemical imaging.[228] Green *et al.* presented a systematic study of the factors that affect the repeatability of DESI measurements.[229] The results of this work highlighted the impact of probe configuration, sprayer tip to surface distance, sprayer tip protrusion, the voltage applied to the capillary and position of the ion transfer capillary upon the intensity of the molecular ion for a sample of Rhodamine B.[229] Subsequent work from Green *et al.* highlighted the influence of the organic solvent fraction in the DESI spray. This work demonstrated that increasing the organic fraction of the spray decreases the size of the solvent spot diameter, and as a result, smaller solvent droplets produced. The production of smaller droplets was shown to enhance the transfer of the analyte to the mass spectrometer.[230]

2.2. Mass Analysers

Mass analysers represent the heart of the mass spectrometer, separating ions based on their mass-to-charge ratios (*m/z*). The diverse range of mass analysers available is often compared using a few key parameters that aid in the selection of a mass analyser for a specific application. These include:

- Mass accuracy – The figure defining the range of uncertainty over which the measured *m/z* value has been recorded, as defined by **Equation 2.12**.[231]

  $$mass\ accuracy = \frac{m/z_{theoretical} - m/z_{measured}}{m/z_{theoretical}} \qquad \textbf{(2.12)}$$

  This value, often quoted in parts-per-million (ppm) is the primary determinant of the possible elemental compositions for a particular intimated peak in a mass spectrum. This is particularly important in the analysis of unknowns and in tandem MS applications.

- Resolving power – A measure of the ability of a mass analyser to separate two ions of different but defined *m/z* value.[231] In Figure 2.12(a), for two overlapping singly charged peaks m_1 and m_2 of equal intensity the resolving power is defined by **Equation 2.13**.

  $$R = \frac{m_1}{\Delta \mathrm{m}} \qquad \textbf{(2.13)}$$

  Where **R** is the resolving power, $\mathbf{m_1}$ is the *m/z* of m_1 and **Δm** is the mass difference between m_1 and m_2 with a defined inter-peak valley. In this instance the defined inter-peak valley is 10 % of the peak intensity, it can also be defined at 50 %, which is also known as the Full Width at Half Maximum (FWHM).

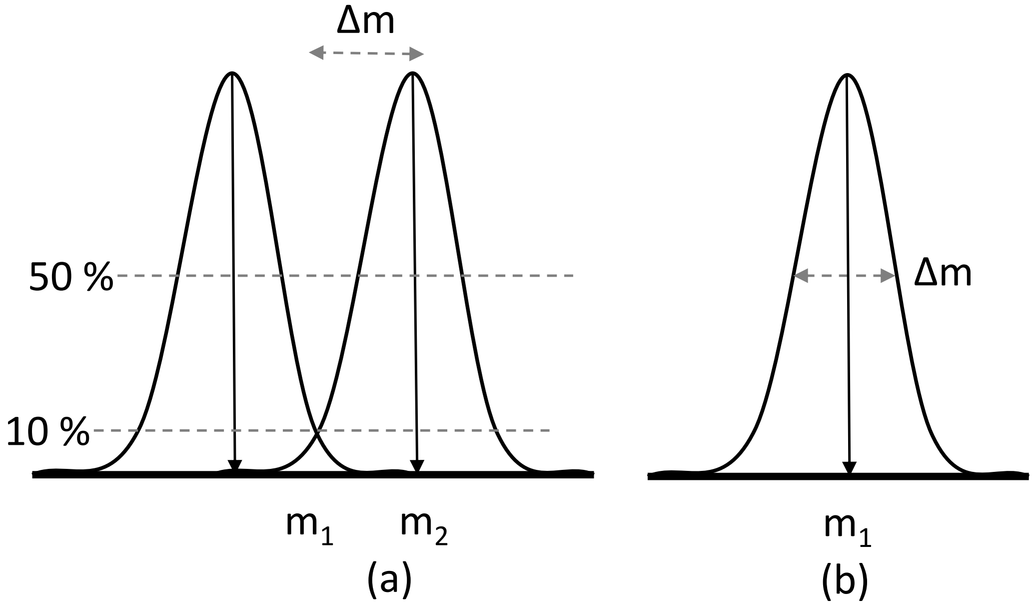

Figure 2.12 Resolving power (a) two overlapping peaks and (b) isolated peak.

This unitless parameter can also be applied to isolated peaks observed in a mass spectrum as shown in Figure 2.12(b), where **Equation 2.13** remains valid where **Δm** is now defined as the peak width at 50 % peak intensity. Instruments with high resolving powers are essential for the separation of ions with the same nominal mass.

- Limit of detection – The smallest amount of analyte that can be detected above the background signal, often defined as signal-to-noise ratio (S/N).[231] Instruments with lower limits of detection require lower sample concentrations, an important consideration when the quantity of sample is limited.
- Duty cycle – The time period it takes for an analyser to complete one full MS analysis.[231] This is an important consideration for time dependent applications such as LC-MS or high throughput analysis.

2.2.1. Quadrupolar devices

Quadrupolar devices perform multiple functions in a mass spectrometer including mass analysers, ion guides, ion containment regions and intermediate reactions regions. Despite not being used as a mass analyser in the instrumentation discussed in this thesis, the presence of quadrupolar devices as ion guides, precursor ion selectors and collision cells requires discussion of their operation. Quadrupolar devices aim to form a quadrupolar field within the space between the electrodes. These devices exist with four, six (hexapole) and eight (octapole) electrodes where increasing the number of electrodes results in a less focussed packet of ions but an increase in the transmission bandwidth, i.e. the *m/z* range that can be transmitted in a single scan. The simplest example of a quadrupolar device is the quadrupole. A quadrupole is constructed of four identical rod electrodes arranged symmetrically around the z axis as shown in Figure 2.13. The position and arrangement of the rods are essential for effective mass separation.

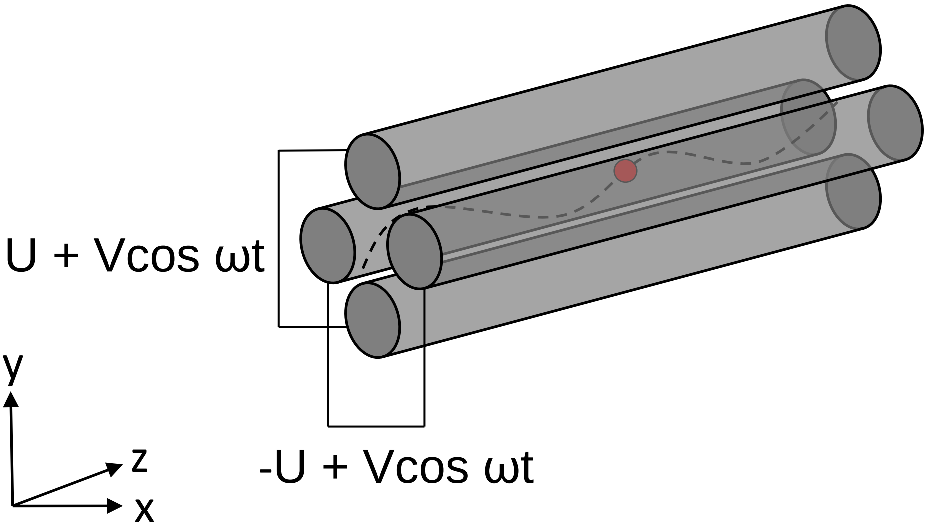

Figure 2.13 Quadrupole.

The application of RF and DC waveforms to opposing pairs of electrodes creates an oscillating electric field within the device. The components of the time dependent RF waveform are **Vcos ωt**, where **V** is the amplitude, **ω** is the angular frequency (Hz) and **t** (s) is time. The magnitude of the DC potential, **U**, applied to all electrodes is identical however one pair is 180° out of phase with the corresponding pair. This oscillating electric field generated manipulates the motion of the ions within the cavity between the electrodes. Ion separation is based on the stability of the ion trajectory, where motion is confined to the centre of the quadrupole. Ions with a trajectory that is unstable collide with the electrodes and are annihilated and consequently are not detected. The trajectory of the ions defined by the Mathieu equation **(Equation 2.14)**, that effectively maps the areas of stability within the device

$$\frac{d^2u}{d\xi^2} = (a_u - 2q_u cos2\xi)u = 0 \qquad \textbf{(2.14)}$$

Equation (2.14) describes the displacement of an ion in 3 dimensional space with respect to the dimensionless parameter, **ξ** (**ξ** = **Ωt**/2, where **Ω** = frequency (s^{-1}) and **t** = time(s)).The trapping parameters $\mathbf{a_u}$ and $\mathbf{q_u}$ are functions of the magnitude of DC and RF voltage respectively. Plotting the Mathieu parameters **a** and **q** generates stability plots as shown in Figure 2.14.

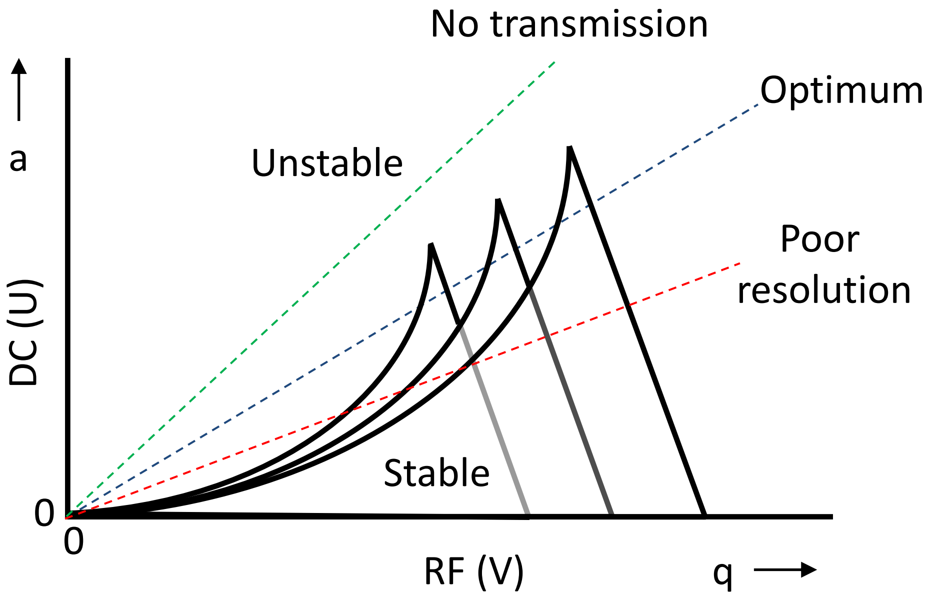

Figure 2.14 Stability profiles for ions in a quadrupole mass analyser.

A mass spectrum is generated by increasing the DC potential and the amplitude of the RF, which result in an increase in the values of **a** and **q**. It is important that the ratio between the DC and the RF is maintained, as any change in this ratio can lead to poor mass spectra. Here, the optimum scan line, shown in blue in Figure 2.14, demonstrates good separation of each ion allowing individual measurement of each peak with 1 Da resolution. When the DC/RF ratio is below this value, a number of the ions are measured simultaneously leading to poor mass resolution as shown by the red line in Figure 2.14. If the DC/RF ratio increases beyond the optimum, ions do not have a stable trajectory and ion transmission through the device is prevented as demonstrated by the green line in Figure 2.14.

As mentioned previously quadrupoles have multiple functions in mass spectrometers. It is possible for quadrupoles to operate as precursor ion selectors, where the application of a specific DC and RF generate **a** and **q** values where only the ion of desired *m/z* has a stable trajectory. To function as ion guides the DC voltage (**U**) of the quadrupole set to zero creating an RF only device. This corresponds to **a** = 0 line in Figure 2.14 that allows a wide *m/z* range of ions to have a stable trajectory within the quadrupolar field. The addition of an inert gas to an RF only quadrupole allows the quadrupole to be used as a collision cell for gas phase reactions.

2.2.1.1. Xevo QToF

The Xevo QToF is an instrument that contains quadrupoles performing different functions within the mass spectrometer. The first quadrupole is a conventional quadrupole that can be operated in RF only mode that transmits all ions to a second mass analyser, or as a precursor ion selector for tandem MS experiments through the application of a specific DC voltage. The Xevo also contains a travelling-wave collision cell (T-Wave) for tandem MS experiments. The T-Wave is an ion guide containing stacked ring electrodes. The application of opposite RF waveforms to adjacent rings and the movement of a DC potential from one ring to the next creates a moving electric field or travelling wave. The T-Wave collision cell is filled with argon gas maintained at 4.8 x 10^4 Pa, where the movement of the ions through the cell causes ion-gas molecule collisions. This allows CID tandem MS to be performed and the resultant ions are separated by *m/z* in the second mass analyser.

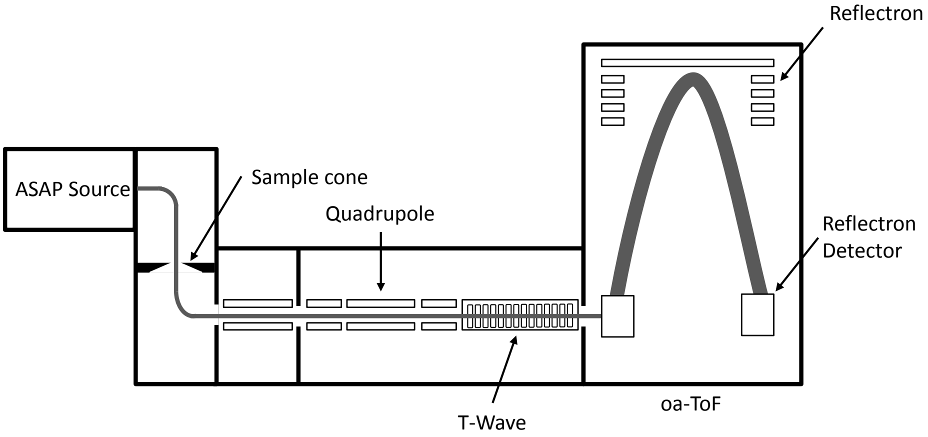

Figure 2.15 Xevo QToF.

2.2.2. Time of Flight (ToF)

The ToF mass analyser is a relatively simple method of mass analysis where ions are separated spatially. The principle of the ToF mass analyser relies on the use of a field free region or drift region that permits separation based on the velocity of the ions. Ions are generated in source and enter an electric field region where the ions experience an accelerating voltage (**V_{acc}**) as shown in Figure 2.16. As the ions enter the field free drift region, the kinetic energy of ions of mass (**m**) and number of charges (**z**) can be calculated using **Equation 2.15**.

$$E_{kin} = \frac{1}{2}mv^2 = zeV_{acc} \tag{2.15}$$

where **v** is the velocity of the ion and **e** is the charge of an electron (1.6 x10^{-19} C). As velocity corresponds to the distance travelled, **d** (m), in time , **t** (s), this formula can be re-written as:

$$\frac{1}{2}m\left(\frac{d}{t}\right)^2 = zeV_{acc} \tag{2.16}$$

$$m/_z = 2eV_{acc}\left(\frac{t}{d}\right)^2 \tag{2.17}$$

As **e**, **V_{acc}** and **d** are constants, therefore: $m/_z \propto t^2$ **(2.18)**

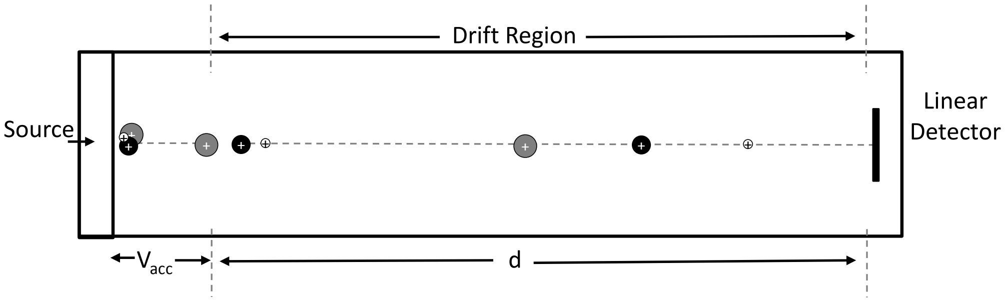

Figure 2.16 ToF.

As ions are separated in physical space, increasing the length of the drift region, **d** will extend ion separation and improve mass resolution. However, it is not practical to extend the drift region indefinitely; therefore alternative methods of increasing the ion flight path without physically lengthening the ToF have been investigated. One principle that is used in a number of modern ToF instruments is the incorporation of a reflectron. A reflectron is an ion mirror that uses sequentially higher voltages to slow down and reverse the direction of ions towards a second detector (Figure 2.17). This not only increases the effective drift region without physically increasing the size of the drift tube, but also permits additional ion separation. As the reflectron has an electric field gradient, low *m/z* ions penetrate the field less than larger ions and consequently the low *m/z* ion will exit the reflectron earlier and achieve better time separation. The reflectron can additionally focus the ions onto the detector improving mass resolution.

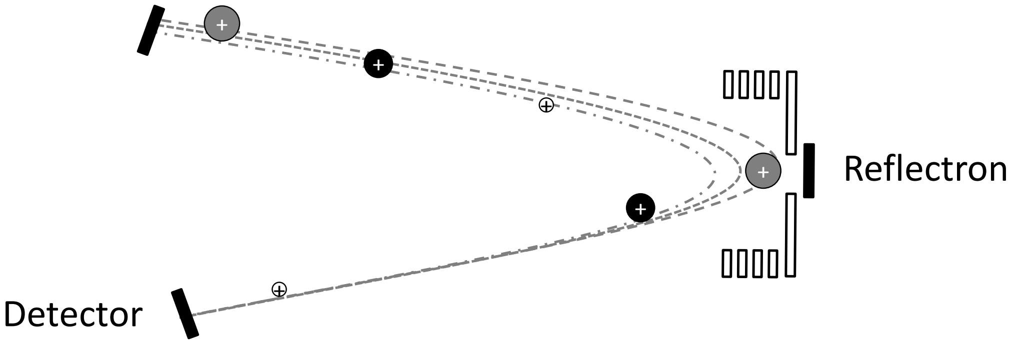

Figure 2.17 Reflectron.

2.2.2.1. Autoflex II ToF

The Autoflex II featured in Figure 2.18 with an axial design creates a linear flight path from the source to the ToF. The ion flight path is extended through the incorporation of a two-stage reflectron ion mirror. There are a number of additional features present on the Autoflex II that enhance the use of this instrument, particularly in tandem MS applications. In particular the LIFT device increases the amount of product ion information for a tandem MS experiment. Post-source decay (PSD) of a precursor ion generates product ions with a range of kinetic energies. In order for the reflectron to effectively focus the ions onto the detector, the range of kinetic energies must be within 30 % of the precursor ion. The role of the LIFT device (Figure 2.18) is to increase the kinetic energies of the fragment ions in such a way that a larger *m/z* range of ions are within the 30 % kinetic energy of the precursor ion. This is achieved through increasing the potential difference experienced by the ions within the LIFT device (as shown in Figure 2.18. On entering the LIFT device the ions experience an electric potential of 19 kV. When this potential is decreased the ions experience an additional acceleration dependent upon the decrease in potential. This allows all of the ions to exit the LIFT arrangement with a narrower range of kinetic energies, increasing the range of *m/z* values that can be detected.

The Autoflex II can perform additional tandem MS experiments using a CID collision cell (Figure 2.18). The ions generated in the MALDI process are accelerated through the collision cell which is filled with argon gas. Collisions between the ions and the gas molecules can result in fragmentation.

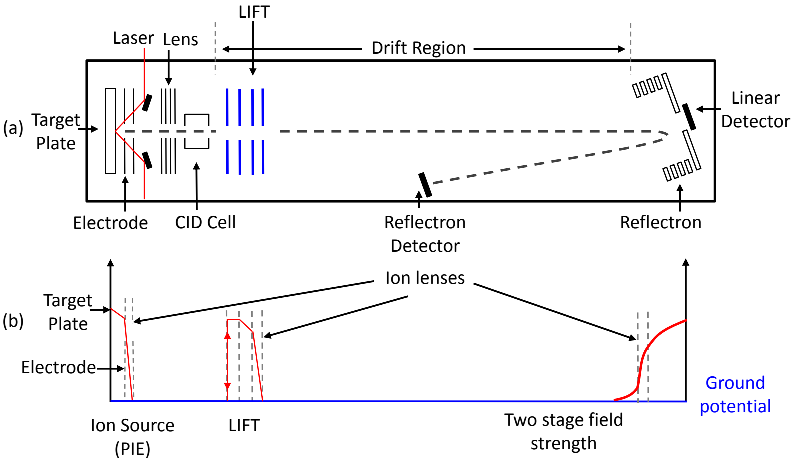

Figure 2.18 (a) Autoflex II schematic highlighting LIFT and CID, (b) A voltage diagram for PIE, LIFT and the reflectron.

Ion detection in the Autoflex II uses a micro-channel plate detector with a schematic provided in Figure 2.19. A micro channel plate is a solid core with millions of tiny channels that are coated with a semi-conducting layer inside. The principle behind this method of detection is to amplify the signal generated from the impact of a single particle in the channel which causes a cascade of electrons to be generated that are recorded electronically. Importantly this method of detection delivers of an output voltage on a timescale up to ten times faster than other detectors.[216] The limiting factor upon detection is the speed at which the digitizer converts the analogue signal to digital information. In the Autoflex II the digitizer is capable of 2 GS sec^{-1}. The Autoflex II can achieve resolving powers of 20000 FWHM, given the presence of the two-stage reflectron, with mass accuracies of 5 – 10 ppm.[215] It is possible to achieve higher resolving powers of up to 40000 FWHM on other axial ToF instruments.

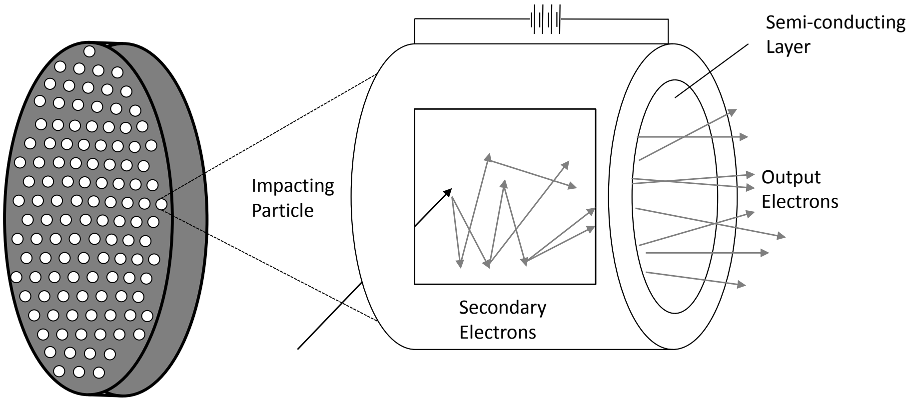

Figure 2.19 Micro channel plate detector schematic and expanded view of electron multiplier.

2.2.2.2. Xevo QToF

Ionisation techniques such as ESI and ASAP that provide continuous streams of ions are not suitable for analysis using an axial ToF, where discrete packets of ions are required for effective ion separation. One method to circumvent this issue, found in the Xevo instrument is an orthogonal acceleration ToF (oa-ToF). In this arrangement the ToF is mounted perpendicular to the direction of the ion beam as shown in Figure 2.20. Discrete packets of ions are created using a pulsed orthogonal accelerating voltage that deflects the ions into the ToF. This ensures that all ions entering the ToF have equivalent energies regardless of their origin, which simplifies the calibration and improves mass accuracy. This instrument incorporates a two-stage reflectron that increases the flight path of the ions improving ion separation and mass resolution. Oa-ToF devices can routinely achieve 10000-20000 FWHM resolving power with a < 10 ppm mass accuracy. [215]

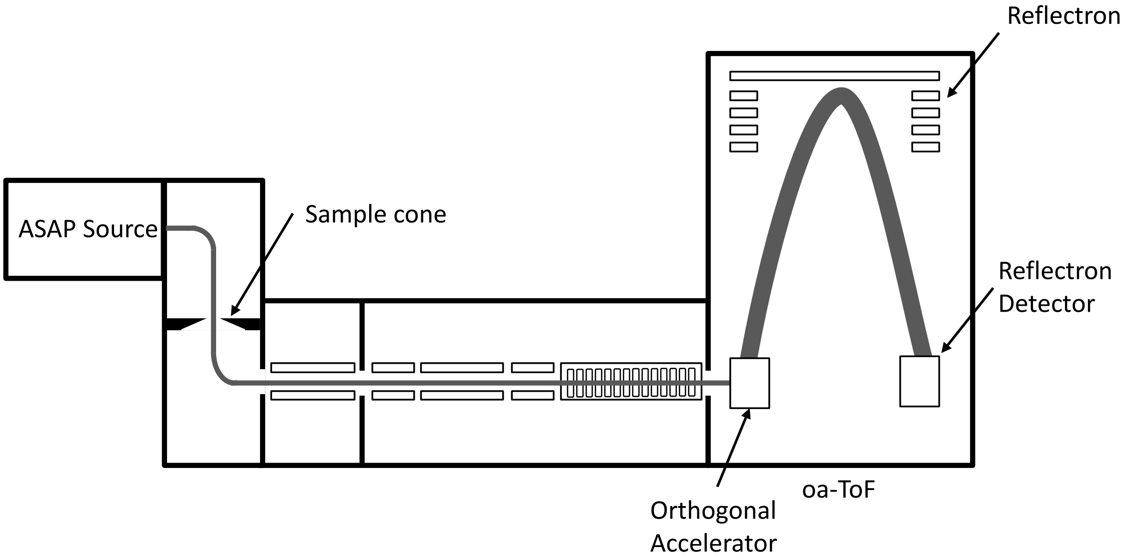

Figure 2.20 Xevo oa-ToF.

2.2.3. Linear ion trap with off-axis detection (LTQ)

The previous two mass analysers separate ions spatially, one alternative to this is to trap the ions in a confined space and use RF potentials to separate ions in timed events. One class of mass analyser that takes advantage of this phenomenon are ion traps. There are two varieties of ion trap, the quadrupole ion trap, also known as the Paul trap or the linear ion trap such as that featured in the LTQ-FT (Figure 2.21). Ions traps perform a number of roles such as: ion accumulator, precursor ion isolator, collision cell for tandem MS experiments and as a mass analyser. The major advantages of ion traps are that they are robust instruments with high scan speed and high sensitivity. The resolving power of this instrument uses well defined peak widths of 0.1 Da and therefore the mass resolution increases with increasing *m/z*.[215]

The linear ion trap (LTQ) featured in the LTQFT is composed of three distinct sections where the view in the **z** direction is similar to that of a quadrupole with two pairs of hyperbolic rods present as shown in Figure 2.21.The front and rear electrodes, depicted in light grey in Figure 2.21, allow ions to enter the device, where the application of trapping voltages across the electrodes restricts the motion of ions in the *z* direction. The application of a **DC** potential in the *z* direction forms a potential well leading to the accumulation of ions within the central section of the mass analyser (dark grey, Figure 2.21). Efficient trapping of the ions is achieved through the addition of a helium buffer gas which reduces the kinetic energy of the ions through inelastic collisions. The ions motion is thus focussed around the centre of the trap where the effective potential is at a minimum, this leads to improved transmission and detection of ions compared to a linear ion trap operated at lower pressures.[232]

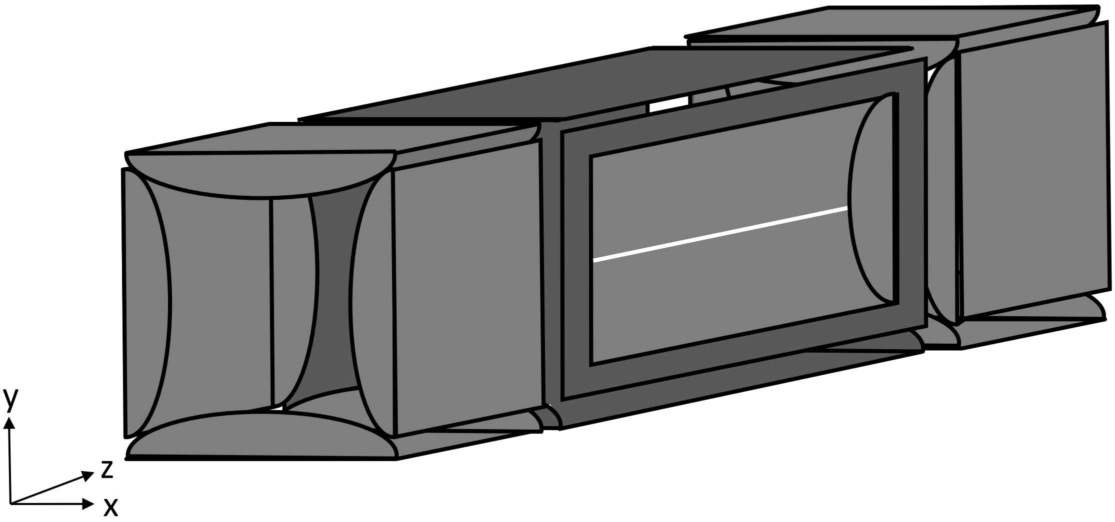

Figure 2.21 LTQ (Thermo Finnigan).[219]

The motion of ions within the LTQ can be described as that observed for the quadrupolar devices, where the Mathieu equation describing ion motion (**Equations 2.14**) is upheld.[211] Ion separation in the LTQ is dependent upon the resonant frequency of the ions which is directly related to the *m/z* of the ion. To achieve separation, an AC voltage is applied to opposing electrode pairs of the ion trap causing a change in the RF potential in the *x* direction as shown in the profile depicted in Figure 2.22. A specific amplitude correlates with a fundamental resonant frequency of certain *m/z* that increases the kinetic energy of ions with that *m/z*. This results in additional radial motion where the ions are eventually ejected from the trap through slits in the *x* electrodes shown in white in Figure 2.21. Detectors are present on both sides of the ion trap as ions can be ejected in both *x* directions maximising the sensitivity of the ion detection.

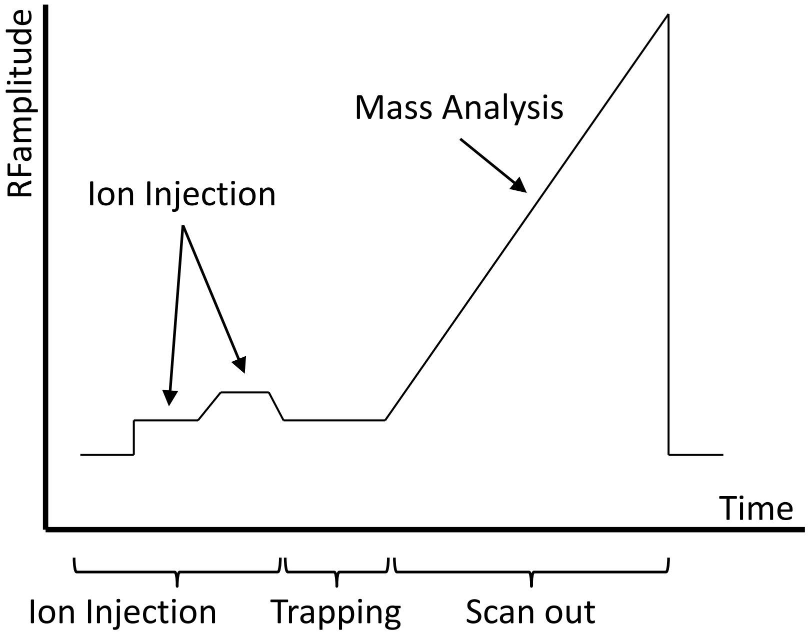

Figure 2.22 Scan mode for mass detection in a linear ion trap.

Ejection of ions from the ion trap has two significant benefits, firstly to reduce the number of ions present in the trap diminishes space charge effects associated with an overfilled device and secondly the selective isolation of a specific *m/z* in the initial stage of a tandem MS experiment. The remaining isolated ions can be activated for CID tandem MS experiments by dipole or quadrupole excitation; in both cases the presence of an additional voltage causes an initial increase in the amplitude of the oscillation of the parent ion. The presence of the helium buffer gas in the cell leads to ion-molecule collisions which converts translational energy to internal energy. If sufficient internal energy is present, unimolecular decomposition of the precursor ion can occur, resulting in the formation of product ions. Detection of the product ions formed is ultimately determined by the stability of the ions within the ion trap, which is presented graphically in Figure 2.23. As the detectors in the LTQ are placed in the *x* directions the Mathieu parameter of interest is $\mathbf{q_x}$. The value of $\mathbf{q_X}$ can be related to the *m/z* of the ion of interest through **Equation 2.19**, where **V** is the RF voltage, **e** is the charge of an electron (1.6 x 10^{-19} C), **k** is the Boltzmann constant (1.38 x1 10^{-23} m^2 kg s^{-1} K^{-1}) and **m** and **z** are the mass and number of charges of the ion respectively.

$$q_x = k\frac{V}{\left(\frac{m}{ze}\right)} \qquad \textbf{(2.19)}$$

As there is no DC potential applied the ion stability profile follows the q_x axis. Evaluation of the formula determines that a $\mathbf{q_x}$ value up to 0.908 is stable within the ion trap, this corresponds to the ejection of ions whose *m/z* values are less than one third that of the precursor ion. As the 'one third cut-off' rule, restricts the observable mass range, this limits the amount of product ion information that can be obtained from CID tandem MS experiments performed in an ion trap.

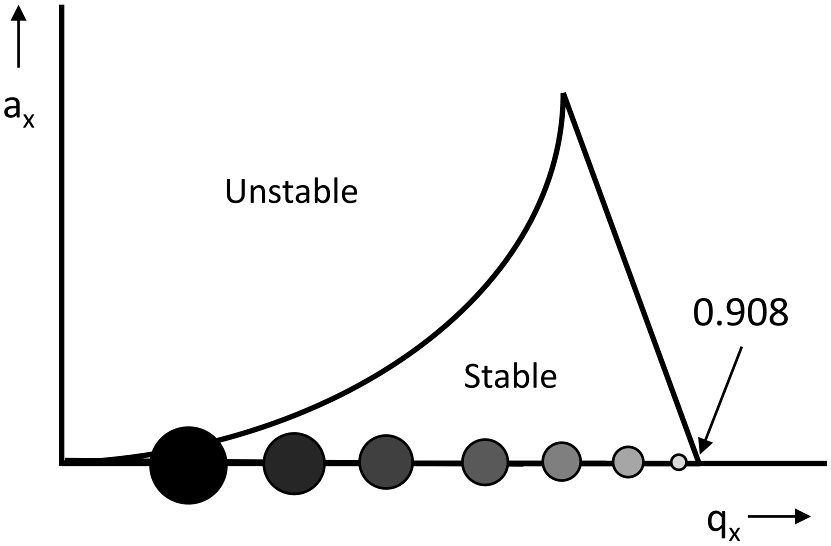

Figure 2.23 Product ion stability profile.

Ion detection in the LTQ involves the use of a conversion dynode as shown in Figure 2.24. As ions exit the ion trap they are attracted to the concave conversion dynode that has the opposite polarity to the ions of interest. Collision of the ions with the surface of the dynode generates secondary particles that are directed towards a secondary electron multiplier. These particles collide with the inner walls of the lead oxide cathode generating electrons. These electrons travel towards the anode due to a potential gradient applied across the device. Continuous collisions with the walls of the device leads to a cascade of electrons being generated resulting in a measurable current, where the number of electrons recorded is proportional to the number of secondary particles generated.[219]

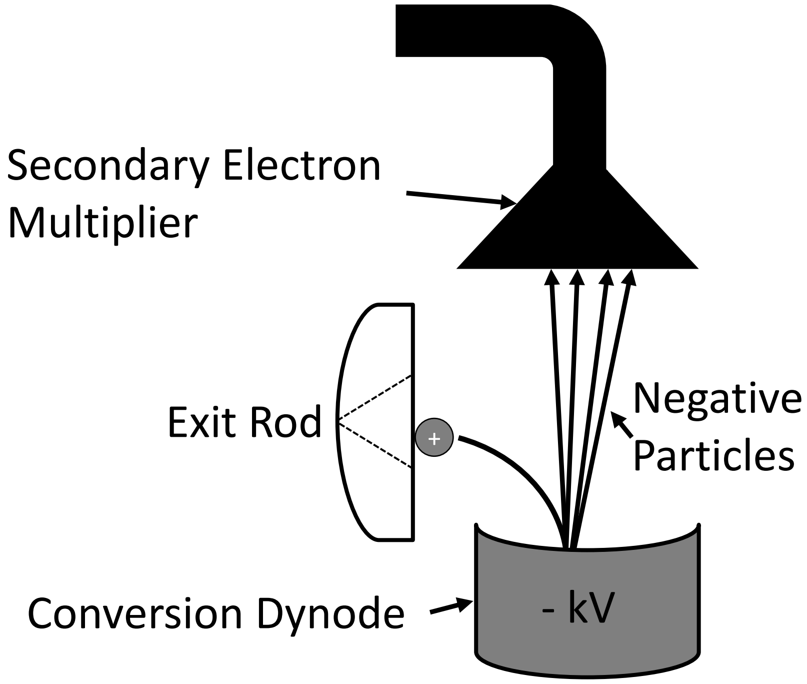

Figure 2.24 LTQ conversion dynode detector.

2.2.4. Fourier Transform Ion Cyclotron Resonance (FTICR)

Fourier transform mass spectrometry (FTMS) currently provides the highest mass resolution and highest mass accuracy analysers that are commercially available. FTMS includes both FTICR and Orbitrap mass analysers,[233,234] where the device used in this thesis was an FTICR. FTMS instruments can achieve extremely high resolving powers of 24 000 000 FWHM (at *m/z* 609)[235] and very high mass accuracy of up to 300 ppb.[236]

In an FTICR the presence of a homogeneous magnetic field is essential for the principle of ion motion within the analyser cell. Numerous types of magnet including permanent, electro and superconducting magnets have been utilised as sources of magnetic fields. Many properties including mass resolution, mass accuracy, dynamic range and upper *m/z* limit were found to scale linearly or quadratically with magnetic field as shown in Figure 2.25. This has restricted the application of permanent and electric magnets for use in FTMS instruments. The most popular means of generating a stable magnetic field is using a superconducting magnet.

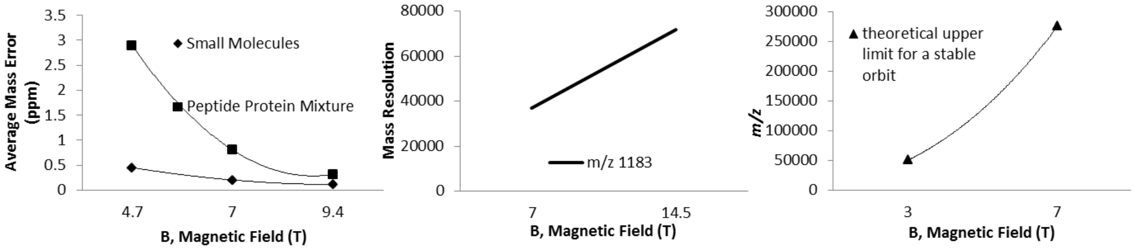

Figure 2.25 The scaling effect of the magnetic field strength upon: (a) mass accuracy (quadratic),[237] (b) mass resolution (linear)[236] and (c) dynamic range (quadratic).[238]

The motion of an ion within a magnetic field is influenced by two fundamental forces which involve interaction of the charged ion with electric and magnetic fields. In an idealised world with no influence from the electric field, the forces acting on an ion result in a circular motion perpendicular to the magnetic field as shown in Figure 2.26.

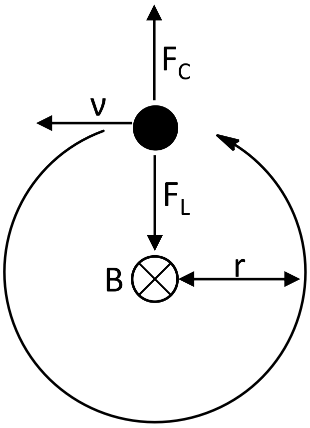

Figure 2.26 Ion motion in a magnetic field.

$$F_L = zevB \qquad \textbf{(2.20)}$$

$$F_C = \frac{mv^2}{r} \qquad \textbf{(2.21)}$$

The angular frequency of the ion can be calculated when the radius of motion is constant, this is achieved when the Lorentz force ($\mathbf{F_L}$, **Equation 2.20**) and Centrifugal forces ($\mathbf{F_C}$, **Equation 2.21**) are equal. This equilibrium state allows the simplification of **Equations 2.20** and **Equation 2.21** to yield **Equation 2.22**, where, **z** is the number of charges, **m** is the mass, **e** is the charge of an electron (1.6 x 10^{-19} C), ***v*** is the velocity, **B** is the magnetic field strength and **r** is the radius of the ions orbit.

$$\omega_C = \frac{v}{r} = \frac{zeB}{m} \qquad \textbf{(2.22)}$$

The angular frequency can be related to the fundamental parameter of cyclotron frequency with the addition of an angular measurement, corresponding to one complete revolution of the ion as shown in **Equation 2.23**.

$$f_c = \frac{\omega_c}{2\pi} = \frac{zeB}{2\pi m} \qquad \textbf{(2.23)}$$

As the magnetic field is constant, the cyclotron frequency is only dependent upon the mass and charge of the ion, where the kinetic energy and velocity of the ion has no influence upon the cyclotron frequency. It is important to note that despite the influence of the Lorentz force perpendicular to the magnetic field, it has no influence upon the ion motion parallel to the magnetic field. Consequently the ion is free to move within this plane with only the trapping voltages of the end plates limiting the motion.

The presence of trapping voltages, which limit ion motion in the magnetic field, have a detrimental impact upon the motion of the ion, as the electric potential at the centre of the cell is not zero. It has been estimated that the electric potential is approximately one third of the trapping voltage applied. The magnitude of this force (F_E) is dependent upon the charge of the ion and acts in the same direction as the centrifugal force as shown in Figure 2.27.

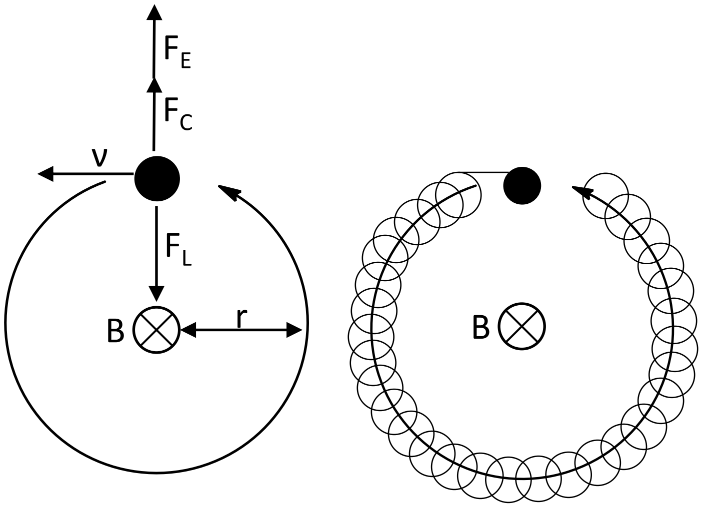

Figure 2.27 Ion motion in a magnetic and electric field (left) and magnetron motion (right) (not drawn to scale to emphasise motion).

This force creates an additional motion, known as the magnetron motion whose frequency is independent of the mass of the ion. The orbit of this motion centres on the idealised circular orbit of the cyclotron motion due to the magnetron frequency (Hz) being orders of magnitude lower than the cyclotron frequency (kHz-MHz). This produces a flight path similar to that shown right in Figure 2.27, where the magnitude of the magnetron motion has been enhanced to demonstrate the effect. The effect of this motion leads to a deviation from the ideal cyclotron only measurement and corresponds to 10-100 ppm in a mass measurement.[211]

In order for measurements to be made accurately it is important to control the motion of the ions within the magnetic field, this is achieved through the use of an analyser cell. Many cell designs have been trialled; including the open cylindrical cell shown in Figure 2.28, however the only commercially available FTICR cell currently is the Infinity cell.[239] FTICR cell development remains an active research area, with the recent work by Nikolaev *et al.* demonstrating a new cell design capable of ultra-high resolution.[235] The cylindrical Penning Trap used in the LTQFT is oriented within the magnetic field such that *z* axis is aligned with the direction of the magnetic field (**B**, Figure 2.28).[240-243]

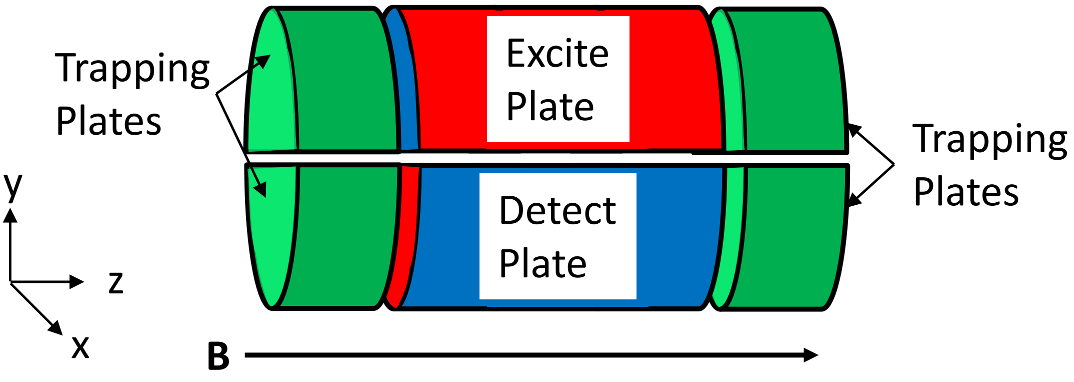

Figure 2.28 FTICR cell schematic.

Like the ion trap, the cell is comprised of three principle components. The front and rear electrodes shown in green in Figure 2.28 are trapping plates, that restrict the ions movement in the *z* direction. Initially the front trapping plate will have no potential applied, permitting ions to enter the cell where the trapping voltage (approximately 1 V) of the rear trapping plate reverse the direction of motion of the ions. Application of an equivalent voltage to the front trapping plate confines the oscillations of the ions in the *z* direction to centre of the ICR cell. The central section is comprised of two pairs of opposing plates. The first pair shown in red in Figure 2.28 induce excitation and the second pair, shown in blue in Figure 2.28, detect the trapped ions. In order to provide accurate measurements of cyclotron frequency, collisions with background gases must be avoided. It is therefore essential that an ultra-high vacuum of 10^{-9}-10^{-10} Torr is maintained within the ICR cell.

As shown in **Equation 2.23** the frequency of cyclotron motion is based on the *m/z* of an ion and the magnetic field in which the measurement takes place. To perform measurements of the cyclotron frequency, ions are excited through the application of an RF frequency to the excitation plates. Ions whose resonant frequency corresponds to the applied RF waveform accelerate to a radius approximately 75% the radius of the ICR cell as shown in Figure 2.29. Ions produce an image current by perturbing electrons in the pair of detector plates (blue, Figure 2.29). Detection using this method is non-destructive and means that ions can be trapped within the analyser for extended periods of time, where an increase in the detection time results in better resolution. This is a useful feature particularly in tandem mass spectrometry experiments where CID, IRMPD and ECD have been performed in FTICR instruments.[117]

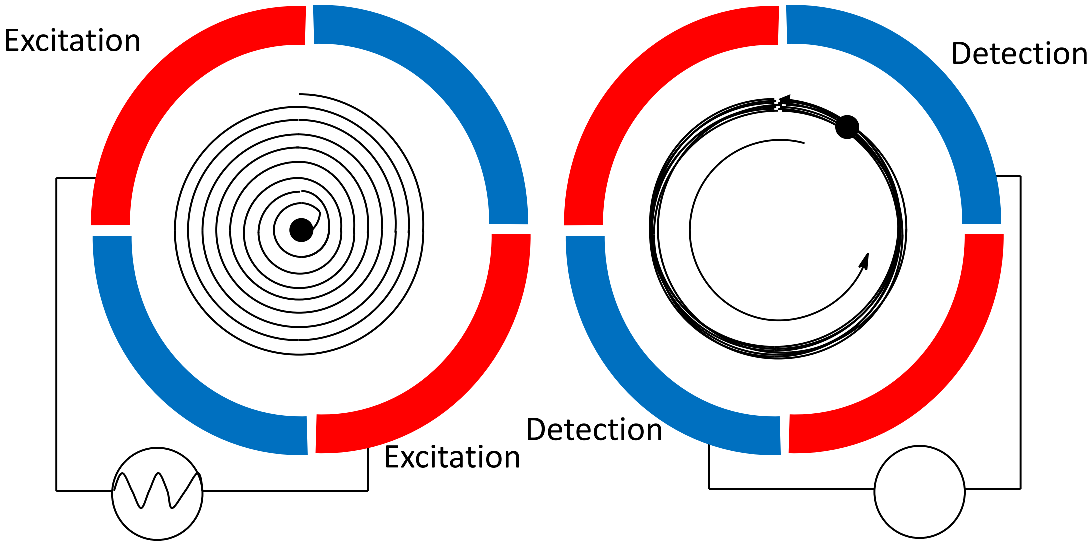

Figure 2.29 Left, ion excitation using a sinusoidal waveform. Right, ion detection.

Ion detection in the FTICR mass analyser is a none-destructive process where electronic signals are generated through perturbation of the electrons in the detector plate caused by excited ions. This perturbation forms a sinusoidal image current signal, where composite amplification of the signals generates a transient that is formed of the cyclotron frequencies of all ions in the ICR cell. This transient is subsequently digitised using an analogue-to-digital converter (ADC), following digitisation the Fast Fourier Transform (FFT) algorithm is applied which extracts the frequency and amplitude of each frequency component. With effective detection of each frequency component a mass spectrum of relative intensity vs. *m/z* can be generated.

2.2.4.1. LTQFT

The LTQFT is a mass spectrometer combining the LTQ and FTICR mass analysers in series. Quadrupolar ion guides are used to transmit ions between the source and the two different mass analysers. The Penning Trap of the FTICR mass analyser is placed within a 7.0 T superconducting magnet. This instrument has the capability of performing tandem MS experiments using two different methods of precursor ion activation. CID tandem MS experiments involve precursor ion selection in the LTQ, ion activation in the LTQ using helium collision gas (1.3×10^{-1} Pa) followed by *m/z* measurement in either the LTQ or FTICR mass analysers. The indirectly heated dispenser cathode within the FTICR MS can be used to generate electrons of controllable kinetic energy. This allows electron-based fragmentation techniques such as ECD, HECD, EDD and EID to be performed, where precursor ion isolation occurs in the LTQ, with subsequent ion transfer to the FTICR where activation takes place. The resultant ions are separated by *m/z* in the FTICR MS. Although not fitted to the instrument used in this work, a laser can be attached as shown in Figure 2.30 that permits IRMPD tandem MS experiments to be performed in the FTICR.

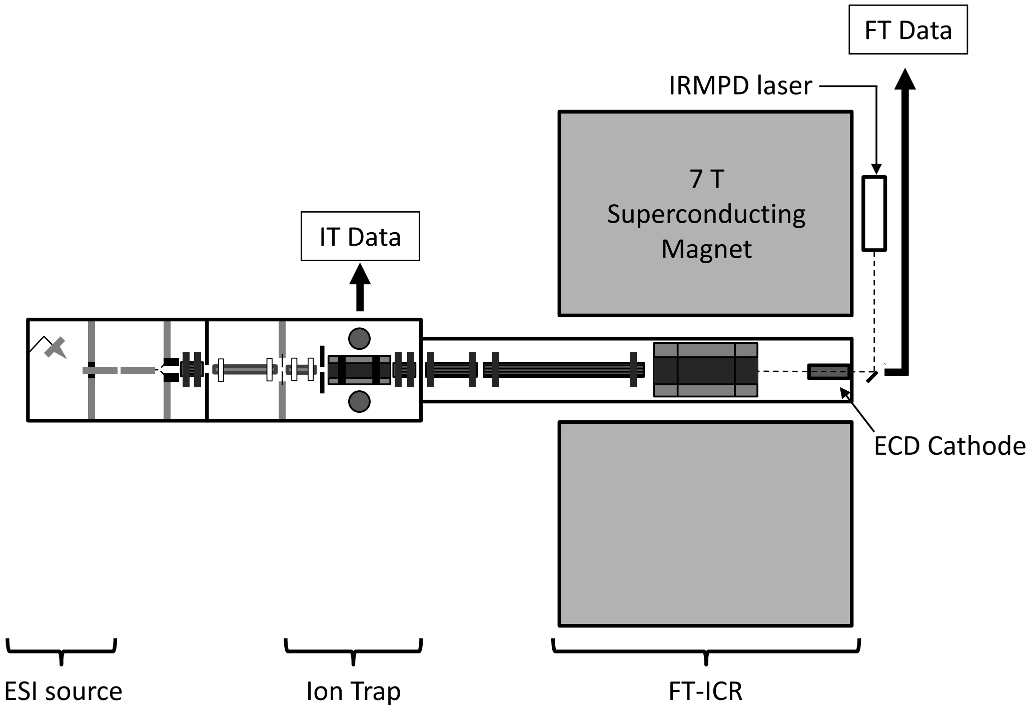

Figure 2.30 LTQFT.

2.3. Experimental Instrument Parameters

2.3.1. Sample preparation for ESI

All samples for ESI were prepared as dilute solutions in methanol or acetonitrile at a concentration of 1 – 10 µg mL^{-1} unless otherwise stated. Samples with poor solubility in these polar solvents were dissolved in binary solvent systems incorporating dichloromethane or water. Samples containing metal salts involved dissolving the metal salt in methanol: water (50:50) to a concentration of 1 mM into which the sample was diluted to the concentration range specified previously.

2.3.2. LTQFT

The LTQ-FT mass spectrometer (Thermo-Finnigan Corporation, Germany) constitutes an ESI source, LTQ and FTICR mass analysers, where the FTICR mass analyser is contained within a 7.0 Tesla superconducting magnet. All samples were administered to the ESI source through direct infusion, through a syringe pump with a flow rate of 5 µL min^{-1}. ESI ion source parameters including sheath gas flow (0-10 arb), auxiliary gas flow (0-10 arb), sweep gas flow, capillary voltage (10 V – 35 V) and tube lens voltage (80 V – 250 V) were optimised to achieve a precursor ion peak of maximum intensity with a stable signal. The source cone voltage was maintained at 4 kV and the capillary needle was heated to 250 °C. Ions were detected in the FTICR mass analyser for both MS and tandem MS experiments, where the default injection time was 1000 ms and 1500 ms respectively. Data were recorded at a resolving power of 100,000 FWHM to ensure good mass resolution. Spectra were analysed using XCalibur QualBrowser version 2.0.7 (Thermo Fisher Scientific Inc.)

For tandem MS experiments, the precursor ion was isolated in the LTQ using a 4 *m/z* isolation window (unless otherwise stated). For LTQ-CID experiments, the helium damping gas present at a pressure of the 1.3 x 10^{-3} Pa within the LTQ was utilised with the resultant ions recorded in the FTICR mass analyser. The normalized collision energies applied during CID analysis have been stated in arbitrary units, as per the manufacturer's software. ECD and EID analyses were carried out using incident electrons of controllable energy, which were generated by an indirectly heated dispenser cathode situated behind the FTICR cell. Calibration of the cathode was performed using Substance P, where the voltage offset is adjusted to achieve the most efficient fragmentation under ECD conditions. Therefore the actual energy of the incident electrons can be calculated using **Equation 2.24**.

$$Electron\,Energy = Energy\,Level - Voltage\,Offset \tag{2.24}$$

The electron energies quoted in this thesis have been adjusted to account for the voltage offset applied to the cathode at the time of the analysis. A default electron irradiation time of 70 ms was utilised unless otherwise stated. IRMPD analyses were performed on a similarly equipped LTQFT mass spectrometer at Astra Zeneca (Alderley Edge, UK). IRMPD was performed using a 20 W CO_2 IR laser situated behind the FTICR cell. The power and duration of the laser pulse was varied to achieve optimal dissociation between 10- 100 % and 50 – 300 ms respectively.

2.3.3. QToF Premier

The QToF premier mass spectrometer (Waters, Manchester, United Kingdom) comprises a QToF mass analyser fitted with an ESI source. ESI analysis was carried out via direct infusion using a syringe pump with a flow rate of 10 µL min^{-1}. ESI source parameters source temperature (120 °C), desolvation temperature (450 °C), cone gas flow (0 L hr^{-1}), desolvation gas flow (800 L hr^{-1}) and capillary voltage (3.5 kV) remained constant throughout the analysis. The sampling cone voltage (10 V- 50 V) and the extraction cone (2 V – 5 V) were manipulated to achieve the maximum intensity for the precursor ion peak of interest. Tandem MS experiments were performed using CID using argon collision gas (7 psi), where the collision energy was increased to achieve optimal dissociation (30 V – 50 V). Spectra were analysed using MassLynx version 4.1 suite of software (Waters Corporation, Manchester, United Kingdom), where accurate mass measurements were carried out using the embedded program Elemental Composition version 4.0.

2.3.4. Sample preparation for ASAP

Solid polymer samples were applied directly to the glass melting point tube through simple stirring in the sample, unless otherwise stated. For poly(ethylene) it was necessary to increase the temperature of the sample to the melting point so that the sample could be applied effectively to the glass melting point tube.

2.3.5. Xevo QToF

The Xevo mass spectrometer (Waters, Manchester, United Kingdom) comprises a QToF mass analyser fitted with an ASAP ion source. Samples were applied directly, as solids, to the glass melting point tube unless otherwise stated, where excess sample was removed using a Kimtech wipe. MS and tandem MS spectra were recorded between 50 – 2000 Da and averaged over 50 scans to ensure consistency. The ASAP ion source parameters capillary voltage (3.00 kV), corona current (2.5 µA), extraction cone (2 V), source temperature (150 C), cone gas flow (0 L h^{-1}) and desolvation gas flow (600 L h^{-1}) remained constant throughout the analyses. The ion source parameters sampling cone (10 V – 50 V) and the desolvation gas temperature (300 °C – 600 °C) were manipulated to achieve intact precursor ion peaks with an optimal S/N ratio. Tandem MS experiments were performed using CID using argon collision gas (4.8×10^4 Pa), where the collision energy was increased linearly increased 5 V to 50 V during the experiment. Spectra were analysed using MassLynx version 4.1 suite of software (Waters Corporation, Manchester, United Kingdom), where accurate mass measurements were carried out using the embedded program Elemental Composition version 4.0.

2.3.6. Sample preparation for MALDI

Samples of PEG (M_n = 1500), PS (M_n = 1900) and PMMA (M_n = 1000) were dissolved in THF to a concentration of approximately 5 mg mL^{-1}. α- cyano-4-hydroxycinnamic acid (CHCA), dithranol and 2,5-dihydroxybenzoic acid (DHB) were prepared to 50 mg mL^{-1} in THF. Lithium bromide, silver trifluoroacetate and sodium iodide were prepared at 5 mg mL^{-1} in THF. The solutions were combined so that the ratio of polymer: matrix: salt was 1:1:1. 1 µL of the subsequent mixture was applied to the ground steel target using the dried droplet technique.

2.3.7. Autoflex II

The Autoflex II mass spectrometer (Bruker Daltonics, Coventry, United Kingdom) comprises a ToF/ToF mass analyser fitted with a MALDI source equipped with a 337 nm nitrogen laser. The mass spectrometer was calibrated using sodium adducts of poly(ethylene glycol) (M_n = 1500). MS and tandem MS measurements were recorded over 50 – 2000 Da and utilised the reflectron for enhanced performance. Tandem MS experiments conducted using LIFT in the absence of a collision gas at a source pressure of 2.5×10^{-7} mbar unless otherwise stated. For CID experiments, argon was used as a collision gas at a source pressure of approximately 8.5×10^{-7} mbar. Isolation of the precursor ion was sufficient with the instrumental defaults. The laser power was set at the lower threshold for peak detection. The number of laser shots was optimised for each experiment to achieve a good S/N ratio for all ions detected. Spectra were analysed using Flex Analysis 3.0 (Bruker Daltonics, Coventry, United Kingdom).

3. ESI Tandem MS of poly(ethylene glycol)

3.1. Introduction

Interest in the application of mass spectrometry to the analysis of synthetic polymers increased dramatically with the introduction of MALDI and ESI ionisation techniques that allowed the production of ions of high molecular weight for common synthetic polymers, MALDI in particular, has been able to successfully ionise polymers up to 1.5 MDa[15]. Accurate and precise mass analysis can be used on instruments with high resolving power to give empirical formula that can provide structural information regarding the monomer sequence, terminal groups present and charge carrier.[120] In situations where there is some uncertainty in the polymer structure, tandem MS experiments have been shown to provide structural information that allows the assignments of individual end groups,[145] differentiates ions of identical nominal mass,[244] and identifies polymers of novel architecture.[138] As discussed in Section 1.7.4.2, the most widely used activation method for synthetic polymer tandem MS experiments is CID. The application of electron-based fragmentation techniques to synthetic polymer analysis has been minimal with a small number of publications regarding ECD[201-203] and ETD[245] of synthetic polymers. This thesis reports the investigation of electron-based fragmentation techniques ECD, HECD and EID for the analysis of common synthetic polymers, with particular focus on the polyether class of synthetic polymers. Of particular interest with regards to the application of electron-based tandem MS experiments to synthetic polymer analysis are:

- The amount of structurally significant analytical information that a technique can provide.
- The greatest depth of analytical information, regardless of charge carrier.
- The ability to generate complementary information giving enhanced confidence in the extent of sequence information.

3.2. ESI and MALDI MS and tandem MS of [PEG + Li]$^+$

PEG is a polar synthetic polymer that has a repeating unit that has a linear arrangement of carbon and oxygen atoms that form the polymer backbone. The regular occurrence of oxygen atoms results in PEG forming pseudo-molecular ions with alkali metal cations,[87,88,131,132,246,247] where lithium has been proven theoretically[150] and experimentally[87,88,132] to be the most effective metal cation for CID-tandem MS experiments. This was proposed to be due to the high Lewis acidity of lithium and the superior strength of the interaction formed between the metal cation and the polymer.[150] Indeed when hydroxyl terminated PEG (M_n = 1500) is doped with lithium bromide during sample preparation, MALDI MS generates the characteristic molecular weight distribution for a polymer of narrow polydispersity as shown in Figure 3.1(a). The major series of peaks labelled (●) correspond to intact **[PEG$_n$ + Li]$^+$**(n=22–45). The presence of a second series of peaks, labelled (▲) that are 16 Da above (●), correspond to **[PEG$_n$ + Na]$^+$** (n=22–42) demonstrating that this sample preparation has not resulted in complete ionisation with lithium alone. ESI MS analysis of hydroxyl terminated PEG (M_n = 1500) doped with lithium bromide resulted in a mass spectrum containing three molecular weight distributions as shown in Figure 3.1(b). The first series of peak in the region *m/z* 600- *m/z* 1000 labelled (♦) corresponded to **[PEG$_n$ + 2Li]$^{2+}$** (n=28–39), which was confirmed by accurate mass analysis (*m/z* 698.42737 = **[HO(C_2H_4O)$_{31}$H + 2Li]$^{2+}$**). The series of peaks of greatest intensity labelled (●) in Figure 3.1(b), correspond to **[PEG$_n$ + Li]$^+$** (n=21 –39) confirmed by accurate mass analysis (*m/*z 1389.89058 = $C_{62}H_{126}O_{32}Li$ = **[HO(C_2H_4O)$_{31}$H + Li]$^+$**). As with MALDI analyses, ESI MS of PEG contains a second series of ions 16 Da above the **[PEG$_n$ + Li]$^+$** series. Accurate mass analysis of *m/z* 1405.81003 gives an empirical formula of $C_{62}H_{126}O_{32}Na$, which is consistent with **[HO(C_2H_4O)$_{31}$H + Na]$^+$** indicating that the series of peaks labelled (▲) correspond to **[PEG$_n$ + Na]$^+$** (n=25–36).The presence of such a series despite not adding sodium salts to the sample, demonstrates the high affinity of PEG for sodium, but also the abundance of sodium salts as contaminants in solvents and glassware.[87]

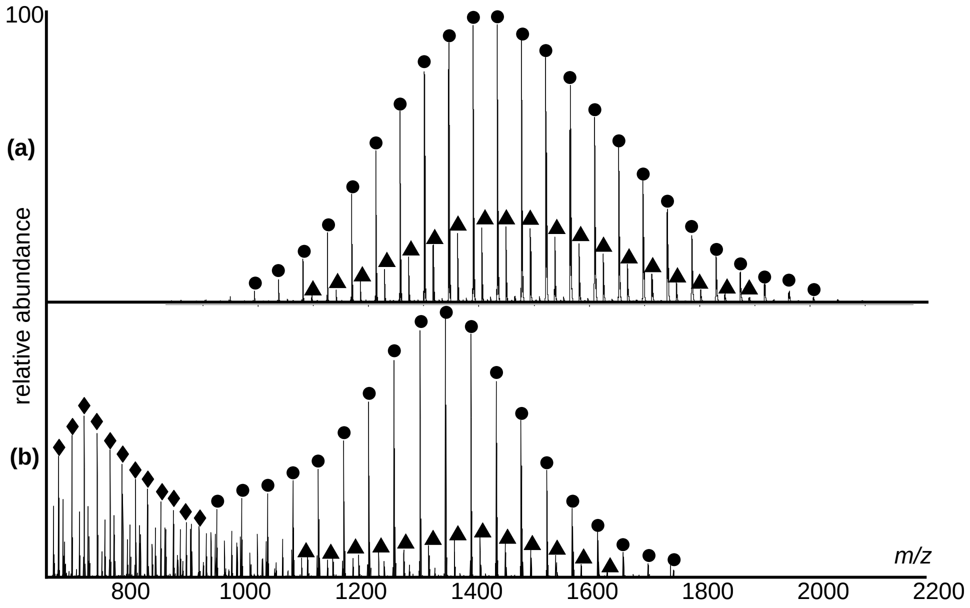

Figure 3.1 (a) MALDI MS of PEG (PEG (5 mg mL^{-1}), ACHA (10 mg mL^{-1}) and LiBr (5 mg mL^{-1}) in 5:5:1 ratio and (b) ESI Full MS of PEG (5.7 μg mL^{-1} in 1 mM LiBr solution) (● = [PEG + Li]$^+$, ▲ = [PEG + Na]$^+$ and ♦ = [PEG + 2Li]$^{2+}$).

To perform tandem MS, a peak that represents an individual degree of polymerisation was selected. The precursor ion at *m/z* 1389.8 containing 31 monomer units, **$[HO(C_2H_4O)_{31}H + Li]^+$**, (**$[PEG_{31} + Li]^+$**) was isolated and fragmented using different tandem MS techniques as shown in Figure 3.2. MALDI-CID of **$[PEG_{31} + Li]^+$** resulted in extensive polymer dissociation as shown in Figure 3.2(a). The product ions are observed throughout the measured *m/z* range, providing confirmation of the monomer sequence for 23 of the 31 monomers present. As shown in the expansion (inset, Figure 3.2(a)) the product ions are found to result from cleavage of the carbon-ether oxygen backbone bond. There are three series of peaks with the same motif, where the ions within each series are separated by 44 Da, the mass of the PEG monomer unit (C_2H_4O). The series of peaks denoted **b_n** (n=2–26) are formed through cleavage of the carbon-ether oxygen bond, where the new terminal group is an unsaturated vinyl moiety. The series denoted **c_n** (n=4–24) involves cleavage of the same carbon-ether oxygen bond where the terminal group generated is an unsaturated carbonyl functionality. The series of peaks labelled as **c_n''** is related to the **c_n** series, result from cleavage of the same carbon-ether oxygen bond, generating a saturated terminal group. Due to the end-groups present in this particular polymer, a degree of molecular symmetry arises preventing determination of which end group is present, as the product ions generated have the same nominal mass, where **b_{10}** = **z_{10}**, therefore product ion assignments have been simplified to include only one set of product ion nomenclature.

ESI QToF-CID of **[PEG$_{31}$ + Li]$^+$** generated the same three types of product ions observed in MALDI-CID as shown in Figure 3.2(b). As ToF mass analysers are used to generate the spectra in Figure 3.2(a) and Figure 3.2(b), the usable *m/z* range is the same and product ions are detected throughout this range providing comparable information. Inspection of the relative product ion peak intensities generated by QToF-CID, demonstrates that the pattern mimics that observed by MALDI-CID where the most intense product ion series of peaks corresponds to the **b$_n$** ions (n =4-27). It is also noted that the ratio of **c$_n$** (n=7-25) to **c$_n$$''$** (n=7-25) is similar in both MALDI-CID and QToF-CID. Performing CID in the LTQ provides a number of challenges for synthetic polymer characterisation; in particular the 1/3 cut-off rule restricts the detectable *m/z* range and consequently limits low mass product ion detection. LTQ-CID is shown to generate fewer product ions than observed by other tandem MS approaches as shown in Figure 3.2(c), where product ions are not observed throughout the detectable *m/z* range. Three major product ion series can be observed, that on closer inspection, are found to have the same nominal masses as those observed for MALDI-CID and QToF-CID as shown inset in Figure 3.2(c) (**b$_n$** (n=12-27), **c$_n$** (n=13-31) and **c$_n$$''$** (n=13-31). The intensity of the product ion peaks relative to each other is different in MALDI-CID (or QToF-CID) and LTQ-CID, and is particularly noticeable for the **c$_n$** ion peaks, which have comparable intensity to **b$_n$** by MALDI-CID, but are present at a much lower intensity than **b$_n$** in the LTQ-CID spectrum. Also the **c$_n$$''$** peaks, that were the least intense in MALDI-CID are more intense than the **c$_n$** peak when LTQ-CID is used.

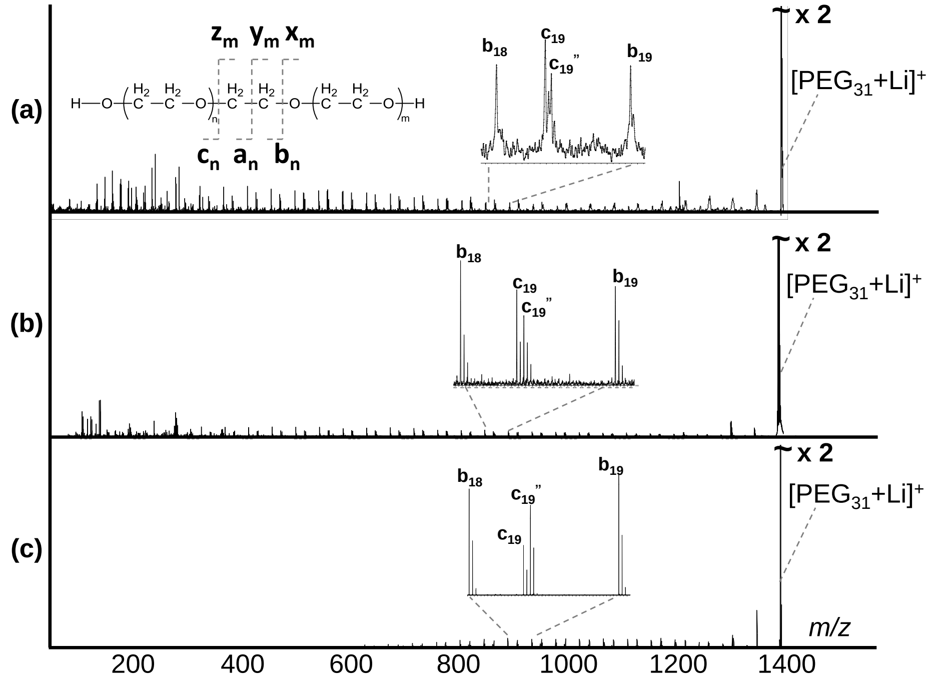

Figure 3.2 Tandem MS of [HO(C$_2$H$_4$O)$_{31}$H + Li]$^+$: (a) MALDI-CID + product ion nomenclature, (b) ESI QToF-CID and (c) ESI LTQ-CID.

Polce and Wesdemiotis previously demonstrated that that the relative intensities of the product ions generated during tandem MS of PEG are representative of the mechanism of fragmentation.[120] The major product ions **b_n** and **c_n**″ observed in LTQ-CID (Figure 3.2(c)) can be formed through the charge directed dissociation mechanism (Scheme 3.1). Charge-directed fragmentations are generally associated with mechanisms that involve lower critical energies, where LTQ-CID is an example.

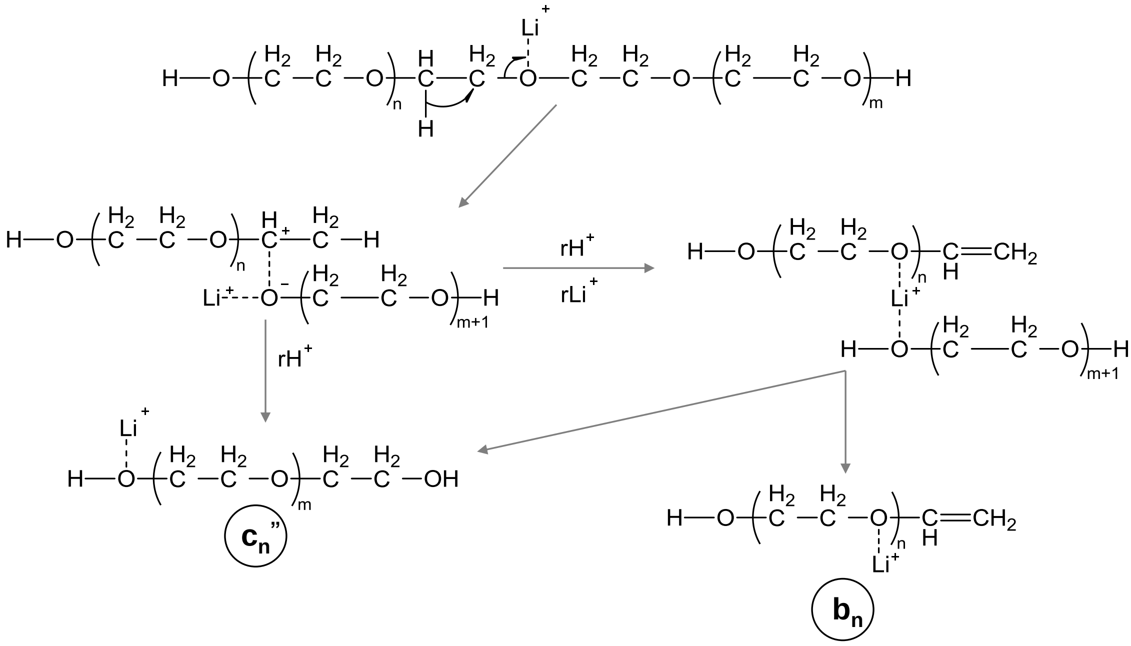

Scheme 3.1 Charge directed fragmentation of PEG.

In contrast, MALDI-CID and QToF-CID, which preferentially form $\mathbf{b_n}$ and $\mathbf{c_n}$ product ions, are better represented by a charge remote fragmentation mechanism outlined in Scheme 3.2. The generation of $\mathbf{b_n}$ and $\mathbf{c_n}$ involves initial homolytic cleavage of the carbon-ether oxygen bond leading to radical formation where subsequent loss of a hydrogen radical generates the product ions. It is noted that none of the major product ions result from cleavage of the stronger carbon-carbon bond favouring fragmentation of the weaker carbon-ether oxygen bond.

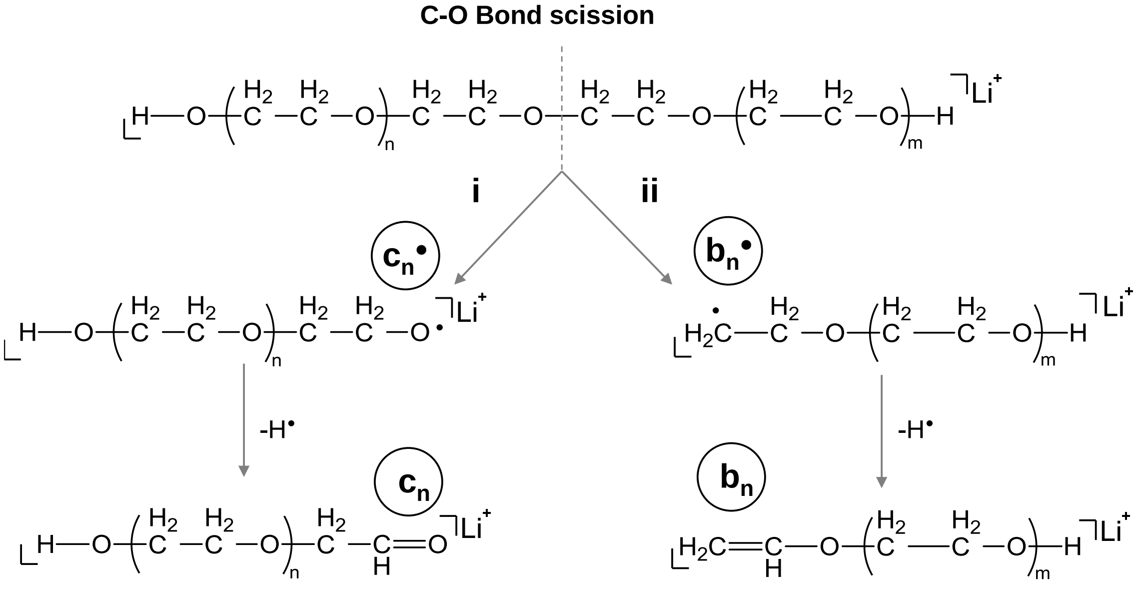

Scheme 3.2 Charge remote fragmentation of PEG.

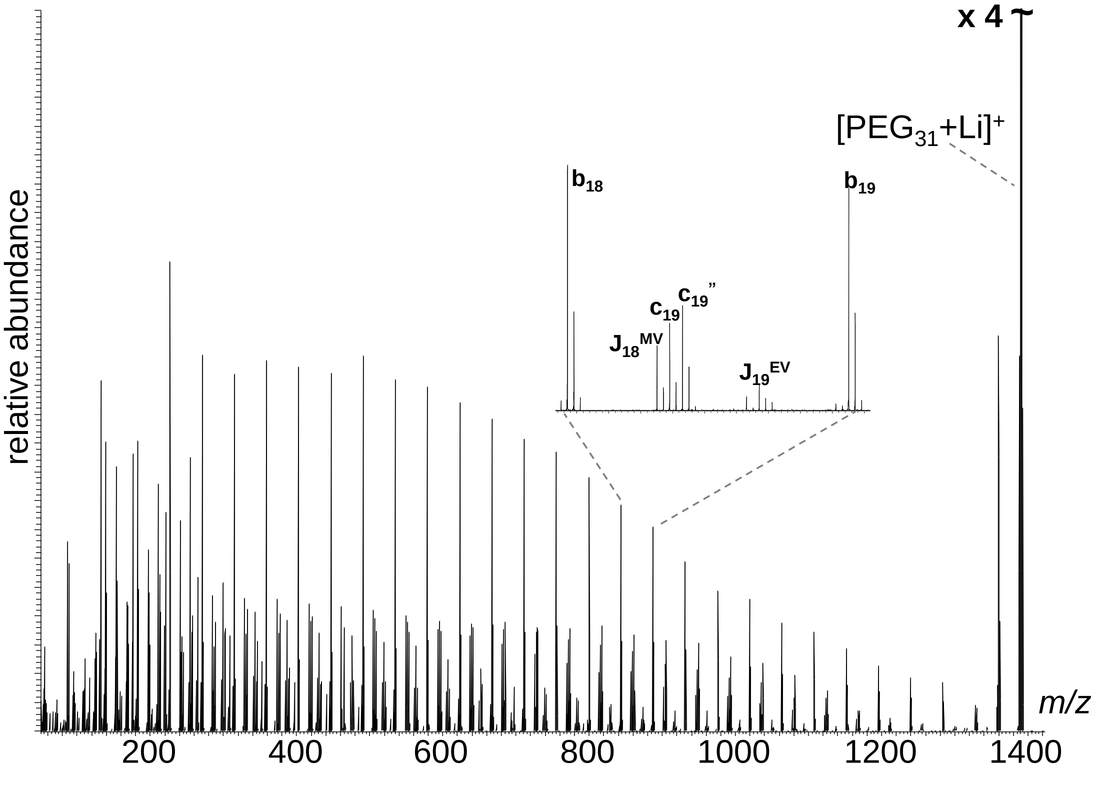

Figure 3.3 EID (20.1 eV) tandem MS $[HO(C_2H_4O)_{31}H + Li]^+$.

Irradiation of the **$[PEG_{31} + Li]^+$** precursor ion with incident electrons of 20.1 eV is sufficient to induce extensive dissociation of the polymer as shown in Figure 3.3 EID (20.1 eV) tandem MS $[HO(C_2H_4O)_{31}H + Li]^+$.Figure 3.3. EID is shown to generate product ions that are present throughout the full *m/z* range, providing comparable sequence information to MALDI-CID (or ESI QToF-CID). Close inspection of the expansion shown inset, allows the identification of five series of peaks where the difference between the peaks within the same series is the characteristic 44 Da. Following product ion assignment, it is clear that the three of the five series of peaks correspond to dissociation of the polymer backbone observed from the CID experiments: $\mathbf{b_n}$(n=2-30), $\mathbf{c_n}$ (n=5-27)and $\mathbf{c_n}''$(n=5-27). The relative intensities of the product ion peaks in EID are different to those observed using CID. The intensities of peaks $\mathbf{c_n}''$ and $\mathbf{c_n}$ are approximately equal for EID, whereas for ToF-CID $\mathbf{c_n} > \mathbf{c_n}''$ and $\mathbf{c_n} < \mathbf{c_n}''$ in LTQ-CID. It must be noted that this comparison of the ratios of the product ion peak intensities is based upon the expanded product ion sequences shown inset in Figure 3.2 and Figure 3.3, and is not expected to be the same for every value of **n**. If the fragmentation in EID was a solely charge-remote process, then formation of $\mathbf{b_n}$ and $\mathbf{c_n}$ ions could be expected to result in peaks of similar intensity as in MALDI-CID (Figure 3.2(a)). Further differences in the product ion spectra can be observed in the expansion (Figure 3.3) where there are a number of other peaks not observed during CID. Accurate mass analysis of these peaks gives empirical formula that corresponds to internal ions, resulting from multiple backbone cleavages. The $\mathbf{J_n^{EV}}$ (n=3-23) internal fragments are formed through carbon-ether oxygen bond cleavages to generate a PEG chain that contains unsaturated vinyl and saturated ethyl terminal groups. This internal fragment can be generated through initial homolytic bond cleavage followed by radical migration to a proximal position, where β–scission of C-O bond generates $\mathbf{J_n^{EV}}$ as shown in Scheme 3.3.

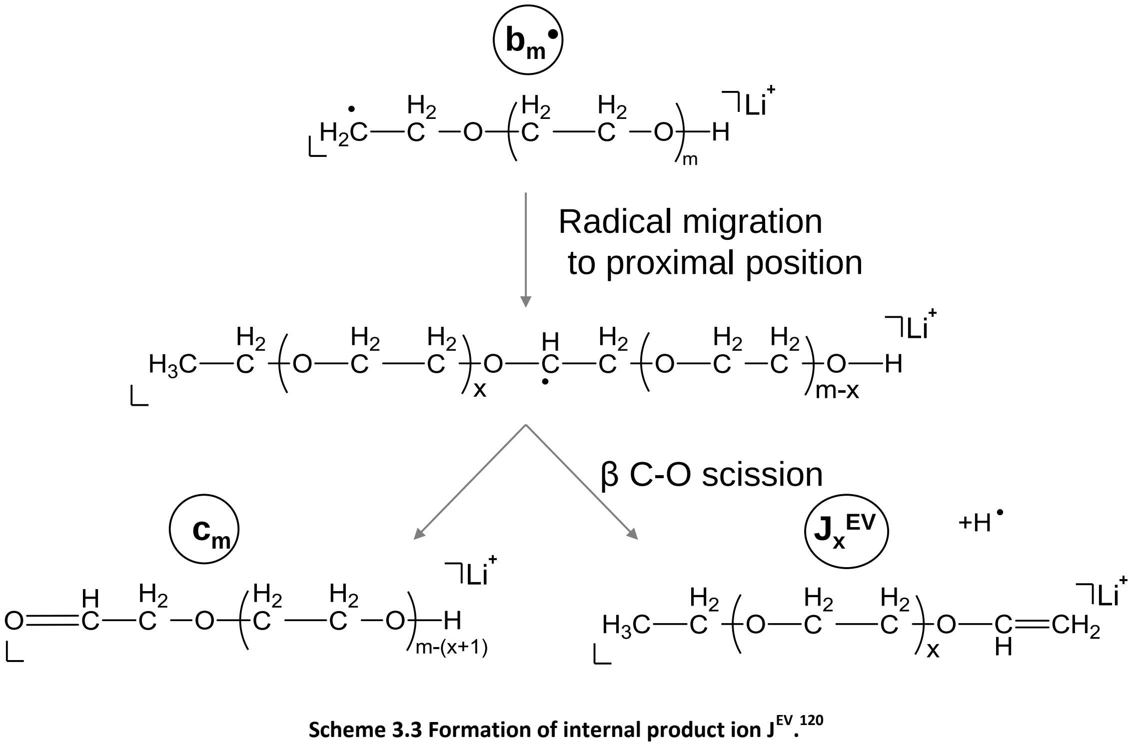

Scheme 3.3 Formation of internal product ion J^{EV}.[120]

The $\mathbf{J_n}^{MV}$ (n=4-26) product ions are unusual as the empirical formula yields an odd number of carbon atoms, suggesting that formation involves cleavage of the stronger carbon-carbon bond. When the empirical formula is used to propose a structure it corresponds to a PEG chain that has an unsaturated vinyl terminal group and a methoxy terminal group. Although these internal fragments do not enhance the characterisation of PEG, carbon-carbon bond cleavage poses an exciting prospect for EID analysis for synthetic polymers that have a backbone containing only carbon-carbon bonds, such as PMMA and PS. Cleavage of the carbon-carbon bond is rarely observed in CID MS analysis of PEG, however it has been observed in FAB-CID experiments performed on a sector-hybrid instrument where a laboratory frame-collision energy of 50 eV is used.[132]

When the intensity of the product ion peaks across the entire spectrum are compared; it is noted that the intensity of the peaks increase with decreasing *m/z* in MALDI-CID, QToF-CID and EID. This could suggest that fragmentation is more prevalent towards the polymer chain ends. From previous studies it is known that the metal cation is most effectively coordinated at the polymer chain end[45] which may influence the fragmentation chemistry. Alternatively the higher intensity of the low *m/z* peaks may be due to the higher stability of the product ions that the peaks represent.

3.3. CID, ECD and HECD tandem MS of $[PEG + 2Li]^{2+}$ and $[PEG + 3Li]^{3+}$

The success of the EID technique in the analysis of singly charged **$[M + Li]^+$** encouraged the development of further experiments that would yield a better understanding of how fragmentation occurs under conditions when the energy of the electrons is 15-25 eV. Of particular interest was the investigation of the effect of precursor ion charge state upon the spectra generated by the electron-based fragmentation techniques.

3.3.1. Investigation into the effect of charge state upon EID and HECD of $[PEG + nLi]^{n+}$

ESI MS analysis of PEG doped with lithium bromide presented in Figure 3.1(b), demonstrated the presence of doubly charged molecular ions. Manipulation of ESI source parameters optimised the intensity of the doubly charged peaks, so that tandem MS experiments could be performed. The precursor ion selected for this investigation was *m/z* 698.42737, which gives an empirical formula of $C_{62}H_{126}O_{32}Li_2$ corresponding to **$[HO(C_2H_4O)_{31}H +2Li]^{2+}$**,(**$[PEG_{31} + 2Li]^{2+}$**) the doubly charged equivalent of **$[PEG_{31} + Li]^+$** analysed in Section 3.2.

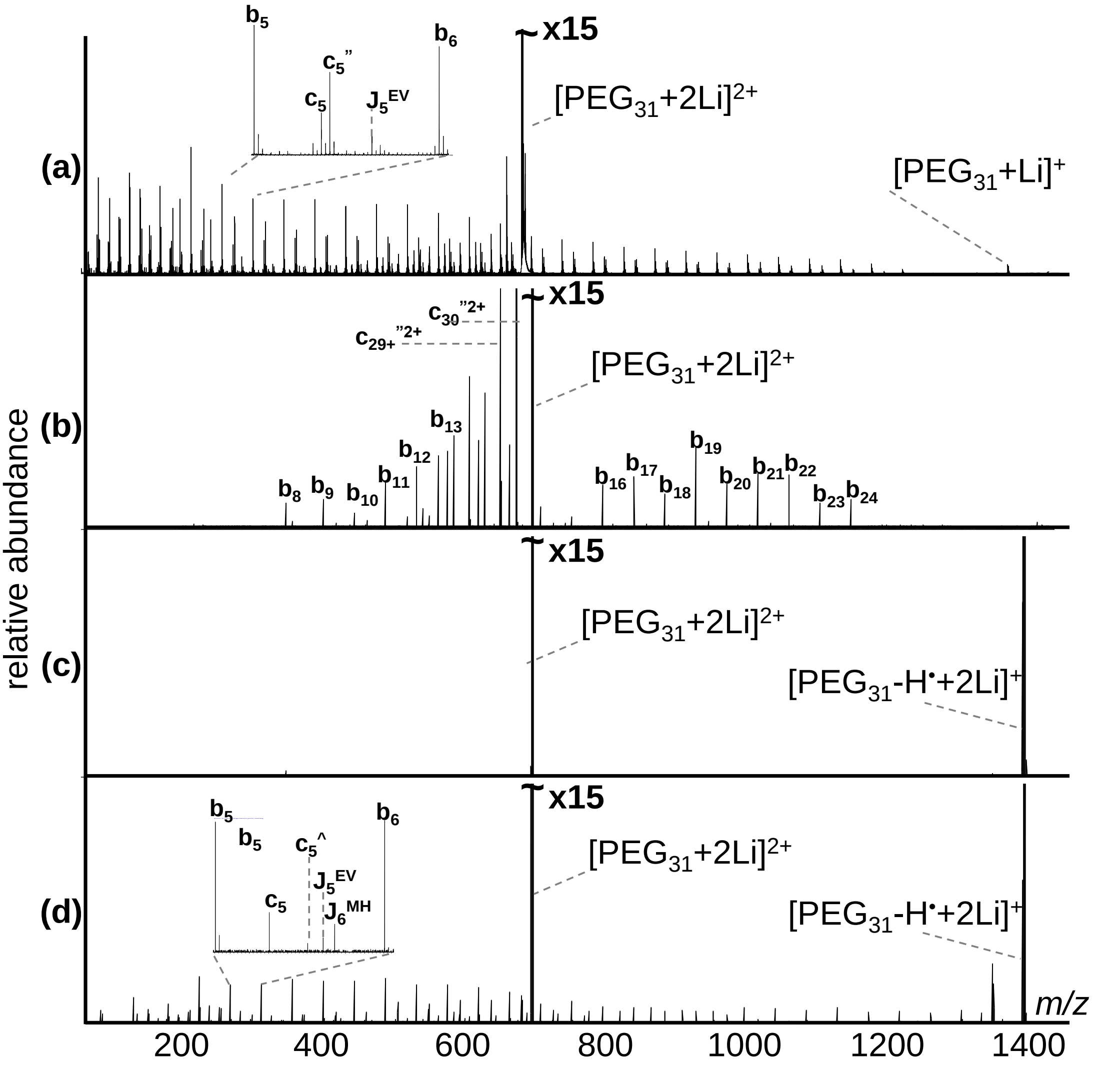

Figure 3.4 Tandem MS of $[HO(C_2H_4O)_{31}H + 2Li]^{2+}$: (a) QToF-CID, (b) LTQ-CID, (c) ECD 3.1 eV and (d) HECD 21.1 eV.

QToF-CID of **$[PEG_{31} + 2Li]^{2+}$** results in extensive polymer dissociation as shown in Figure 3.4(a). Product ions are observed across the full *m/z* range, where the series of peaks with the greatest intensity are the product ions **b_n**, analogous to the results observed in the analysis of **$[PEG_{31} + Li]^+$**. Like QToF-CID of **$[PEG_{31} + Li]^+$**, the intensity of the product ions increase with decreasing *m/z*. Close inspection also reveals the presence of internal fragment **J_n^{EV}** (n=3-13) a product of multiple bond cleavages alongside the product ions **b_n** (n=2-27), **c_n** (n=5-26) and **c_n''** (n=5-26) that result from single backbone bond cleavage, as shown inset in Figure 3.4(a). The **J_n^{EV}** product ions were not detected in the equivalent analysis of **$[M + Li]^+$** suggesting that the multiple charge carriers may be required for the generation of internal fragments under CID conditions. One proposal for the formation of internal fragments is, through the fragmentation mechanisms outlined previously in Scheme 3.1 and Scheme 3.2, where both lithium cations induce polymer dissociation simultaneously. In comparison, LTQ-CID, generates a very different product ion spectrum to that obtained by QToF-CID as shown in Figure 3.4(b). The product ion series is less complex for LTQ-CID than is observed for the QToF-CID, where $\mathbf{b_n}$ (n=8-24) are the most abundant product ions observed throughout the detectable *m/z* range. It is noted that the product ion peaks of greatest intensity in the LTQ-CID spectrum correspond to doubly charged $\mathbf{c_n}''^{2+}$ (n=27-30) product ions formed through neutral loss of individual monomers from the precursor ion with retention of both lithium cations.

When **[PEG$_{31}$ + 2Li]$^{2+}$** is irradiated with incident electrons with 3.1 eV electron energy, no product ions resulting from polymer dissociation are detected. The only product ion formed is a charge reduced singly charged molecular ion. Performing accurate mass analysis of *m/z* 1395.84669 gives an empirical formula of $C_{62}H_{125}O_{32}Li_2$ with 0.1 ppm error. This is an unusual observation, as the singly charged ion retains both lithiums and contains one hydrogen fewer than the precursor ion. The presence of two lithium cations in a singly charged ion, suggests that electron capture is occurring. Formation of this product ion can be accounted for by the mechanism outlined in Scheme 3.4, where electron capture by a lithium cation results in a lithium atom being covalently bound to the polymer with subsequent ejection of a hydrogen radical. This concept is known from ECD analysis of doubly charged peptides, where an initially formed singly charged hypervalent intermediate is stabilised through ejection of a hydrogen radical.[248]

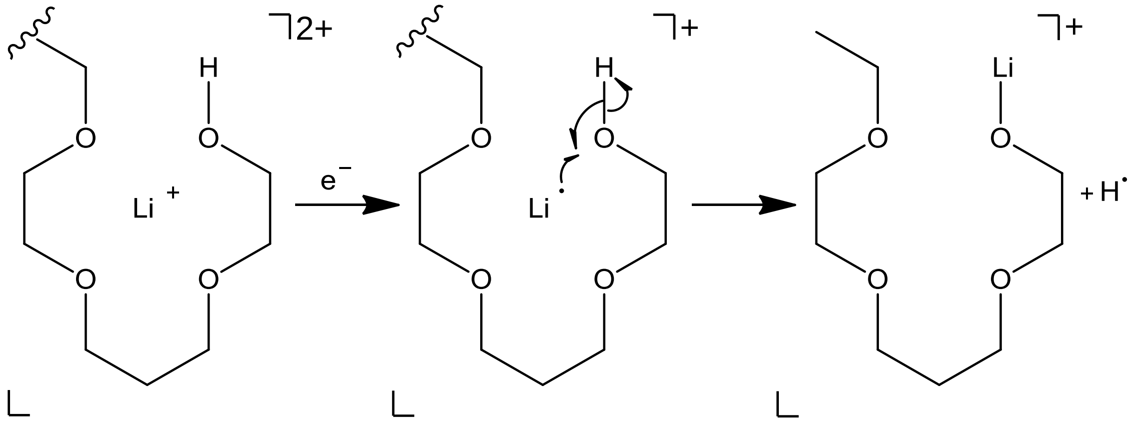

Scheme 3.4 Mechanism accounting for the formation of a singly charged product ion containing two metals.

Increasing the energy of the incident electron to 21.1 eV (akin to EID), allows HECD to be performed. This increase in the energy of the electrons is sufficient to induce polymer dissociation as shown in Figure 3.4(d). Like ECD, the most intense product ion peak present under HECD conditions corresponds to **[PEG$_{31}$ – H$^{\bullet}$+ 2Li]$^{+}$** generated by electron capture and hydrogen radical ejection. Inspection of the product ions resulting from dissociation of the polymer, shows that like QToF-CID and LTQ-CID the product ion peaks of greatest intensity are **b_n** (n=2-29). Alongside **c_n** (n=5-22) there are internal fragments (**J_n**, n=5-15) present that are formed through multiple bond dissociations as shown inset. It is noted that HECD has generated a unique series of product ion peaks with an example at *m/z* 295.19161. This product ion gave empirical formula of $C_{12}H_{25}O_7Li_2$ (0.4 ppm) by accurate mass analysis. This empirical formula could correspond to the structure proposed in Figure 3.5. The structure proposes that a lithium atom is covalently bound at hydroxyl chain end similar to the mechanism outlined in Scheme 3.4, where subsequent backbone dissociation allows formation of the saturated hydroxyl terminal group, therefore this product ion has been assigned as **$c_5^{\wedge}$**. The presence of the **$c_n^{\wedge}$** product ion series demonstrates that two processes must be occurring that lead to formation of this product ion. The first, involves electron capture by a lithium resulting in covalent attachment of the lithium at a hydroxyl terminus. The second process involves dissociation of the polymer backbone leading to the formation of a hydroxyl terminal group. The order in which these processes occur is not clear, however both are required to form the product ion. O'Connor *et al.* demonstrated that H/D scrambling was possible in long lived radical species prior to final dissociation for a doubly charged peptide containing deuterated glycine residues by ECD.[175] It is not yet clear whether the initially formed **$[PEG_{31} - H^{\bullet} + 2Li]^+$** undergoes subsequent polymer dissociation to yield the **$c_n^{\wedge}$** product ions, to investigate this proposal an experiment that involves selected ion ejection of the **$[PEG_{31} - H^{\bullet} + 2Li]^+$** during the HECD experiment could provide an insight depending on the presence or lack of the **$c_n^{\wedge}$** species.

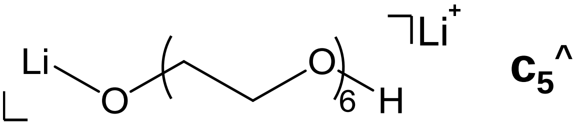

Figure 3.5 Potential structure of product ion *m/z* 295.19161.

Further optimisation of ESI source conditions permitted the isolation of **$[PEG_{31} + 3Li]^{3+}$**. Tandem MS of **$[PEG_{31} + 3Li]^{3+}$** is shown in Figure 3.6. QToF-CID is shown to readily dissociate the triply charged precursor ion with singly charged product ions observed throughout the *m/z* range (Figure 3.6(a)). The most intense product ion observed in the spectra is **$[PEG_{31} + 2Li]^{2+}$**. The formation of **$[PEG_{31} + 2Li]^{2+}$** from the **$[PEG_{31} + 3Li]^{3+}$** is likely to involve cation detachment. Support for cation detachment from PEG ionised with alkali metals can be found in Appendix 10.3 where CID of **$[PEG_6 + Cs]^+$** provides evidence for the product ion **Cs^+**. Further evidence of cation detachment can be found in work by Girod *et al.* who identified a number of raw metal cations when analysing doubly charged PEG ionised with alkali metals in a QToF instrument.[88]

As with the QToF-CID spectra recorded for **$[PEG_{31} + Li]^+$** and **$[PEG_{31} + 2Li]^{2+}$**, the series of product ion peaks of greatest intensity in the **$[PEG_{31} + 3Li]^{3+}$** corresponds to the singly charged **b_n** (n=3-28) product ion, shown inset in Figure 3.6(a). Close inspection of the repeat unit, allows the identification of the **c_n** (n=5-18) and **c_n''** (n=5-18) product ions as shown inset in Figure 3.6(a). In common with QToF-CID of **$[PEG_{31} + 2Li]^{2+}$**, there is evidence of internal fragment **J_n^{EV}** (n=4-14) formation. This provides further support for the proposal that multiple charge carriers are required to allow formation of **J_n^{EV}** by CID. In contrast, CID performed in the LTQ provides limited numbers of product ions resulting from polymer dissociation as shown in Figure 3.6(b). As with QToF-CID, the major product ion corresponds to **$[PEG_{31} + 2Li]^{2+}$** which results from cation detachment. A significant difference in the LTQ-CID spectrum, are a small number of triply charged product ions. These intense product ion peaks labelled **$c_{29}''^{3+}$** and **$c_{28}''^{3+}$** are proposed to form through small neutral losses of one and two monomers respectively from the precursor ion. Additionally there is a small product ion series that corresponds to the singly charged **b_n** ion which provides limited structural information.

Irradiation of **$[PEG_{31} + 3Li]^{3+}$** with incident electron with 3.1 eV energy is not sufficient to induce dissociation of the polymer as shown in Figure 3.6(c). The major product ions correspond to the charge reduced species at *m/z* 701.43292 and 1401.86353. Interestingly, accurate mass analysis of these peaks yields empirical formulae corresponding to **$[PEG_{31} – H^\bullet + 3Li]^{2+}$** and **$[PEG_{31} – 2H^\bullet + 3Li]^+$**. The presence of **$[PEG_{31} – 2H^\bullet + 3Li]^+$** is evidence of sequential electron capture by the precursor ion with the ejection of two hydrogen radicals. This is proposed to occur in a similar way to the mechanism outlined in Scheme 3.4, where the most likely locations for lithium attachment are the hydroxyl groups present at the polymer chain ends. To minimise the electrostatic repulsion that exists between the cations, it is likely that the location of two of the lithium cations will be close to the polymer chain ends in the precursor ion. This adds confidence to the proposal for lithium to exchange with the labile hydrogen atoms of the hydroxyl polymer terminal groups, eliminating a hydrogen radical and forming the charge reduced species following electron capture. The third lithium is believed to be coordinated to the polymer through interaction with oxygen atoms.

Increasing the energy of the electrons to 20.1 eV resulted in the product ion spectrum shown in Figure 3.6(d). **$[PEG_{31} – H^\bullet + 3Li]^{2+}$** and **$[PEG_{31} – 2H^\bullet + 3Li]^+$**, proposed to result from electron capture, are the most intense product ions peaks observed. Inspection of this spectrum reveals there is no evidence of any product ions that retain all three metals as shown inset in Figure 3.6(d). This supports the proposal that attachment of lithium occurs at each of the polymer chain ends, where dissociation of the polymer results in loss of at least one lithium. Expansion of the product ion series, shown inset in Figure 3.6(d), is dominated by singly charged product ions including the characteristic $\mathbf{b_n}$ (n=2-23), $\mathbf{c_n}$ (n=4-18) and $\mathbf{c_n}''$ (n=4-18) ions. There is once again evidence of a peak from the $\mathbf{c_n}^{\wedge}$ series (n=5-22), who's empirical formula contains two lithium atoms, where one lithium atom is believed to be covalently bound to the polymer.

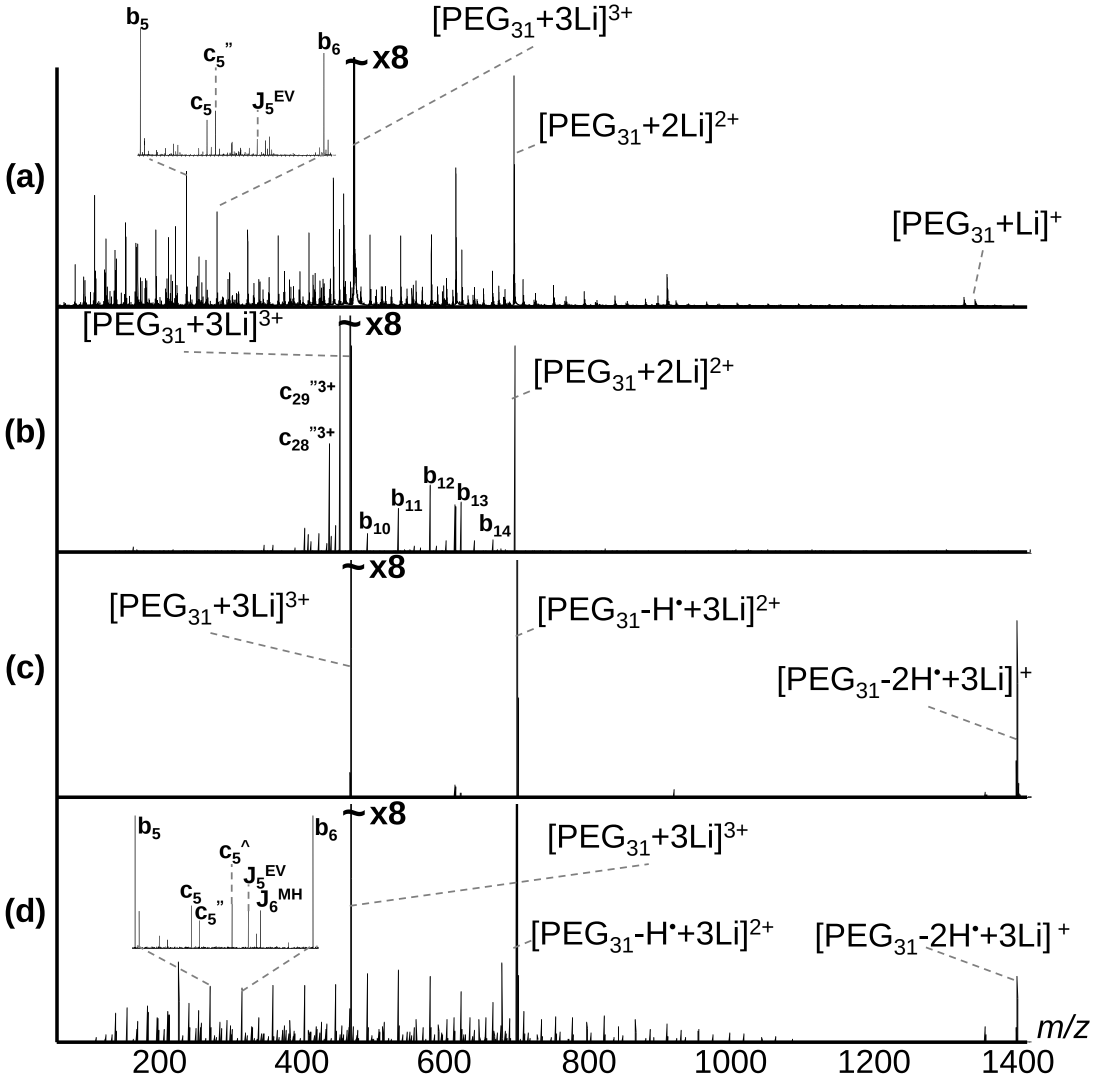

Figure 3.6 Tandem MS of $[HO(C_2H_4O)_{31}H + 3Li]^{3+}$: (a) QToF-CID, (b) LTQ-CID, (c) ECD 3.1 eV and (d) HECD 20.1 eV.

When comparing the spectra for the different precursor ions by technique, there are some interesting observations. QToF-CID generated an unbroken series of $\mathbf{b_n}$ ions that represent 75 % of the monomer units regardless of precursor ion charge state as shown in Table 3.1. QToF-CID of the multiply charged ions ($\mathbf{[PEG_{31} + 2Li]^{2+}}$,Figure 3.4(a) and $\mathbf{[PEG_{31} + 3Li]^{3+}}$, Figure 3.6(a) shows that higher charge states enabled the formation of internal fragments $\mathbf{J_n^{EV}}$, which suggests that formation of these ions may require multiple charge carriers.

Table 3.1 b_n product ion series by fragmentation technique and precursor ion.

	$[M + Li]^+$	$[M + 2Li]^{2+}$	$[M + 3Li]^{3+}$
MALDI-CID	b_2 - b_{26}	N/A	N/A
QToF-CID	b_4 - b_{27}	b_2 - b_{27}	b_3 - b_{28}
LTQ-CID	b_{12} - b_{27}	b_8 - b_{24}	b_{10} - b_{14}
EID and HECD	b_2 - b_{30}	b_2 - b_{29}	b_2 - b_{23}

For LTQ-CID an initial increase in charge state to the **$[PEG_{31} + 2Li]^{2+}$** resulted in product ions being detected across a wider mass range. This is mainly a result of a precursor ion with a lower *m/z* and consequently a lower *m/z* cut-off meaning that there is larger usable *m/z* range. Increasing the charge state further to the **$[PEG_{31} + 3Li]^{3+}$** leads to the formation significantly fewer product ions. This observation was also found for EID and HECD where increasing the charge state from **$[PEG_{31} + 2Li]^{2+}$** to **$[PEG_{31} + 3Li]^{3+}$** reduced the percentage product ion sequence coverage from 87 % to 67 %. One potential reason for this is that the addition of extra metal cations will increase the Coulombic cation repulsion experienced by the molecule and cause a change in the gas-phase conformation adopted by the precursor ion. Ude *et al.* demonstrated that the conformation of PEG changed from compact to linear with increasing charge state.[249] Therefore increasing the charge state will cause a conformational change, which may be responsible for a reduced number of product ions observed for LTQ-CID and the electron-based fragmentation techniques, suggesting that the conformation of the precursor ion is important for successful fragmentation using LTQ-CID, EID and HECD.

3.4. Investigation into the influence of the charge-carrying species upon the fragmentation mono-methyl terminated PEG

3.4.1. Tandem MS of methyl terminated PEG with monovalent charge carriers

In Section 3.2, tandem MS of hydroxyl terminated **$[PEG_{31} + Li]^+$** was shown to generate product ions that provide structural information regarding monomer sequence and terminal groups. The presence of hydrogen and hydroxyl terminal groups resulted in product ions with the same nominal mass and it was therefore impossible to determine which terminal group was present in a product ion. Consequently mono-methyl terminated PEG (M_n = 660) (Figure 3.7), was selected for tandem MS analysis as the presence of asymmetric terminal groups would allow separation of the product ions theoretically permitting directional sequencing.

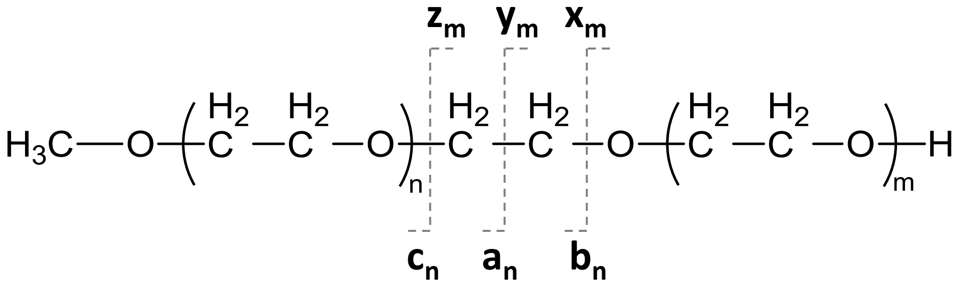

Figure 3.7 Structure of PEG methyl ether, annotated to indicate cleavage sites and the nomenclature used to differentiate between resulting product ions.

LTQ-CID of the mono-methyl terminated PEG containing precursor ions: **$[PEG_{13} + NH_4]^+$**, **$[PEG_{13} + Li]^+$**, **$[PEG_{13} + Na]^+$**, **$[PEG_{13} + K]^+$**, **$[PEG_{13} + Ag]^+$**, and **$[PEG_{13} + Cu]^+$** resulted in the product ion spectra shown in Figure 3.8. LTQ-CID of **$[PEG_{13} + NH_4]^+$** resulted in extensive polymer fragmentation, however the **$z_m^{!}$**, **$b_n^{!}$** and **$c_n^{\prime\prime!}$** product ions do not retain the **NH_4** charge carrier as denoted by the "**!**" symbol used in the assignments in Figure 3.8(a). The most intense product ion peak corresponds to neutral loss of NH_3 resulting in a protonated molecular ion, **$[PEG_{13} + H]^+$**. This would suggest that the precursor ion initially formed is not stable under CID conditions and proton transfer to the polymer forming **$[PEG_{13} + H]^+$** is favoured. The remaining product ions are found to result from carbon-ether oxygen backbone cleavages, where the *m/z* values are 1 Da heavier the theoretical neutral molecules and consequently presumed to include a proton. As demonstrated in Section 3.2, a PEG precursor ion containing lithium results in extensive polymer backbone dissociation. LTQ-CID of **$[PEG_{13} + Li]^+$** Figure 3.8(b) generated characteristic product ions that result from carbon-ether oxygen bond cleavage, where $\mathbf{b_n}$ (n=6-11), $\mathbf{c_n}''$ (n=5-12), $\mathbf{x_m}''$ (m=6-12) and $\mathbf{z_m}$ (m=5-11) provide evidence of both terminal groups individually consequently yielding directional sequence information. In this instance, the metal cation is retained in the product ions demonstrating a more stable polymer-cation interaction. In comparison LTQ-CID of **[M + Na]$^+$** and **[M + K]$^+$**, (Figure 3.8(c) and (d) respectively), do not yield any product ions, where cation detachment is the only dissociation pathway. This observation may suggest that increasing the size of the alkali metal cation, reduces the strength of the polymer-cation interaction, making cation detachment the dominant fragmentation pathway over polymer dissociation. Subsequent data with larger cations disproves that size alone is not the only determining factor, as shown in Figure 3.8(e) and (f). The addition of monovalent transitions metal cations silver and copper (I) to PEG, are seen to form stable precursor ions, whose dissociation includes cleavage of bonds in the polymer chains. This may be due to the presence of d-orbitals in the transition metals that can overlap effectively with the p-orbitals of the oxygen atoms of the polymer. The observed product ions for LTQ-CID of **[PEG$_{13}$ + Ag]$^+$** and **[PEG$_{13}$ + Cu]$^+$** confirm the two terminal groups present and provide comparable sequence coverage to **[PEG$_{13}$ + Li]$^+$**, as shown in Table 3.2.

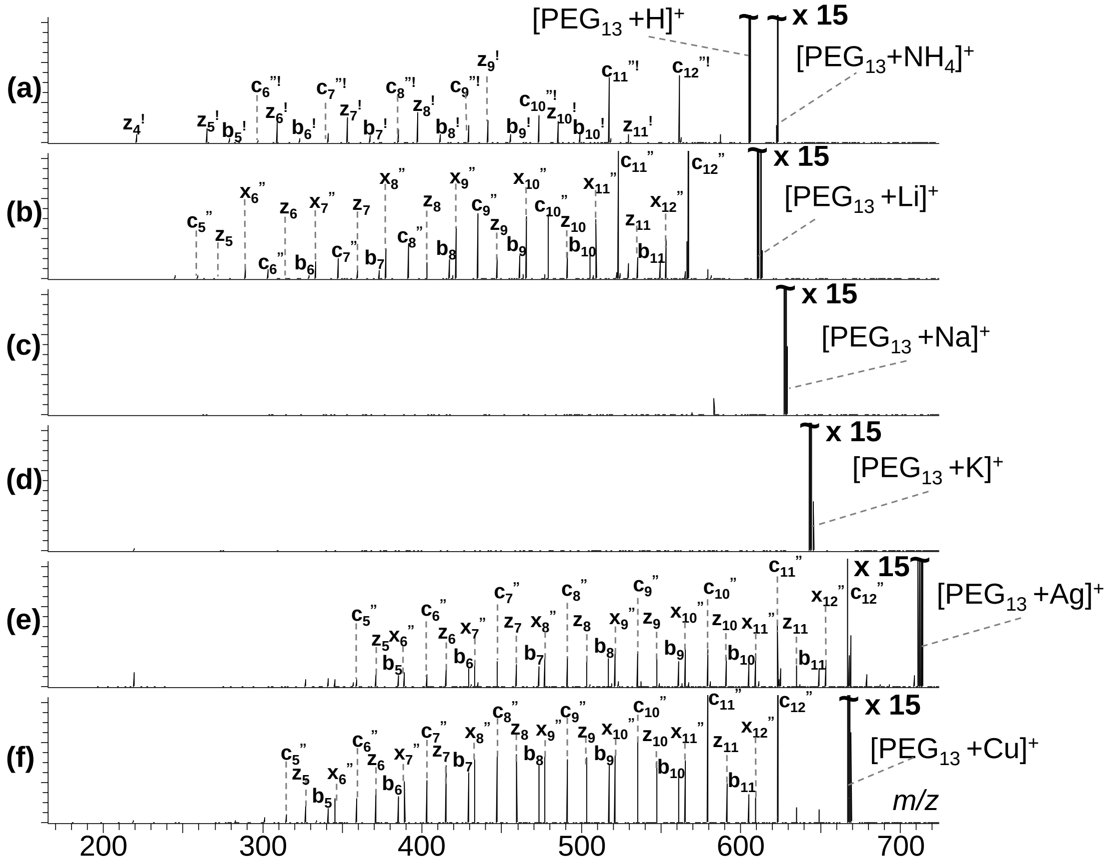

Figure 3.8 LTQ-CID tandem MS of [$CH_3O(C_2H_4O)_{13}H$ +X]$^+$ where X = (a) NH_4, (b) Li, (c) Na, (d) K, (e) Ag, and (f) Cu.

Table 3.2 A summary of the product ion series observed during LTQ-CID of $[CH_3O(C_2H_4O)_{13}H + X]^+$.

Product ion	$\mathbf{b_n}$	$\mathbf{c_n}''$	$\mathbf{z_m}$	$\mathbf{x_m}''$
Charge Carrier				
NH_4	5--10	6--12	4--11	-
Li	6--11	5--12	5--11	6--12
Na	N/A	N/A	N/A	N/A
K	N/A	N/A	N/A	N/A
Ag	5--11	5--12	5--11	6--12
Cu	5--11	5--12	5--11	6--12

For all precursor ions investigated, EID generated product ions that spanned the detectable *m/z* range, where the product ions retain the original charge carrier in all experiments as demonstrated in Table 3.3 and Figure 3.9. This experimental observation provides evidence that the fragmentation mechanism occurring in EID is less reliant upon the strength of the cation-polymer interaction than LTQ-CID. This is particularly prominent in Figure 3.9(a), where the product ions generated during EID tandem MS of **$[PEG_{13} + NH_4]^+$** retain the original NH_4^+ charge carrier, in contrast to CID (Figure 3.8(a)).

Despite forming product ions for all precursor ions under identical experimental conditions, there are some significant differences in the intensities of the product ion peaks clearly relating to the charge carrier present. For the alkali metals lithium, sodium and potassium there is little difference in the intensity of the product ion peaks suggesting that the physical property that influences fragmentation is similar for all alkali metals, unlike CID. The product ion peaks of lowest intensity are generated from the transition metal, (**$[PEG_{13} + Ag]^+$**) and the non-metal (**$[PEG_{13} + NH_4]^+$**) containing precursor ions.

Table 3.3 A summary of the product ion series observed during EID of $[CH_3O(C_2H_4O)_{13}H + X]^+$.

Product ion	$\mathbf{b_n}$	$\mathbf{c_n}''$	$\mathbf{z_m}$	$\mathbf{x_m}''$
Charge Carrier				
NH_4	3-11	3-10	3-11	N/A
Li	2-11	1-10	2-11	3-10
Na	1-11	1-10	1-11	4-10
K	1-11	1-10	1-11	2-10
Ag	1-11	1-10	1-11	2-10
Cu	2-11*	1-10*	2-11*	2-10*

Irradiation of **$[PEG_{13} + Cu]^+$** with high energy electrons generated an unusual product ion series that were dominated by odd electron product ions. For instance, accurate mass analysis of *m/z* 314.07906 shown inset in Figure 3.9, gives an empirical formula of $C_{11}H_{23}O_6Cu$, which is denoted a $\mathbf{c_5}^{\wedge}$ product ion, a polymer radical with a copper (I) cation aiding ionisation. This is plausible, however the majority of product ions observed from EID are closed shell even electron species, consequently EID of PEG ionised with copper is the focus of further investigation in Section 3.4.3.

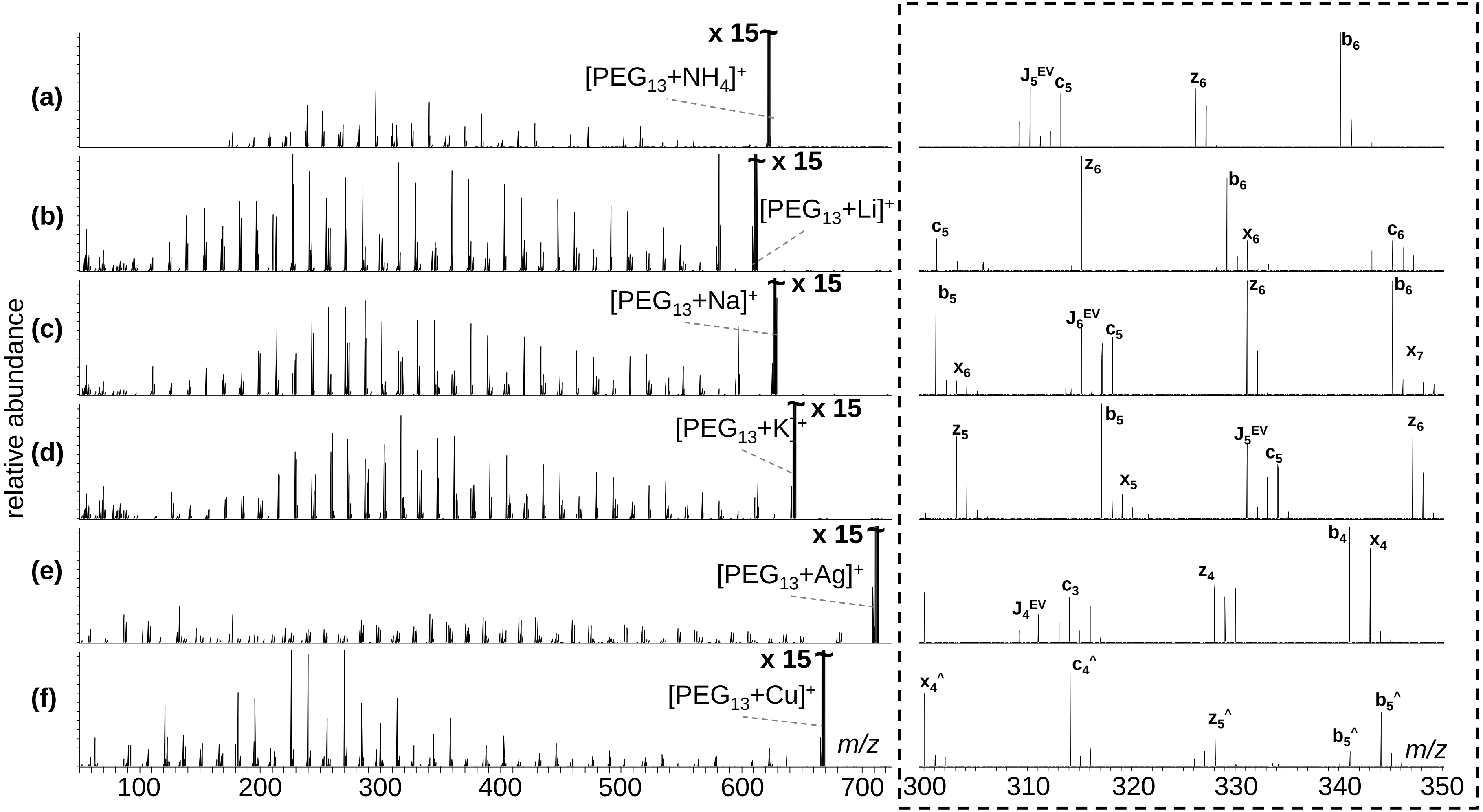

Figure 3.9 EID tandem MS of $[CH_3O(C_2H_4O)_{13}H + X]^+$ at 21.1 eV where X = (a) NH_4, (b) Li, (c) Na, (d) K, (e) Ag and (f) Cu. Inset: repeat product ion series 300 – 350 *m/z*.

Table 3.4 Physical properties of monovalent charge carriers.[250]

Charge Carrier	Standard Reduction Potential at 298 K (V)	Electron Affinities (eV)	Charge Density (C m^{-1})
	$X^{n+} + ne^- \rightarrow X$	$X + e^- \rightarrow X^-$	
NH_4 / H	0.00	-0.754	3.01e-09
Li	-3.05	-0.62	2.67e-09
Na	-2.71	-0.55	1.68e-09
K	-2.93	-0.50	1.20e-09
Ag	0.80	-1.30	1.27e-09
Cu (I)	0.52	-1.22	1.67e-09

As the fragmentation technique is electron-based, it is worth considering the physical properties of the charge carriers. For **$[PEG_{13} + Li]^+$**, **$[PEG_{13} + Na]^+$** and **$[PEG_{13} + K]^+$**, the product ion intensities decrease relative to the precursor ion in line with the electron affinity of the cation. This trend is not adhered to by other charge carriers, where silver has a larger electron affinity than lithium but generates noticeably less intense product ion peaks. This result would suggest that the trend in product ion intensities is not related to the electron affinity of the charge carrier. For **$[PEG_{13} + Li]^+$**, **$[PEG_{13} + Na]^+$** and **$[PEG_{13} + K]^+$** the product ion intensities decrease relative to the precursor ion correlates with the decreasing charge density. Once again EID of **$[PEG_{13} + Ag]^+$**, provides an exception to this trend, where the intensity of the product ions are low relative to the precursor ion despite having comparable charge density to **$[PEG_{13} + K]^+$**. The physical property that reflects the experimental observations most effectively are the standard reduction potentials of the charge carriers as shown in Table 3.4. Despite this parameter being established in the solution phase and the experiment being performed in the gas phase, the calculated values correlate well with the observed tandem MS spectra. The negative reduction potentials of lithium, sodium and potassium demonstrate that these metal ions are strong reducing agents and are not easily reduced. Precursor ions containing these metals were found to generate product ion peaks of strong intensity. In contrast, silver has a positive reduction potential where reduction is more favourable. The silver containing precursor ion was shown to generate less intense product ion peaks than the corresponding alkali metal containing precursor ion under identical conditions. Based on the results observed here, the presence of a strong reducing agent as the charge carrier leads to more intense product ion peaks under EID conditions. The standard reduction potential has been proposed to be a factor influencing the fragmentation of lanthanide complexes using ECD. Mosely *et al.* demonstrated that the lanthanide metal most easily reduced provided the most structural information.[251] This is an interesting observation, as the trend for ECD of lanthanides is the opposite of what is proposed in this thesis for EID. This difference may be due to the requirement for electron capture to induce fragmentation in ECD of the lanthanide precursor ions, whereas electron capture of **$[PEG_{13} + X]^+$** would result in charge neutralisation. The trend proposed here would suggest that the most effective charge carriers for polymer dissociation by EID are those that are less easily reduced under EID conditions.

3.4.2. Tandem MS of methyl terminated PEG with divalent charge carriers

Ionisation of PEG using divalent metal cations copper, zinc, calcium with a high tube lens voltage (125 V - 170 V) were found to generate predominantly singly charged molecular ions, whose empirical formulae contain one hydrogen atom less than the proposed close shell structure. This suggests that the metal cation is covalently bound to the PEG molecule where ejection of a proton accounts for ion observed as shown in Scheme 3.5.

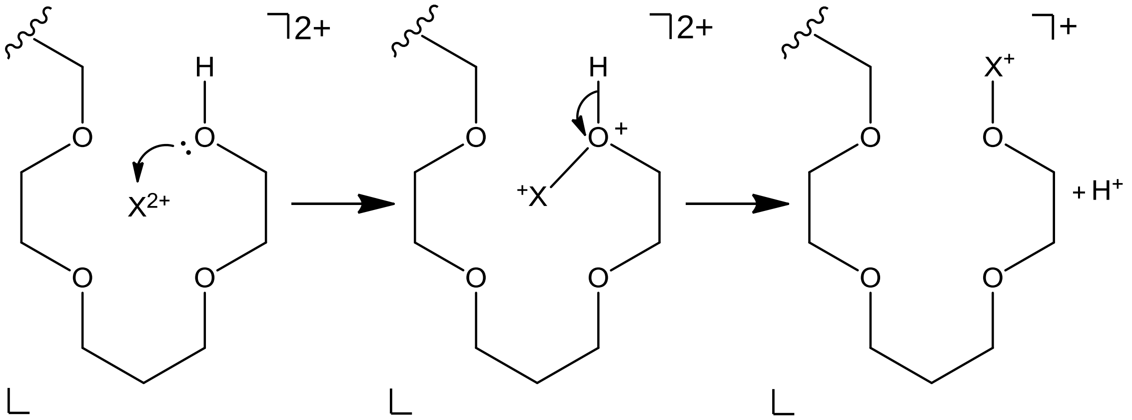

Scheme 3.5 Formation of ($PEGX^{2+} – H^+$).

Confidence in the assignment of the charge reduced species comes from work by Chen *et al.* who demonstrated that doping PEG with transition metals generated weak **($PEGX^{2+}–H^+$)** molecular ions alongside the dominant **$[PEG + Na]^+$** species.[87]

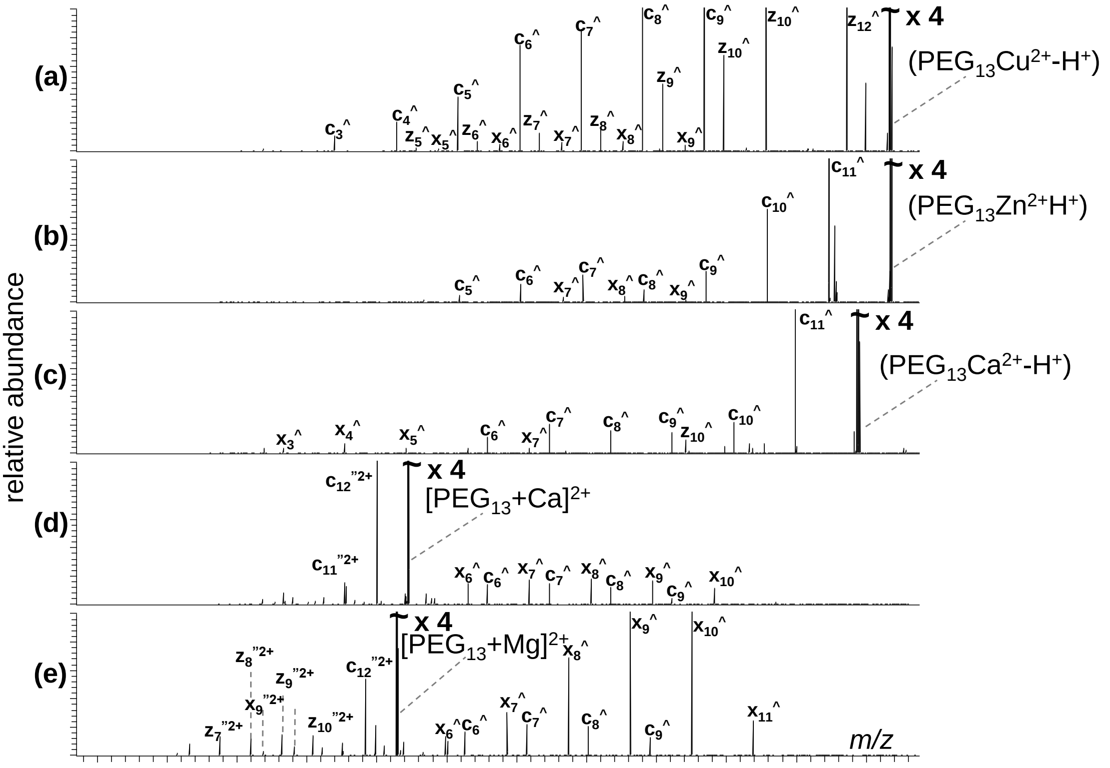

Figure 3.10 LTQ-CID tandem MS of ($CH_3O(C_2H_4O)_{13}H + X^{2+}-H^+$) where X = (a) Cu, (b) Zn and (c) Ca and LTQ-CID of $[CH_3O(C_2H_4O)_{13}H + X]^{2+}$ at 22.1 eV where X = (d) Ca and (e) Mg.

LTQ-CID is shown to generate product ions that are assigned as $\mathbf{c_n}^{\wedge}$ and $\mathbf{x_m}^{\wedge}$ for the **($PEGX^{2+}–H^+$)** precursor ions as shown in Figure 3.10(a) - Figure 3.10(c). Accurate mass analysis of these product ions, gives empirical formulae that contain one hydrogen atom less than $\mathbf{c_n}''$ and $\mathbf{x_m}''$. This adds support for the covalent attachment of the divalent metal cation to the polymer with potential structures for these product ions outlined in Figure 3.11.

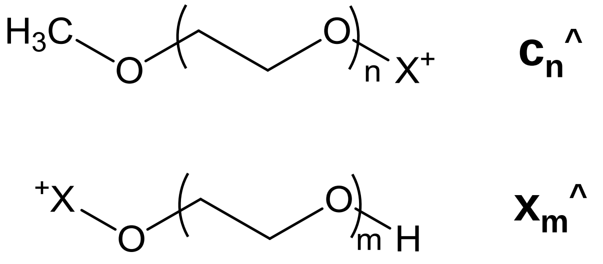

Figure 3.11 Potential structures of $c_n^{\wedge}$ and $x_m^{\wedge}$ product ions where X is the divalent cation present in the precursor ion, where the metal X is directly bound to PEG.

The prevalence of the $\mathbf{c_n}^{\wedge}$ and $\mathbf{x_m}^{\wedge}$ product ions and the lack of $\mathbf{b_n}$ and $\mathbf{z_m}$ product ions demonstrates significant differences exist in the fragmentation mechanisms of LTQ-CID of PEG containing monovalent and divalent charge carriers. The intense $\mathbf{c_n}^{\wedge}$ and $\mathbf{x_m}^{\wedge}$ product ion peaks suggests that the highly electronegative oxygen atom is a preferred site for cation attachment, and that it is not possible to coordinate the divalent cation with the unsaturated vinyl terminal group present in $\mathbf{b_n}$ and $\mathbf{z_m}$ product ions. The presence of the $\mathbf{c_n}^{\wedge}$ product ion series where the cation is bound to an ether oxygen atom and not the terminal hydroxyl oxygen atom, provides evidence that cation attachment does not have to occur at the terminal hydroxyl moiety. One proposed explanation for this is that fragmentation of the polymer is charge directed fragmentation as shown in Scheme 3.6.

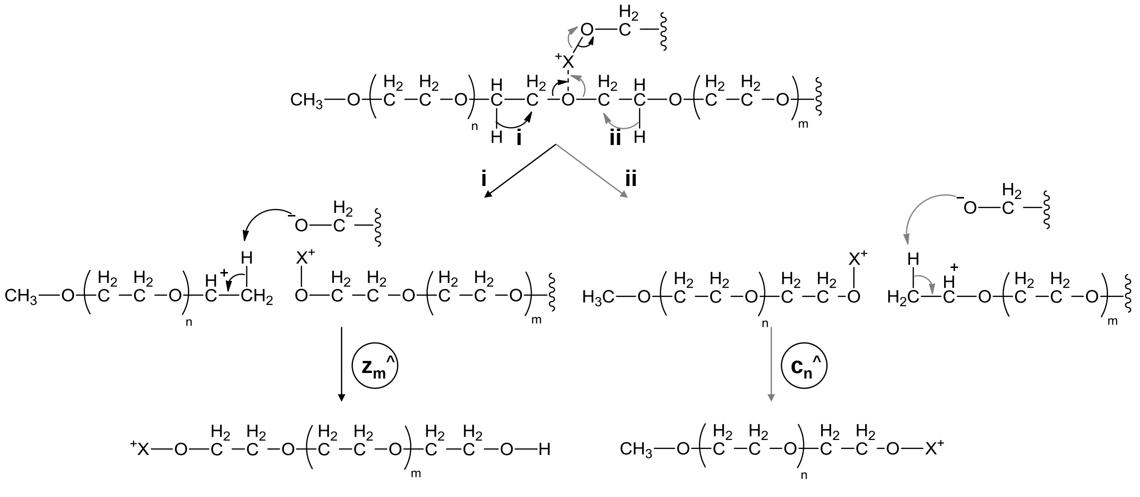

Scheme 3.6 Charge directed fragmentation of ($PEGX^{2+}$-H^+) precursor ions to form $c_n^{\wedge}$ and $z_m^{\wedge}$.

Analysis of the doubly charged precursor ions formed with calcium and magnesium give empirical formulae that correspond **[PEG_{13} + Ca]$^{2+}$** and **[PEG_{13} + Mg]$^{2+}$** respectively. The higher *m/z* range of the spectra generated by LTQ-CID of **[PEG_{13}+ Ca]$^{2+}$** and **[PEG_{13}+ Mg]$^{2+}$** are dominated by singly charged $\mathbf{c_n}^{\wedge}$ and $\mathbf{x_m}^{\wedge}$ product ions that are one hydrogen atom deficient and have the analogous empirical formula to the structures presented in Figure 3.11. In the lower *m/z* ranges of Figure 3.10(d) and Figure 3.10(e), there are a number of doubly charged product ions that result from small neutral losses, forming close shelled $\mathbf{c_n}^{''2+}$, $\mathbf{x_m}^{''2+}$ and $\mathbf{z_m}^{''2+}$ product ions.

The EID tandem MS spectrum of **($PEG_{13}Cu^{2+}$–H^+)** (Figure 3.13(a)), contains three different series of product ion peaks. Alongside the $\mathbf{c_n}^{\wedge}$ and $\mathbf{x_m}^{\wedge}$ product ions that were observed in LTQ-CID, the third product ion series of peaks, labelled $\mathbf{z_m}^{\wedge}$ is unique to EID, where accurate mass analysis of *m/z* 256.03729 gives an empirical formula of $C_8H_{17}O_5Cu$, which is formed through cleavage of the carbon-ether oxygen bond, leading to formation of a saturated ethyl terminal group. The likely location of the covalently bound cation is at the hydroxyl oxygen, which leads to a potential structure given in Figure 3.12. The lack of the corresponding $\mathbf{b_n}^{\wedge}$ series is surprising however the proposed structure of such an ion would have ethyl and methyl ether terminal groups providing no location for the divalent cation to covalently bind.

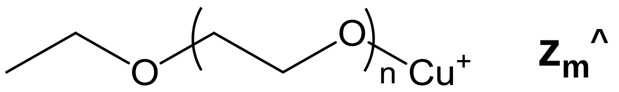

Figure 3.12 Potential structure of z_m^ product ion.

A similar trend is observed for EID of **($PEG_{13}Zn^{2+}$–H^+)**, where EID provides enhanced sequence coverage yielding a larger number of different product ions series including **c_n**^, **x_m**^ and the unique, **z_m**^ across a larger mass range than LTQ-CID. For all product ions, the empirical formulae contain an odd number of hydrogen atoms supporting covalent attachment of the divalent metal to the polymer. EID analysis **($PEG_{13}Ca^{2+}$–H^+)** resulted in **c_n**^, **x_m**^ and **z_m**^, where the intensity of the product ion peaks generated from calcium are significantly more intense than the copper and zinc analogues as shown in Figure 3.13(c). This experimental observation reflects the general trend in reduction potential observed for EID of the monovalent charge carriers, such that Ca^{2+} (electronic configuration [Ar]) the cation least likely to be reduced owing to a negative reduction potential, provides the largest number and most intense product ion peaks. Zn^{2+} ([Ar]$3d^{10}$), which has a smaller but still negative reduction potential provides a larger number of product ions than is observed for copper. Cu ([Ar] $3d^9$), which has a positive reduction potential meaning that reduction is more favourable, is shown to provide the least number of product ions out of **($PEG_{13}Cu^{2+}$–H^+)**, **($PEG_{13}Zn^{2+}$–H^+)** and **($PEG_{13}Ca^{2+}$–H^+)**.

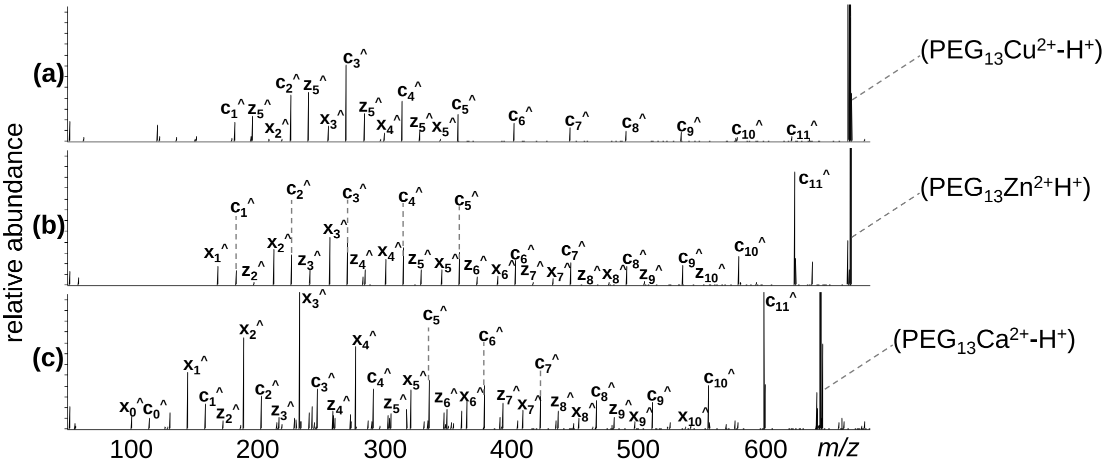

Figure 3.13 EID tandem MS of ($CH_3O(C_2H_4O)_{13}H$ +X^{2+}-H) at 22.1 eV where X = (a) Cu, (b) Zn and (c) Ca.

Table 3.5 Physical properties of divalent charge carriers.

Charge Carrier	Standard Reduction Potential at 298 K (V)	Electron Affinities (eV)	Charge Density (C m^{-3})
	$X^{n+} + ne^- \rightarrow X$	$X + e^- \rightarrow X^-$	
Cu^{2+}	0.34	-1.22	3.68e-09
Zn^{2+}	-0.76	0	3.64e-09
Ca^{2+}	-2.87	-0.02	3.37e-09
Mg^{2+}	-2.36	0	4.92e-09

HECD of the doubly charged precursor ion **$[PEG_{13} + Ca]^{2+}$** resulted in a simplified product ion spectrum compared to EID of **$(PEG_{13}Ca^{2+}–H^{+})$** as shown in Figure 3.14(a). There is evidence of electron capture occurring through the generation of a peak that corresponds to **$[PEG_{13}\text{-}H^{\bullet}+Ca]^{2+}$.** Evidence for covalent attachment of the cation to the polymer is given by the product ions **c_n**$^{\wedge}$ and **x_m**$^{\wedge}$, as shown in Figure 3.14(a). The product ion spectrum generated by HECD of **$[PEG_{13} + Mg]^{2+}$** in Figure 3.14(b), is very similar in profile to HECD of **$[PEG_{13} + Ca]^{2+}$**, which is not surprising given that they are both alkali earth metals. The product ion peaks observed during HECD of **$[PEG_{13} + Mg]^{2+}$** are more intense compared to the equivalent calcium ions. As electron capture is now required to observe singly charged product ions, the intensity of the product ions relative to the precursor ion can be related to the standard reduction potentials of the charge carriers. Mg^{2+} the most easily reduced of the two alkali earth metals yields product ions of greater intensity under HECD conditions than Ca^{2+}. These experimental observations support the findings of Mosely *et al.* who proposed a similar trend for the ECD analysis of lanthanide complexes.[251]

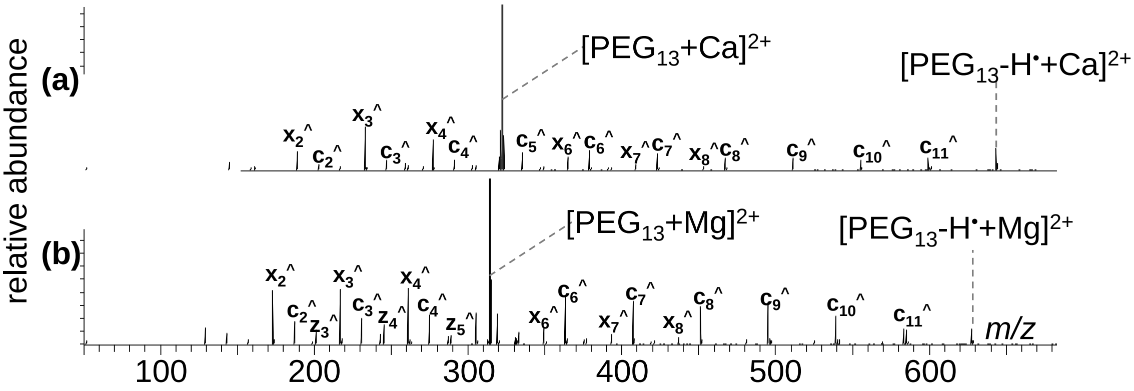

Figure 3.14 HECD tandem MS of $[CH_3O(C_2H_4O)_{13}H +X]^{2+}$ at 22.1 eV where X = (a) Ca and (b) Mg.

3.4.3. Tandem MS of PEG with copper (I) and copper (II) salts

Copper is an interesting metal for electron-based tandem MS investigations due to the presence of stable 1+ and 2+ charge states. The previous experiments investigating the effect of charge carrier have related the reduction potential of the charge carrier to the relative intensities of the product ion peaks. Copper is an intriguing proposition in this regard, as the charge states have very similar reduction potentials as shown in Table 3.6. In fact redox experiments involving Cu^{+}/Cu^{2+} established a redox potential of 0.15 V between the two species.

Table 3.6 Physical properties of copper (I) and copper (II).

Charge Carrier	Standard Reduction Potential at 298 K (V)	Charge Density ($C\ m^{-1}$)
	$X^{n+} + ne^{-} \rightarrow X$	
Cu^{+}	0.52	1.67e-09
Cu^{2+}	0.34	3.68e-09

ESI of PEG doped with copper (I) methyl salicylate and copper (II) chloride resulted in the molecular ions shown in Figure 3.15(a) and Figure 3.15(b) respectively.

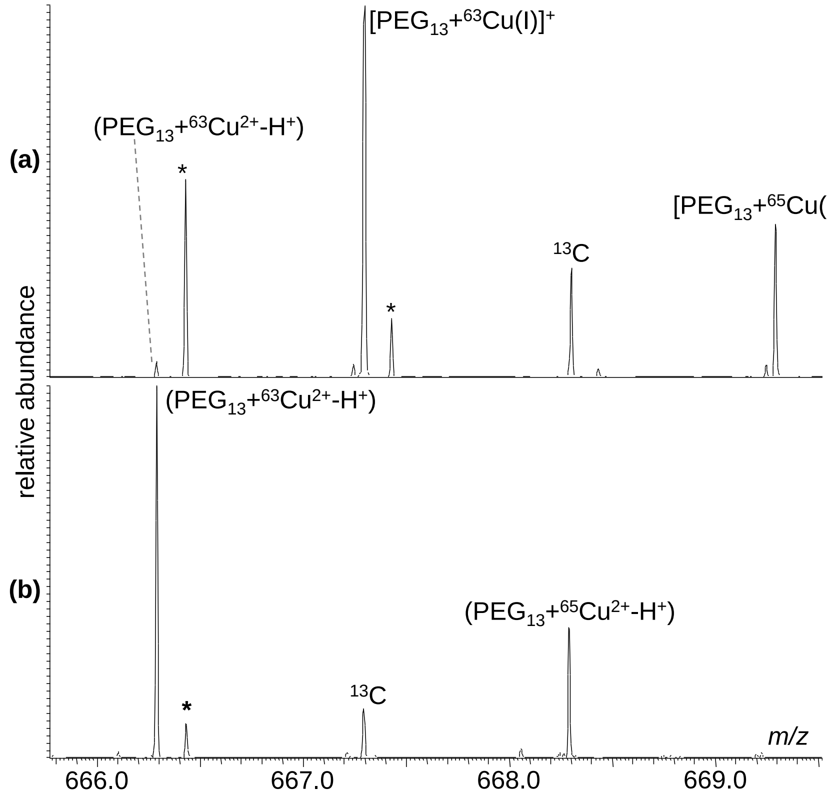

Figure 3.15 ESI MS of PEG doped with Cu salts: (a) Copper (I) Methyl Salicylate and (b) Copper (II) Chloride (* = unknown contaminant).

ESI MS of **$[PEG + Cu(I)]^+$** resulted in a mass spectrum, an expansion of which is given in Figure 3.15(a). The peak at *m/z* 667.29508, corresponds to **$[CH_3O(C_2H_4O)_{13}H + Cu(I)]^+$** which is labelled **$[PEG_{13} + {}^{63}Cu(I)]^+$**. The peaks at *m/z* 668.29855 and *m/z* 669.29311 correspond to the ^{13}C and ^{65}Cu (**$[PEG_{13} + {}^{63}Cu(I)]^+$**) isotopes respectively. ESI MS of **$[PEG + Cu(II)]^+$** resulted in a peak at *m/z* 666.28904 that gives an empirical formula of $C_{27}H_{55}O_{14}Cu$ by accurate mass analysis corresponding to **$(PEGCu^{2+}–H^+)$** where the copper is covalently bound to the polymer. Once again, an isotopic distribution is observed, where peaks at *m/z* 667.29253 and *m/z* 668.28707 correspond to the ^{13}C and ^{65}Cu isotopes respectively.

LTQ-CID tandem MS of **$[PEG_{13} + Cu(I)]^+$** and **$(PEG_{13}Cu^{2+}–H^+)$** precursor ions generated significantly different product ion spectra, as shown in Figure 3.16(a) and Figure 3.16(b). LTQ-CID of **$[PEG_{13} + Cu(I)]^+$** generated the characteristic **b_n**, **c_n''**, **z_m** and **x_m''** product ions that were regularly observed from CID and EID of monovalent charge carriers, as shown inset in Figure 3.16(a). Likewise, LTQ-CID of **$(PEG_{13}Cu^{2+}–H^+)$** generated only **$c_n^{\wedge}$** and **$z_m^{\wedge}$** product ions, where the cation is covalently bound to the polymer, as shown in Figure 3.16(b).

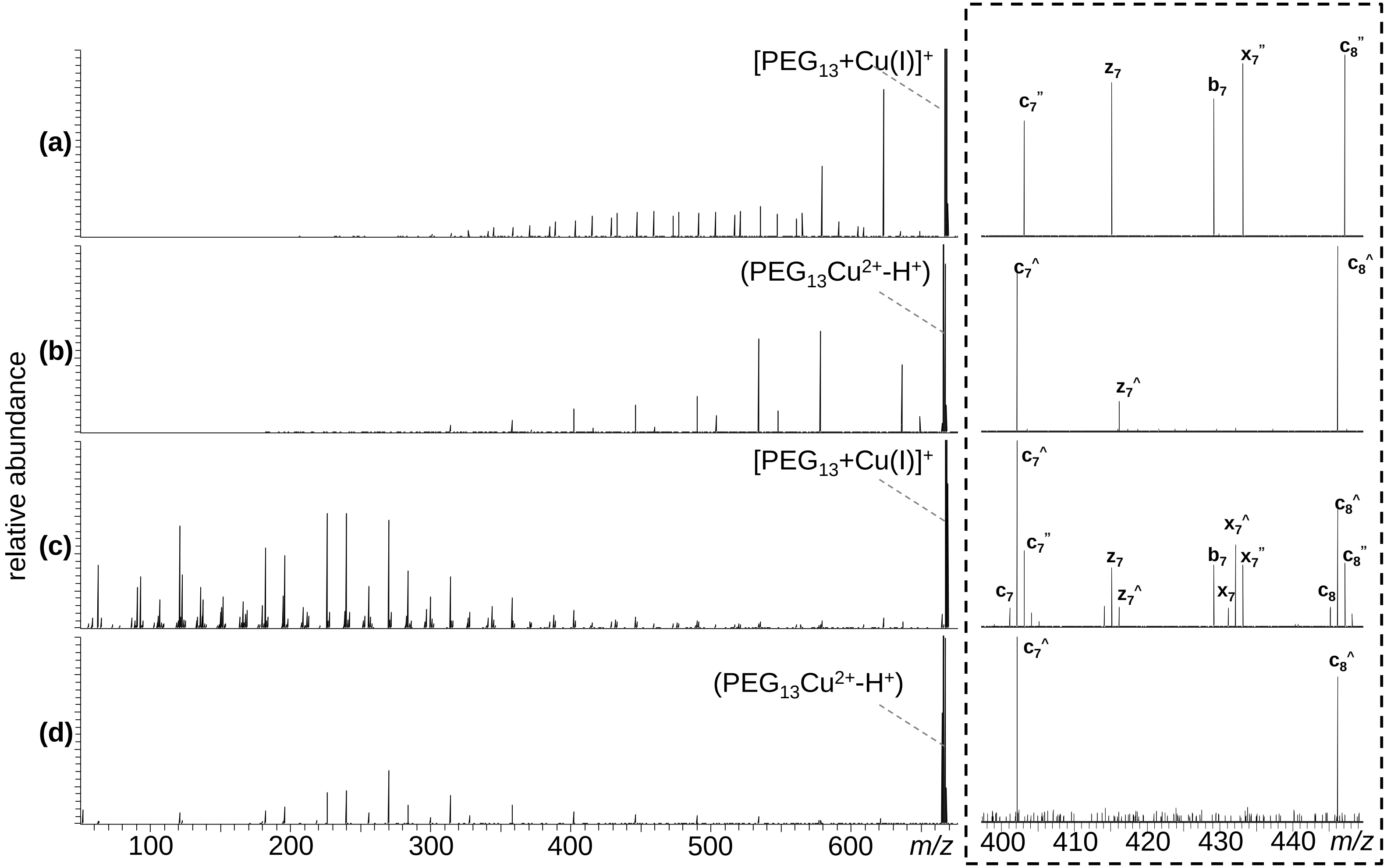

Figure 3.16 Tandem MS of PEG ionised with Cu salts: (a) LTQ-CID of [PEG$_{13}$ + Cu(I)]$^+$ (b) LTQ-CID of (PEG$_{13}$Cu^{2+}–H$^+$), (c) EID of [PEG$_{13}$ + Cu(I)]$^+$ and (d) EID of (PEG$_{13}$Cu^{2+}–H$^+$), inset expansion of product ions in *m/z* 400-450 range.

Table 3.7 Summary of product ions observed for tandem MS of copper (I) and copper (II).

Charge Carrier	Tandem MS Technique	**b_n**	**c_n**	**$c_n^{\wedge}$**	**c_n''**	**x_m**	**$x_m^{\wedge}$**	**x_m''**	**z_m**	**$z_m^{\wedge}$**
$[M + Cu(I)]^+$	CID	✓			✓			✓	✓	
$[M + Cu(II) – H]^+$,	CID			✓						✓
$[M + Cu(I)]^+$	EID	✓	✓	✓	✓	✓	✓	✓	✓	✓
$[M + Cu(II) – H]^+$,	EID			✓			✓			✓

Irradiation of **$[PEG_{13} + Cu(I)]^+$** with high energy electrons generated a significantly more complex product ion spectrum as shown in Figure 3.16(c). All of the product ions previously observed during LTQ-CID of **$(PEG_{13}Cu^{2+}–H^+)$** and **$[PEG_{13} + Cu(I)]^+$** are present in the EID tandem MS spectra of **$[PEG_{13} + Cu(I)]^+$** as summarised in Table 3.7. The **b_n**, **z_m**, **c_n''** and **x_m''** product ions correspond to unsaturated and saturated product ions, to which the copper cation is coordinated. These are the expected product ions based upon previous results for EID analysis of PEG ionised with a monovalent charge carrier. The presence of **$c_n^{\wedge}$** and **$z_m^{\wedge}$** , where the cation is covalently bound to the polymer is unusual for a monovalent charge carrier, as these ions have only been observed during tandem MS analysis of **$(PEG_{13}X^{2+}–H^+)$** precursor ions. This suggests that it is possible to form product ions where copper can be in different oxidation states under EID conditions. This proposal requires the second ionisation energy of copper to be overcome to allow formation of **$(PEG_{13}Cu^{2+}–H^+)$**. As the copper is bound to the molecule in the singly charged ion, the required second ionisation energy is of the whole molecule and not the copper ion alone (20.298 eV per molecule).[252] The required energy is likely to be lower than the value calculated for pure copper as the coordinated polymer provides additional charge stabilisation. EID of **$[M + Cu(I)]^+$** is also shown to generate some unique product ions that have not been observed during other tandem MS experiments shown in Figure 3.16(c). Evidence for multiple fragmentation mechanisms occurring during EID of **$[M + Cu(I)]^+$** are proposed due to the presence unsaturated **c_n** and **x_m** product ions that are likely to be ionised with a copper (I) cation that is coordinated to the polymer and not directly attached. In the equivalent EID analysis of **$[M + Cu(II) – H]^+$**, the product ion spectra is markedly more simple to interpret, with **$c_n^{\wedge}$**, **$x_m^{\wedge}$** and **$z_m^{\wedge}$** product ions observed in the tandem MS spectra in Figure 3.16(d). This has a strong resemblance to the EID spectra generated from other divalent metal cations zinc and calcium.

Comparing the spectra generated by EID and CID for the copper containing precursor ions it is clear to see the complementary nature of the techniques. LTQ-CID generates predominantly high *m/z* product ions where the intensity of the product ion peaks decrease with decreasing *m/z*. In contrast EID analysis of the copper precursor ions generates product ions throughout the spectra, where the more intense product ion peaks are located in the lower *m/z* regions of the spectra as demonstrated in Figure 3.16(c) and Figure 3.16(d).

3.4.4. ECD, HECD and CID of doubly charged PEG precursor ions containing two different charge carriers

As shown, the electron-based fragmentation technique EID is able to readily give full sequence information with a range of cations, whereas low energy CID resulted in dissociation only when selected charge carriers were present. To generate a direct comparison of the role of the cation in each experiment, a competitive environment was established through the generation of doubly charge precursor ions that contain two different alkali metal cations. The doubly charged precursor ions were isolated in the linear ion trap and subsequently activated using low energy CID, ECD and HECD. Lithium, sodium and potassium salts were used to create three combinations of precursor ion, that when activated by CID generated the spectra shown in Figure 3.17.

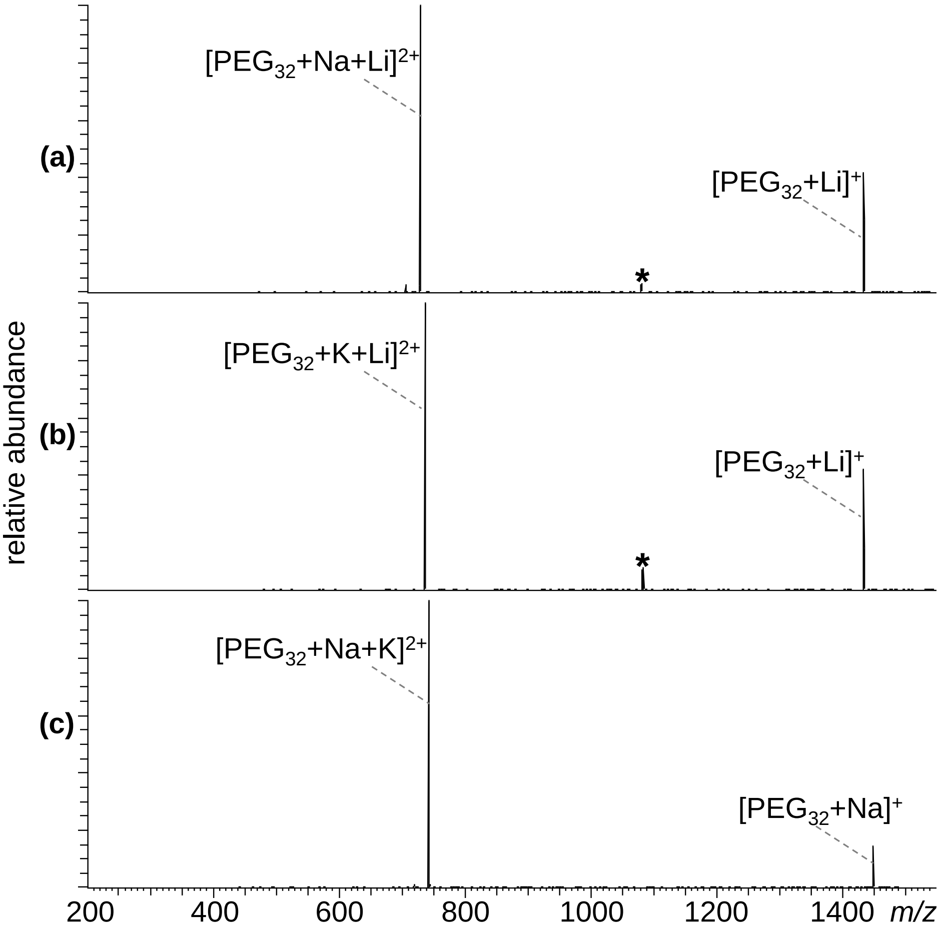

Figure 3.17 LTQ-CID tandem MS of $[HO(C_2H_4O)_{32}H + X^1 + X^2]^{2+}$ where (a) X^1 =Li and X^2 = Na, (b) X^1 = Li and X^2 = K and (c) X^1 = Na and X^2 = K (* = experimental artefacts).

As shown in Figure 3.17 there is an absence of product ions that result from fragmentation of the polymer backbone. The major product ion in each case is a singly charged molecular ion that contains the cation with the highest Lewis acidity. It has been shown in the literature that lithium, the cation with the highest Lewis acidity investigated here, can coordinate PEG more effectively than the alkali metal other cations.[150] The research presented in Figure 3.17(c), presents evidence that sodium forms a stronger interaction with PEG than potassium as demonstrated by the presence of a **$[PEG_{32} + Na]^+$** ion. Bogan *et al.* demonstrated that this trend in Lewis acidity was true for all alkali metals, using an analogous CID experiment performed in a quadrupole ion trap.[91]

When the doubly charge precursor ions were irradiated with low energy electrons (3.1 eV), the spectrum shown in Figure 3.18 resulted. This shows that like CID, ECD does not provide sufficient energy to induce polymer fragmentation as all product ions contain the intact polymer.

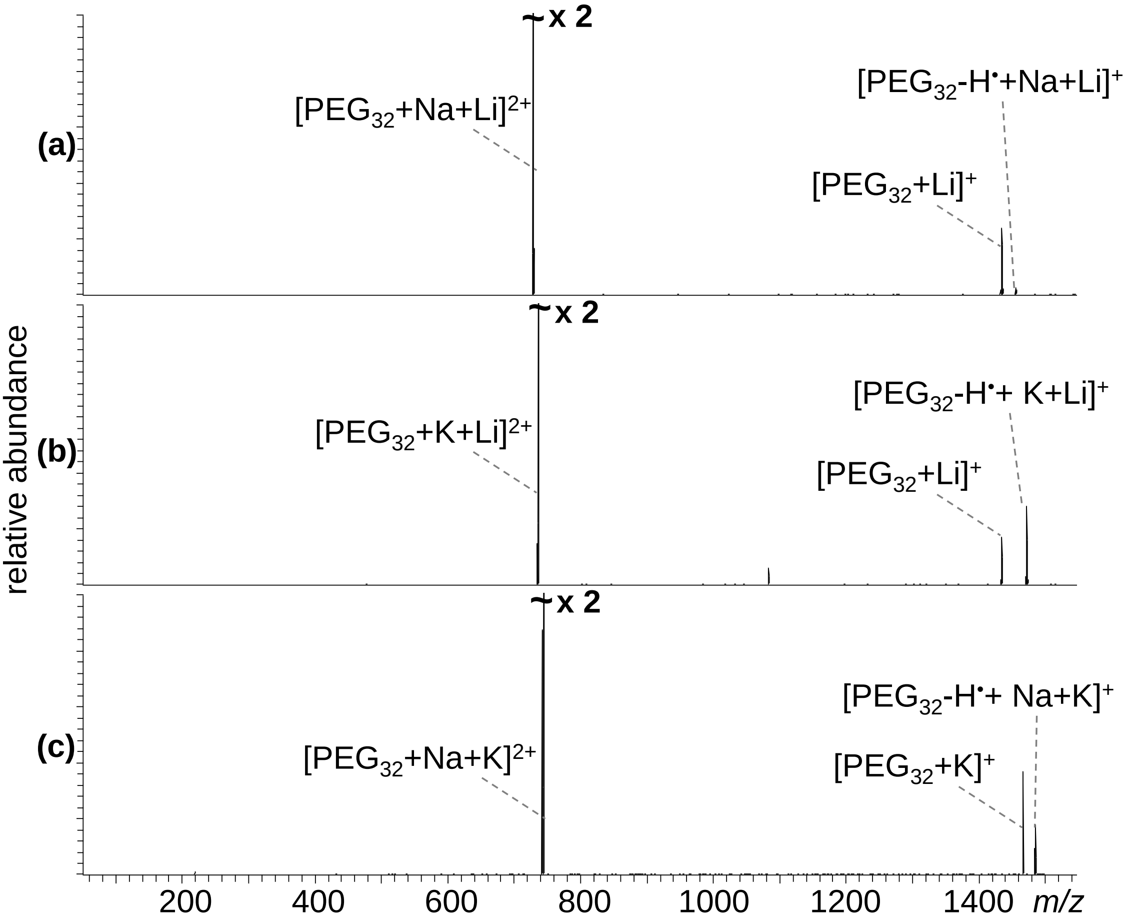

Figure 3.18 ECD (3.1 eV) tandem MS of $[HO(C_2H_4O)_{32}H + X^1 + X^2]^{2+}$ where (a) X^1 = Li and X^2 = Na, (b) X^1 = Li and X^2 = K and (c) X^1 = Na and X^2 = K.

Irradiation of the **[PEG_{32} + Na + Li]$^{2+}$** precursor ion with low energy electrons (3.1 eV) results in the formation of two product ions that do not result from dissociation of the polymer as shown in Figure 3.18(a). The product ion at *m/z* 1433.87368 corresponds to the **[PEG_{32} + Li]$^{+}$** formed through loss of the sodium cation, which mimics the Lewis acidity trend observed during CID. ECD analysis of **[PEG_{32} + K + Li]$^{2+}$**, also generated two product ions as shown in Figure 3.18(b). The peak at *m/z* 1433.86731, once again represents **[PEG_{32} + Li]$^{+}$** formed through loss of potassium, which was observed previously during CID of **[PEG_{32} + K + Li]$^{2+}$**. In Figure 3.18(c) the singly charged ion observed is **[PEG_{32} + K]$^{+}$** rather than **[PEG_{32} + Na]$^{+}$**, that was observed following CID. This would suggest that the formation of the singly charged ion is dependent upon a different physical property of the metal cations. In the previous experiment investigating cation selection for tandem MS of **[PEG + X]$^{+}$**, the standard reduction potentials of the charge carriers (Table 3.4) were shown to correlate with extent of dissociation observed under EID and HECD conditions. From Table 3.4, sodium is shown to require a lower amount of energy to be neutralised than potassium and is therefore a better oxidising agent than potassium. The result of this experimentally would be that sodium would be preferentially neutralised leading to formation of **[PEG_{32} + K]$^{+}$**. This, indeed, is the experimental observation made in Figure 3.18(c). This correlation can be extended to the other experiments investigated in Figure 3.18(a) and Figure 3.18(b), as the singly charged ion in both cases is **[PEG_{32} + Li]$^{+}$**, containing lithium, the strongest reducing agent investigated in these experiments.

In all ECD experiments (Figure 3.18(a) - Figure 3.18(c)), the second product ion peak at *m/z* 1455.85600, *m/z* 1471.82202 and *m/z* 1484.90210 respectively were found to represent singly charge PEG molecule that is one hydrogen deficient but retains both metals **[PEG_{32} – $H^{\bullet}$ + X^{1} + X^{2}]$^{+}$**. This type of ion was previously observed in the analysis of **[PEG + nLi]$^{n+}$** (where n = 2 or 3) and was proposed to be formed by the mechanism outlined in Scheme 3.4 where a cation is attached directly to the polymer with subsequent loss of a hydrogen radical.

The **[PEG_{32} – $H^{\bullet}$ + X^{1} + X^{2}]$^{+}$**product ions are observed in two of the three spectra when the electron energy is increased to 18.1 eV as shown in Figure 3.19. **[PEG_{32} – $H^{\bullet}$ + X^{1} + X^{2}]$^{+}$** is not present when X^{1} and X^{2} are sodium and potassium respectively, suggesting that the presence of lithium, the strongest reducing agent may be an important factor in the formation of this ion at this increased electron energy. The presence of singly charged **[PEG_{32} + X]$^{+}$** product ions, where the metal cation retained is the better reducing agent supports the proposal that the reduction potential is the physical property that determines cation loss. Importantly, the additional electron energy has resulted in extensive polymer dissociation with the generation of series of peaks separated by the characteristic 44 Da. An expanded view of the repeat series of peaks (inset in all spectra in Figure 3.19) demonstrates that all the major peaks correspond to **b_n** ions where carbon-ether oxygen bond cleavage generates the unsaturated vinyl terminal group. Accurate mass analysis allowed the identification of separate series of peaks that contain each of the metal cations individually as shown in the product ion assignments used inset in Figure 3.19. It also differentiated $\mathbf{b_n^{Na}}$ from $\mathbf{c_n^{Li}}$, which have the same integer mass.

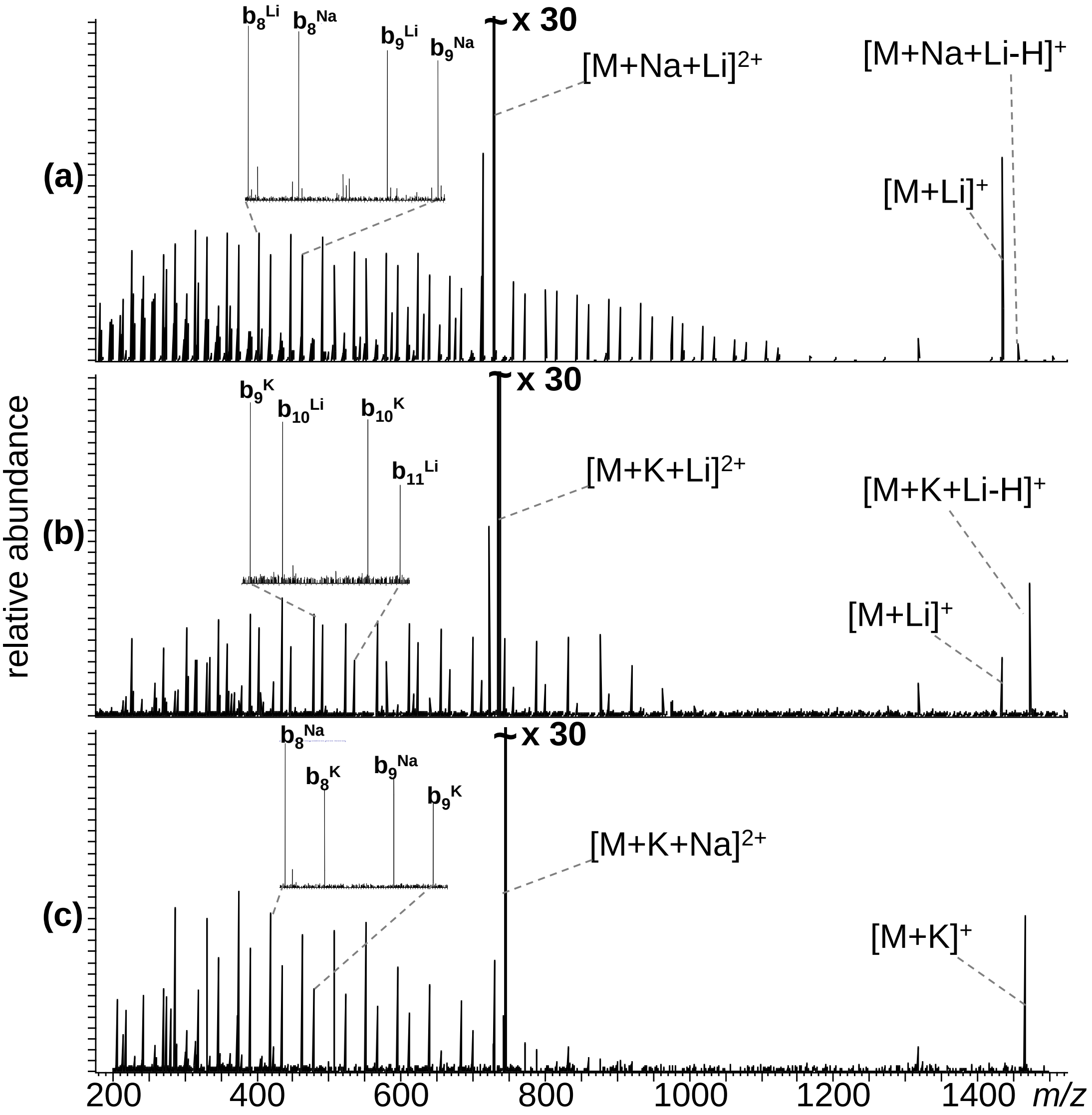

Figure 3.19 HECD (18.1 eV) tandem MS of $[HO(C_2H_4O)_{32}H + X^1 + X^2]^{2+}$ where (a) X^1 =Li and X^2 = Na, (b) X^1 = Li and X^2 = K and (c) X^1 = Na and X^2 = K.

The degree of sequence coverage varies between the spectra despite being recorded at the same electron energy. This indicates that the charge carriers heavily influence the dissociation of the polymer. Lithium and sodium are the combination that yield the best sequence coverage with peaks detected that represent 24 of the 32 monomers present in the precursor ion, whereas sodium and potassium provide the lowest degree of monomer sequence coverage with peaks representing 17 of the 32 monomers detected. This supports the proposal made previously for EID of singly charged PEG, that the charge carriers present influence the observed polymer fragmentation.

3.4.5. Investigation into neutral loss from the centre of a polymer ion using EID

To determine whether product ions generated under EID conditions resulted from backbone cleavage or internal neutral losses, a H/D exchange experiment was performed. Hydroxyl terminated PEG (M_n = 1500) was dissolved in CH_3OH and CH_3OD, and the corresponding precursor ions at *m/z* 1405.83196 (**$[HO(C_2H_4O)_{31}H +Na]^+$**) and *m/z* 1407.86918 (**$[DO(C_2H_4O)_{31}D +Na]^+$**) were investigated by EID as shown in Figure 3.20. EID of *m/z* 1405.83196 generates a series of product ion peaks typical of that observed previously as shown in Figure 3.20(a). Accurate mass analysis of the peak at *m/z* 903.51661 gives an empirical formula consistent with the **b_{19}** product ion. EID of *m/z* 1407.86918 generated a series of product ion peaks that are 1 *m/z* unit above those observed in Figure 3.20(a). Accurate mass analysis of 904.53127 *m/z* confirms the replacement of one hydrogen atom with a deuterium. The observation of product ion peaks that contain one deuterated hydroxyl group supports the proposal that the fragmentation mechanism taking place in EID is via homolytic backbone cleavages and not through the loss of internal fragments. There is evidence of incomplete deuterium exchange as shown by the b_{20} peak observed at *m/z* 947.4.

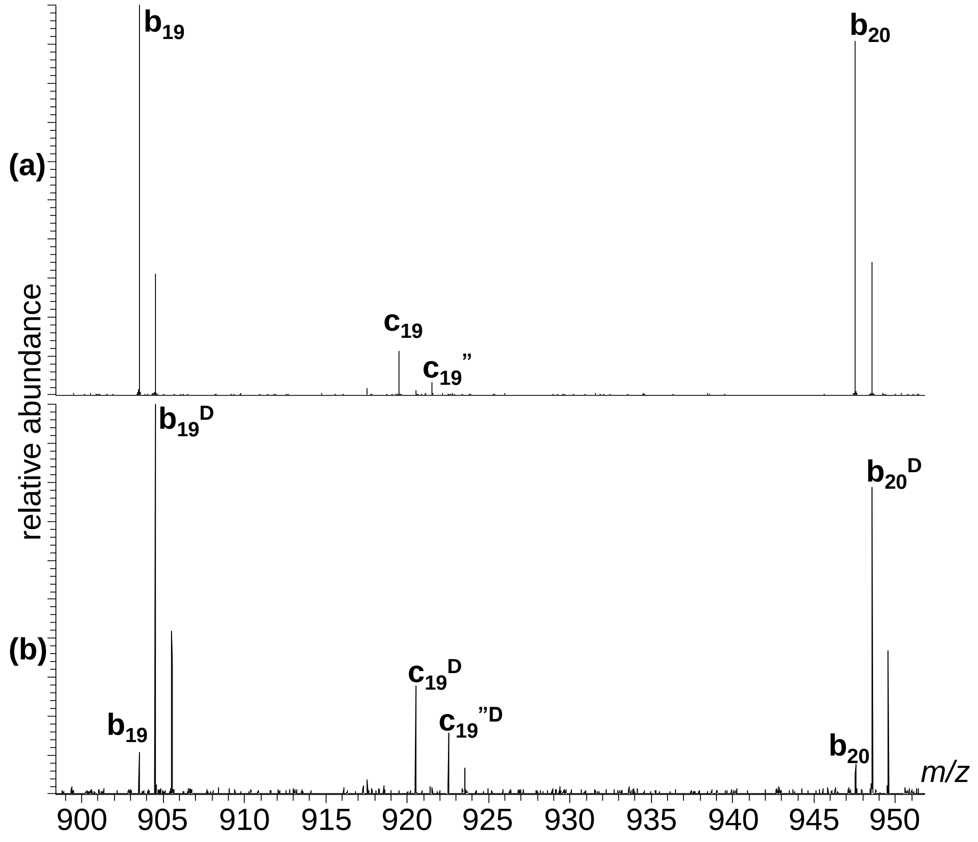

Figure 3.20 EID tandem MS of $[HO(C_2H_4O)_{31}H +Na]^+$ expansion of 900-950 *m/z* (a) 18.1 eV in methanol and (b) 18.1 eV in deuterated methanol.

In a related experiment, mono-methyl terminated PEG (M_n = 660) was prepared in deuterated methanol to confirm the presence of H/D exchange at the hydroxyl terminal group. In Figure 3.21(a) EID analysis in of *m/z* 627.35609 ($\mathbf{[CH_3O(C_2H_4O)_{13}H + Na]^+}$) prepared in CH_3OH resulted in the $\mathbf{b_n}$, $\mathbf{c_n}$, $\mathbf{c_n}''$, $\mathbf{z_m}$, $\mathbf{x_m}$ and $\mathbf{x_m}''$ series of product ions that were observed in Section 3.4. EID analysis of *m/z* 628.36943 ($\mathbf{[CH_3O(C_2H_4O)_{13}D + Na]^+}$) in CH_3OD generates the spectrum shown in Figure 3.21(b). It is noted that $\mathbf{b_n}$, $\mathbf{c_n}$ and $\mathbf{c_n}''$ product ions are identical to the equivalent ions observed in Figure 3.21(a), however there is an increase in the observed *m/z* of the $\mathbf{z_m}$, $\mathbf{x_m}$ and $\mathbf{x_m}''$ product ions that contain the hydroxyl terminal group. Accurate mass analysis confirms that this increase in *m/z* is due to the replacement of hydroxyl hydrogen with a deuterium atom. This not only confirms that the only exchangeable hydrogen present in PEG is that present in the hydroxyl terminal group functionality but also supports the findings made for hydroxyl terminated PEG, that the product ions generated are formed through backbone cleavage and not by loss of internal fragments.

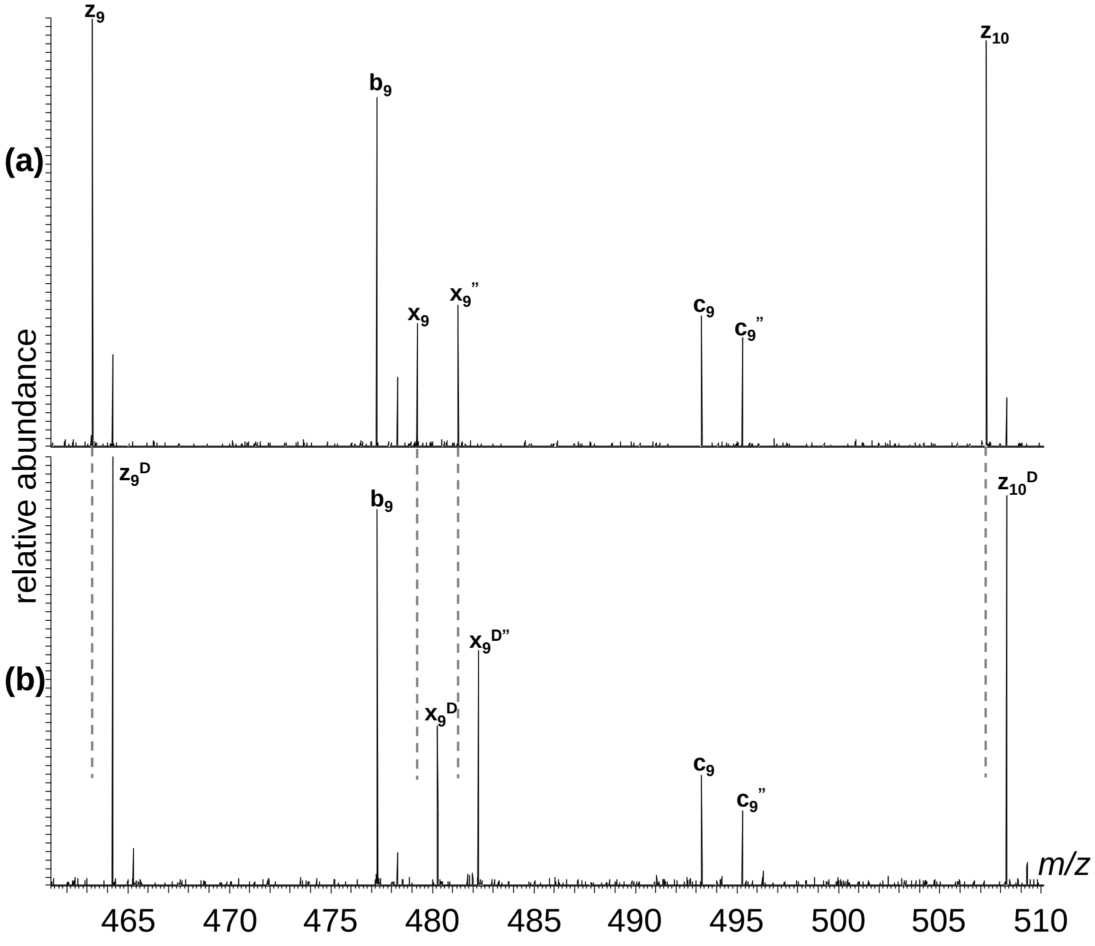

Figure 3.21 Tandem MS of $[CH_3O(C_2H_4O)_{13}H + Na]^+$ (a) EID 18.1 eV in methanol and (b) EID 18.1 eV in deuterated methanol.

3.5. EID tandem MS of hydroxyl terminated PEG: fragmentation as a function of electron energy

The electron-based fragmentation techniques EID and HECD have been shown to be highly successful in the dissociation of PEG and that a choice of charge carrying cation can be used advantageously. It has been shown to provide superior structural information in comparison with LTQ-CID. Typically the electron energy is optimised to generate the largest number of product ions that provide the greatest coverage of the detectable *m/z* range. It was of interest to investigate whether there was a threshold for dissociation along the polymer chain.

To investigate this parameter, a precursor ion was isolated and an automated method incrementally increased the energy of the incident electrons from 0 eV to 25.1 eV at 90 second intervals, with the mass spectrometer recording data continuously. Following completion of the experiment, the absolute intensity of each peak was recorded at an individual energy level. In this experiment hydroxyl terminated PEG (M_n = 1500) was utilised, where the selected precursor ion corresponded to **$[HO(C_2H_4O)_{31}H + Na]^+$**. From initial inspection of the data, it was found that product ions resulting from polymer fragmentation were not observed until electron energy = 14 eV. The intensity of the individual **b_n** ions which retain the sodium charge carrier are displayed graphically in Figure 3.22.

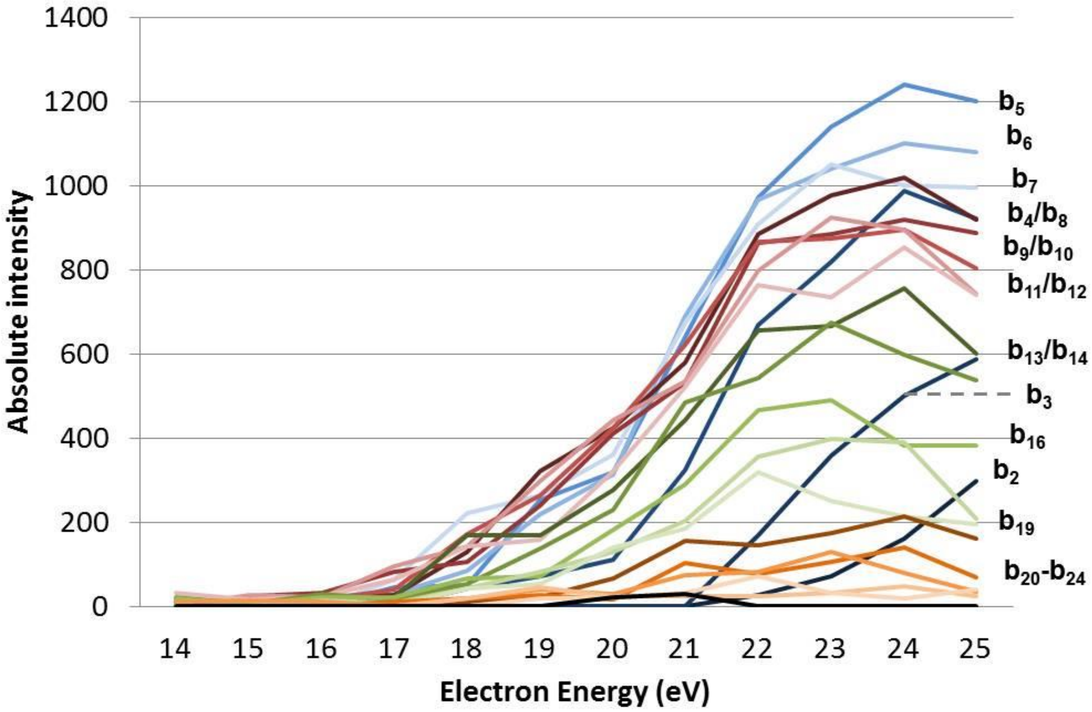

Figure 3.22 The intensity of b_n ions as a function of electron energy.

It is clear from Figure 3.22, that increasing the electron energy results in an increase the product ion peak intensity where a maximum intensity is achieved at an electron energy of 23 eV – 24 eV. One further observable trend in Figure 3.22, is that the intensity of the ions decreases with the increasing *m/z* of the product ion. This trend is true for all product ions, except the smallest product ions **b_2** and **b_3** which are not observed until an electron energy of 21 eV. The correlation of decreasing intensity with increasing mass of the product ions raises possible questions relating to the fragmentation mechanism. Firstly, the data in Figure 3.22 could be interpreted to postulate that fragmentation under EID conditions is most favourable close to the chain end, yielding the lower mass product ions preferentially with the exception of **b_2** and **b_3** ions. As the cation is retained by the product ions in all cases, this data provides evidence that the fragmentation is occurring at the polymer end where the sodium charge carrier resides. Gidden *et al.* have previously demonstrated that a low energy conformation of **$[PEG_n + Na]^+$** places the sodium cation close to a chain end where the hydroxyl terminal group contributes to the coordination of the cation.[45] This group also demonstrated that the most lowest energy conformations of **$[PEG_n + Na]^+$** have 5 – 8 PEG monomers in the coordination shell, which is an interesting observation as the product ion peaks of greatest intensity correspond to the **b_4** - **b_8** product ions. This would suggest that the proximity of the cation may influence the observed fragmentation. One alternative explanation to the source of the difference in the intensity of the product ions may be the stability of the product ions generated. The data in Figure 3.22 would suggest that the lower mass product ions are more stable than the higher mass ones.

4. ESI Tandem MS of synthetic homopolymers and copolymers

4.1. Tandem MS of synthetic homopolymers

Poly(styrene), PS, and poly(methyl methacrylate), PMMA, were selected to expand the range of chemical and physical properties of polymers analysed by tandem MS. Unlike PEG, these synthetic polymers have backbones consisting of carbon-carbon bonds only. This is of interest as tandem MS techniques predominantly broke the weaker carbon-oxygen backbone bonds in PEG. The presence of backbones with little variance in the bond energy will allow further investigation of the fragmentation techniques. Given the many industrial uses of PS and PMMA, the research interest is extensive. PS and PMMA have been regularly characterised in CID tandem MS experiments, with a number of publications investigating fragmentation mechanism,[120,142,143] charge carrier selection[38,39,90] and gas phase conformation.[43,44] This provides a useful source of reference to which the results presented in this thesis can be compared.

4.1.1. MS and tandem MS of PMMA

PMMA, like PEG is a polar synthetic polymer containing oxygen atoms, however unlike PEG the oxygen atoms are present on the side chain of the polymer, resulting in a polymer backbone containing only one type of bond. As PMMA is a polar polymer, it ionises effectively with alkali metal cations.[44,73] This is demonstrated in the full MS scan in Figure 4.1, where PMMA is simultaneously ionised with multiple alkali metal cations. The major series of peaks (●) are separated by 100.1 Da, which corresponds to the monomer unit ($C_5H_8O_2$). Accurate mass analysis of *m/z* 1425.75292, a peak in the series labelled (●) gave an empirical formula of $C_{70}H_{114}O_{28}Na$ that corresponds to **$[PMMA_{14} + Na]^+$**. A second series of peaks (■) is found 16 Da above the (●) series of peaks. Accurate mass analysis of *m/z* 1441.71403 a peak in the series labelled (■) corresponded to **$[PMMA_{14} + K]^+$**. A doubly charged ion series (▲) is observed, confirmed by accurate mass analysis (*m/z* 1174.60099 = $C_{115}H_{186}O_{46}Na_2$ = (**$[PMMA_{23} + 2\ Na]^{2+}$**).

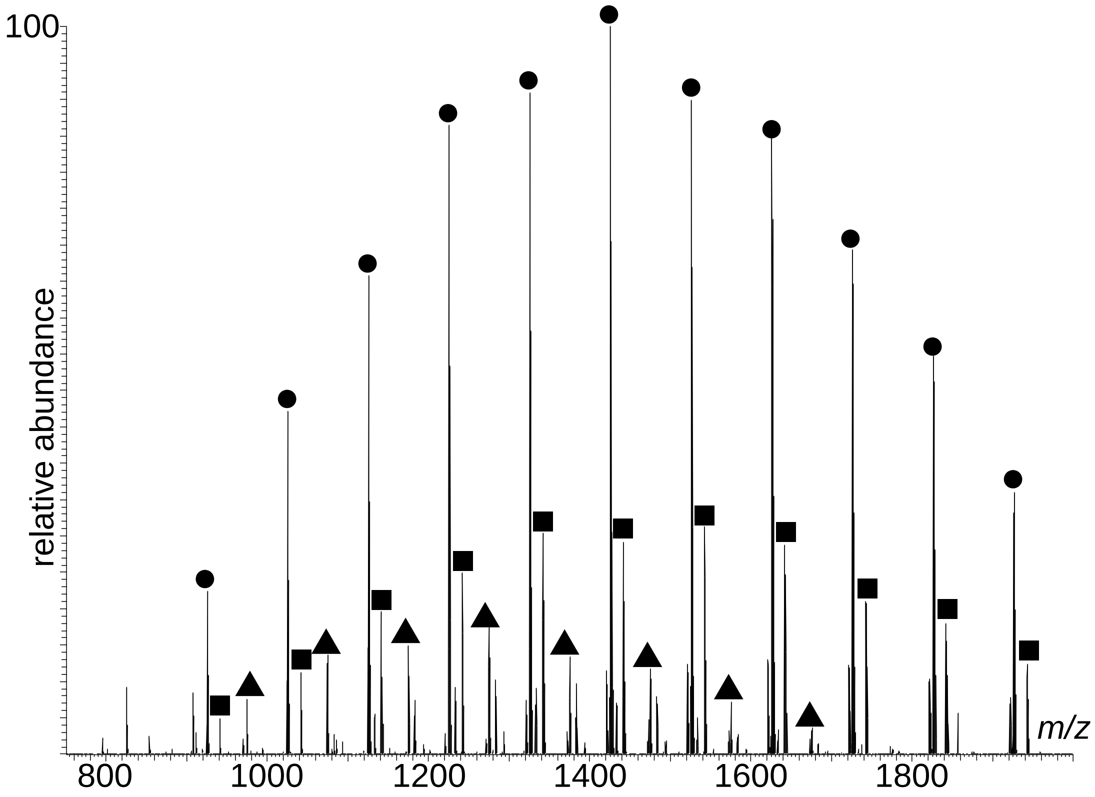

Figure 4.1 ESI Full MS of PMMA (● = $[M + Na]^+$, ■ = $[M + K]^+$ and ▲ = $[M + 2Na]^{2+}$).

The spectral base peak of the full MS spectrum at *m/z* 1425.75384 was selected as the precursor ion for tandem MS experiments. The resultant tandem MS of **$[PMMA_{14} + Na]^+$** spectra are provided in Figure 4.2. LTQ-CID of **$[PMMA_{14} + Na]^+$** resulted in product ions that represented polymer backbone cleavage towards the centre of the polymer chain. This is an unusual observation as fragmentation is normally observed close to polymer chain ends, where product ion peaks of highest intensity would be expected at the top and bottom of the *m/z* range analysed. The presence of an asymmetric monomer unit allows directional sequencing. Some of the observed product ion peaks give empirical formulae that can correspond to multiple product ions, where the empirical formula of **b_n** can also represent **a_{na}**, and **z_m** can also represent **y_{ma}**. Despite having the same empirical formula, these product ions with the same nominal mass can be formed through two different fragmentation mechanisms, outlined in Scheme 4.1.

The first mechanism involves homolytic backbone bond cleavage, where the **$b_n^\bullet$** and **$z_m^\bullet$** radicals formed are more effectively stabilised at the tertiary carbon centre, where subsequent loss of a hydrogen radical generates an unsaturated terminal group, as shown in Scheme 4.1. The second mechanism also involves homolytic bond cleavage; however, in this case, the intermediate **$a_n^\bullet$** and **$y_m^\bullet$** radicals lose a methyl group through β–scission, forming **a_{na}** and **y_{ma}**

product ions. The product ions formed have the same nominal mass, and consequently cannot be differentiated. The fact that two different fragmentation mechanisms generate product ions of the same nominal mass may explain the high intensity of the $\mathbf{b_n}$ (or $\mathbf{a_{na}}$) and $\mathbf{z_m}$ (or $\mathbf{y_{ma}}$) peaks, relative to the other product ion peaks observed. The remaining product ion series $\mathbf{a_{nb}}$ and $\mathbf{y_{mb}}$ are generated through initial formation of $\mathbf{a_n}^\bullet$ and $\mathbf{y_m}^\bullet$ radical intermediates, through homolytic backbone bond cleavage. Subsequent β–scission of the CO_2CH_3 unit, labelled E in Scheme 4.1, from the radical intermediates generates the observed product ions.

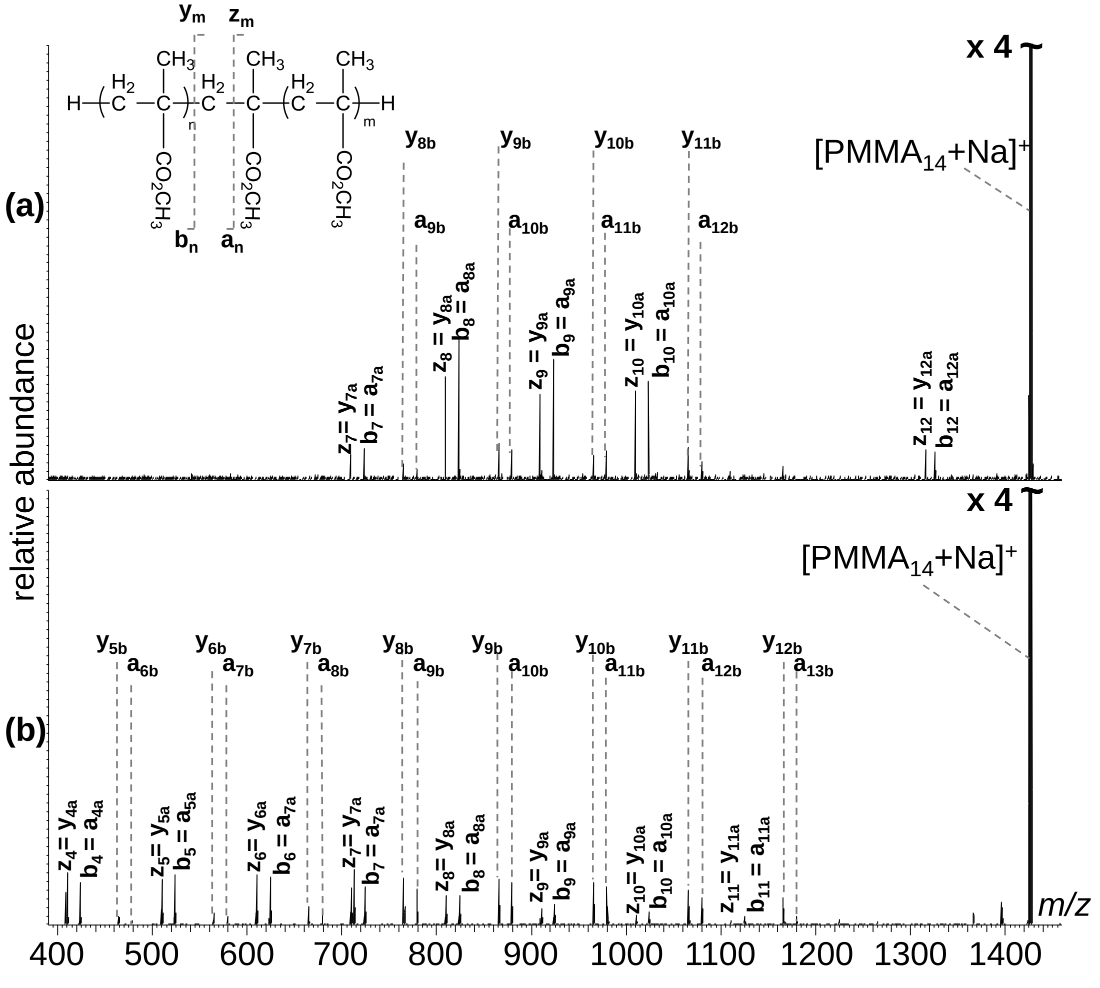

Figure 4.2 Tandem MS of $[H(C_5H_8O_2)_{14}H + Na]^+$ (a) CID 16 V and (b) EID 18.1 eV, ($b_n = a_{na}$ and $z_m = y_{ma}$), inset: structure of PMMA, annotated to indicate cleavage sites and the nomenclature used to differentiate between resulting product ions.

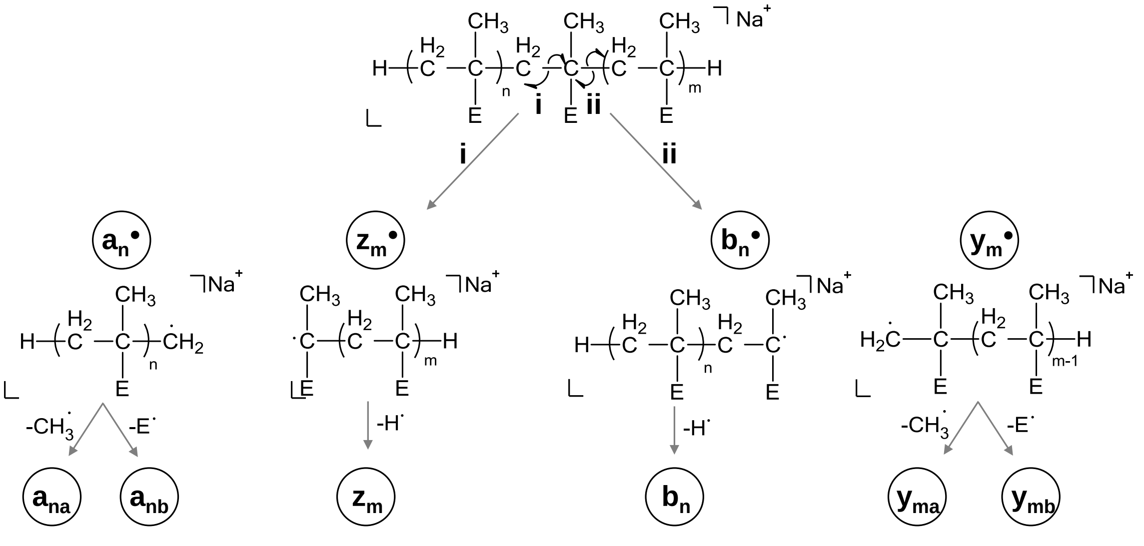

Scheme 4.1 Charge remote fragmentation of PMMA and the potential product ions generated (E = CO_2CH_3).

Irradiation of **$[PMMA_{14} + Na]^+$** with electrons with 18.1 eV resulted in extensive polymer dissociation, as shown in Figure 4.2(b). The product ions span a larger proportion of the detectable mass range, and as a consequence EID provides product ions that give more structural information. The intensity of the product ion peaks vary with *m/z*, such that the **b_n** (or **a_{na}**) (n=4-11) and **z_m** (or **y_{ma}**)(m=4-11) product ion peak intensities decrease with increasing *m/z*. This would suggest that the most favourable cleavage points are close to the polymer chain ends. Molecular modelling by Gidden *et al.* proposed that the interaction between the polymer and metal cation involves coordination of the oxygen atoms of the polymer side chains with the sodium cation. The lowest energy conformation calculated involves coordination of oxygen atoms from both ends of the polymer with the cation, leading to the formation of a U-shaped structure.[44] This conformation supports the proposal that bond cleavage is more prevalent for monomer units in close proximity to the sodium cation, leading to the formation of the **b_n** or (**a_{na}**) and **z_m** or (**y_{ma}**) product ions. In contrast, the intensity of the **a_{nb}** and **y_{mb}** product ion peaks, where the ester bond on the side chain has been cleaved, are found to increase with increasing *m/z*. In a hypothetical reaction leading to formation of higher mass **a_{nb}** and **y_{mb}** ions, the resultant radical would correspond to a low mass **$b_n^\bullet$** or **$z_m^\bullet$**. This would suggest that detection of each product ion is dependent on the location of the cation relative to the bond cleaved. The product ion intensities also suggest that certain backbone bonds within the polymer may cleave more favourably than others. For example, the formation of **b_4/z_4** and **y_{9b}/a_{9b}**, whose peak intensities are high relative to other product ions, involve the cleavage of the same C-C backbone bond.

The extent of dissociation observed by EID is comparable to that generated when MALDI-CID tandem MS experiments are performed (Figure 4.3). Inspection of the repeat product ion series generated by MALDI-CID (inset in Figure 4.3) shows that the same product ions are formed by MALDI-CID, LTQ-CID and EID.

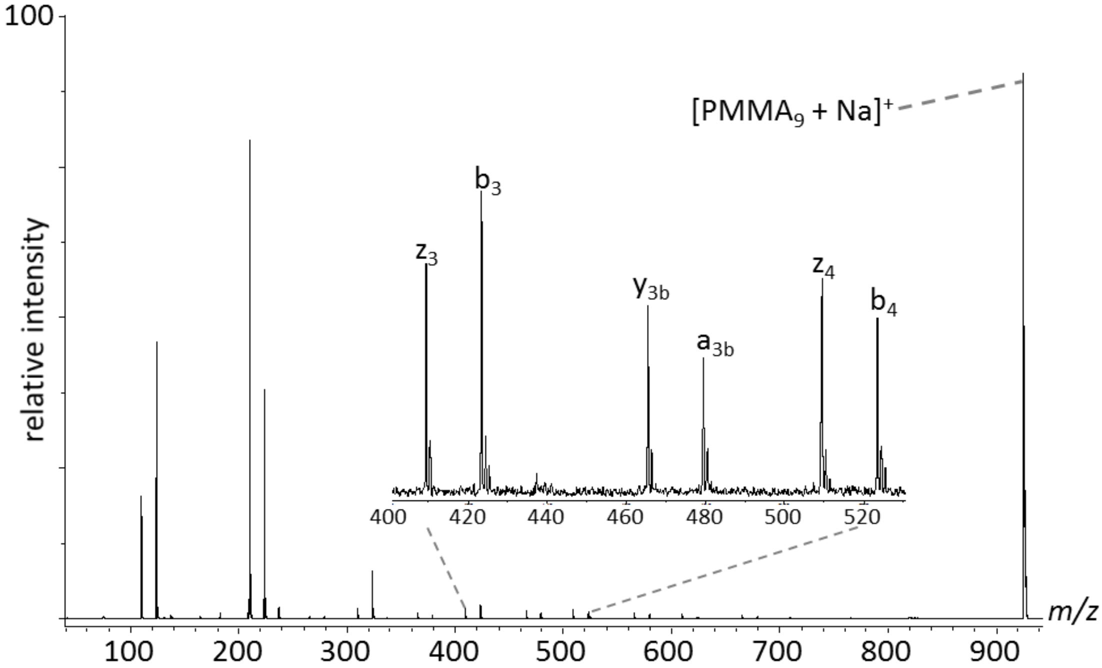

Figure 4.3 MALDI CID of $[H(C_5H_8O_2)_9H + Na]^+$.

4.1.2. MS and Tandem MS of PS

PS, a synthetic polymer composed purely of hydrogen and carbon atoms, has a carbon backbone with pendant phenyl groups at alternating carbon atoms. The lack of any heteroatoms reduces the polarity and hence solubility of PS in polar solvents. Gidden *et al.* studied the effect of charger carriers on the tandem MS spectra, and found that the selection of the charge carrier used to promote ionisation had less influence upon the CID tandem MS spectra than was reported for PMMA and PEG. They propose this to be due to an electrostatic interaction between the metal and the polymer involving coordination of the metal by two adjacent phenyl groups.[43] The majority of publications for PS analysis by mass spectrometry report the use of transition metal salts such as silver, whose d-orbitals overlap more effectively with the π-systems of the phenyl rings.[43]

Analysis of PS with silver generated a spectrum containing one series of peaks (●) separated by 104 Da and corresponding to the ion **$[PS_n + Ag]^+$**, (where n = 8 – 17) (Figure 4.4). Accurate mass analysis of *m/z* 1415.73924 gave an empirical formula of $C_{100}H_{106}Ag$, which is consistent with the proposed structure containing 12 styrene units. Isolation of *m/z* 1415.73924 permitted tandem MS experiments to be performed, the resultant spectra are presented in Figure 4.5.

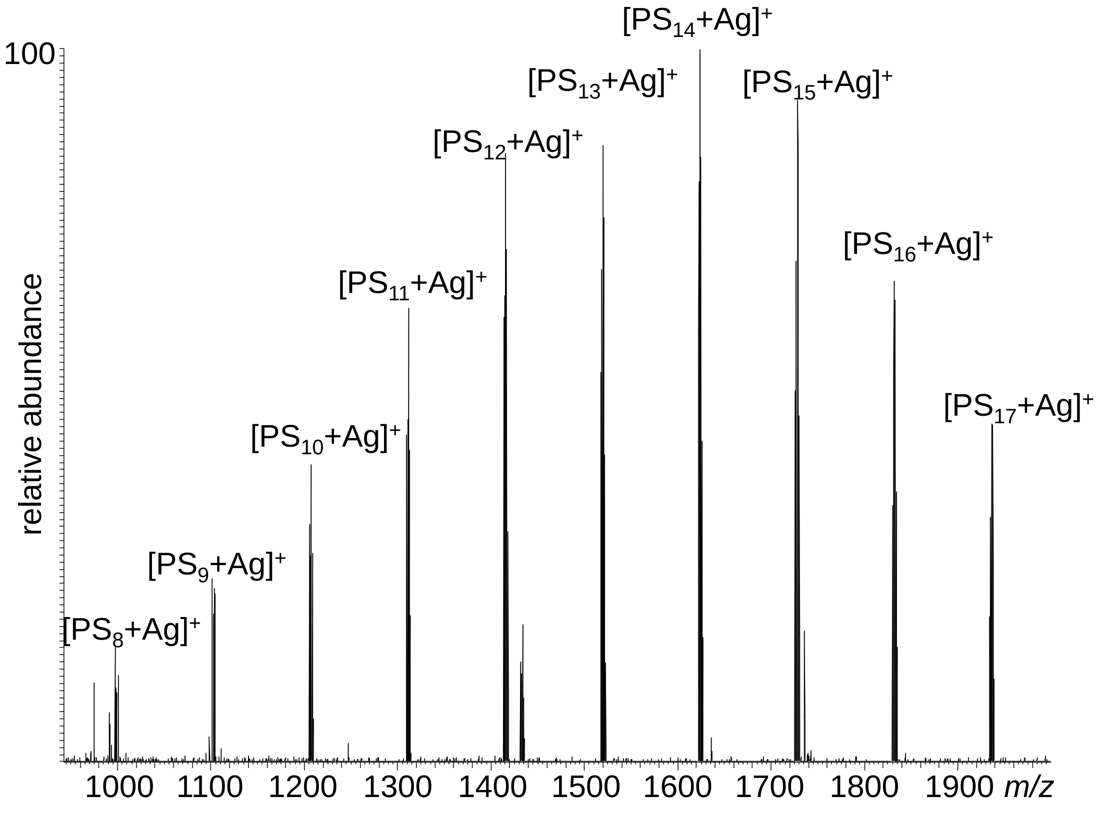

Figure 4.4 ESI Full MS of PS with AgTFA.

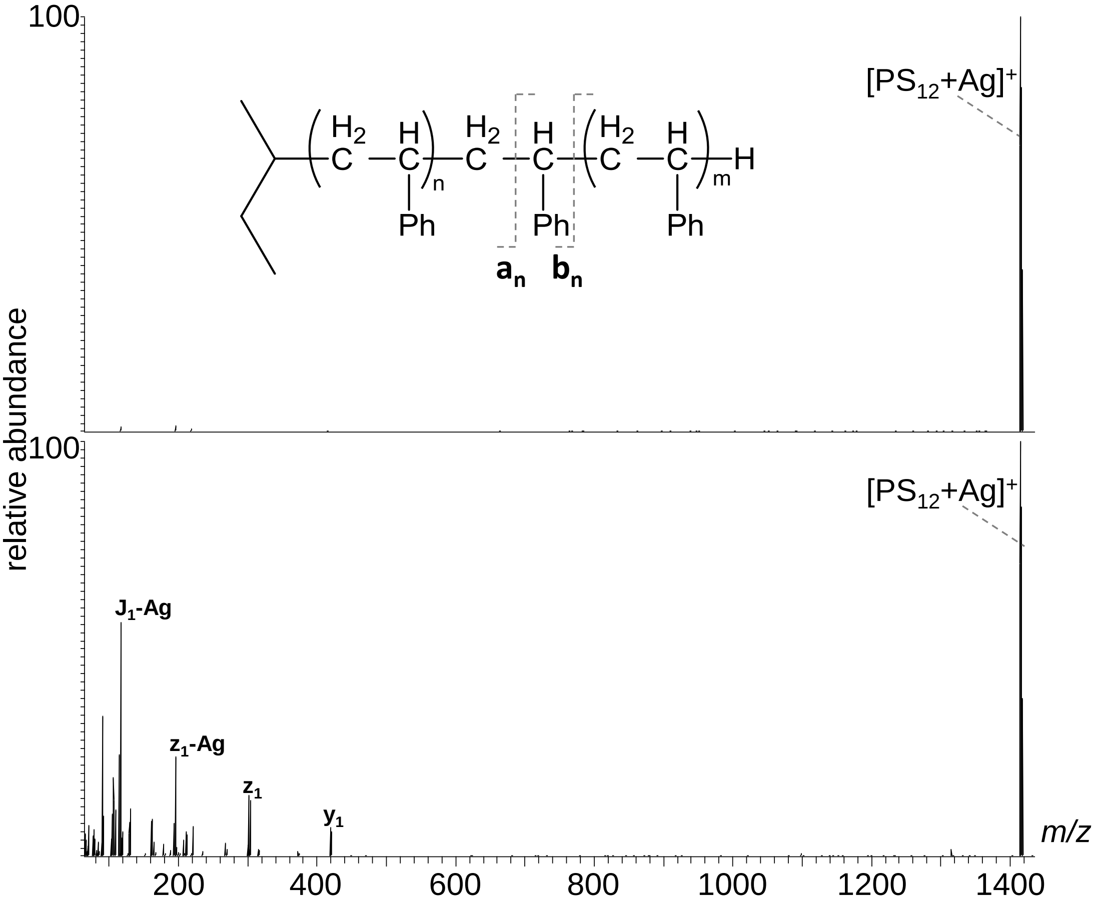

Figure 4.5 Tandem MS of $[C_4H_9(C_8H_8)_{12}H + Ag]^+$ (a) CID 20 V and (b) EID 21.1 eV, inset: structure of PS, annotated to indicate cleavage sites and the nomenclature used to differentiate between resulting product ions.

The absence of any product ion from LTQ-CID of **$[PS_{12} + Ag]^+$** (Figure 4.5(a)) is in line with observations outlined in Section 3 for PEG, where cation detachment was shown to be a major fragmentation pathway (Figure 4.5(a)). Cation detachment with no observable product ion peaks is supported by molecular modelling, where the metal cation interaction with the polymer was calculated to be 300 kJ mol^{-1}; close to the calculated bond dissociation energies of PS (270-400 kJ mol^{-1}).[43] In contrast, irradiation of the precursor ions with electrons of 21.1 eV was sufficient to induce polymer dissociation, as shown in Figure 4.5(b). The product ions observed are all in the low *m/z* range, and are found to contain only one intact monomer unit, suggesting that fragmentation occurs more favourably at the chain ends. It is also noted that the product ions **J_1-Ag** and **z_1-Ag** do not contain the original silver charge carrier, suggesting that charge transfer has occurred to the polymer, where these low molecular weight ions can stabilise the charge effectively. The limited dissociation observed in these tandem MS spectra could be attributed to a number of factors, one that could be readily examined is the influence of the charge carrier present. As shown in Section 3.2, the selection of charge carrier does influence the observed tandem MS spectrum of PEG, where alkali metals were shown to generate superior spectra using EID. The addition of a sodium salt to PS generated a molecular ion series of peaks that corresponded to **$[PS_n + Na]^+$**, where n = 9 – 18. The precursor ion selected for tandem MS experiments at *m/z* 1642.00878, gives an empirical formula of $C_{124}H_{130}Na$ by accurate mass analysis, which corresponds to **$[PS_{15} + Na]^+$**.

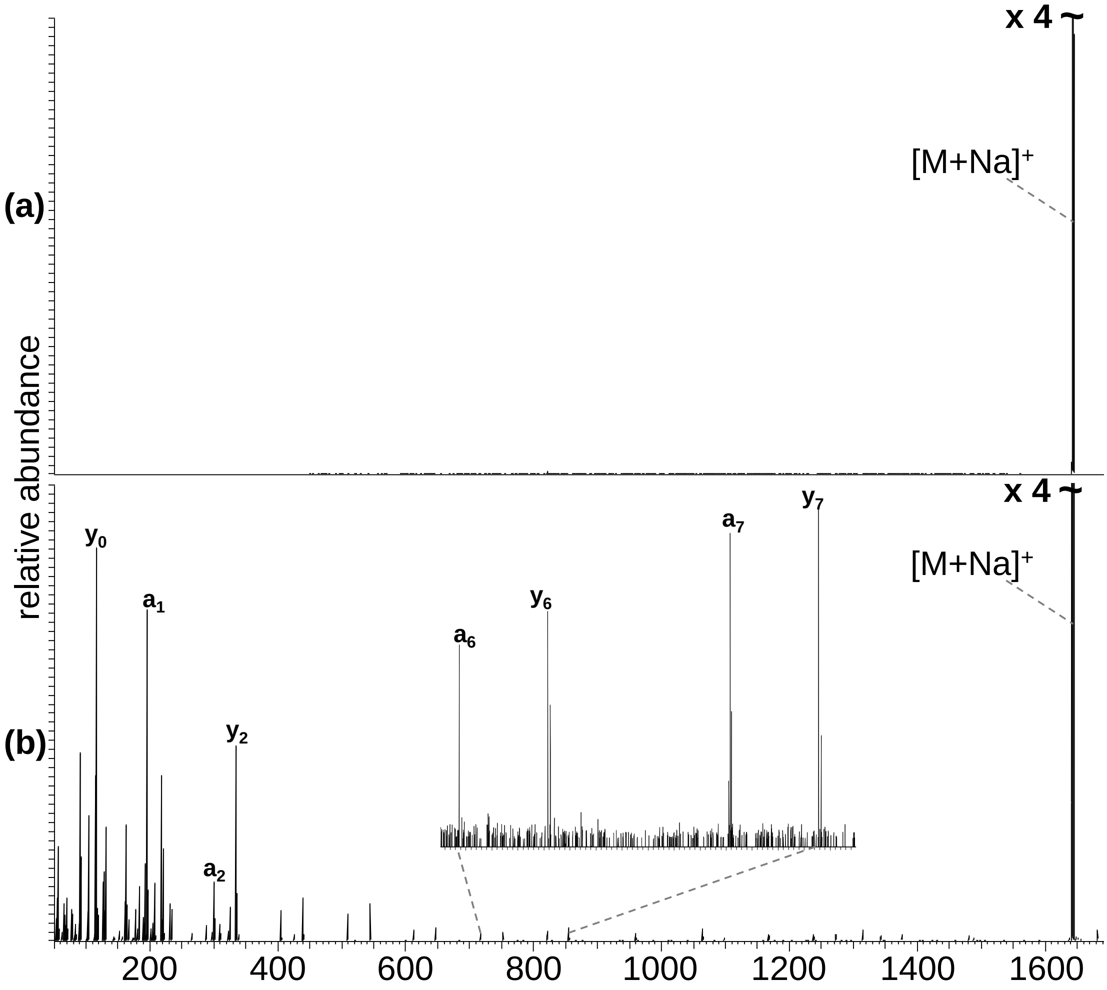

Figure 4.6 Tandem MS of $[C_4H_9(C_8H_8)_{15}H + Na]^+$ (a) CID 15 V and (b) EID 21.1 eV.

The major fragmentation pathway observed in LTQ-CID of the **$[PS_{15} + Na]^+$** was cation detachment similar to the results obtained for LTQ-CID **$[PS_{15} + Ag]^+$**. This would suggest that the electrostatic cation-polymer interaction is unable to survive the dissociation pathway, where cation detachment is preferential. EID analysis of **$[PS_{15} + Na]^+$** generates extensive polymer dissociation with product ion peaks distributed over a significant proportion of the mass range, accounting for 12 of the 15 monomers present in the precursor ion. The presence of extensive polymer dissociation in Figure 4.6(b) and limited dissociation in Figure 4.5(b) demonstrate that the charger carrier influences the fragmentation observed in EID tandem MS experiments, adding further confidence to the observations made for PEG in Section 3.4. In the analysis of PS, the selection of charge carrier is shown to influence the resultant EID tandem MS spectrum more significantly than previously observed for PEG, where cation selection is found to affect the formation of product ions and not simply the intensity of the product ion peaks. The presence of asymmetric terminal groups permits directional sequencing of the polymer, with two major series of peaks detected that correspond to **a$_n$** (n=1-11) and **y$_m$** (m=2-12).[142,143] Formation of these product ions is proposed to be through charge remote fragmentations involving homolytic backbone cleavage that produce four potential radical intermediates, as shown in Scheme 4.2.

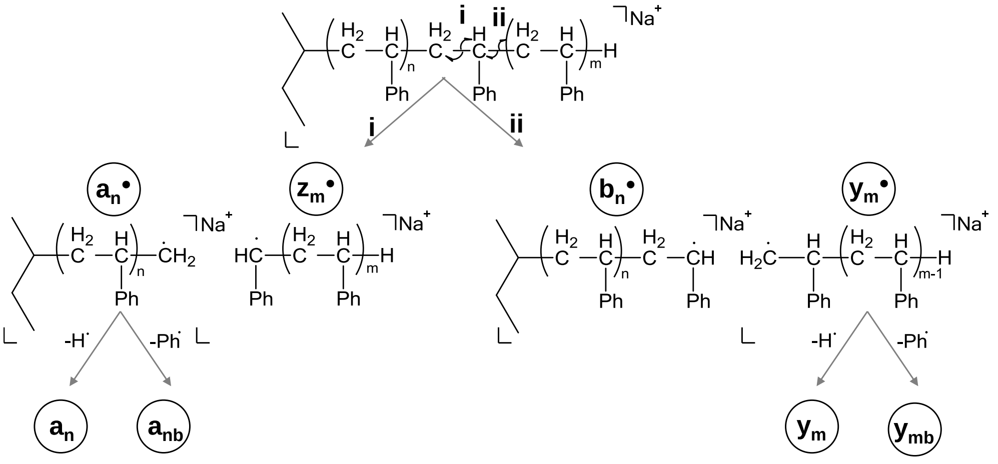

Scheme 4.2 Charge remote fragmentation of PS.

Formation of **a$_n$** and **y$_m$** product ions can theoretically be generated from all of the radical intermediates, where the simplest mechanism involves β–hydrogen radical elimination from **a$_n^•$** and **y$_m^•$**, as shown in Scheme 4.2. Generation of the desired product ions by this pathway is hindered due to the instability of the primary radical intermediates, which are not observed during the experiment. A more energetically favourable route to the formation of **a$_n$** and **y$_m$** involves backbone cleavage to generate the more stable secondary **b$_n^•$** and **z$_m^•$** radicals, where a backbiting rearrangement allows for the formation of the desired product ions, as shown in Scheme 4.3.

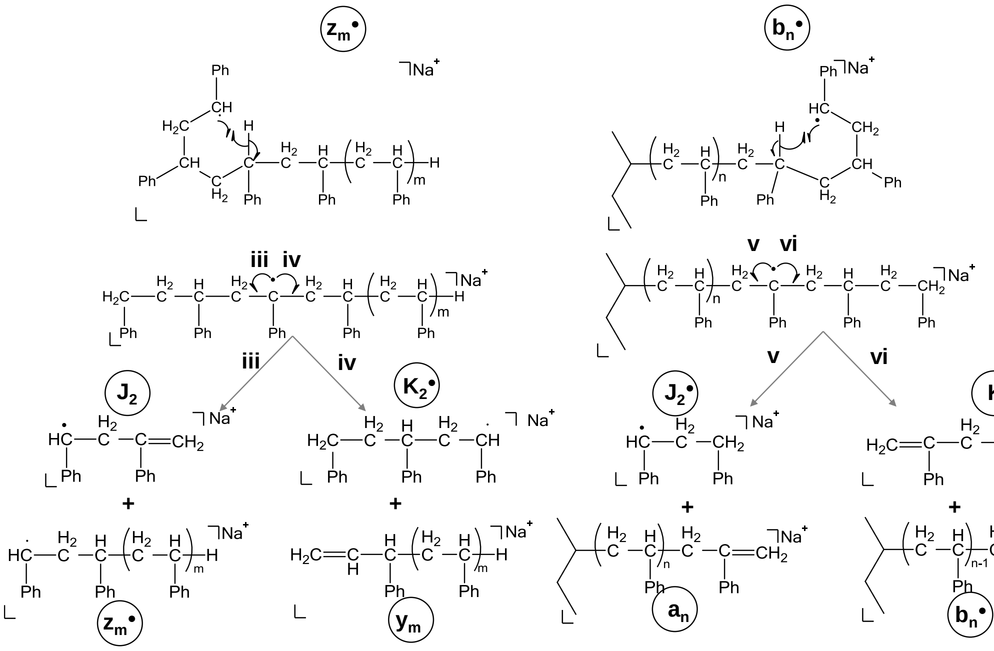

Scheme 4.3 Backbiting rearrangement reaction and theoretical product ions.

This fragmentation mechanism also accounts for the formation of the low molecular weight radical species that are observed in the < *m/z* 400 range of the spectrum in Figure 4.5. Like EID of PMMA and PEG, the intensity of the product ion peaks increases with decreasing *m/z*. Again, this would suggest that fragmentation is more prevalent close to the chain ends of the polymer. In comparison, MALDI-CID performed with a silver cation generated both $\mathbf{a_n}$ and $\mathbf{y_m}$ product ions, where the number of product ions observed is comparable to EID. This demonstrates that if sufficient energy is imparted into the molecule dissociation of the polymer can occur when silver salts are used. The intensity of the product ion peaks increase with decreasing *m/z* demonstrating, that like EID, the formation of low *m/z* product ions is favourable. In the lower *m/z* region (<400 Da), MALDI-CID is shown to generate fewer product ions compared to EID, suggesting that more complex rearrangements can be achieved under EID conditions.

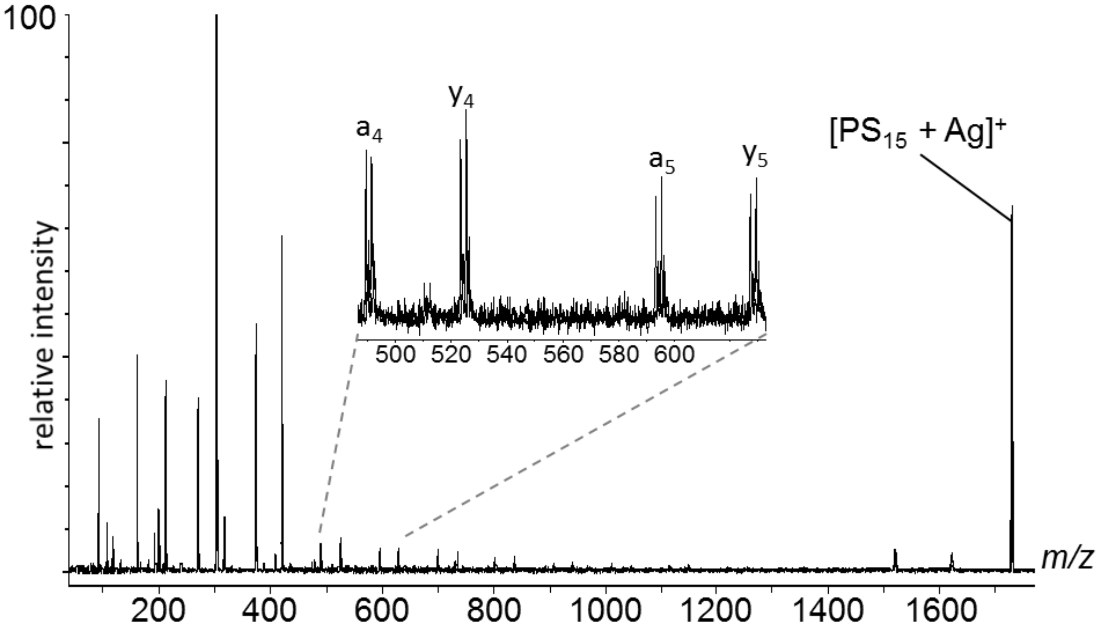

Figure 4.7 MALDI CID of [$C_4H_9(C_8H_8)_{15}H$ +Ag]$^+$.

4.2. Tandem MS of synthetic copolymers

Characterisation of synthetic copolymers containing multiple monomer types is of significant interest due to the wide-ranging industrial applications of such materials. It is essential to effectively characterise copolymers, as the physical and chemical properties of such materials depend upon the microstructure, end group functionality and chain architecture.[159] The additional complexity of copolymer analysis represents a real challenge for the analytical chemist, as no single technique can provide all the required structural information. Building upon the findings in Chapter 3 for the analysis of PEG, a series of copolymers that contain ethylene glycol (EG) as a constituent of a copolymer with propylene glycol (PG) are analysed using tandem MS. Copolymers containing PG units were selected due to the closely related chemistries of EG and PG. This is demonstrated in the tandem MS of poly(propylene glycol) (PPG), where dissociation of PPG was found to emulate that observed previously for PEG, with predominant cleavage of carbon-oxygen bonds (Figure 10.2, Appendix 10.3). The first, Synperonic, an industrially significant copolymer used as a non-ionic surfactant, is a block copolymer comprising ethylene glycol (EG) and propylene glycol units (PG), where the major block present was proposed to be PG. The terminal groups present in this molecule are hydroxyl functionalities, as shown in Figure 4.8.

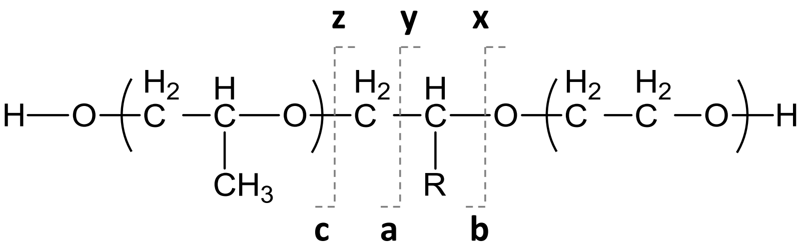

Figure 4.8 Structure of hydroxyl terminated PPG-b-PEG, annotated to indicate cleavage sites and the nomenclature used to differentiate between resulting product ions, R = H (EG) or R = CH_3 (PG).

Jeffamine, a second commercially important block copolymer comprising EG and PG units, was investigated as shown in Figure 4.9. In contrast to Synperonic, Jeffamine contains primary amine and methyl ether terminal groups in place of hydroxyl functionalities, which results in a difference in the chemistry of the copolymers.

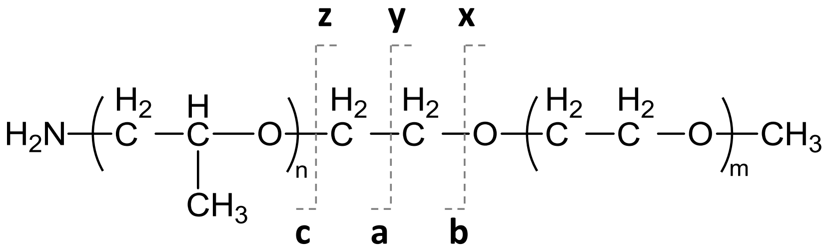

Figure 4.9 Structure of Jeffamine, annotated to indicate cleavage sites and the nomenclature used to differentiate between resulting product ions.

4.2.1. Tandem MS of block copolymers

ESI MS of the Synperonic allowed the identification of four repeat series of peaks, where the peaks in each series were separated by 58 Da, the mass of the PG unit (C_3H_6O). The most intense series of peaks labelled (●) gives an empirical formula that corresponds to **[HO(PG)$_n$H + Na]$^+$**, a PPG homopolymer. The remaining series are all found to be block copolymers containing different numbers of EG units, where (▲), corresponds to **[HO(PG)$_n$(EG)$_1$H + Na]$^+$**, (■) corresponds to **[HO(PG)$_n$(EG)$_2$H + Na]$^+$** and (♦) corresponds to **[HO(PG)n(EG)$_3$H + Na]$^+$**. Fours species in the range *m/z* 750 – 800, one from each series, were selected for tandem MS experiments, where the precursor ion contained 13 repeat units of varying composition.

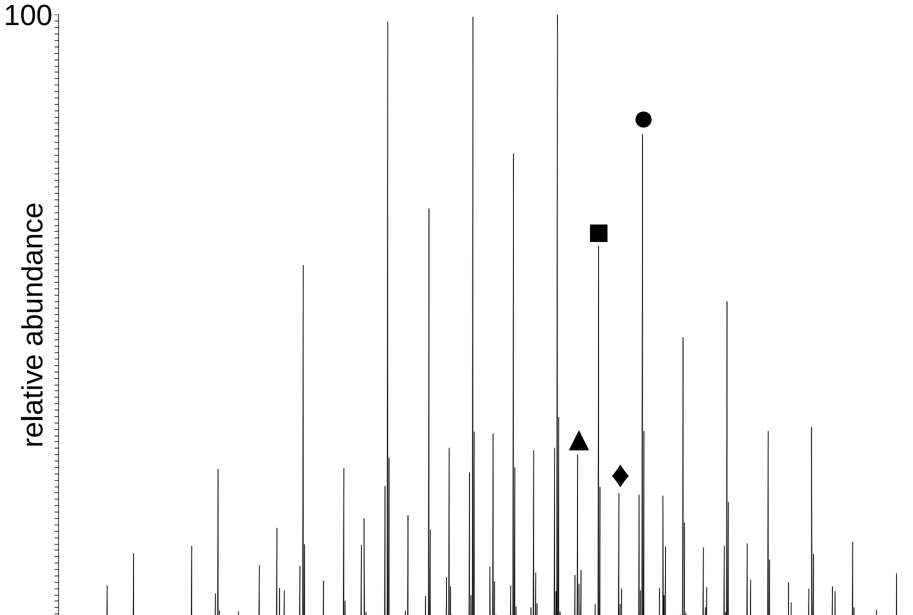

Figure 4.10 ESI Full MS of PG-b-EG (● = [PG$_n$ + Na]$^+$,▲ = [PG$_n$EG$_1$ + Na]$^+$ ■ = [PG$_n$EG$_2$ + Na]$^+$ and ♦ = [PG$_n$EG$_3$ + Na]$^+$).

The nomenclature used in product ion assignment of copolymers is largely similar to that used previously, as shown in Figure 4.8. The letter denotes the bond cleaved in the formation of each product ion, where **a**, **b** and **c** denote product ions containing the lowest number of EG units, and **x**, **y** and **z** the product ions containing the most EG units. The assignment also contains the number of intact units of each monomer present in the copolymer product ion in superscript. For example, a **b** product ion containing 5 PG units and 2 EG units would be $\mathbf{b^{PG5EG2}}$.

4.2.1.1. CID and EID of $[HO(C_3H_6O)_{12}(C_2H_4O)_1H + Na]^+$

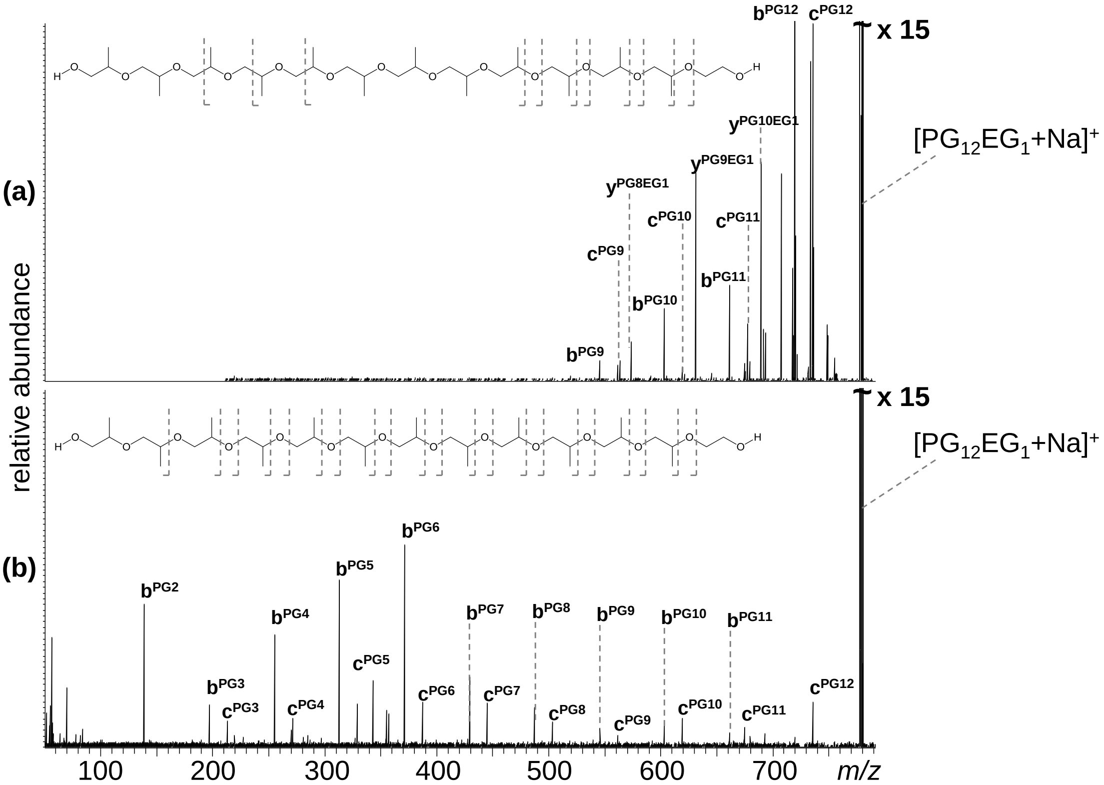

Figure 4.11 Tandem MS of $[HO(C_3H_6O)_{12}(C_2H_4O)H +Na]^+$ (a) CID 17 V and (b) EID 19.1 eV.

Accurate mass analysis of *m/z* 779.52039 gave an empirical formula of $C_{38}H_{76}O_{14}Na$ that corresponds to $\mathbf{[HO(C_3H_6O)_{11}(C_2H_4O)_2H + Na]^+}$ ($\mathbf{[PG_{12}EG_1 + Na]^+}$). In Figure 4.11, the product ions observed from both tandem MS experiments provide evidence that the block copolymer structure has the EG unit located at the terminus of the copolymer. LTQ-CID generated a number of product ions that support this proposal. The peak at *m/z* 703.46164 corresponds to $\mathbf{c^{PG12}}$, which is formed through neutral loss of the EG unit. Subsequent product ions detected correspond to dissociation of the PG block close to the chain end from which the EG unit is lost. The presence of **y** product ions, which retain the EG unit are formed through sequential losses of PG units, support the proposal that the EG unit is present at a terminal group, but are unable to confirm the proposal. In comparison, irradiation of the precursor ion using electrons with 19.1 eV generates a simplified spectrum that contains two product ion series of peaks that provide more structural information than LTQ-CID, as shown in Figure 4.11 (b). The presence of an unbroken series of product ions from PG_2 to PG_{12} provides conclusive evidence that all of the PG units are present as a single block within the precursor ion. Again, the presence of the $\mathbf{c}^{\mathbf{PG12}}$ product ion peak confirms that the location of the EG unit is at a chain end. The absence of product ions that contain an EG unit suggests that sodium is likely to be located at the end of the polymer chain consisting solely of PG units. Location of the EG unit at the opposite chain end would explain its initial loss, where charge remote fragmentation accounts for the observed product ions.

4.2.1.2. CID and EID of $[HO(C_3H_6O)_{11}(C_2H_4O)_2H + Na]^+$

Accurate mass analysis of *m/z* 765.50244 gave an empirical formula of $C_{37}H_{74}O_{14}Na$ that corresponds to $\mathbf{[HO(C_3H_6O)_{11}(C_2H_4O)_2H + Na]^+}$ ($\mathbf{[PG_{11}EG_2{+}Na]^+}$). These components have the potential to form two structural isomers; the first a di-block copolymer where the EG units are present as a single block, or alternatively a tri-block copolymer with an EG present at each chain end. The literature supplied by the manufacturer proposed that the major isomer was the tri-block structure.

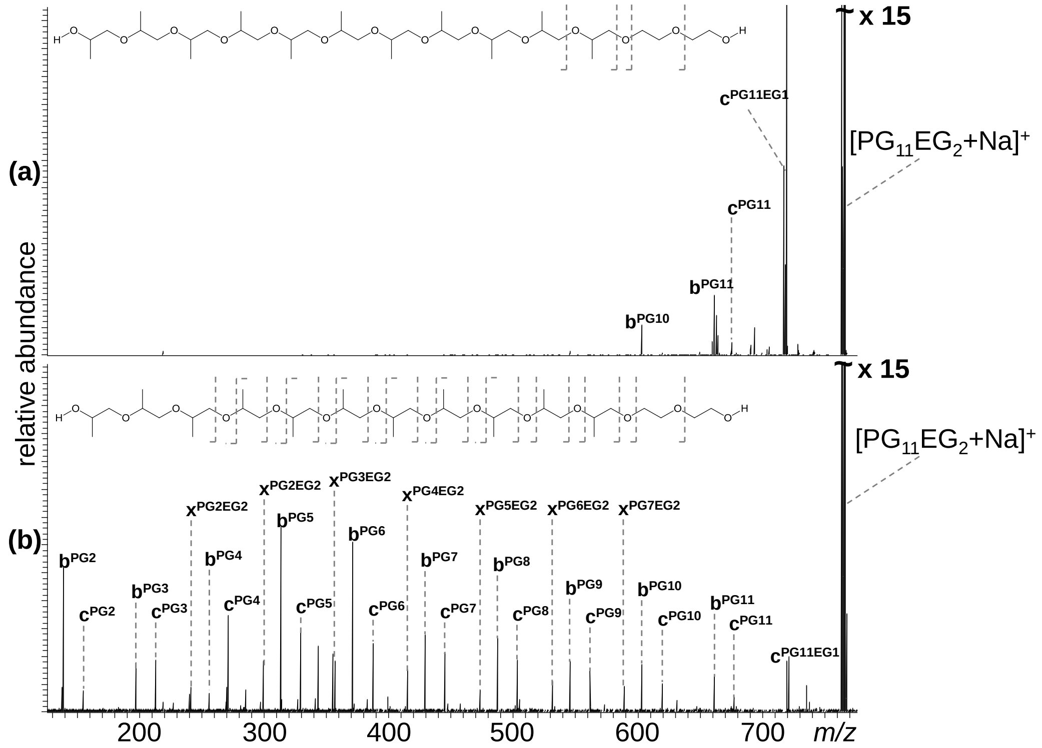

Figure 4.12 Tandem MS of $[HO(C_3H_6O)_{11}(C_2H_4O)_2H + Na]^+$ (a) CID 16 V and (b) EID 19.1 eV.

In Figure 4.12, the product ions observed support the presence of a di-block copolymer. LTQ-CID generates minimal dissociation of the polymer, with $\mathbf{b}^{PG10}$, $\mathbf{b}^{PG11}$, $\mathbf{c}^{PG11}$ and $\mathbf{c}^{PG11EG1}$ product ions accounting for neutral losses of 2 EG units and 1 PG unit. The product ions demonstrate that dissociation of the copolymer at the chain end containing the EG units is favoured under LTQ-CID conditions. Like CID, EID generates product ion peaks $\mathbf{b}^{PG10}$, $\mathbf{b}^{PG11}$, $\mathbf{c}^{PG11}$ and $\mathbf{c}^{PG11EG1}$ that demonstrate neutral loss of the EG unit, confirming its presence at a chain end. The remaining peaks of the **b** and **c** ion series contain only PG units, where the observed peaks account for 9 of the 11 PG units present, suggesting that all 11 PG units are present as a single block. These product ions support the proposal that the precursor ion has a di-block structure. The presence of a reciprocal **x** ion series that contains both EG units and with sequential losses/additions of PG units provides further evidence for a di-block structure where the EG units are present as a single block. The **x** product ion series of peaks demonstrates that it is possible to induce backbone cleavage with the sodium cation located at the terminus containing both EG units under EID conditions. Cerda *et al.* demonstrated that the addition of EG monomers to a PG block favoured the formation of di-block copolymers of EG and PG by anionic polymerisation. This preference over tri-block copolymer formation was proposed to be due to differences in the reactivity, where addition of EG is preferable at $–OCH(CH_3)CH_2O^-$ compared to $–OCH_2CH(CH_3)O^-$.[203]

4.2.1.3. CID and EID of $[HO(C_3H_6O)_{10}(C_2H_4O)_3H + Na]^+$

Accurate mass analysis of *m/z* 751.48287 generated an empirical formula of $C_{36}H_{72}O_{14}Na$, which corresponds to **$[HO(C_3H_6O)_{10}(C_2H_4O)_3H + Na]^+$** (**$[PG_{10}EG_3+Na]^+$**). Like the previous copolymer, this polymer can take the form of two structural isomers; the first is a di-block structure with all EG units located on a single chain end, and the second a tri-block structure, where the 3 EG units are separated into 1 EG and 2EG blocks respectively at opposite chain ends. This means that the precursor ion can take one of two forms, where evidence of both is investigated in Figure 4.13.

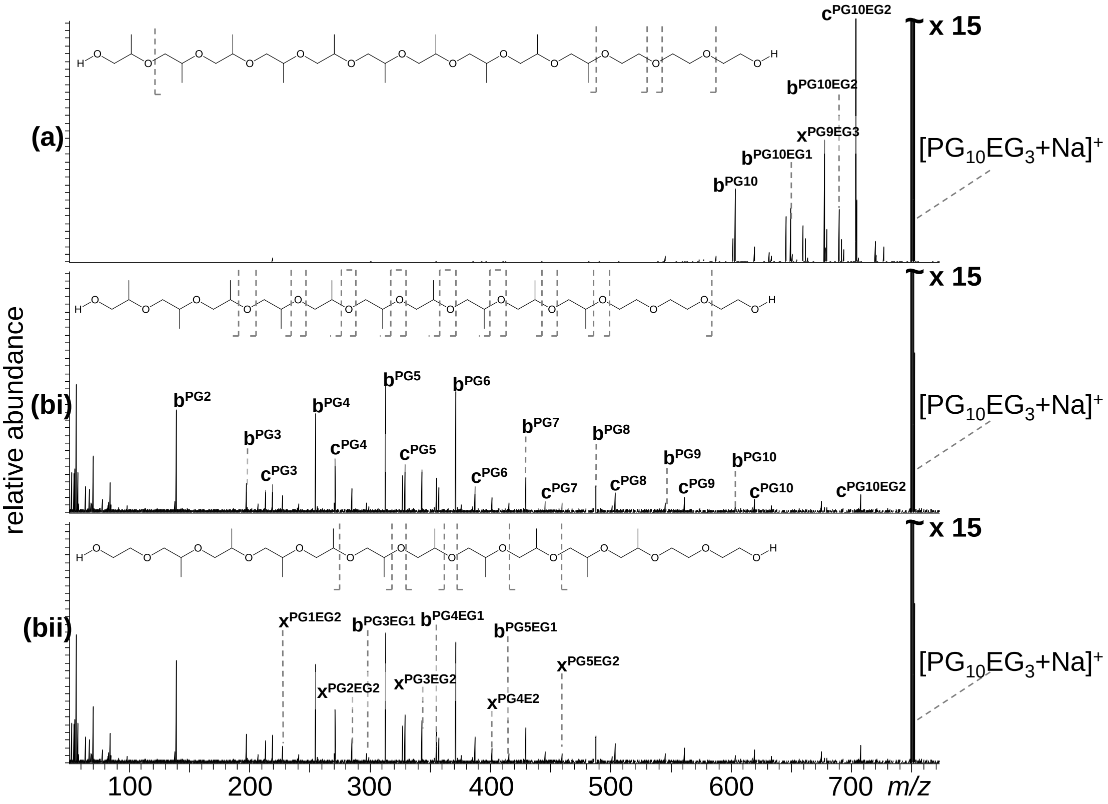

Figure 4.13 Tandem MS of $[HO(C_3H_6O)_{10}(C_2H_4O)_3H +Na]^+$ (a) CID 15 V (b) and EID 18.1 eV including product ion assignment for di-block structure (c) EID 18.1 eV including product ion assignment for tri-block structure.

LTQ-CID generated a small number of product ions in the higher *m/z* range in close proximity to the precursor ion, as shown in Figure 4.13(a). The observed ions support the presence of a di-block copolymer where all of the EG units reside at the same chain end. The series of peaks labelled **b** account for sequential losses of EG units, whereas the sole **x** peak provides evidence of the 3 EG units as a single block. The results obtained by EID in Figure 4.13(b) also support the presence of a di-block species. The series of peaks labelled **b** contain only PG units, demonstrating that all EG units are initially lost from the same chain end. The **c** series of peaks adds further confidence to the di-block structural assignment. An unusual observation from this work was the identification of peaks that could correspond to two potential ions with the same nominal mass. Accurate mass analysis of *m/z* 329.19438 generates an empirical formula of $C_{15}H_{30}O_6Na$, which can correspond to either of the two structures outlined in Figure 4.14. $\mathbf{c^{PG4}}$ (Figure 4.14(a)) is a product ion with a terminal PG group and contains no EG units, whereas $\mathbf{x^{PG2EG3}}$ has an EG terminal group, and contains 3 EG units and two intact PG units. It is not unusual to generate product ions with the same nominal mass, especially given the similarity of the monomers present in this copolymer.

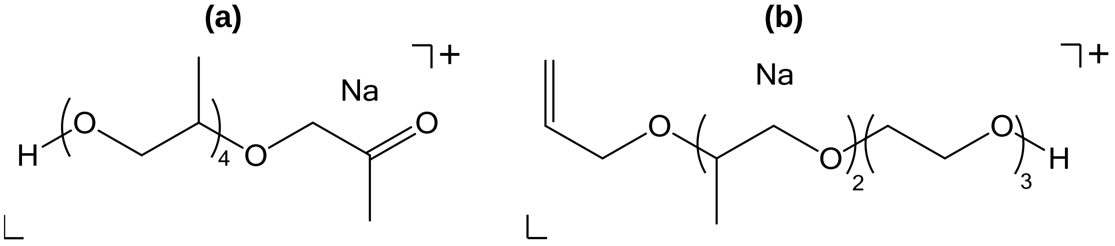

Figure 4.14 Structures of ions of the same nominal mass, (a) c^{PG4} and (b) x^{PG2EG3}.

Cerda *et al.* proposed that there is a difference in the reactivity in the chain ends of the PPG block during EG unit addition by anionic polymerisation. Given that reaction at each chain end is a probability, the likelihood of detecting product ions corresponding to a tri-block copolymer increases with an increasing number of EG units added. As Synperonic is synthesised using anionic polymerisation, it was of interest to examine the peaks not assigned for the di-block structure as potential evidence of a tri-block structure. Further analysis of the EID spectrum for $\mathbf{[HO(C_3H_6O)_{10}(C_2H_4O)_3H + Na]^+}$ reveals a number of product ions that support the presence of a tri-block structure, as shown in Figure 4.13(bii). The **b** series of peaks contains one EG unit with an increasing number of PG units, and a reciprocal **x** series of peaks contain 2 EG units with an increasing number of PG units. EID has therefore helped to establish the presence of two different copolymer structures that have the same nominal mass that could not be obtained by LTQ-CID. Although the possibility of molecular rearrangement involving carbon-carbon bond cleavages cannot be eliminated, the previous work on PEG and PPG homopolymers have demonstrated that formation of product ions involving carbon-oxygen bond cleavage are more favourable under tandem MS conditions.[87,88,129,201,203]

4.2.1.4. CID and EID tandem MS of Jeffamine

ESI MS analysis of Jeffamine resulted in 3 singly charged series of peaks, where the peaks within each series are separated by 44 Da, the EG repeat unit as shown in Figure 4.15. Each series of peaks, labelled (●), (■) and (▲), correspond to $\mathbf{[H_2N(PG)_2(EG)_nCH_3 + H]^+}$, $\mathbf{[H_2N(PG)_3(EG)_nCH_3 + H]^+}$ and $\mathbf{[H_2N(PG)_4(EG)_nCH_3 + H]^+}$ respectively, where EG is shown to be the major constituent. It is also noted that ESI of Jeffamine has resulted in the formation of a doubly charged molecular weight distribution in the lower mass region of Figure 4.15 (*m/z* 400 – 600).

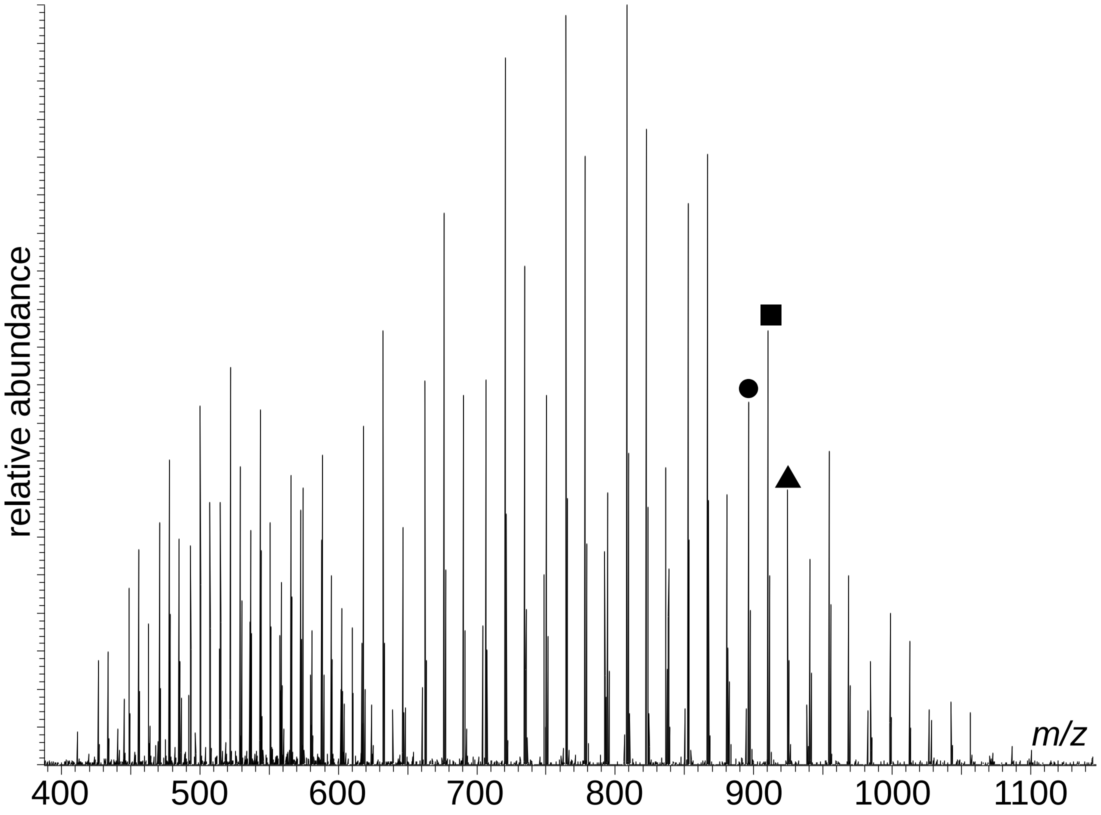

Figure 4.15 ESI Full MS of Jeffamine (● = $[PG_2EG_m + H]^+$, ■ = $[PG_3EG_m + H]^+$, ▲ = $[PG_4EG_m + H]^+$ and $[PG_nEG_m + 2H]^{2+}$ present *m/z* 400 - 600.

In contrast to all previous studies of EG and PG based polymers that preferentially formed sodium containing molecular ions, the presence of the amine terminal group has resulted in the preferential formation of protonated molecular ions, when no salts were added. A single peak from the (■) series at *m/z* 910.59622 was selected for tandem MS experiments. Accurate mass analysis gave an empirical formula of $C_{42}H_{88}O_{19}N$, which corresponds to **$[H_2N(PG)_3(EG)_{16}CH_3 + H]^+$**. Once again, this copolymer can represent two different structural isomers, the first a di-block copolymer where all PG units are present as a single block (Figure 4.17(a)), or alternatively a tri-block copolymer where there are 2PG and 1PG blocks at either end of the EG block (Figure 4.17(b)).

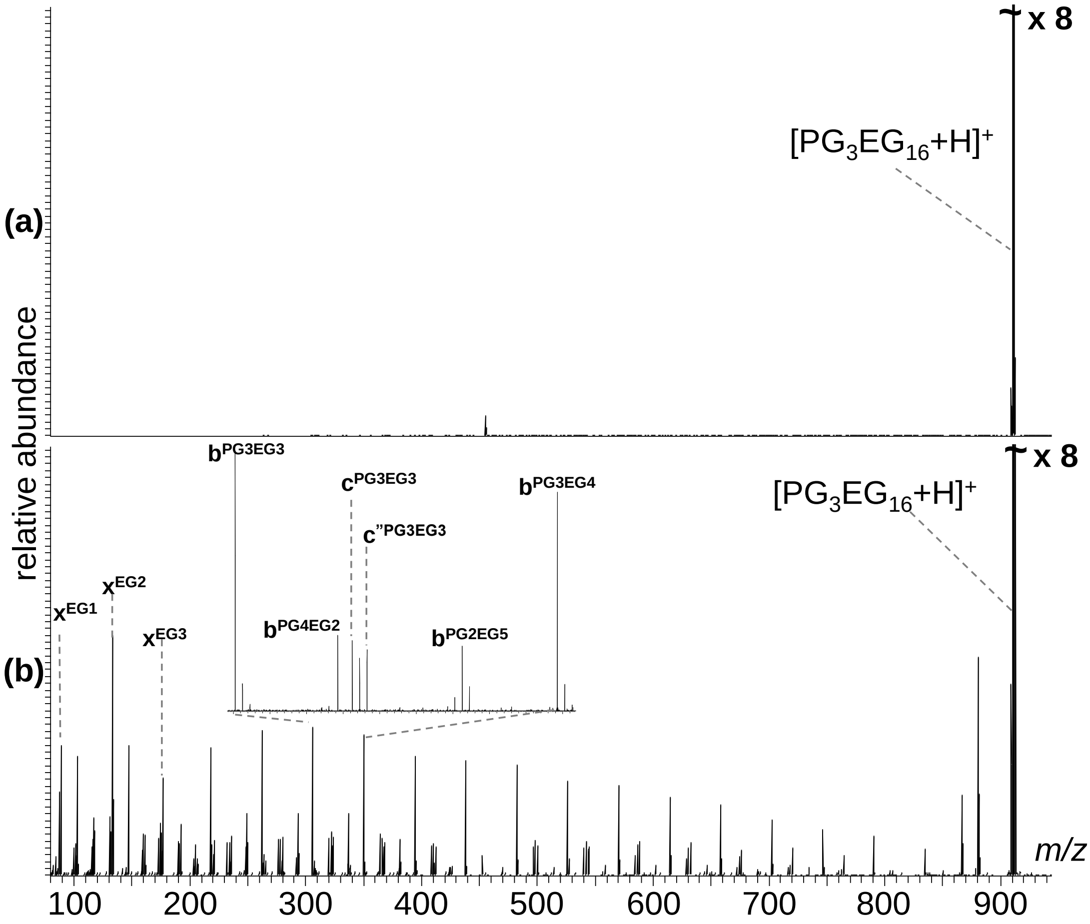

Figure 4.16 Tandem MS of $[NH_2(C_3H_6O)_3(C_2H_4O)_{16}CH_3 +H]^+$ (a) CID 25 V and (b) EID 20.1 eV (inset expansion of *m/z* 350 -400).

LTQ-CID of this precursor ion resulted in no dissociation of the copolymer, as shown in Figure 4.16(a), and consequently no conclusion can be drawn to determine the copolymer structure. In contrast, irradiation of the protonated precursor ion with 20.1 eV electrons results in extensive polymer dissociation that provides structurally useful information (Figure 4.16(b)). The product ion peaks of highest intensity correspond to **b** ions that contain 3PG units, an increasing number of EG units and the amine terminal group. This provides strong evidence that the major copolymer species present for this precursor ion is the di-block copolymer species. It also demonstrates that the likely location of the PG units is at the copolymer end containing the primary amine. The high intensity of the product ion peaks that retain the amine terminal group suggests that a likely location for the proton is the amine group. Given the high proton affinity of the amine over the remainder of the copolymer, this is a reasonable proposal. In the low *m/z* region (< 200 Da) there are reciprocal **x** ions containing only EG units and the methyl terminal group. Close inspection of the product ion repeat series, shown inset (Figure 4.16), demonstrates that the **b**, **c** and **c**$''$ peaks that correspond to the di-block structure have the highest intensity relative to the other product ion peaks detected. Evidence of the tri-block structure can be found from a second **b** series at *m/z* 381.27628 that contains 2 PG units and 5 EG units, as shown inset. There is no evidence of the reciprocal **x** series, supporting the proposal that the location of the proton charge carrier is at the primary amine terminal group. One unusual peak was observed at *m/z* 364.27314, whose empirical formula ($C_{18}H_{36}O_6N$) corresponds to a product ion containing a minimum of 4 PG units and retains the amine terminal group. This ion indicates that a third structural isomer could be present in the isolated precursor ions. The structure proposed in Figure 4.17(c) corresponds to the same empirical formula as the structures previously discussed, where the major difference is the replacement of the methyl ether terminal group with a hydroxyl terminal group. The presence of copolymers with different terminal groups is not a new concept, and the presence of functionality type distributions is common in MS of polymers.[16] It would not have been possible to determine the presence of this structural isomer had it not been for the extensive dissociation caused by EID, and the high resolving power and the accurate and precise mass measurement of the FTICR mass analyser. One approach that may be able to separate these molecules with the same nominal mass would be the incorporation of ion-mobility separation, as these molecules may adopt different gas phase conformations, and consequently IMS would be able to separate based on this physical property. A second method that would allow separation of the structural isomer shown in Figure 4.17(c) from Figure 4.17(a) and Figure 4.17(b) would be the use of H/D exchange experiments. Deuterium would replace the exchangeable hydrogen of the hydroxyl group, giving a change in the *m/z* of the precursor ion, which may allow isolation of this specific isomer, where tandem MS could provide conclusive structural information for the presence of a copolymer with the proposed structure.

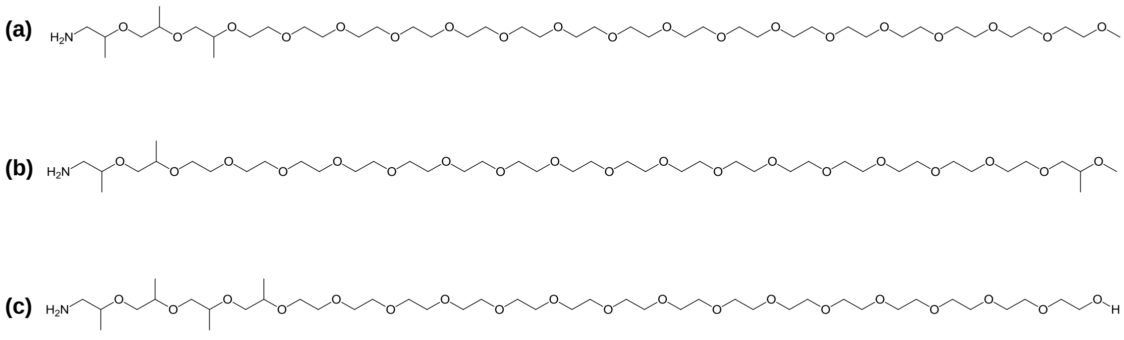

Figure 4.17 Proposed structural isomers for the precursor ion.

4.2.2. Tandem MS of a random copolymer

Miladinovic *et al.* demonstrated that CID tandem MS could be used to differentiate random and block copolymers of methyl methacrylate and butyl methacrylate. The authors reported that specific neutral losses were indicative of a block copolymer structure, as one block was preferentially cleaved over the other. The corresponding random copolymer did not generate the defined series of peaks, where product ions were distributed randomly over the detectable mass range.[160] Given the success of the electron-based fragmentation techniques for the analysis of block copolymers containing EG and PG units, it was of interest to examine a random copolymer made up of the same constituent molecules. Full MS analysis of EG-ran-PG copolymer (M_n = 2500) generated the mass spectrum shown in Figure 4.18.

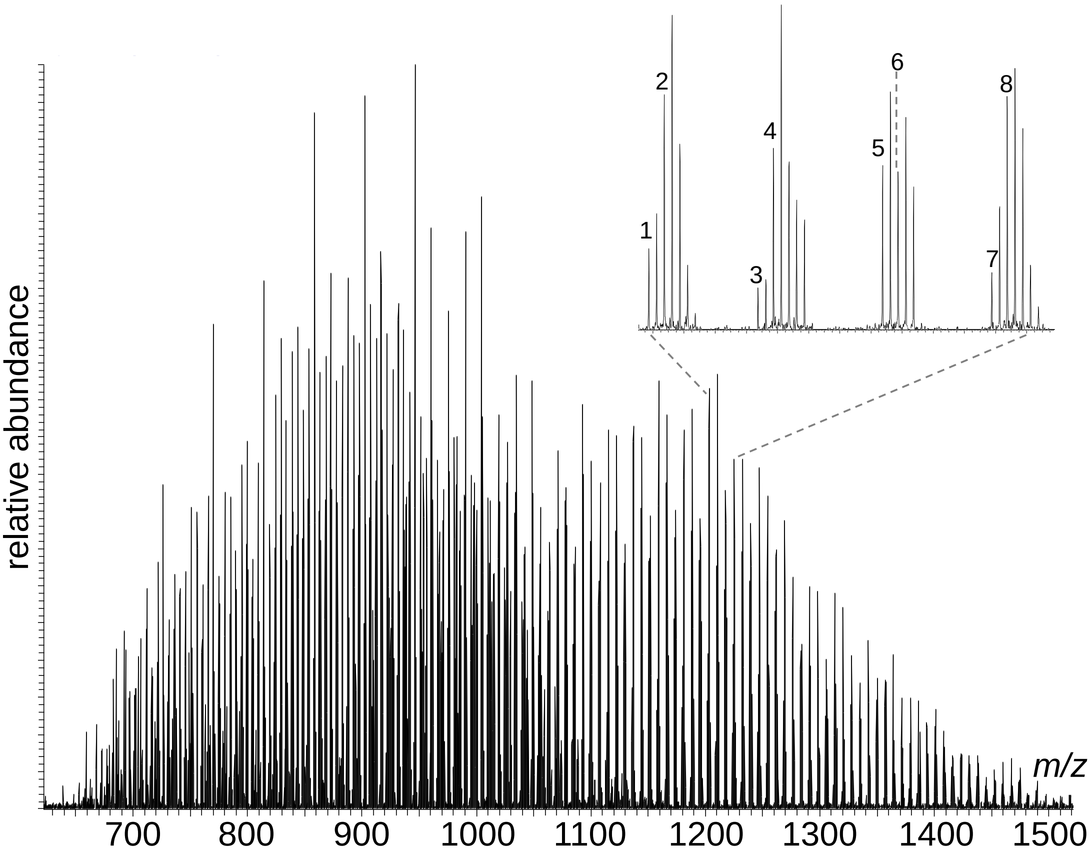

Figure 4.18 ESI Full MS of EG-ran-PG copolymer.

Table 4.1 Empirical formula and proposed block ratios for molecular ions *m/z* 1200 – 1225, inset in Figure 4.18.

Assignment	*m/z*	Empirical Formula	Monomer Ratios
1	1201.74113	$C_{111}H_{224}O_{50}Na_2$	$HO(C_3H_6O)_{13}(C_2H_4O)_{36}H + 2Na$
2	1202.72786	$C_{110}H_{222}O_{51}Na_2$	$HO(C_3H_6O)_{10}(C_2H_4O)_{40}H + 2Na$
3	1208.74510	$C_{112}H_{226}O_{52}Na_2$	$HO(C_3H_6O)_{14}(C_2H_4O)_{35}H + 2Na$
4	1210.73863	$C_{111}H_{224}O_{51}Na_2$	$HO(C_3H_6O)_{11}(C_2H_4O)_{39}H + 2Na$
5	1216.74624	$C_{112}H_{226}O_{51}Na_2$	$HO(C_3H_6O)_{12}(C_2H_4O)_{38}H + 2Na$
6	1217.73334	$C_{111}H_{224}O_{52}Na_2$	$HO(C_3H_6O)_9(C_2H_4O)_{42}H + 2Na$
7	1223.75349	$C_{113}H_{228}O_{51}Na_2$	$HO(C_3H_6O)_{13}(C_2H_4O)_{37}H + 2Na$
8	1224.74269	$C_{112}H_{226}O_{52}Na_2$	$HO(C_3H_6O)_{10}(C_2H_4O)_{41}H + 2Na$

As it was not possible to obtain a random copolymer whose M_n was within the observable *m/z* range, it was necessary to generate multiply charged species for PEG-ran-PPG (M_n = 2500), as shown in Figure 4.18. ESI MS of PEG-ran-PPG generates two molecular weight distributions that correspond to the doubly and triply charged molecular ions respectively, which adds a degree of complexity. The accurate and precise mass measurement of the FTICR gave empirical formulae for the doubly charged ions, shown inset in Figure 4.18. Despite the overlap of isotopic profiles, the empirical formulae allowed ratios of the different monomers to be proposed for each ion, which are summarised in Table 4.1. To investigate the impact of electron-based fragmentation techniques upon the dissociation of a random copolymer, a doubly charged precursor ion was selected at *m/z* 1210.73863 that gave an empirical formula of $C_{111}H_{224}O_{51}Na$.

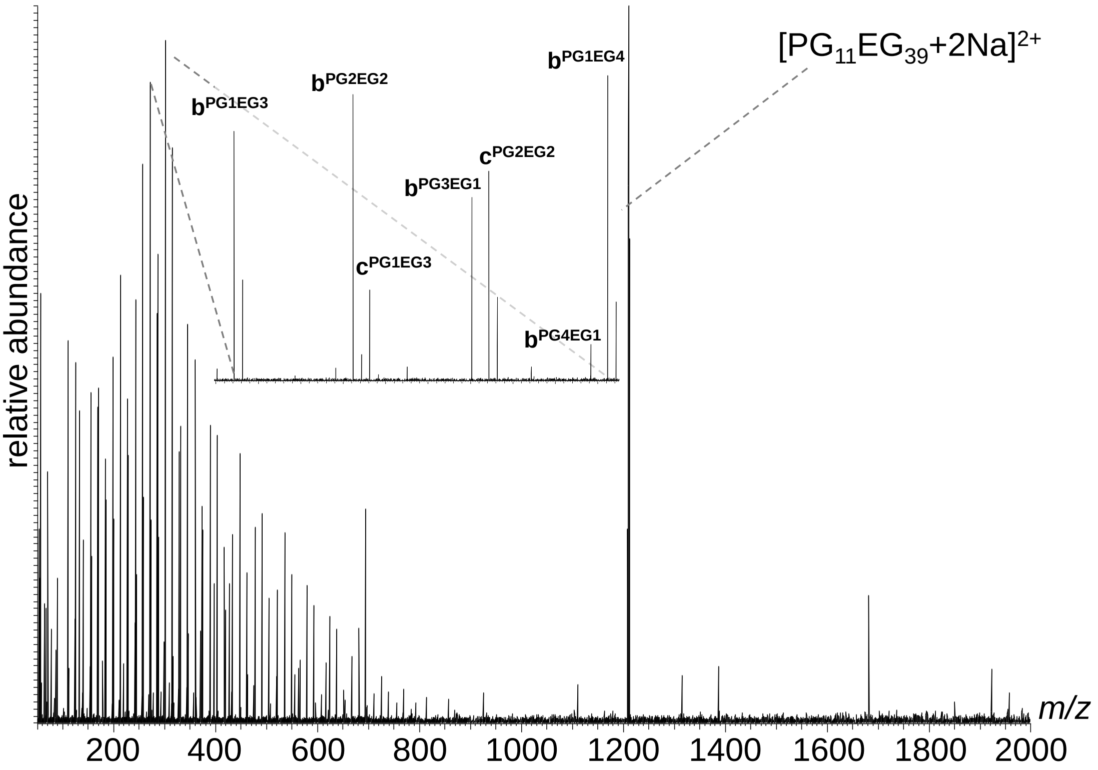

Figure 4.19 HECD (22.1 eV) tandem MS of $[HO(C_3H_6O)_{11}\text{-ran-}(C_2H_4O)_{39}H + 2Na]^{2+}$.

HECD tandem MS of this ion gave a very different product ion spectrum to that observed for the block copolymers analysed previously in Sections 4.2.1.1 - 4.2.1.4. For this copolymer containing two different monomers, there are theoretically $1.12e^{15}$ different monomer combinations that can yield a precursor ion of this nominal mass. It is therefore not surprising that the product ion spectrum is complex. The difference in the shape and the lack of defined product ion series allows facile differentiation of this random copolymer from the block-copolymers analysed previously. Despite the lack of product ions series, accurate and precise mass measurement in the FTICR cell can be used to provide empirical formula that allows the composition of product ions to be determined, as shown inset in Figure 4.19. For this 50 Da section of the mass range, there are a large number of peaks that correspond to different monomer combinations. Although the bond broken can be determined and assigned using the existing nomenclature, and the composition in terms of EG and PG units can be calculated, determination of the structure of each product ion is not possible. However, the lack of obvious repeat ion series and systematic product ion peaks at 12-16 Da intervals allows the simple distinction of copolymers with block and random structures.

4.2.3. Tandem MS of an alternating copolymer

Tandem mass spectrometry has proven to be an effective tool for copolymer characterisation, as it can differentiate block and random copolymers and provide evidence of different structural isomers of a precursor ion. To expand the application of tandem mass spectrometry a synthetic copolymer comprising butadiene (BD) and diphenylethylene (DP) monomers was investigated. This copolymer synthesised by anionic polymerisation at Durham University and was proposed to have an alternating copolymer structure, as DP cannot homopolymerise. It was therefore of interest to determine whether tandem mass spectrometry could provide evidence supporting the proposed structure. ESI-MS analysis of this copolymer doped with silver generated the mass spectrum shown in Figure 4.20.

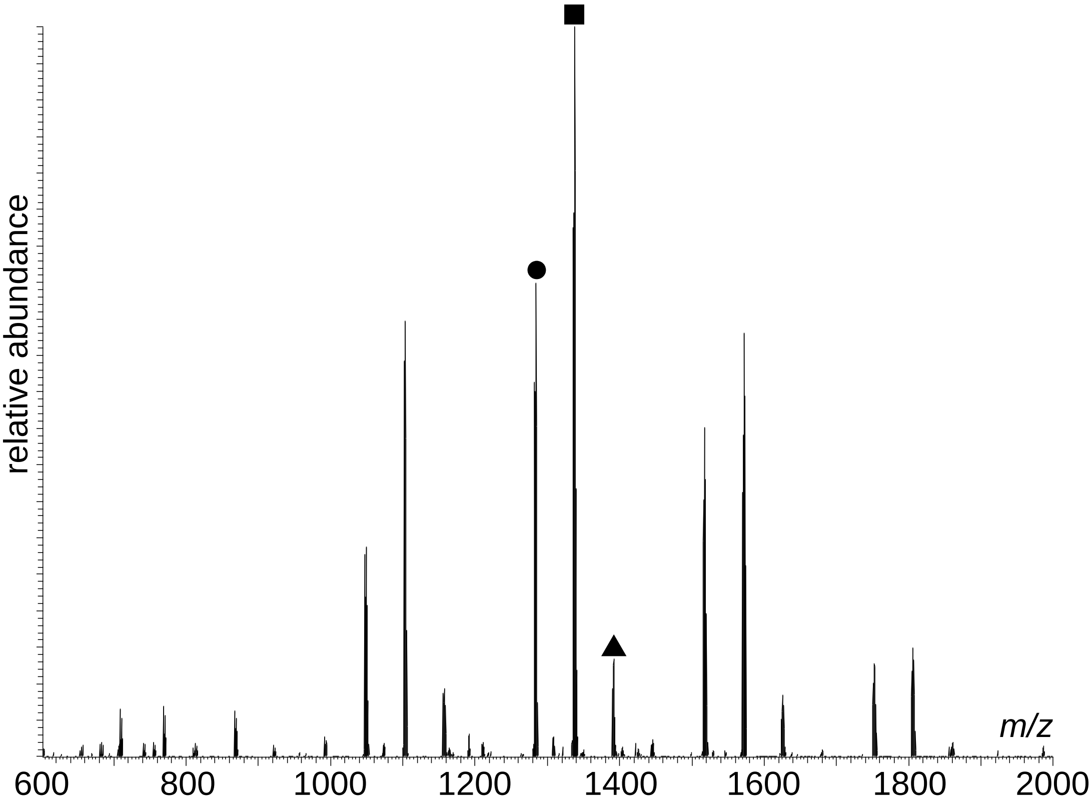

Figure 4.20 ESI Full MS of BD-alt-DPE: (●) =$[C_4H_9(BD)_{n-1}(DP)_nH + Ag]^+$, (■) =$[C_4H_9(BD)_n(DP)_nH + Ag]^+$ and (▲) = $[C_4H_9(BD)_{n+1}(DP)_nH + Ag]^+$.

From Figure 4.20, it is possible to identify 3 repeat series of peaks, where the peaks in each series are separated by 234 Da, the cumulative mass of BD and DP repeat units ($C_{18}H_{18}$). The ion series labelled (●) are found to have a general formula of **$[C_4H_9(BD)_{n-1}(DP)_nH + Ag]^+$**. The subsequent ion series (■) and (▲) correspond to the general formula **$[C_4H_9(BD)_n(DP)_nH + Ag]^+$** and **$[C_4H_9(BD)_{n+1}(DP)_nH + Ag]^+$** respectively. The highlighted series of peaks contain different 5

DP monomer units with an increasing number of BD monomers. As this monomer composition can only create an alternating copolymer, the ratios of monomers observed would suggest that initiation with butyl lithium can occur with either monomer. Establishing a fragmentation nomenclature for an alternating copolymer with multiple potential structures can result in numerous assignments for a single product ion peak. Therefore, the empirical formulae of the observed product ions have been tabulated, and are related directly to potential bond cleavages in the proposed structures, which are included inset in each spectrum.

4.2.3.1. Tandem MS of $[C_4H_9(C_4H_6)_4$ -alt- $(C_{14}H_{12})_5H + Ag]^+$

Isolation of *m/z* 1281.64047, a peak in the (●) series of peaks containing 5 DP units and 4 BD units, was subsequently activated using CID and EID, which generated the product ion spectra shown in Figure 4.21.

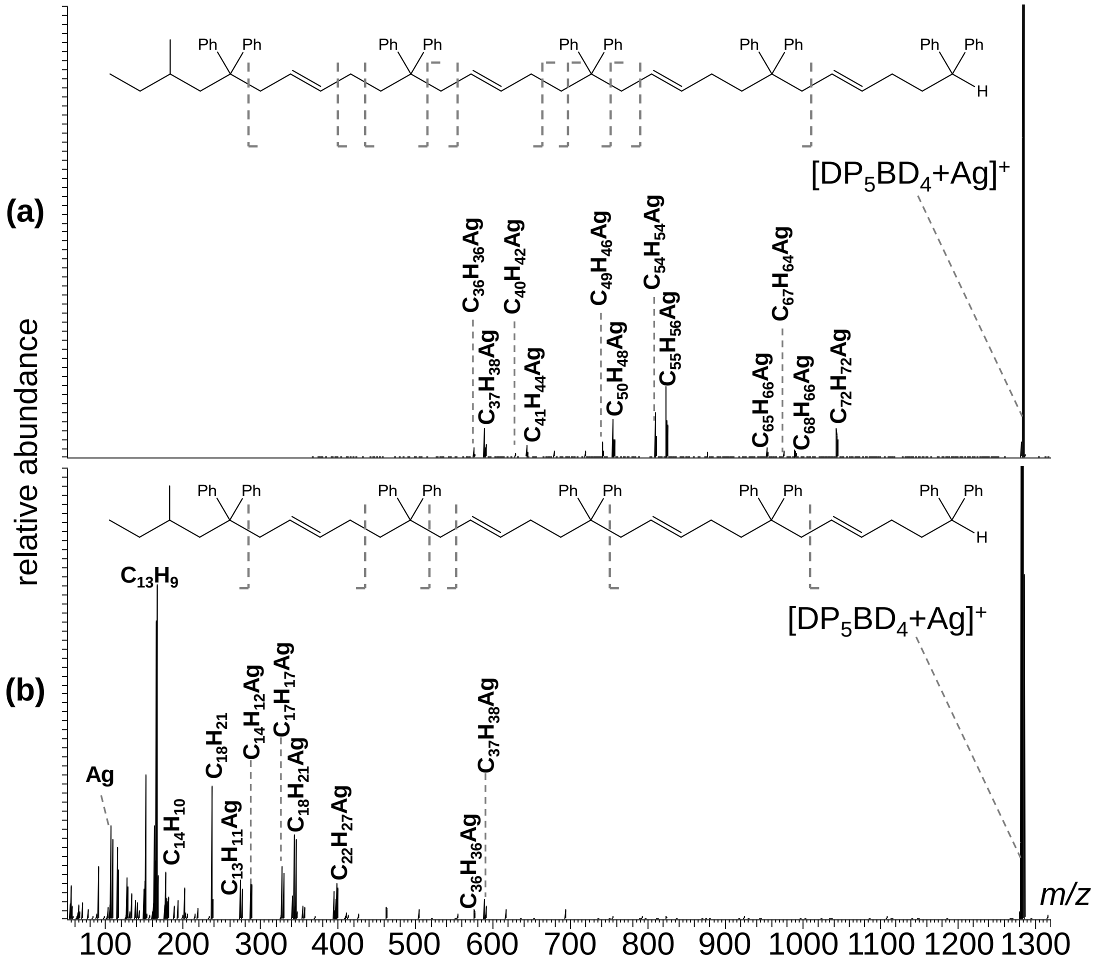

Figure 4.21 Tandem MS of $[C_4H_9(C_{14}H_{12})_5(C_4H_6)_4H + Ag]$+ (a) CID 20 V and (b) EID 18.1 eV.

LTQ-CID of the silver containing precursor ion was found to generate product ions that would suggest an alternating structure, as shown in Figure 4.21(a). The observed product ions confirm the presence of both linear terminal groups, with product ions containing each end group individually. The difference between each peak in a product ion series is 234 Da, the cumulative mass of BD and DP units. In contrast, EID provides relatively low sequence coverage, with the majority of ions found below *m/z* 600, as shown in Figure 4.21(b). A number of these ions correspond to individual monomer units, terminal groups and the raw metal cation. It is also noted that, unlike CID, a number of these ions are formed without the original silver charge carrier, as demonstrated by the empirical formulae of the product ions labelled in Figure 4.21(b). This may be due to the fact that silver was required to ionise the sample effectively. Previous tandem MS analysis of silver containing precursor ions has generated mixed results in comparison with alkali metals, and the charge carrier may be responsible for the limited polymer dissociation. Despite this, the product ions that are observed do support the proposed alternating structure. Combination of the results observed by both tandem MS techniques demonstrate that the techniques provide complementary information, where the combined product ions generated by both techniques provide enhanced sequence coverage.

4.2.3.2. Tandem MS of $[C_4H_9(C_{14}H_{12})_5\text{-alt-}(C_4H_6)_5H + Ag]^+$

The situation is more complex when the precursor ion labelled (■) in Figure 4.20 is analysed in tandem MS experiments. One peak from this series at *m/z* 1335.68733 corresponds to a structure containing both terminal groups, 5 BD units, 5 DP units and a silver cation. Unfortunately, the presence of equal numbers of each repeat unit results in the possibility of two structural isomers, whose formation is dependent upon which monomer is initiated by butyl lithium. LTQ-CID tandem MS analysis of this precursor ion generates the product ion spectrum shown in Figure 4.22. The observed product ions support the alternating copolymer structure with repeat product ion series separated by 234 Da. The majority of the product ions correspond to an ambiguous empirical formula that can be rationalised by bond cleavage in both proposed structures. Despite this observation, it is possible to identify product ion peaks that represent unique bond cleavages in a specific structure, as shown by the black bond cleavage markers on the structures shown inset in Figure 4.22. The presence of unique peaks observed for both structures provide evidence of both structural isomers for the isolated precursor ion. In contrast, EID analysis generated fewer product ions than low energy CID, however the product ions observed confirm the presence of an alternating copolymer. Again, there are product ions that can be generated from both structural isomers; however there are product ions that are unique to each structure, labelled black on the inset structures in Figure 4.23.

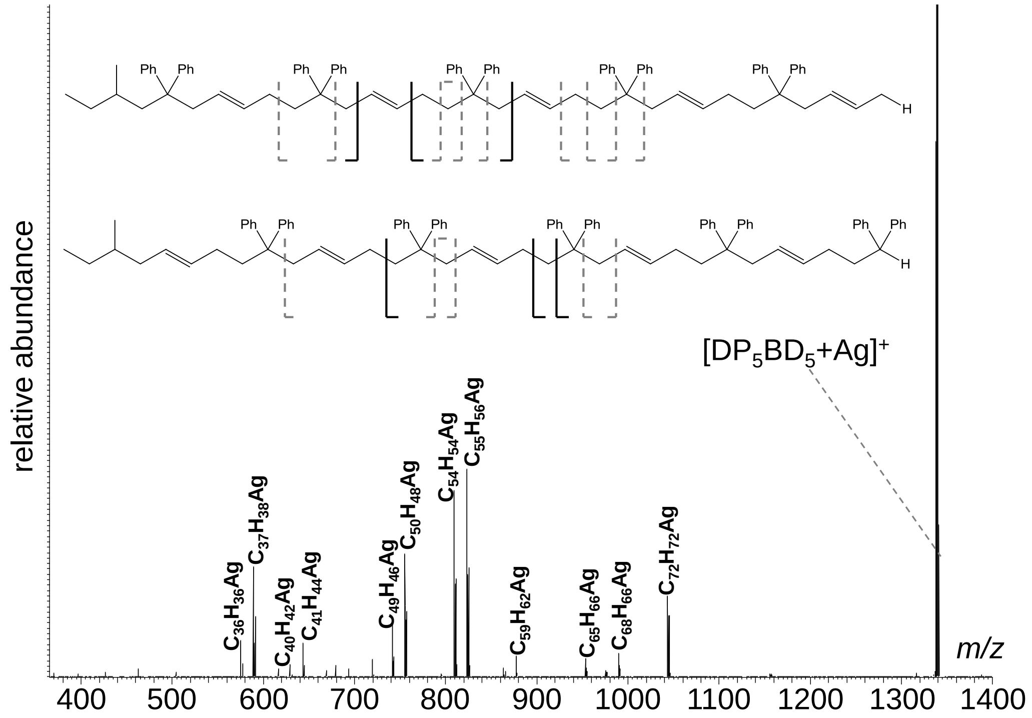

Figure 4.22 CID tandem MS of [$C_4H_9(C_{14}H_{12})_5(C_4H_6)_5H$ + Ag]$^+$ and assignments to the proposed structures.

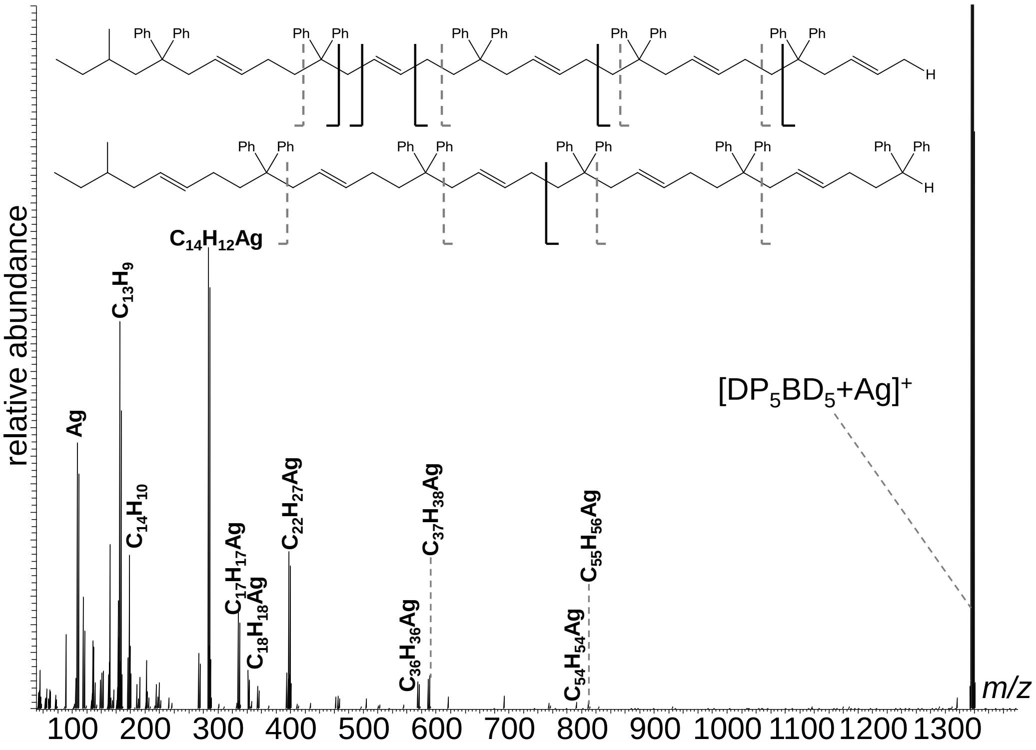

Figure 4.23 EID tandem MS of [$C_4H_9(C_{14}H_{12})_5(C_4H_6)_5H$ + Ag]$^+$ and assignments to the proposed structures.

5. RAFT polymerisation

5.1. Introduction

For the synthetic polymer chemist, there are a diverse range of strategies to create synthetic polymers and copolymers. These can be largely classified into two subsections, step growth polymers and chain growth polymers. Polymers formed by step-growth polymerisation are obtained by intermolecular condensation or addition reactions of reactive groups on multi-functional monomers. Chain growth polymers utilise active initiators to induce rapid chain growth through sequential monomer addition that produces a new active centre. Initiators can typically be anionic, cationic or free radical. Conventional free radical polymerisations are difficult to control, because of numerous fast irreversible termination and chain transfer reactions that occur. The effect of these reactions is a broad molecular weight distribution, and lower than expected molecular weights.[253] The development of controlled radical polymerisation methods has provided reactions that generate well-defined polymers of low polydispersity. This includes Atom Transfer Radical Polymerisation (ATRP), Nitroxide Mediated Polymerisation (NMP) and Reversible Addition-Fragmentation chain Transfer (RAFT). Unlike ATRP and NMP, RAFT relies on a degenerative chain transfer process to establish control, rather than the persistent radical effect employed in ATRP and NMP.[254] Control of the polymerisation is achieved through the minimisation of radical-radical termination reactions, through the reversible trapping of the growing polymeric radical as a dormant species. In the RAFT polymerisation process, dithioester and trithioester compounds are used to form the dormant species, where the propagating radical adds to the thiocarbonyl centre of the thioester to produce an intermediate carbon-centred radical, as shown in Scheme 5.1. This RAFT-adduct radical can undergo subsequent β–scission to form either the propagating radical or liberate a new carbon-centred radical, referred to as the leaving group in Scheme 5.1.

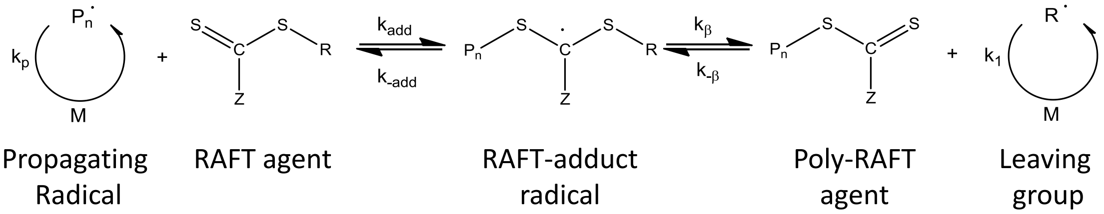

Scheme 5.1 The RAFT polymerisation process.

The R group of the RAFT agent is chosen on the basis that it undergoes β –scission preferentially to the propagating radical, but is capable of re-initiating the polymerisation process.[254] This ensures that the radical intermediate quickly forms the dormant species, where an equilibrium is established where $k_{add} = k_{\beta}$ and $k_{-add} = k_{-\beta}$. Control of the reaction is achieved through a delicate balance of these rates, to achieve conditions where the concentration of the dormant species is orders of magnitude greater than the active species. The Z group controls the addition and fragmentation steps through effective stabilisation of the radical intermediate. The Z and R groups are optimised for each RAFT polymerisation, as no one RAFT agent is universally applicable to all monomers. The detection of RAFT agents as chain end functionalities is common in mass spectrometry.[255-257] It is therefore of interest to investigate the dissociation chemistry associated with such molecules before analysing them as components of synthetic polymers. As the RAFT agents are involved in a radical driven process, activation using electron based fragmentation techniques such as EID are of significant interest.

5.2. MS of 4-Cyano-4-(phenylcarbonothioylthio) pentanoic acid (CPADB)

4-Cyano-4-(phenylcarbonothioylthio) pentanoic acid (CPADB), a dithioester RAFT agent incorporating both aromatic and aliphatic functional groups, was selected for initial experiments. The aliphatic R group, 4-cyano pentanoic acid, contains nitrogen and oxygen heteroatoms that represent potential locations for charge carrier coordination. The ESI-MS spectrum shown in Figure 5.1 contains 3 peaks relating to CPADB. The first peak, at *m/z* 280.04463, gave an empirical formula of $C_{13}H_{14}NO_2S_2$, which corresponds to a protonated molecular ion. At *m/z* 302.02910, a second peak gave an empirical formula of $C_{13}H_{13}NO_2S_2Na$, which represents **[CPADB + Na]**$^+$. The third peak, at *m/z* 318.00237, gave an empirical formula of $C_{13}H_{13}NO_2S_2K$, which is corresponds to **[CPADB + K]**$^+$.

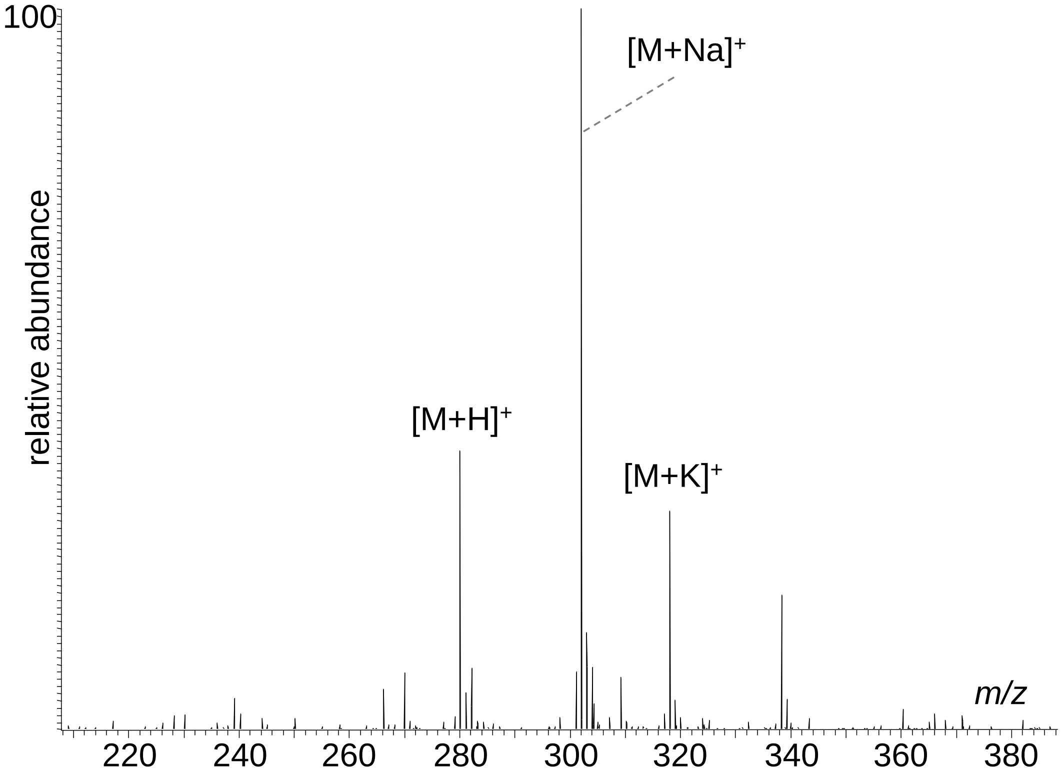

Figure 5.1 ESI MS of CPADB.

5.2.1. Tandem MS of $[CPADB + H]^+$

To maximise the amount of structural information that could be obtained by tandem MS experiments, three dissociation techniques were employed. Alongside CID and EID there was the opportunity to explore IRMPD of this compound. This would allow a comparison of the amount of structural information that each dissociation technique could provide for the same precursor ion.

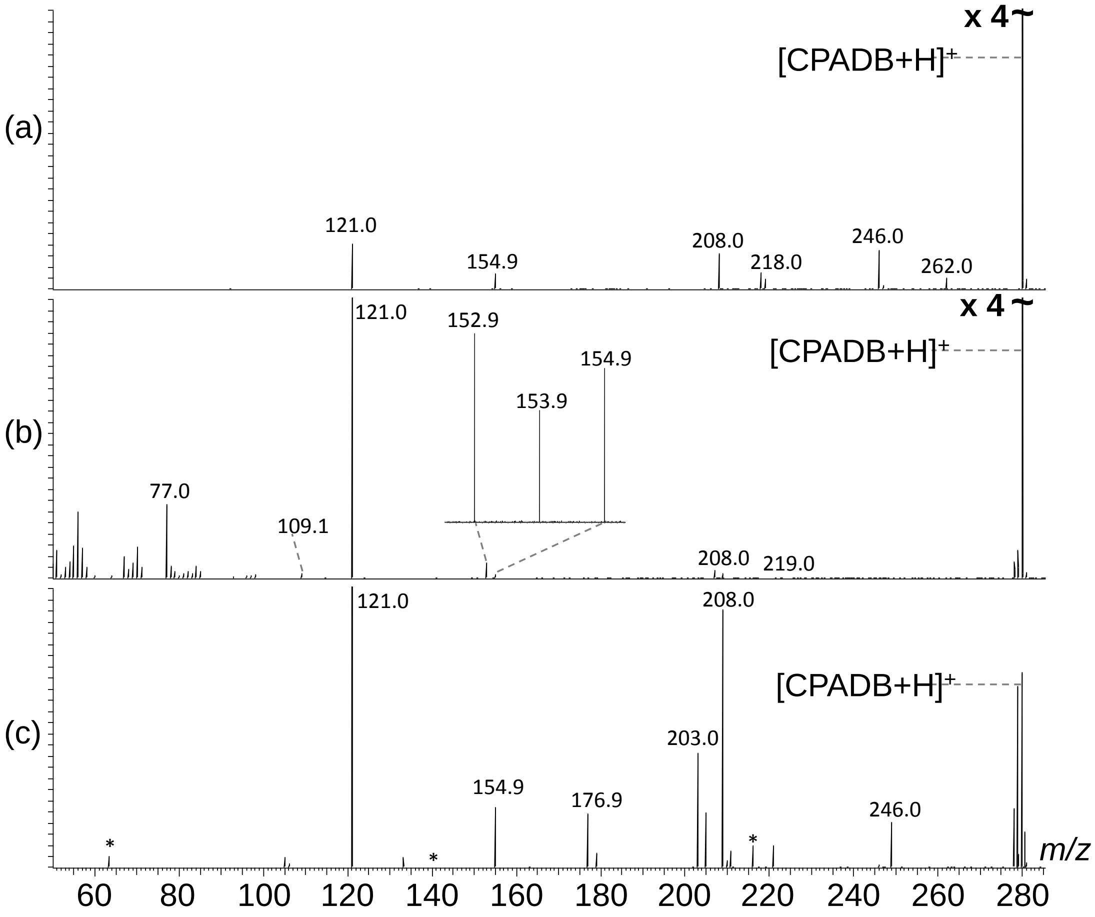

Figure 5.2 Tandem MS of $[CPADB + H]^+$ (a) CID 30 V, (b) EID 22.1 eV and (c) IRMPD.

For all tandem MS techniques investigated, structurally significant product ions were obtained, as summarised in Table 5.1. Accurate mass analysis of these peaks provided an empirical formula that facilitated the identification of likely cleavage site as shown in Table 5.1. All but one product ion observed during tandem MS of **$[CPADB + H]^+$** contained the aromatic phenyl group. This would suggest that one likely location for the proton is close to the phenyl group, where the electron cloud can effectively stabilise the proton.

Table 5.1 Summary of product ions generated from tandem MS of $[CPADB + H]^+$.

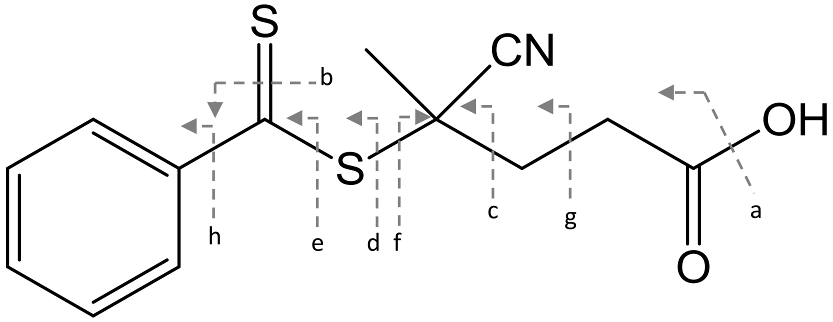

m/z	Empirical Formula	Accuracy/ppm	Proposed Bond Cleavage
280.04952	$C_{13}H_{14}NO_2S_2$	-0.5	N/A
262.35420	$C_{13}H_{12}NOS_2$	-0.2	a
246.05826	$C_{13}H_{12}NO_2S$	-0.3	b
219.01262	$C_{11}H_9NS_2$	-2.0	g
218.06431	$C_{12}H_{12}NOS$	-2.5	ab
208.02492	$C_{10}H_{10}NS_2$	0.1	c
154.99865	$C_7H_7S_2$	-0.1	d
153.99088	$C_7H_6S_2$	-1.4	d
152.98304	$C_7H_5S_2$	1.5	d
121.01660	C_7H_5S	-0.4	e
109.05239	C_6H_7NO	-3.4	af
77.03868	C_6H_5	1.3	h

As LTQ-CID and IRMPD are fragmentation techniques that increase the vibrational energy of the molecule, typically resulting in cleavage of the lowest energy bonds, the formation of product ions with the same nominal mass and empirical formula was a likely result. It is noted that the S/N ratio of the product ion peaks vary significantly between CID and IRMPD in Figure 5.2(a) and Figure 5.2(c) and this is likely to be the result of the different experimental approaches used, where LTQ-CID was performed until the observation of product ions, whereas IRMPD was performed until the precursor ion was no longer the spectrum base peak. In contrast, the spectrum obtained from EID demonstrates some significant differences from those obtained by CID and IRMPD as shown in Figure 5.2 Alongside the product ions at *m/z* 208.0 and 121.0 observed by CID and IRMPD, EID generated a number of a unique product ion peaks. In the region, *m/z* 152.9-154.9 (expansion shown inset in Figure 5.2(b)), three peaks were detected that correspond to dissociation of the bond labelled **d**, where the resultant product ions contain different numbers of hydrogen atoms. Accurate mass analysis of *m/z* 154.99865 gives an empirical formula of $C_7H_7S_2$, which would correspond to a protonated product ion with a hydrogen atom attached to the singly bonded sulphur atom. The corresponding peaks at *m/z* 153.99088 and 152.98304 contain one and two hydrogen atoms less respectively, and are proposed to represent the same product ion minus a hydrogen radical and H_2 respectively. This is an unusual observation as EID has generated both odd and even electron species from the same bond cleavage, including C_7H_5S, which indicates direct charge transfer to the CPADB molecule. Additionally, a product ion unique to EID is observed at *m/z* 77.03868, the empirical formula of this ion is C_6H_5, which corresponds to cleavage **h** in Table 5.1. This ion is believed to be an odd electron radical cation species that does not retain the proton charge carrier, indicating charge transfer to the molecule has occurred.

Based upon the product ions observed using CID, IRMPD and EID, it is clear that the combined results of all dissociation experiments provide significantly more structural information than any one technique, demonstrating the complementary nature of the different tandem MS approaches.

5.2.2. Tandem MS of [CPADB + Na]$^+$

The molecular ion at *m/z* 302.02870 corresponding to **[CPADB + Na]$^+$** was analysed by CID, EID and IRMPD as shown in Figure 5.3.

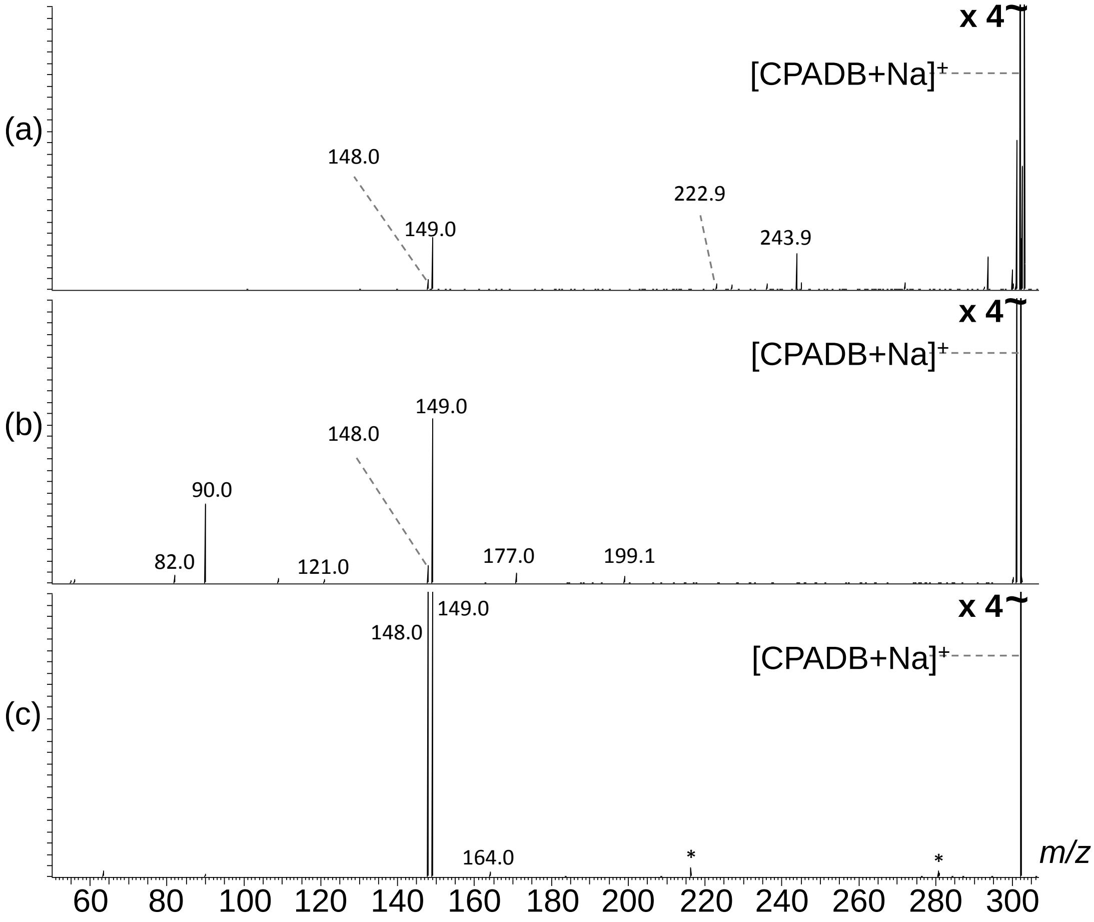

Figure 5.3 Tandem MS of [CPADB + Na]$^+$ (a) CID 30 V, (b) EID 27.1 eV and (c) IRMPD (peaks labelled * correspond to chemical noise established using IRMPD in the absence of sample.

Table 5.2 Summary of product ions generated from tandem MS of [CPADB + Na]$^+$ and proposed bond cleavages.

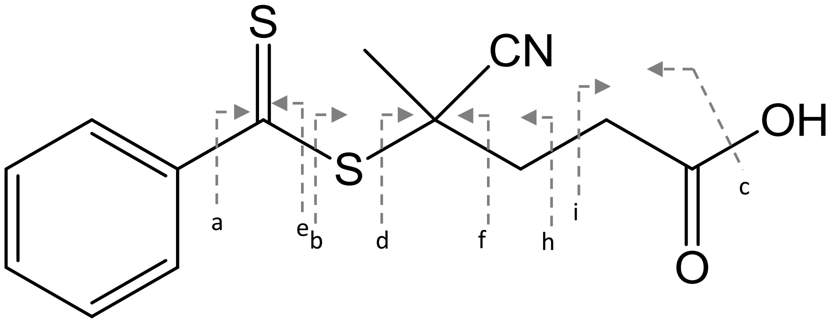

m/z	Empirical Formula	Accuracy/ppm	Proposed Bond Cleavage
302.02910	$C_{13}H_{13}NO_2S_2Na$	3.7	N/A
222.96742	$C_7H_6NO_2S_2Na$	3.3	a
164.01421	C_6H_7NOSNa	-2.4	bc
149.04506	$C_6H_8NO_2Na$	2.2	d
148.03722	$C_6H_7NO_2Na$	2.2	d
121.01086	C_7H_5S	-2.8	e
108.99584	C_3H_4NSNa	1.6	bf
90.03155	C_4H_5NNa	1.4	dh
82.00264	$C_2H_3O_2Na$	1.4	i

From the spectra observed in Figure 5.3, analysis of **[CPADB + Na]$^+$** generated fewer structurally significant product ions than the equivalent **[CPADB + H]$^+$** experiment (Figure 5.2(a) - Figure 5.2(c)). LTQ-CID, EID and IRMPD (Figure 5.3(a) - Figure 5.3 (c)) generated two intense product ion peaks at *m/z* 148.03722 and 149.04056, which gave empirical formulae of $C_6H_7NO_2Na$ and $C_6H_8NO_2Na$ respectively. Structural assignment for these empirical formulae correspond to the 4-cyano pentanoic acid section of the molecule, where the product ions are generated through dissociation of the bond labelled **d** in Table 5.2. The presence of product ions containing the 4-cyano pentanoic acid functionality provides complementary information to the product ions observed during tandem MS of **[CPADB + H]$^+$**, which predominantly formed ions corresponding to the dithiobenzoate part of the molecule. This demonstrates that by changing the charge carrier, dissociation of the molecule using the same activation methods has resulted in the formation of complementary product ions. A proposed reason for this observation is that the location of the charge carrying species within the molecule is different for each of the precursor ions. It would appear that the sodium cation is more effectively coordinated on the 4-cyanopentanoic acid portion of the molecule (aliphatic), where the proton is more effectively coordinated on the dithiobenzoate functionality (aromatic).

When LTQ-CID and IRMPD product ion spectra are compared, noticeable differences can be seen between them, with each showing unique peaks that contribute structural information. LTQ-CID of **[CPADB + Na]$^+$** resulted in a peak at *m/z* 222.9 that corresponds to dissociation of the bond labelled **a** in Table 5.2. The product ion peak at *m/z* 222.9 combined with the peak at *m/z* 77.0 detected during EID of **[CPADB + H]$^+$** (Figure 5.2(b)) provide structural information for reciprocal parts of the CPADB molecule. This demonstrates the complementary nature that a change in the charge carrier can have. IRMPD, (Figure 5.3(c)), contains a unique product ion peak at *m/z* 164.01421, which represents an internal fragment corresponding to cleavage of bonds labelled **bc** in Table 5.2.

EID tandem MS of **[CPADB + Na]$^+$** generated five structurally useful product ions, as shown in Figure 5.3(b). Alongside the peaks at *m/z* 149.04506 and 148.03722 following cleavage at **d**, EID also generated internal fragments resulting from multiple bond cleavages. These product ion peaks at *m/z* 108.99584 and 90.03155 correspond to bond cleavages **df** and **dh** respectively (Table 5.2). In addition, EID generated a product ion whose empirical formula, $C_2H_3O_2Na$, corresponds to the carboxylic acid group following dissociation at **i** in Table 5.2.

This investigation demonstrates that as well as the dissociation techniques providing complementary information to each other, it is also possible to generate complementary structural information for CPADB through manipulation of the charge carrier present, where the different locations for charge carrier coordination result in the formation of different product ions.

5.2.3. DFT calculations for CPADB

Tandem MS analysis of **[CPADB + H]$^+$** and **[CPADB + Na]$^+$** have demonstrated that the presence of different charge carriers results in very different product ion spectra. It was of interest to examine whether Density Functional Theory (DFT) calculations could provide support for the suggested charge carrier locations, based upon the experimentally observed product ions. Initially, a 3D model of the CPADB molecule was created using GaussView 4.1.2, and an optimisation and frequency calculation was run using the calculations outlined in Appendix 10.3. Following optimisation of the neutral structures, proton and sodium charge carriers were placed at locations around the CPADB molecule, where a second optimisation and frequency experiment generated potential structures where the charge carrier is most effectively coordinated to the molecule.

5.2.3.1. DFT for $[\text{CPADB} + \text{H}]^+$

From a series of optimisation and frequency calculations involving the addition of a proton charge carrier to the optimised CPADB structure, a number of gas phase conformations were observed. Two of the most common low energy conformations are presented in Figure 5.4, which demonstrate two possible locations for coordination of the proton charge carrier. The first structure in Figure 5.4(a) places the proton in close proximity to the thionyl sulphur atom, where the proton can be coordinated by the lone pairs of electrons of the sulphur atom. The calculated distance between the proton and the sulphur atom is 1.35044 Å. The second possible conformation (Figure 5.4(b)) places the proton in close proximity to the benzene ring, where stabilisation of the charge could be expected to involve interaction of the proton with the delocalised electron cloud. The interatomic bond distance between the proton and the closest carbon atom of the benzene ring is 1.10972 Å.

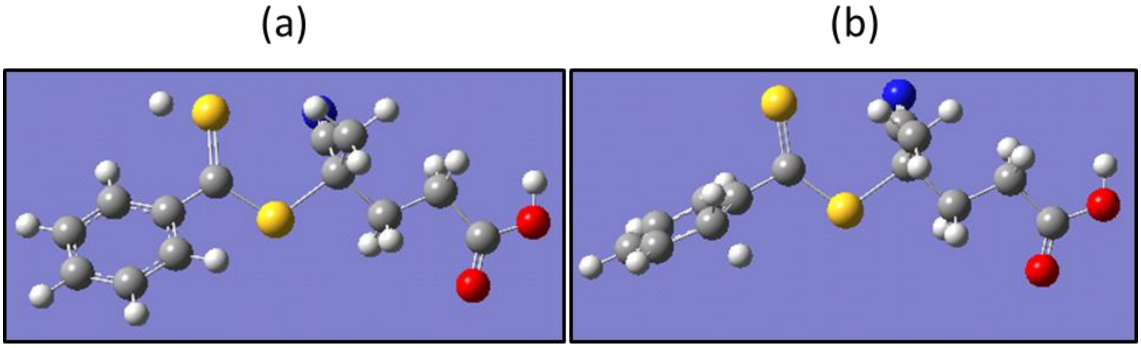

Figure 5.4 Lowest energy conformation generated by DFT for $[\text{CPADB} + \text{H}]^+$.

Tandem MS analysis of **$[\text{CPADB} + \text{H}]^+$** generated product ions at *m/z* 208.0 and *m/z* 154.9 which are examples of product ions that are believed to retain the proton as demonstrated in the structures proposed in Figure 5.5(a) and Figure 5.5(b) respectively. The proposed coordination sites for proton attachment in the DFT calculations can account for the formation of both of the product ions observed experimentally. This result supports the theory that the DFT calculations can be utilised as a predictive tool to identify potential coordination sites.

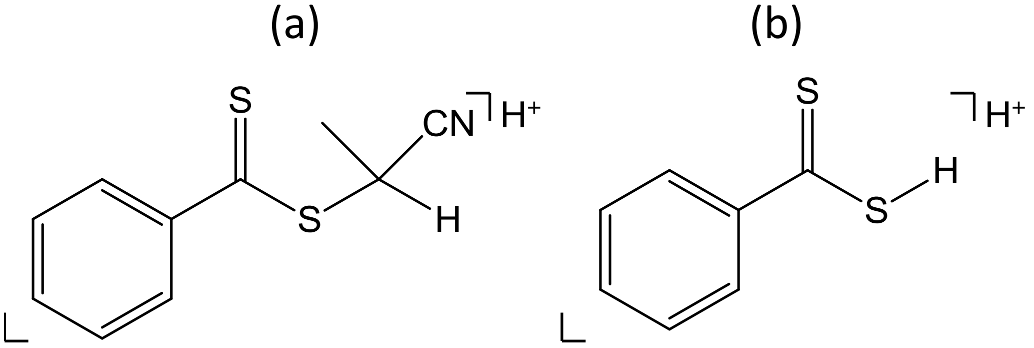

Figure 5.5 Potential structures for product ions (a) *m/z* 208.0 and (b) *m/z* 154.9.

5.2.3.2. DFT calculations for [CPADB + Na]$^+$

In the DFT calculation for **[CPADB + Na]$^+$**, two different low energy conformations were observed, as shown in Figure 5.6. The location of charge carrier coordination for **[CPADB + Na]$^+$** is different to that observed for **[CPADB + H]$^+$**, which reflects the results observed experimentally. In the first structure in Figure 5.6(a), the sodium is stabilised through coordination by electron lone pairs of the thionyl sulphur and the cyano nitrogen respectively. The interatomic distances in Figure 5.6(a) place the sodium 2.78802 Å from the sulphur atom and 2.30687 Å from the nitrogen atom of the cyano group. The nitrogen atom of the cyano group is shown to be important for sodium coordination, as it is involved in the second possible conformation shown in Figure 5.6(b). In this instance coordination does not involve the thionyl sulphur, but a third heteroatom coordination is observed from the carbonyl oxygen through a change in the conformation of the 4-cyanopentanoic acid unit. The structure is also found to have smaller interatomic bond distances, with the sodium 2.20744 Å from the cyano nitrogen atom and 2.28323 Å from carbonyl oxygen atom.

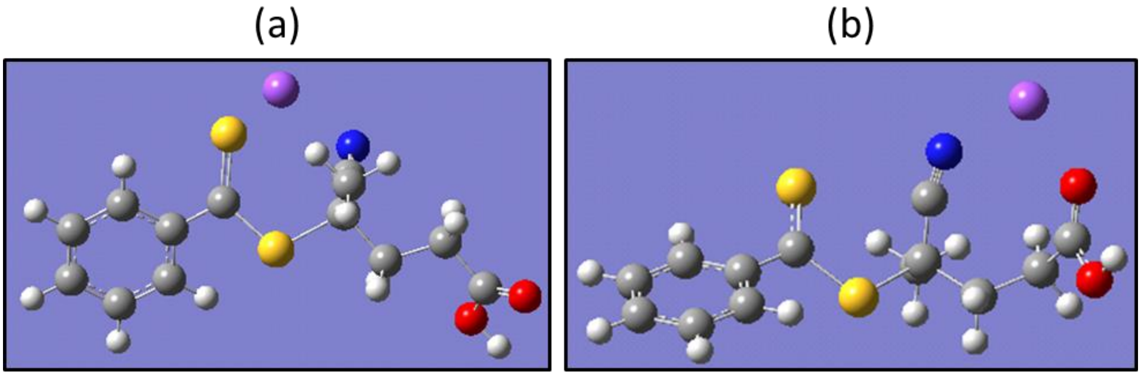

Figure 5.6 Lowest energy conformations generated by DFT for [CPADB + Na]$^+$.

The majority of product ions observed from the tandem MS of **[CPADB + Na]$^+$** involved dissociation within the dithioester functional group and the 4-cyanopentanoic acid section of the molecule, with retention of the sodium charge carrier. Of particular interest are the product ions at *m/z* 108.9, *m/z* 90.0 and *m/z* 82.0, which represent different regions of the 4-cyanopentanoic acid functionality and contain sodium, as shown in Figure 5.7. The product ions at *m/z* 108.9 and *m/z* 90.0, which may correspond to the structures outlined in Figure 5.7(a) and Figure 5.7(b) respectively, could be generated from either of the theoretically derived conformations as the cyano nitrogen coordinates to the metal in both instances. The third product ion at *m/z* 82.0, which corresponds to the carboxylic acid functionality, can only be formed in a facile manner from the conformation presented in Figure 5.6(b), where the carbonyl oxygen coordinates with the sodium cation. This suggests that the conformation presented in Figure 5.6(b) is a likely candidate for a precursor ion conformation prior to dissociation based upon the product ions observed. This does not discount the theoretical presence of the conformation presented in Figure 5.6(a), however confidence in this structure is limited as there are no product ions that can only be formed based on this conformation.

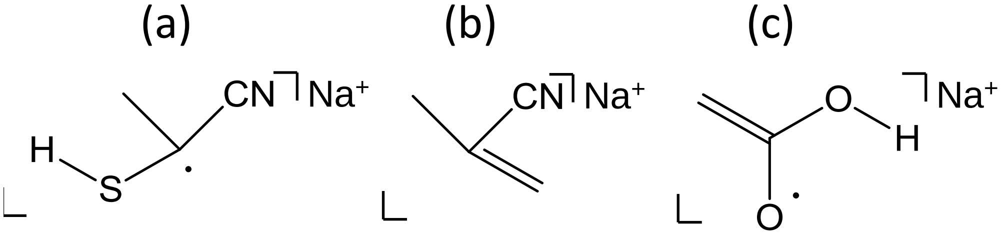

Figure 5.7 Potential structures for product ions (a) *m/z* 108.9, (b) *m/z* 90.1 and (c) *m/z* 82.0.

5.2.4. Fragmentation as a function of electron energy

EID analysis of **[CPADB + H]$^+$** and **[CPADB + Na]$^+$** generated a number of different product ions that are formed through cleavage of a range of bonds within the molecule. Given the variety of bonds and the associated bond energies, it was of interest to examine whether a correlation existed between bond dissociation energy and the energy of the incident electrons. **[CPADB + H]$^+$** and **[CPADB + Na]$^+$** were isolated individually, and an automated EID dissociation method that incrementally increased the energy of the electrons was utilised. To process the data, each individual energy level was extracted from the chromatogram and a spectrum was generated, averaging over the total scans for a given electron energy. The intensities of all peaks in the resultant spectra were recorded and converted to a percentage of total peak intensity. The results of the experiments for incremental electron energy EID of **[CPADB + H]$^+$** are displayed graphically in Figure 5.8. The black line in Figure 5.8 demonstrates that the percentage peak intensity represented by **[CPADB + H]$^+$** decreases with increasing electron energy. This correlates with an increase in product ions forming at the highest electron energy. The decrease in the percentage represented by the precursor ion corresponds almost directly to an increase in the peak intensity of a single product ion, the C_7H_5S ion. This product ion is generated through cleavage of the C-S bond, which based on standard bond enthalpies, is the weakest bond in the molecule (C-S, 259 kJ mol^{-1}), and is first observed at an electron energy of 8 eV. The second most intense product ion peak, C_6H_5, is generated through cleavage of the stronger C-C bond (348 kJ mol^{-1}) is not observed until the electron energy is increased to 15 eV. As the increase in electron energy results in the fragmentation of bonds with higher standard bond enthalpies, the results indicate that a correlation exists between the energy of the electrons and the average bond energies of the bonds present in the molecule.

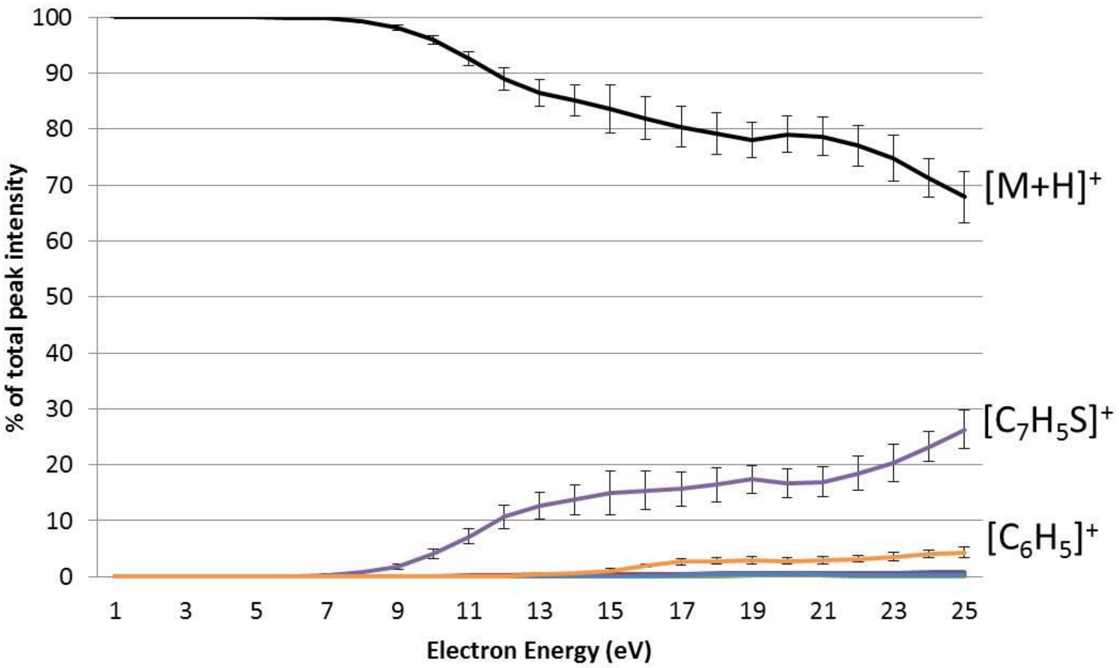

Figure 5.8 EID fragmentation of $[CPADB + H]^+$ as a function of electron energy (product ions $[C_7H_5S_2]^+$, $[C_7H_6S_2]^+$, $[C_7H_5S_2]^+$ and $[C_6H_5ON]^+$ represent < 1 % of total peak intensity and consequently have not been labelled).

The **$[CPADB + Na]^+$** precursor ion was isolated and analysed using the automated incremental EID approach. The processed results of these experiments are displayed graphically in Figure 5.9.

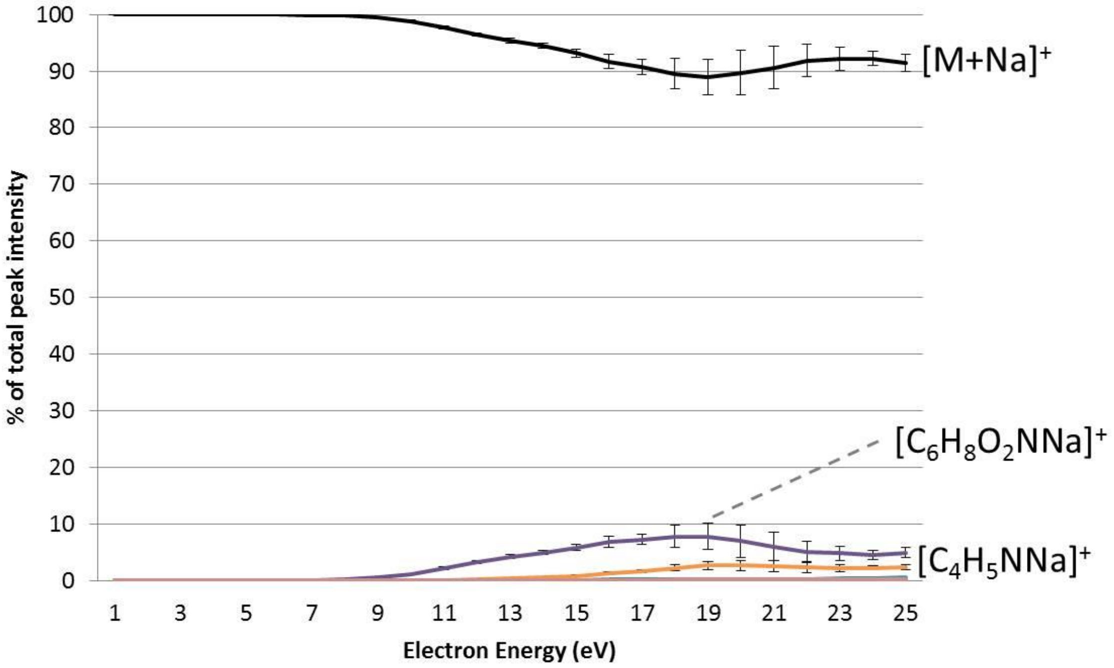

Figure 5.9 EID fragmentation of $[CPADB + Na]^+$ as a function of electron energy (product ions $[C_7H_5S]^+$, $[C_3H_4NSNa]^+$ and $[C_2H_3O_2Na]^+$ represent < 1 % of total peak intensity and consequently have not been labelled.

The efficiency of fragmentation for EID of **[CPADB + Na]**$^+$ is noticeably less than for the equivalent **[CPADB + H]**$^+$, as the percentage representing the intensity of the precursor ion peak does not drop below 88% of the total peak intensity. The profile of the percentage of total peak intensity of **[CPADB + Na]**$^+$ is somewhat different from the equivalent **[CPADB + H]**$^+$ species, as the percentage reaches a minimum at 18 eV, where upon the percentage increases once more. This would suggest that 18 eV represents optimal electron energy for fragmentation of **[CPADB + Na]**$^+$. The decrease in the percentage represented by the precursor ion peak corresponds almost exclusively with the formation of a single product ion, $C_6H_8O_2NNa$, which is first observed at an electron energy of 9 eV. As this product ion also results from cleavage of a C-S bond, the observation of the product ion at a similar electron energy to that observed previously for the major product ion of **[CPADB + H]**$^+$ would suggest that incident electrons with 8 eV – 9 eV of energy are required to dissociate a C-S bond. Additional evidence for this correlation is found in the presence of a second product ion, C_4H_5NNa, an internal fragment. This product is theoretically formed through cleavage of both C-S and C-C bonds, where the C-C bond is the stronger of the two. It is first observed at an electron energy of 15 eV, which is the same energy required to form the C_6H_5 product ion from **[CPADB + H]**$^+$, which also involves C-C bond cleavage.

5.2.5. Fragmentation as a function of EID irradiation time

It is well known that electron based fragmentation techniques such as ECD and EID have a low fragmentation efficiency compared to CID. One of the major issues with ECD and EID performed in an FTICR is the reliance upon effective overlap of the incident electrons with the ion cloud containing the precursor ions. This is one of the reasons to avoid overfilling of the FTICR, as space charge effects can perturb the ions motion from the centre of the cell, reducing the electron-ion overlap. It was of interest to examine the influence of the electron irradiation time on the extent of fragmentation. The electron irradiation time was subsequently increased at 50 ms intervals from 50 ms to 300 ms, with the energy of the electrons held constant. Once again, the peak intensities of all ions are calculated as a percentage of total peak intensity and averaged from three experiments. The resultant data for EID of **[CPADB + H]**$^+$, using incident electrons with 14.1 eV of energy as an example, is depicted graphically in Figure 5.10.

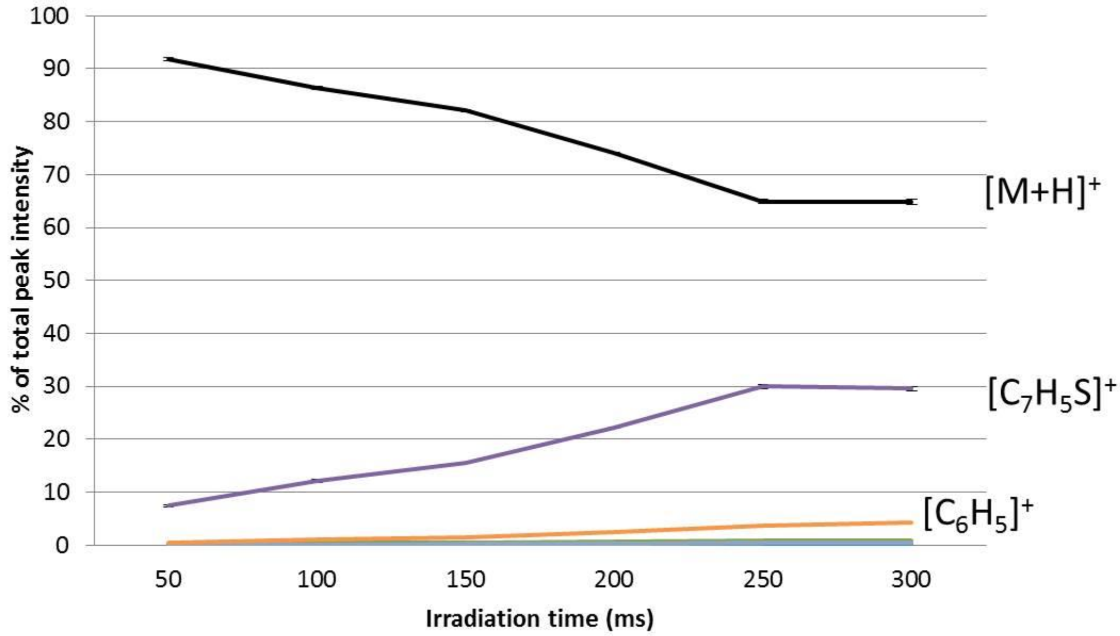

Figure 5.10 EID (14.1 eV) fragmentation of [CPADB + H]$^+$ as a function of electron irradiation time (product ions [$C_7H_5S_2$]$^+$, [$C_7H_6S_2$]$^+$, [$C_7H_5S_2$]$^+$ and [C_6H_5ON]$^+$ represent < 1 % of total peak intensity and consequently have not been labelled).

The general trend observed is that increasing the electron irradiation time results in a decrease in the percentage of total peak intensity represented by the precursor ion. This correlates with an increase in the percentage of total peak intensity for the major product ion, C_7H_5S. It can therefore be inferred that increasing the electron irradiation time leads to increased dissociation of the precursor ion, which is to be expected, as the increased irradiation time will result in more interactions between the precursor ions and the incident electrons.

A similar trend is observed when the duration experiment is performed on **[CPADB + Na]$^+$**, where the percentage of total peak intensity for the precursor ion peak decreases with increasing electron irradiation time. As shown in Figure 5.11, this correlates with an increase in the percentage peak intensity represented by the major product ion $C_6H_8O_2NNa$. This observed change in the percentage peak intensities provides evidence that supports an increase in the dissociation of the precursor ion with increasing electron irradiation time. It is noted that the change in percentage represented by the precursor ion peak is not as large for **[CPADB + Na]$^+$** as observed for **[CPADB + H]$^+$**.

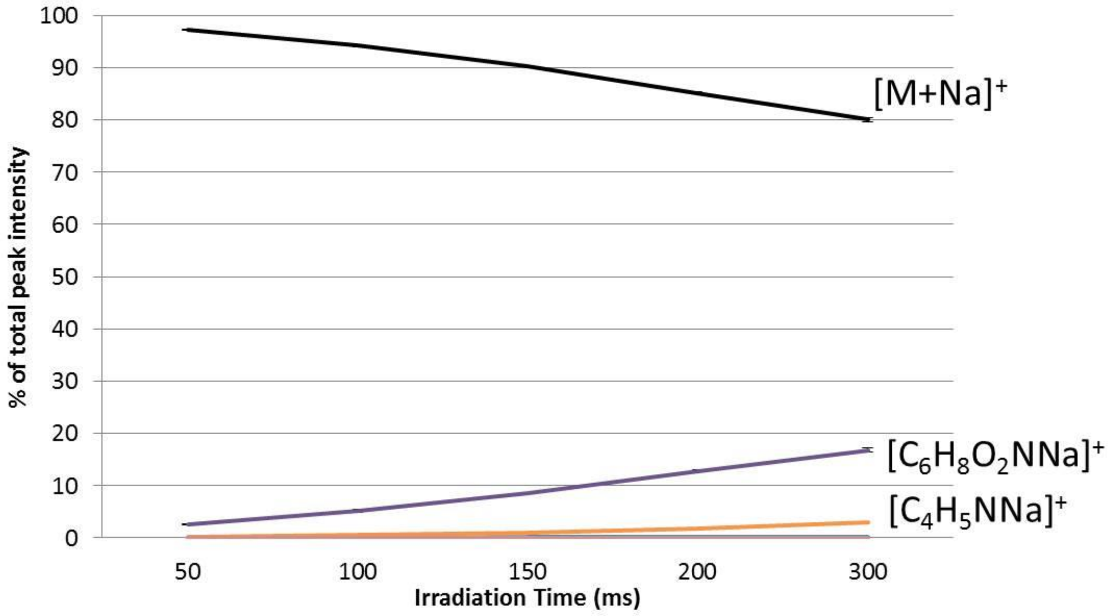

Figure 5.11 EID (14.1eV) fragmentation of [CPADB + Na]$^+$ as a function of electron irradiation time (product ions [C_7H_5S]$^+$, [C_3H_4NSNa]$^+$ and [$C_2H_3O_2Na$]$^+$ represent < 1 % of total peak intensity and consequently have not been labelled.

The correlation of increasing electron irradiation time with an increase in dissociation of the molecule, as measured by a decrease in the percentage of the total ion intensity for the precursor ion and an increase for the major product ion, was also observed when the energy of the electron was held constant at 9.1 eV and 19.1 eV (Appendix 10.3). The repeatability of the experiments is high, as the standard deviation achieved from three experiments generates error bars that are barely visible outside of the trend lines.

5.3. EID tandem MS of RAFT agents

RAFT agents are an interesting prospect as model molecules for fragmentation studies, as the variety of R and Z groups gives the opportunity to analyse aliphatic, aromatic and heteroatom containing functional groups within the same molecule. The five RAFT agents selected for analysis (Table 5.3) comprise a mixture of dithioester and trithioester molecules that contain two different Z groups and four different R groups.

Table 5.3 RAFT agents.

Name	Acronym	Empirical Formula	Structure
4-Cyano-4-[(dodecylsulfanythiocarbonyl) sulfanyl]pentanoic acid	4-CDSPA	$C_{19}H_{33}NO_2S_3$	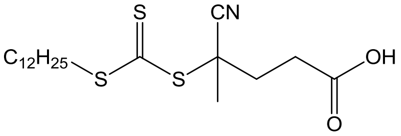
4-Cyano-4-(phenylcarbonothioylthio) pentanoic acid	CPADB	$C_{13}H_{13}NO_2S_2$	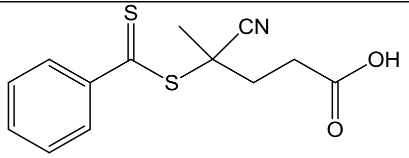
2-Phenyl-2-propyl benzodithioate	PPBD	$C_{16}H_{16}S_2$	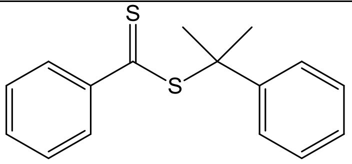
Cyanomethyl dodecyl trithiocarbonate	CMDTC	$C_{15}H_{27}NS_3$	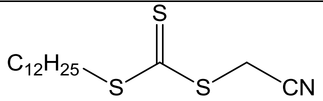
2-(Dodecylthiocarbono thioylthio)-2-methyl propionic acid	DDMAT	$C_{17}H_{32}O_2S_3$	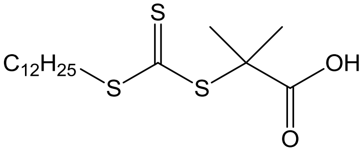

EID analysis of CPADB demonstrated that the charge carrier present influences the product ions observed under tandem MS conditions, therefore where possible **$[RAFT + Na]^+$** and **$[RAFT + H]^+$** molecular ions were both analysed.

5.3.1. RAFT agent functional groups (Z).

Initial EID tandem MS experiments for these RAFT agents identified a series of characteristic product ion peaks that corresponded to the structure of the RAFT agent. RAFT agents containing the dodecyl chain ($C_{12}H_{25}$) in the Z position (4-CDSPA, CMDTC and DDMAT) generated a product ion peak that gave an empirical formula of $C_{13}H_{25}S_3$ under EID conditions, with an example given for **[4-CDSPA + H]$^+$** in Figure 5.12.

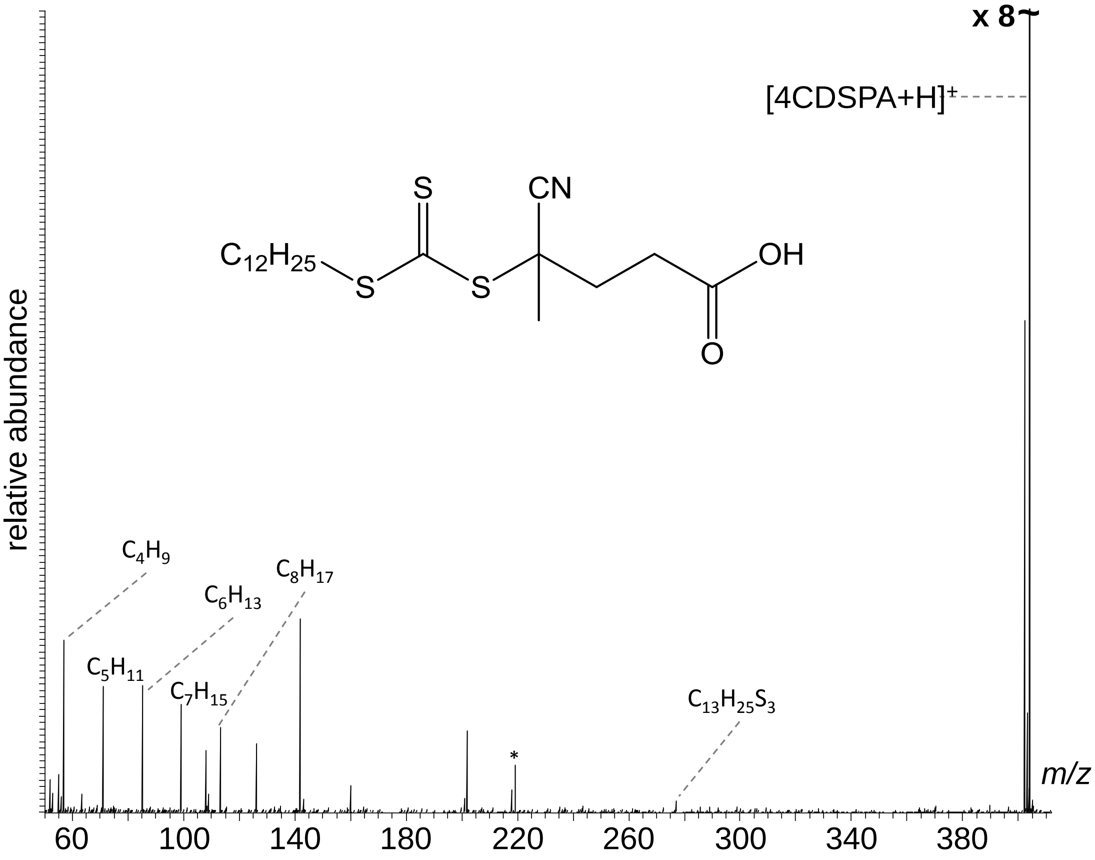

Figure 5.12 EID tandem MS of [4-CDSPA + H]$^+$.

This product ion was detected for both **[RAFT + H]$^+$** and **[RAFT + Na]$^+$** precursor ions demonstrating loss of the sodium charge carrier, where charge transfer to the molecule has occurred. For **[RAFT + H]$^+$** precursor ions, additional evidence for the presence of this alkyl chain is observed in the low mass region of the spectrum, where a series of product ion peaks separated by 14 Da are present. These peaks correspond to short linear hydrocarbon product ions (C_nH_{2n+1}) formed by cleavage within the dodecyl functional group. These peaks were only observed for protonated precursor ions, suggesting the presence of a proton is essential to detection of these product ions. It also suggests that a likely location for the proton is the dodecyl chain. This could be investigated further through the application of DFT molecular modelling calculations similar to those performed for CPADB.

For CPADB and PPDB, that contain a benzene molecule in the Z position, EID tandem MS generates product ions containing this group, as demonstrated in Figure 5.13 for **[PPDB + Na]$^+$**. Once again, it is found that, the **[RAFT + H]$^+$** precursor ions provide more structural information for the Z group, as discussed previously for **[CPADB + H]$^+$**. EID of **[CPADB + H]$^+$**

generated five product ions containing the Z group, including C_6H_5, which is a benzyl radical cation as in comparison, **[CPADB + Na]$^+$** only generated one product ion that contains the Z group.

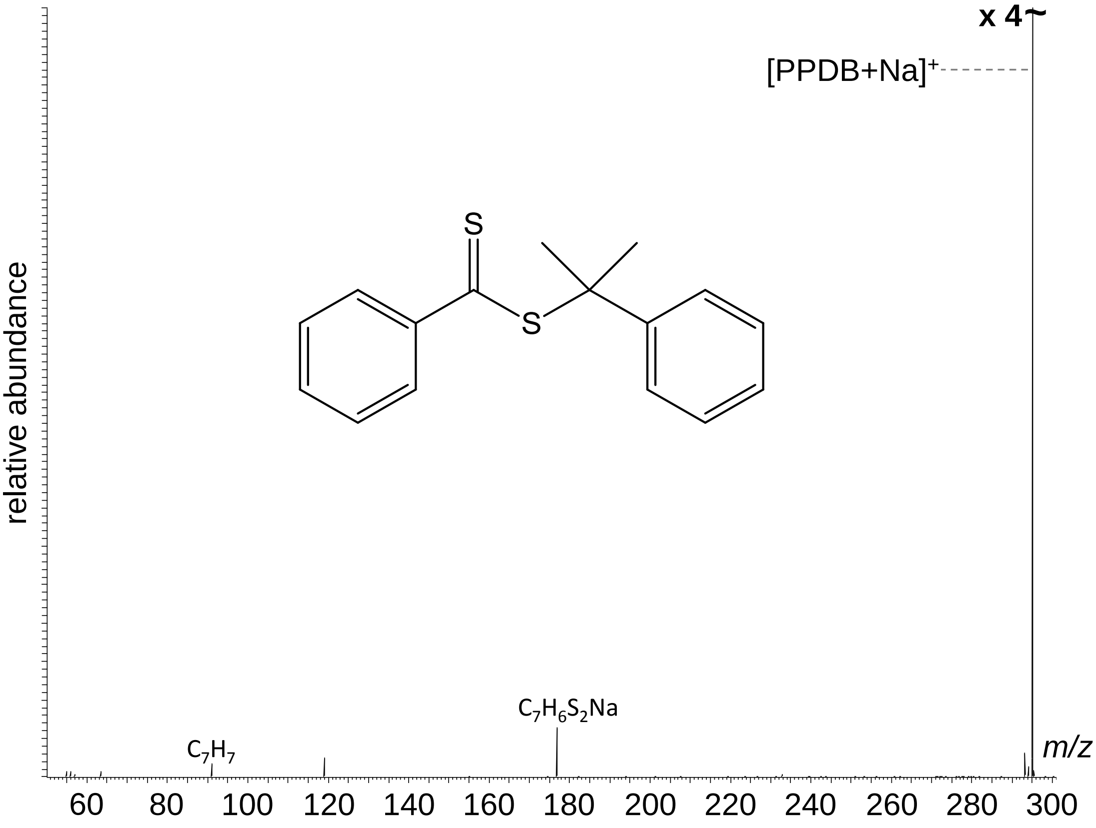

Figure 5.13 EID tandem MS of [PPDB + Na]$^+$.

5.3.2. RAFT agent functional groups (R)

For all precursor ion investigated, EID was able to generate product ion peaks that corresponded to the R groups. In the spectrum for EID of **[DDMAT + Na]$^+$** in Figure 5.14, there are a number of product ion peaks that aid in the identification of the R group. In contrast to the trend observed for the Z groups, there are more structurally significant product ion peaks observed during EID tandem MS of **[RAFT + Na]$^+$** precursor ions than the corresponding **[RAFT + H]$^+$**. This suggests that the coordination site of the charge carrier is essential to product ion detection, and that the likely location for the sodium charge carrier is in proximity to the R group, which is supported by the DFT calculations for **[CPADB + Na]$^+$** in section 5.2.3.2.

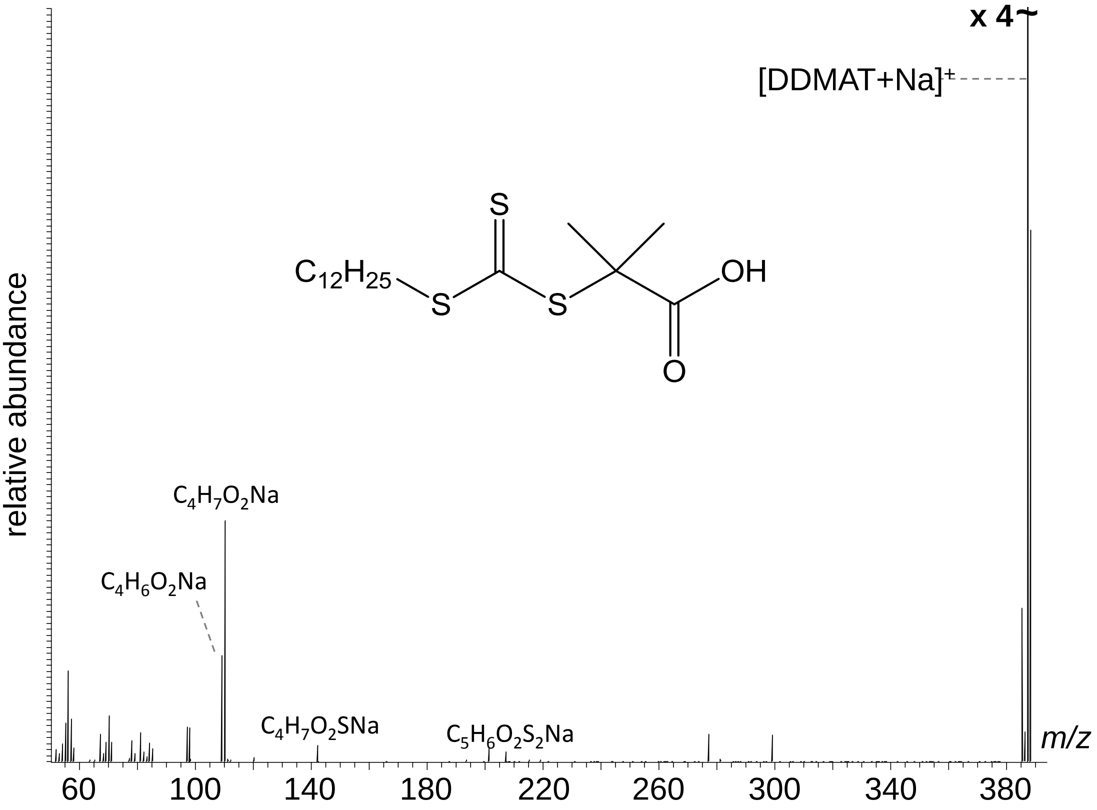

Figure 5.14 EID tandem MS of [DDMAT + Na]$^+$.

5.4. EID tandem MS of RAFT agents as a function of electron energy.

Utilising the automated EID dissociation method, the dissociation of the RAFT agents as a function of electron energy was investigated. It has been shown that the charge carrier significantly influences the dissociation of the molecules, and where possible **[RAFT + Na]$^+$** and **[RAFT + H]$^+$** precursor ions were isolated for this study. The resultant spectra were processed so that the intensity of the observed peaks were converted to a percentage of total peak intensity at a given electron energy. The results depicted graphically for **[RAFT + Na]$^+$** and **[RAFT + H]$^+$** in Figure 5.15 and Figure 5.16 respectively, demonstrate that the decrease in the intensity of the precursor ion peak corresponds with a reciprocal increase in the intensity of one product ion peak. Based on this observation, the product ion was identified, along with the type of bond broken leading to product ion formation, and the energy of the incident electrons at which the product ion was first observed. A summary of these results can be found in Table 5.4.

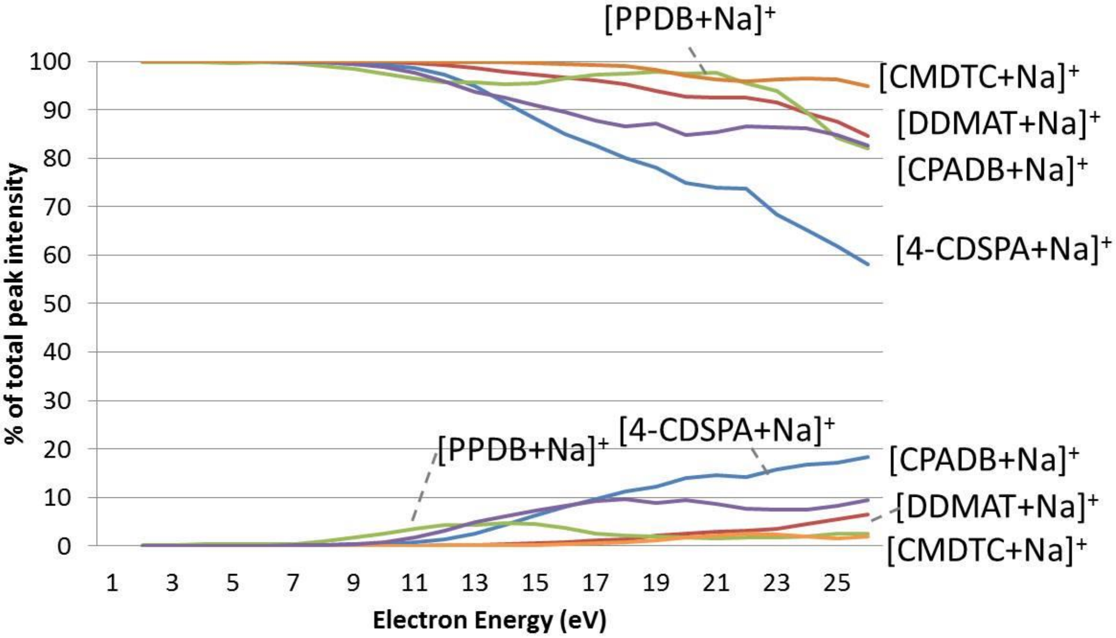

Figure 5.15 Fragmentation as a function of electron energy for [RAFT + Na]$^+$ precursor ions and major product ions.

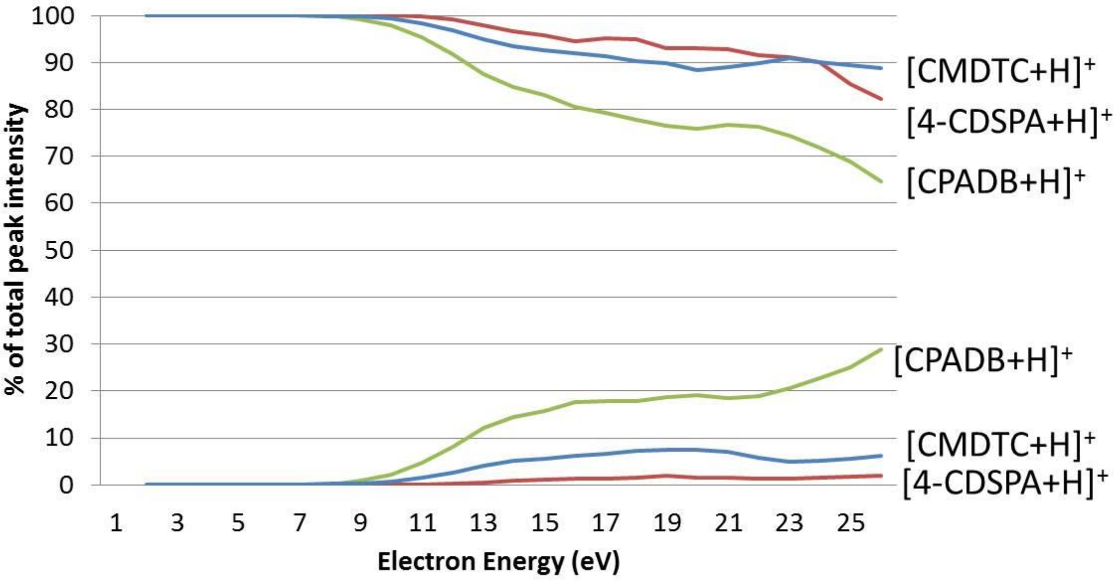

Figure 5.16 Fragmentation as a function of electron energy for [RAFT + H]$^+$ precursor ions and major product ions.

Table 5.4 Summary of major product ions generated during EID of RAFT agents.

Molecule	Structure	Charge Carrier	Major Product Ion	Type of bond broken	Electron energy
CPADB	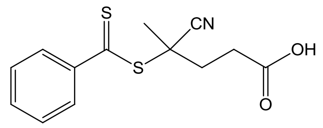	H	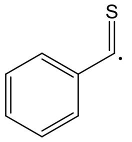	C-S	8 eV
CPADB	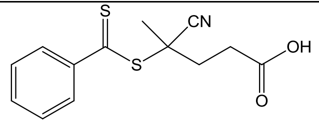	Na	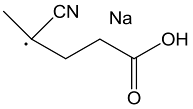	C-S	9 eV
4-CDSPA	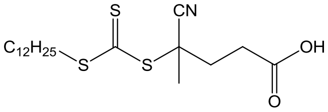	H	C_4H_9	C-C	16 eV
4-CDSPA	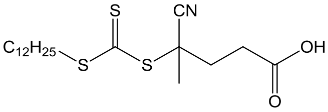	Na	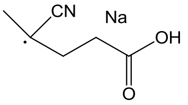	C-S	10 eV
CMDTC	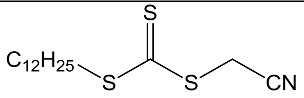	H	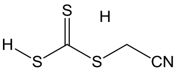	C-S	9 eV
CMDTC	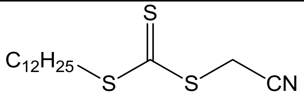	Na	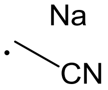	C-S	10 eV
DDMAT	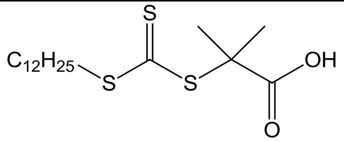	Na	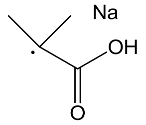	C-S	10 eV
PPDB	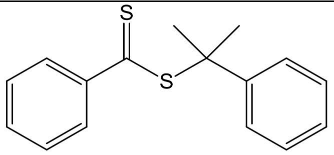	Na	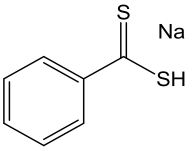	C-S	8 eV

The first experimental observation is that all product ions that result from cleavage of the C-S bond are first observed at an electron energy in the range 8 eV – 10 eV, as shown in Figure 5.16. The single product ion C_4H_9 that results from cleavage of the stronger C-C bond in the alkyl chain of **[4-CDSPA + H]**$^+$ is not observed until an electron energy of 16 eV, again providing support for a correlation between the energy of the incident electrons and the standard bond dissociation enthalpy. Secondly, for the majority of **[RAFT + Na]**$^+$ precursor ions, the most intense product ion peak observed during EID has an empirical formula that corresponds to the R group present in the specific RAFT agent. The empirical formulae for these major product ions indicate that they do not contain the thioester group and where the number of hydrogen atoms, suggest the presence of an odd electron radical. As these molecules are designed to restrict the concentration of active radicals in a polymerisation through ejection of the R radical, it would appear that the interaction of the incident electrons with a **[RAFT + Na]$^+$** precursor ion allows the RAFT agent to operate as it would in solution. A general proposal for formation of the R group radicals during EID of **[RAFT + Na]$^+$** is that the dissociation mechanism mimics the radical driven action of the RAFT agents during polymerisation. Radical addition at the thionyl bond generates a radical carbon centre, where subsequent homolytic cleavage of the C-S bond generates the R radical product ions, as shown in Scheme 5.2(a). This mechanism accounts for the major product ions observed during EID tandem MS analysis of **[CPADB + Na]$^+$**, **[4CDSPA + Na]$^+$**, **[CMDTC+ Na]$^+$** and **[DDMAT + Na]$^+$**. The one exception to this rule is **[PPDB + Na]$^+$**, which generates a product ion that corresponds to the reciprocal portion of the molecules, where the R group is the neutral loss. As the R and Z groups of PPDB are both aromatic, the dissociation chemistry of these functionalities will be more closely related than the other RAFT agents investigated, which may explain the deviation from the general trend.

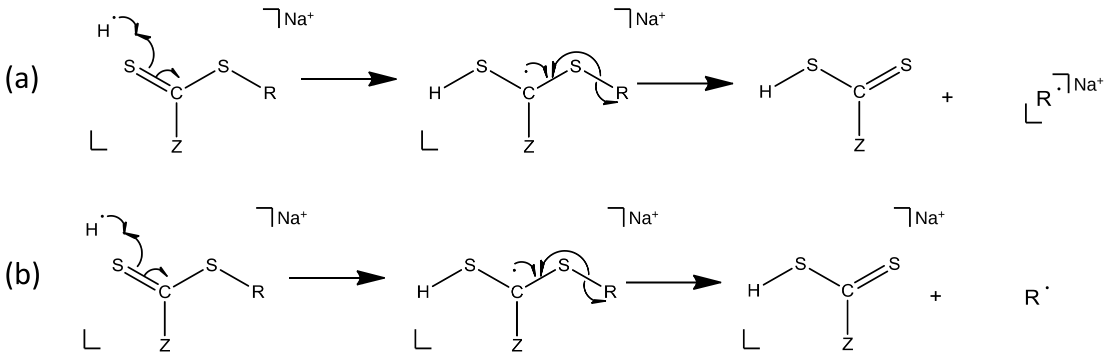

Scheme 5.2 Proposed EID dissociation mechanism for RAFT agents.

The proposal of a hydrogen radical initiating the dissociation is based upon the major product ion observed during EID of **[PPDB + Na]$^+$**, which corresponds to the structure provided in Table 5.4. This product ion is proposed to have formed via an analogous dissociation mechanism, outlined in Scheme 5.2(b), where the location of the charge carrier is the only difference in product ion formation. The source of the hydrogen radicals is not clear, however hot hydrogen radicals were proposed to be initially formed, and facilitated the Cornell "Hot Hydrogen" ECD mechanism for peptides.[166,167] Despite questions being raised about this mechanism, there are a number of publications supporting the presence of radicals in the ECD process.[174,175] One proposal for the results observed here, may involve a free radical rearrangement involving hydrogen radical abstraction to initiate the EID mechanism given in Scheme 5.2.

5.5. MS of poly(6-O-MAMGlc).

Synthetic polymers containing carbohydrate functional groups have been an area of significant interest within polymer chemistry. This is due to high levels of biocompatibility, making these polymers excellent candidates for biological studies, including interactions with lectins as well as cell membranes and cell walls. Poly(Methyl 6-O-Methacryloyl-α-D-glucoside), (6-O-MAMGlc) a synthetic polymer synthesised by RAFT polymerisation, where the carbohydrate functionalities are pendant on the polymer was selected for tandem MS analysis using CID and EID. The product ion fragmentation nomenclature utilised for product ion assignment of poly(6-O-MAMGlc) follows the rules outlined previously in Section 1.7.4.1 as shown in Figure 5.17.

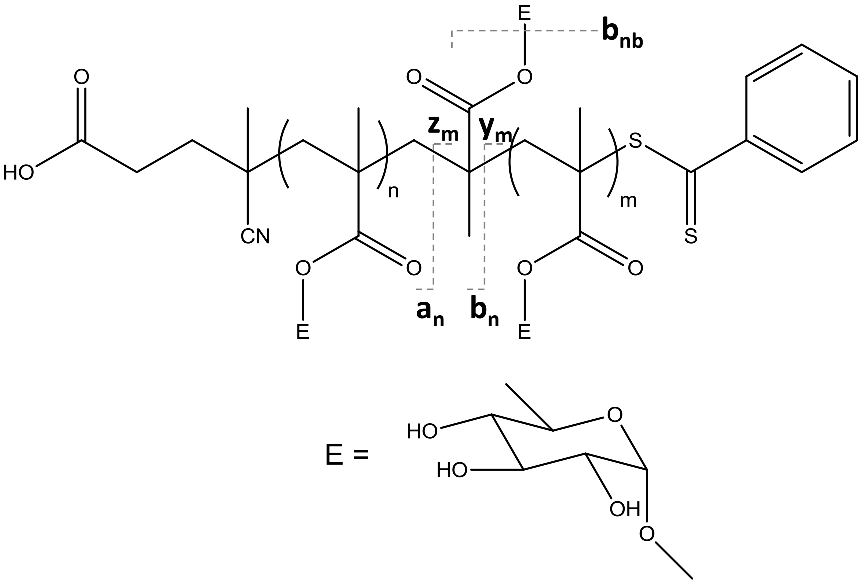

Figure 5.17 Structure of poly(6-O-MAMGlc), annotated to indicate cleavage sites and the nomenclature used to differentiate between resulting product ions.

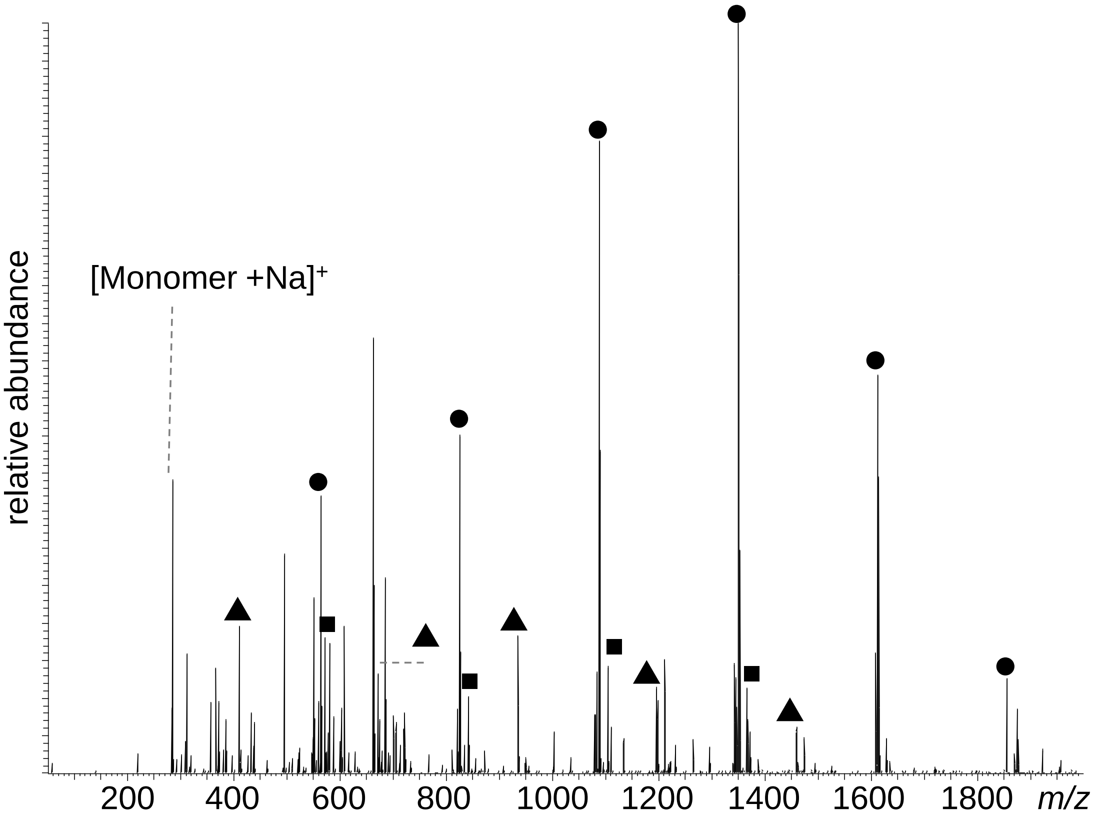

Figure 5.18 ESI-MS of poly(6-O-MAMGlc), ● = $[M+Na]^+$, ■ = [M + K]+ and ▲ =$[M + Na – C_7H_5S_2]^+$.

ESI MS of poly(6-O-MAMGlc) resulted in a complex spectrum containing multiple molecular weight distributions, as shown in Figure 5.18. The series of peaks of highest intensity, labelled (●) corresponds to **$[(6\text{-O-MAMGlc})_n + Na]^+$** (n=1-6), where the mass differences between the peaks corresponds to 262 Da, the mass of the 6-O-MAMGlc monomer unit ($C_{11}H_{18}O_7$). A second series of peaks labelled (■), corresponds to the polymer ionised with a potassium charge carrier. The detection of alkali metal adducts is not surprising, given the presence of a number of heteroatoms within the polymer, that can effectively coordinate the metal cation. The third series of peaks, labelled (▲), is observed 154 Da below the **$[(6\text{-O-MAMGlc})_n + Na]^+$** series of peaks (●). Accurate mass analysis of *m/z* 1196.45758, a peak in the (▲) series, gave an empirical formula of $C_{50}H_{79}O_{30}NNa$, that corresponds to the structure in Figure 5.19. Based on the empirical formula, this ion does not contain the $C_7H_5S_2$ terminal group proposed in the original polymer structure. The presence of this ion demonstrates that alternative termination reactions can occur during RAFT polymerisation, where the structure of the molecule proposed in Figure 5.19 is an example of termination by disproportionation. The ESI-MS spectrum of poly(6-O-MAMGlc) also displays evidence that the RAFT polymerisation reaction has not gone to completion as there is a peak at *m/z* 285.09383 which corresponds to individual monomer units ionised with a sodium charge carrier ($C_{11}H_{18}O_7Na$).

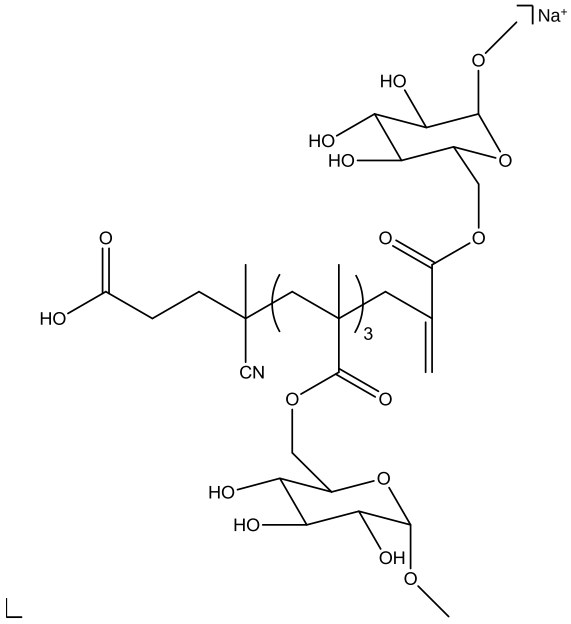

Figure 5.19 Proposed structure for *m/z* 1196 (▲) ion series.

5.5.1. Tandem MS of poly(6-O-MAMGlc)

The precursor ion **[(6-O-MAMGlc)$_4$ + Na]$^+$** at *m/z* 1350.44802 was isolated for tandem MS experiments. LTQ-CID of *m/z* 1350.44802 generated one major product ion at *m/z* 1196.46504, which gave an empirical formula of $C_{50}H_{79}O_{30}NNa$ when the ions were transmitted to the FTICR cell for mass analysis. This empirical formula corresponds to loss of the dithiobenzoate terminal group ($C_7H_5S_2$), and is assigned as a **b$_4$** product ion. This major product ion is proposed to be formed through cleavage of a C-S bond, which is known to fragment readily from the previous tandem MS study of RAFT agents. The single intense product ion provided confirmation of one of the terminal groups present in the precursor ion through neutral loss, but yielded little more structural information about the polymer.

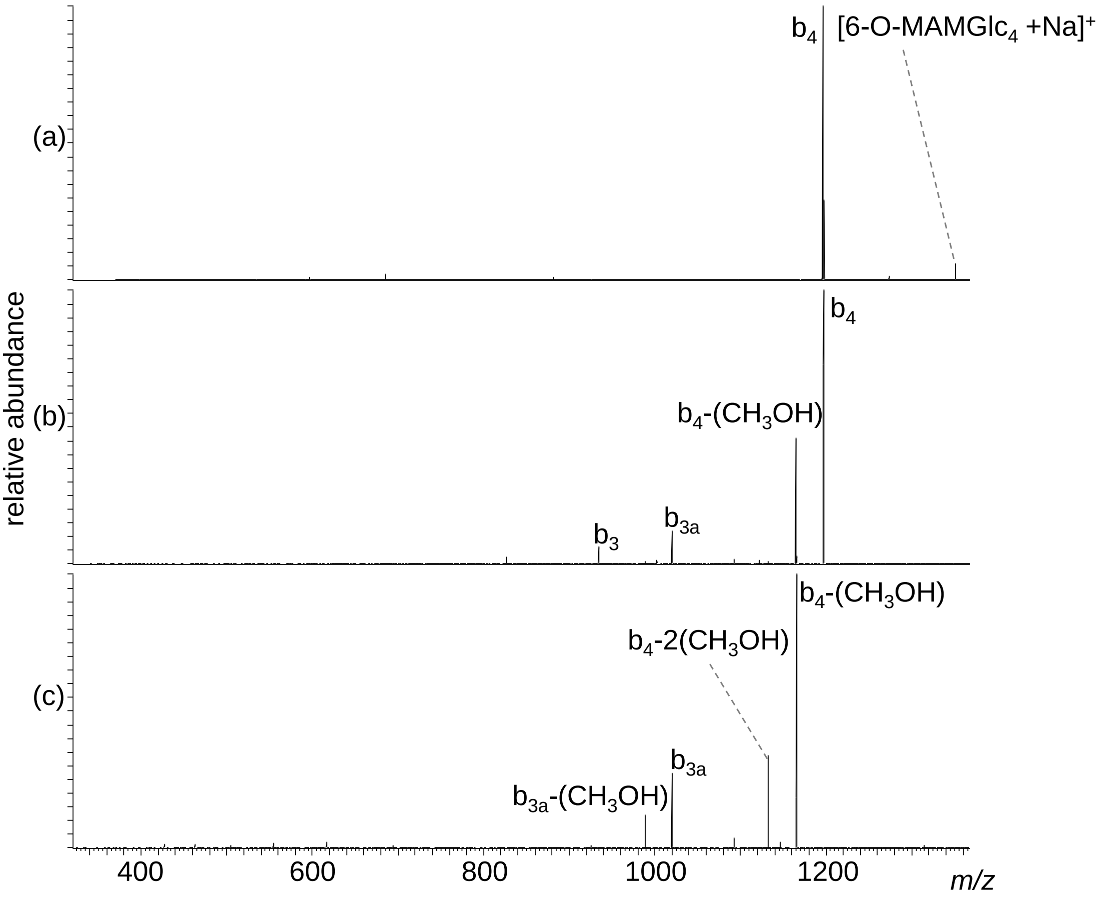

Figure 5.20 LTQ-CID tandem MS of $[C_6H_8NO_2(C_{11}H_{18}O_7)_4C_7H_5S_2 + Na]^+$: (a) MS^2 *m/z* 1350, (b) MS^3 *m/z* 1196 and (c) MS^4 *m/z* 1164.

The product ion peak $\mathbf{b_4}$ was of sufficient intensity to facilitate an MS^3 experiment. The resultant product ion spectrum in Figure 5.20(b) shows more structurally significant product ions, facilitating improved characterisation of the polymer. The major product ion observed in Figure 5.20(b) at *m/z* 1164.46504 corresponds to loss of CH_3OH from the $\mathbf{b_4}$ ion. This product ion is proposed to involve loss of one methoxy unit from a glucose ring. This is a characteristic loss that has been observed by Clarke *et al.* in the tandem MS analysis of glucose monosaccharide.[258] The product ion at *m/z* 1020.38868 gave an empirical formula of $C_{43}H_{67}O_{25}NNa$, and is assigned as a $\mathbf{b_{3a}}$ product ion formed through loss of an entire sugar group (labelled E in Figure 5.17). A third product ion at *m/z* 934.35139 gave an empirical formula of $C_{39}H_{61}O_{23}NNa$ that corresponds to polymer backbone cleavage with the loss of a complete monomer from the precursor ion, forming a $\mathbf{b_3}$ product ion. MS^4 was performed on $\mathbf{b_4\text{-}CH_3OH}$, and gave rise to additional product ions that were not observed in tandem MS or MS^3 experiments, giving enhanced structural information for the precursor ion. There is further evidence of CH_3OH loss, as demonstrated by the product ion peak observed at *m/z*

1132.40382, which is formed through the loss of a second methoxy group from a second glucose ring. The two remaining product ions correspond to $\mathbf{b_{3a}}$ product ions formed through cleavage in the pendant side chain, as discussed previously. The presence of $\mathbf{b_{3a}}$ and $\mathbf{b_{3a\text{-}}}$ **(CH_3OH)** is due to the presence of two different potential glucose containing pendant groups that can be lost from the precursor ion. As the precursor ion (*m/z* 1165.43465) in the MS^4 experiment is missing a CH_3OH group, neutral loss of the glucose ring that has already experienced methoxy loss results in the formation of product ion $\mathbf{b_{3a}}$ at *m/z* 1020.38801. If the glucose ring lost during the MS^4 experiment is intact, then it will form the product ion, $\mathbf{b_{3a}}$**-CH_3OH** at *m/z* 981.36227. The combination of MS^n experiments has proven to be a significant benefit in the characterisation of the poly(6-O-MAMGlc), where a range of common bond cleavages have been identified. As well as the initial loss of the dithiobenzoate terminal group during tandem MS, MS^n experiments demonstrated loss of the methoxy unit from the glucose ring, loss of the glucose ring through cleavage in the pendant group and polymer backbone cleavage, yielding more structural information than could be obtained from a single CID tandem MS experiment.

In comparison, EID tandem MS of **$[(6\text{-O-MAMGlc})_n + Na]^+$** was able to generate product ion peaks that provide enhanced sequence coverage than was obtained by LTQ-CID, as shown in Figure 5.21. The major series of product ions observed corresponds to $\mathbf{b_n}$, where the peaks in this series are separated by the monomer mass of 262 Da, and a product ion is observed for each monomer present in the precursor ion. The $\mathbf{b_n}$ product ions retain the $C_6H_8NO_2$ terminal group in all cases, demonstrating that a likely point of cation attachment is in proximity to the 4-cyanopentanoic acid group. In contrast to the observations made for LTQ-CID, EID does not cause dissociation of the glucose ring, demonstrating the differences in the fragmentation mechanism. There is only evidence of a single product ion (*m/z* 1020.40892, $\mathbf{b_{3a}}$) that corresponds to cleavage in the pendant functionality. This demonstrates that EID preserves the weaker C-O bonds of the glucose ring, with preferential cleavage of the polymer backbone. EID of **$[(6\text{-O-MAMGlc})_n + Na]^+$** also results in the formation of internal fragments, with a monomer and a dimer ionised with a sodium charge carrier detected at *m/z* 285.09539 and *m/z* 547.20451 respectively.

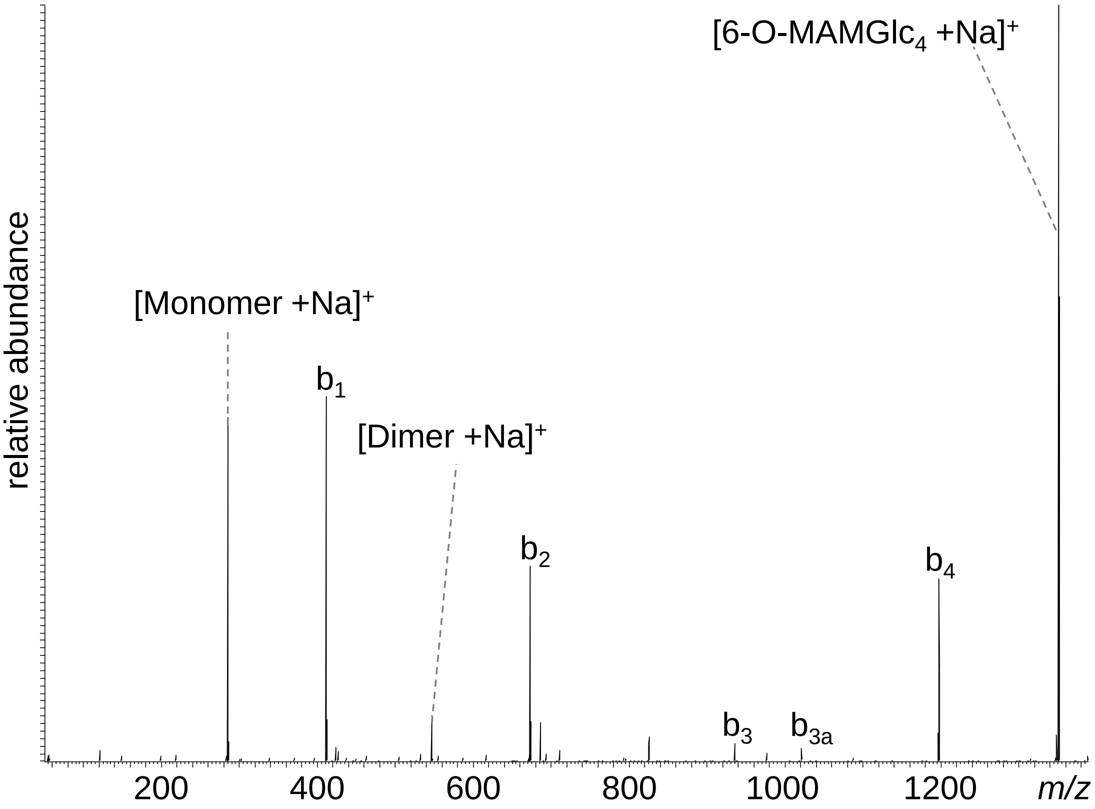

Figure 5.21 EID tandem MS of [$C_6H_8NO_2(C_{11}H_{18}O_7)_4C_7H_5S_2$ + Na]$^+$.

6. Conclusions

Electron based fragmentation techniques EID and HECD have proven to be highly effective tandem MS approaches for the structural characterisation of synthetic polymers. In the analysis of PEG, PMMA and PS, EID provided comparable structural information to MALDI-CID, both in terms of the type of product ions formed and the monomer sequence covered.

EID tandem MS analysis of **$[PEG_{13}+X]^+$** (X = NH_4, Li, Na, K, Ag and Cu), resulted in the formation of product ions for all precursor ions investigated, whereas LTQ-CID yielded product ions only when the charge carrier-polymer interaction was sufficiently strong. The standard reduction potential of the charge carriers was also reflected in the efficiency of EID with product ion abundance greatest when the precursor ion contained cations that are more challenging to reduce (Li> K> Na> NH_4> Ag). The importance of the standard reduction potential of the charge carrier during electron-based dissociation techniques was also evident from the ECD and HECD analysis of doubly charged PEG, ionised with two different alkali metal cations. In this case, ECD and HECD formed a singly charged product ion, where the cation retained in the product ion was the most challenging to reduce (Li> K> Na). There is also evidence of electron capture, with both alkali metals retained by the charge reduced product ion. Formation of this product ion is proposed to involve the covalent binding of one metal to the polymer with ejection of a hydrogen radical. HECD analysis of the doubly and triply charged PEG precursor ions **$[PEG_{31}+nLi]^{n+}$**, (where n=2 or 3) provided further evidence of product ions resulting from electron capture. This included the first observation of **$c_n^{\wedge}$**, a series of product ions formed by dissociation of the polymer, where at least one lithium is covalently bound to the polymer. The analysis of PEG with divalent metal charge carriers resulted in the formation of the charge stripped species **$(PEG_{13}X^{2+}-H^+)$** (X = Cu^{2+}, Zn^{2+} and Ca^{2+}), where the charge carrier is believed to be covalently bound to the polymer. Tandem MS analysis of these precursor ions resulted in noticeably different product ion spectra, where preferential formation of the product ions **$c_n^{\wedge}$** and **$x_m^{\wedge}$** was proposed to be *via* a charge-direct fragmentation pathway, due to the covalently bound cation. EID of **$(PEG_{13}X^{2+}-H^+)$** provided enhanced structural information with the formation of **$z_m^{\wedge}$** alongside the **$c_n^{\wedge}$** and **$x_m^{\wedge}$** observed during CID, that contains a saturated ethyl terminal group.

Application of the electron-based approaches EID and HECD allowed structural characterisation of a series of EG/PG block copolymers, yielding product ions that demonstrated directional sequencing of the copolymer. Providing enhanced structural information to that achieved by LTQ-CID, EID also demonstrated the presence of different structural isomers for the selected precursor ions, including a structural isomer with a nonstandard terminal group. Analysis of an EG/PG random copolymer revealed that electron-based fragmentation techniques provide a facile method of differentiating copolymers of different architectures. Tandem MS of block copolymers demonstrated preferential cleavage of one monomer block resulting in clearly defined series of product ion peaks, whereas tandem MS of random copolymers result in a product ion spectrum with no defined product ion series. The success of tandem MS for copolymer characterisation was demonstrated in the application of CID and EID to the analysis of an alternating block copolymer, where product ions resulting from backbone bond cleavages confirmed the presence of an alternating structure. Identification of structural isomers demonstrated that polymer initiation could occur at either copolymer constituent, a useful resource for the synthetic polymer chemist. In this instance the combination of CID and EID provided enhanced sequence coverage demonstrating the complementary nature of these dissociation techniques.

CID and EID were employed in the characterisation of poly(6-O-MAMGlc), a bio-inspired synthetic polymer made by RAFT polymerisation. CID MS^n experiments identified characteristic losses from the different components including terminal group neutral loss and loss of CH_3OH from the pendant sugar groups. In contrast, EID preserved the labile bonds of the polymer side chains with preferential cleavage of the polymer backbone bonds providing enhanced monomer sequence coverage. The analysis of RAFT agents, the small molecules designed to mediate the polymerisation process, really highlighted the level of analytical control that electron-based techniques can offer. Manipulation of the charge carrier resulted in complementary products providing reciprocal structural information. This result is proposed to be due to different locations of charge carrier attachment within the molecule, supported by molecular modelling calculations. Incremental EID analysis of the RAFT agents identified that specific bond cleavages occurred at different electron energies. Product ions that resulted from C-S bond cleavage were formed in the electron energy range 8 eV -10 eV, in contrast, product ions resulting from C-C bond cleavage were not observed until 16 eV. This result provides evidence that a correlation exists between the standard bond enthalpy and the energy of the incident electrons in EID. It was also found that the major product ion observed during EID of **[RAFT + Na]$^+$** corresponded to the R radical ion. This result is evidence that EID of **[RAFT + Na]$^+$** mimics the action of the RAFT agent in solution phase synthesis and may act as a useful experimental approach to further investigate the RAFT polymerisation mechanism.

7. Future Work

The success of electron-based fragmentation techniques for the structural characterisation of PEG, PMMA and PS makes the prospect of analysing synthetic polymers with other functionalities an intriguing prospect. Examples of common synthetic polymers that may be of interest are, poly(ethylene imine) polyesters and poly(dimethyl siloxane) as these polymers introduce different heteroatoms in the backbone, that may react differently under EID conditions.

Analysis of **[RAFT + Na]$^+$** by EID demonstrated that the major dissociation pathway of the molecules mimics the action of the molecules during RAFT polymerisation. It would be of interest to conduct an in depth investigation of a wider range of RAFT agents containing dithioester and trithioester functionalities. This would allow a comparison to be made between the different thioester species to examine whether EID tandem MS could provide an indication as to why trithioester RAFT agents have an inhibition period at the beginning of a polymerisation.

EID tandem MS analysis of poly(6-O-MAMGlc) demonstrated preferential backbone cleavage, whilst the labile bonds of the glucose ring remained intact. Initial loss of the dithioester containing terminal group demonstrated that the C-S bond is cleaved under EID conditions. It is of interest to perform the incremental electron energy study on this polymer to assess whether this labile bond is the first bond cleaved and the electron energy of C-S bond cleavage correlates with the existing findings for the polymer RAFT agents. It has also been hypothesised, that the energy of this bond will decrease with increasing degrees of polymerisation, therefore the incremental energy approach may be able to investigate this hypothesis where an increase in the number of degrees of polymerisation may result in the requirement of a lower electron energy for C-S bond cleavage. As the change is not likely to be dramatic, a larger number of degrees of polymerisation will be required in the usable mass range to observe this process consequently a polymer with a lower molecular weight monomer than poly(6-O-MAMGlc) will be required.

The results of PEG ionised with a range of charge carriers yielded interesting results, in particular those experiments involving transition metals. It would be of interest to conduct further experiments with other transition metals, with specific focus on those metals with stable integer oxidation states. Analysis of PEG with Fe^{2+} and Cr^{2+}, which have stable 3+ oxidation states and theoretical differences in the +2 to +3 oxidation states of 14.2 eV and 14.6 eV respectively, may be able to provide an insight into the dissociation chemistry observed for PEG ionised with copper.

For macromolecules, the effectiveness of CID tandem MS to induce fragmentation in the polymer decreases with increasing *m/z*. This is believed to be due to the increased number of degrees of freedom that can distribute the energy of the collisions over the molecule. Given the differences established here between CID and EID, it would be of interest to examine the effect of EID on these higher molecular weight species. Therefore the use of MALDI-FTMS could theoretically form higher molecular weight singly charged ions where EID could be used to induce fragmentation in the polymer.

The incorporation of ion mobility spectrometry (IMS) separation combined with tandem MS experiments may enhance the experimental observations made in a number of experiments in this thesis, where:

- IMS experiments can be utilised to accurately determine the gas phase conformation adopted by PEG in the different charge states to investigate whether the conformation of the precursor ion influences dissociation.
- Determination of the conformation adopted by the doubly charged PEG ions that contain two different alkali metals, could provide an insight into the differences in the number of product ion peaks observed during tandem MS experiments.
- IMS could potentially separate the different structural isomers observed during tandem MS experiments involving EG/PG block copolymers. Successful separation would allow each isomer to be dissociated individually providing confirmation for the assignments made in this thesis.

8. Atmospheric pressure Solids Analysis Probe Mass Spectrometry of synthetic polymers

8.1. Introduction

Mass spectrometry has become an increasingly important method for the characterisation of synthetic polymers. The advent of soft ionisation techniques such as MALDI[16,22,23,54,81,152,259] and ESI[73,87,88,90,115,124,145,146] have significantly increased the range of polymers that can be analysed by mass spectrometry. More recently, the development of ambient ionisation techniques have been instrumental in the direct analysis of synthetic polymers; Desorption Electrospray Ionisation (DESI)[104] and Direct Analysis in Real Time (DART)[109] have been utilised in the analysis of a range of low molecular weight synthetic polymers (< 1500 Da), including poly(dimethyl siloxane), poly(methyl methacrylate) and poly(ethylene imine). The multiple charging capabilities of DESI have been demonstrated recently through successful ionisation of PEG homopolymers up to 20 kDa under optimised conditions. Despite this, there are a number of limitations that restrict the application of mass spectrometry to all synthetic polymers. Sample preparation for analysis by conventional methods, such as MALDI or ESI, has a significant number of potential variables that must be optimised in order to achieve ideal analysis. As synthetic polymers are often less basic than their biological equivalents, cation attachment has been shown to be more beneficial than protonation. The addition of metal salts during sample preparation can be the determining factor in successful ionisation for MALDI[16], ESI[90,120] and DESI.[104] This therefore requires some knowledge of the polymer, as cation selection is important to ensure good interaction with the polymer. Metal salts that promote ionisation can add a degree of complexity to polymer analysis through the presence of additional peaks in the isotopic envelope. Silver, which has been shown to effectively ionise poly(styrene), has isotopic abundances of ^{107}Ag and ^{109}Ag at a ratio of 100:93, which create overlapping molecular ion peaks in the mass spectrum.[43,120,143] It is also essential that the polymer is soluble in one of a limited range of MS solvents; in fact if the polymer is not soluble in polar solvents then ESI will be of limited use. One method that has been developed to circumvent this problem is solvent-free MALDI.[59-61] This technique combines the polymer, metal salt and matrix in the solid state using mechanical means.[59] It has proven to be effective in the analysis of a wide range of synthetic polymers, including poly(methacrylate)s, poly(styrene)s and poly(siloxane)s,[64] however the direct analysis of polymers remains restricted, and consequently development in this area is constantly sought.

A method of direct ambient ionisation that has demonstrated promise in this area is the Atmospheric pressure Solids Analysis Probe, which was introduced in 2005 by McEwen *et al*.[97] Together with DESI and DART, these direct ambient ionisation techniques have gained significant interest from the mass spectrometry community and this popularity has resulted in the production of commercial ASAP ion sources. Direct application of samples to a glass capillary permits the analysis of both solutions[260] and solids samples.[261] Solid sampling circumvents issues regarding solubility and minimises sample preparation. As there is no longer a requirement for the polymer to be soluble, ASAP has the potential to expand the range of synthetic polymers that can be characterised by mass spectrometry beyond those amenable to MALDI and ESI. ASAP has also been shown to be an effective method to ionise compounds regardless of polarity or volatility, which is an advantage in synthetic polymer analysis where the chemistries can be diverse.

The application of ASAP to synthetic polymer analysis is limited; initial work by McEwen *et al.* utilised low molecular weight PEGs as calibration materials for the analysis of biological tissue samples.[97] Trimpin *et al.* demonstrated that ASAP could be used for the analysis of polymers through the direct ionisation of nylon, poly(ester) and polymer additives from materials such as carpet and shirt fibres.[64] The analysis of the polymers as a component of their original materials is advantageous, as it ensures that the materials are analysed without modification from any preparative steps. However, while ASAP has been applied to the analysis of synthetic polymers, no systematic study has been reported. Therefore, this work evaluates the ASAP source for the analysis of well-defined synthetic polymers, including the identification of influential source parameters that affect the observed molecular weight distribution and in-source fragmentation. Poly(styrene), poly(ethylene glycol), poly(methyl methacrylate) and poly(ethylene) were selected for this investigation, as they provided diverse chemical functionalities with which to test ASAP. The polymers were also selected as data could be obtained using other ionising techniques, to which ASAP could be compared. Initial analysis demonstrated that molecular ions could be generated without the requirement for metal salt addition, forming protonated, radical cation and hydride abstracted molecular ions. Following ion source optimisation, the molecular ions were utilised in CID tandem mass spectrometry experiments, providing additional structural information about the polymer. The success of ASAP for the analysis of homopolymers as solids led to the application of ASAP in the characterisation of functionalised copolymers that are insoluble in all mass spectrometry appropriate solvents, providing molecular weight and structural information that could not be obtained by other analytical techniques. This work demonstrates the potential to expand the range of low molecular weight polymers amenable to MS analysis, as solubility is no longer an issue.

8.2. MS Analysis

8.2.1. ASAP of Poly(styrene)

Poly(styrene) (PS), a polymer comprised solely of hydrogen and carbon atoms, is a non-polar polymer containing aromatic phenyl pendant groups at alternate carbon atoms along the polymer backbone, as shown inset in Figure 8.1.

To examine the ionising potential of ASAP, analysis was performed on the solid polymer without metal salt doping; generating the spectrum provided in Figure 8.1.

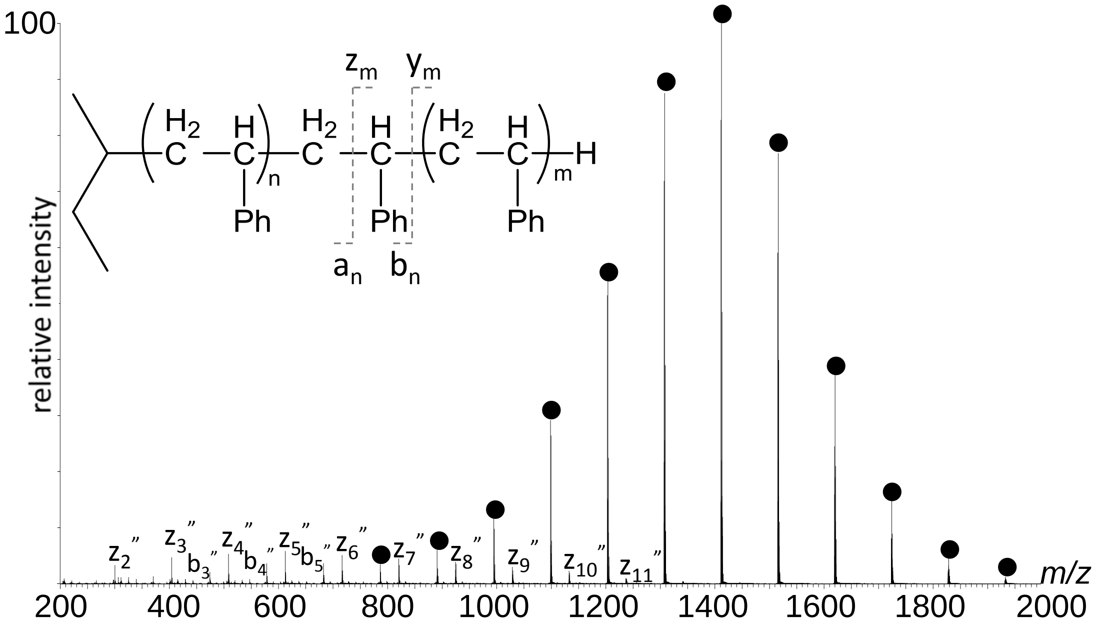

Figure 8.1 ASAP MS of Poly(styrene) (M_n = 1770). ● = $M^{+\bullet}$, Desolvation gas temperature 600 °C and Sample cone voltage 20 eV.(inset Structure of Poly(styrene), annotated to indicate cleavage sites and nomenclature used to differentiate between resulting product ions.)

The most intense series of peaks, labelled with (●), corresponds to singly charged molecular ions, as confirmed by the ^{12}C and ^{13}C isotopic distribution with the *m/z* difference between the peaks corresponding to the mass of the styrene monomer unit 104 Da (C_8H_8). Through inspection of each peak, the cumulative mass of the proposed terminal groups (*m/z* 58) can be deduced. The observed *m/z* values of the (●) series correlate exactly with the expected masses of the PS oligomers, confirming the presence of PS radical cations. PS, which has a low proton affinity (approximately that of benzene, 750 kJ mol^{-1})[262] and is not a polar molecule, is likely to favour ionisation by charge transfer, leading to the formation of radical cations over the competing proton transfer mechanism.[110,226,263] PS radical cations have been observed using Electron Ionisation (EI) mass spectrometry, where they dissociate readily, yielding detailed structural information for the polymer.[264] The fragility of radical cations towards the hostile conditions of the ASAP ion source is observed through the presence of additional series of peaks in Figure 8.1, labelled as $\mathbf{z_m}''$ and $\mathbf{b_n}''$, which result from in-source fragmentation. These assignments correspond to the cleavage of carbon-carbon bonds in the polymer backbone, as shown inset in Figure 8.1. Direct ionisation of the analyte is a real benefit in the analysis of synthetic polymers, as there is no requirement to determine the optimal cation to promote ionisation. As PS is well known to ionise effectively with silver cations by MALDI, as in Figure 8.2, doping a PS sample with silver iodide prior to ASAP analysis resulted in the formation of radical cation molecular ions only. This observation can be rationalised through differences in the energies required to vapourise the polymer and the metal salt (889 kJ mol^{-1}).

The molecular weight distribution observed in the ASAP mass spectrum has the spectral base peak of *m/z* 1410.9*;* however when the PS sample is ionised by MALDI (Figure 8.2) the spectral base peak is at *m/z* 1725.5, which is consistent with the expected value. This discrepancy suggests that determination of molecular weight by ASAP is less reliable than optimised MALDI conditions. It can also be observed that the MALDI spectrum in Figure 8.2 shows no evidence of in-source fragmentation, and consequently the observed $\mathbf{b_n}''$ and $\mathbf{z_m}''$ ions in ASAP result from fragmentation during ionisation and not as components of the original sample.

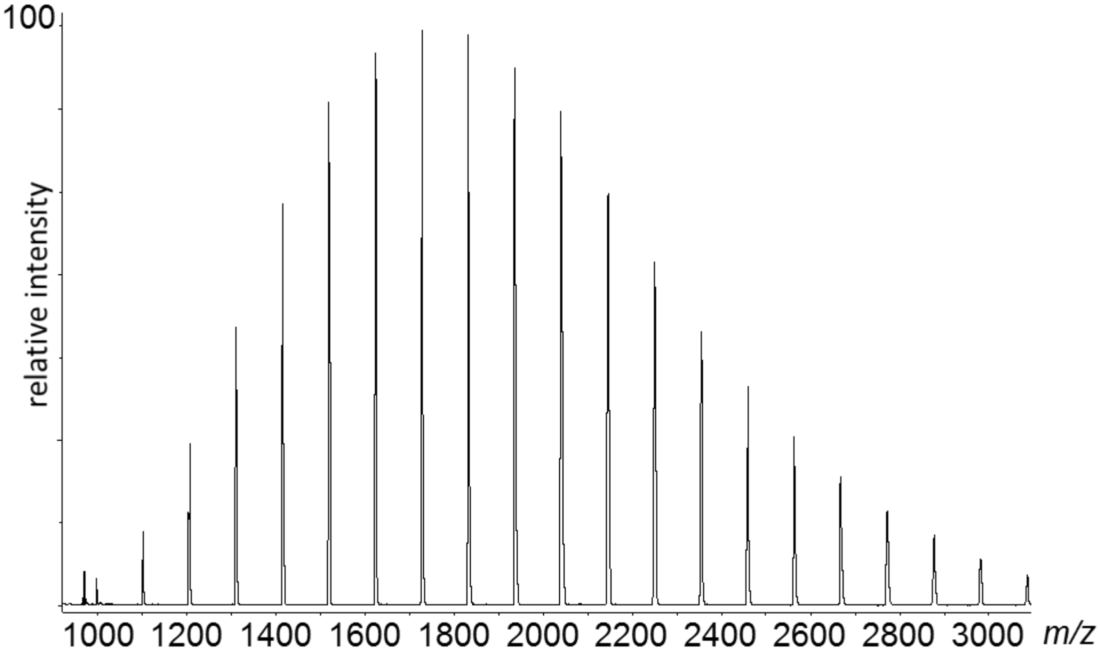

Figure 8.2 MALDI MS of PS (Dried droplet method, using AgI and Dithranol as the matrix).

8.2.2. ASAP of poly(ethylene glycol)

Poly(ethylene glycol) is a polymer containing carbon, hydrogen and oxygen atoms regularly arranged in the polymer backbone, as shown in Figure 8.3. This regular arrangement of oxygen atoms results in a polar polymer, where PEG is routinely ionised with metal cations by ESI[87,88] and MALDI[265]

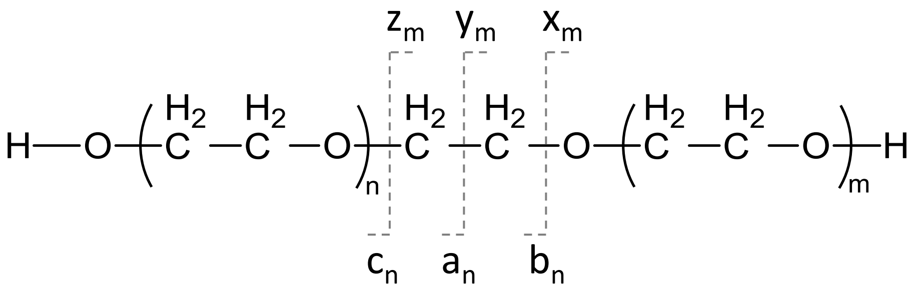

Figure 8.3 Structure of Poly(ethylene glycol), annotated to indicate cleavage sites and nomenclature used to differentiate between resulting product ions.

When PEG was analysed as a solid using ASAP, the spectrum in Figure 8.4 was generated. As can be observed there are multiple series of peaks separated by 44 Da, which corresponds to the mass of an individual monomer unit of ethylene glycol (C_2H_4O).

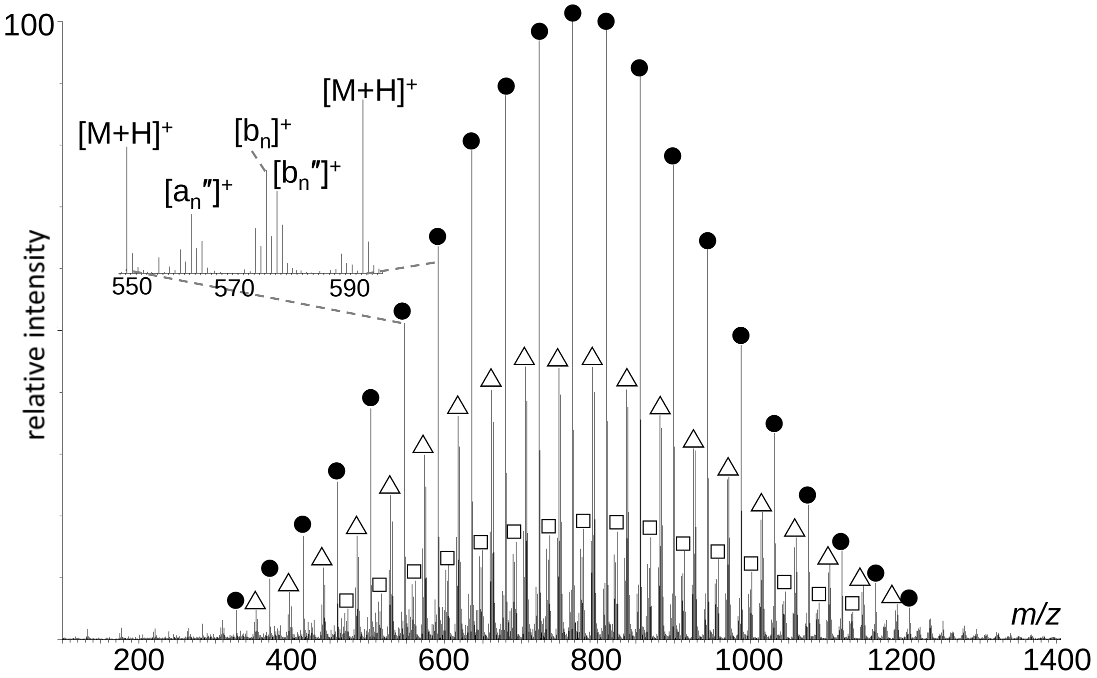

Figure 8.4 ASAP MS of Poly(ethylene glycol) M_n = 1430. ● = [M+H]+, △ = b_n and b_n″ and □ = a_n″. *m/z* 675 – 725 has been expanded for clarity (insertion).

The most intense series of peaks, labelled with (●), corresponds to the PEG molecular ion, which is present as a protonated adduct generated by the proton transfer ionisation mechanism shown in Section 2.1.5.[226] Despite being run in an ion source with no additional co-sprayed solvent present, PEG preferentially proceeds via the proton transfer mechanism, thus demonstrating that the chemistries of the individual polymers influence the resulting molecular ion species. As PEG has a higher proton affinity and is more polar than PS, the observation of PEG as a protonated species is the rational result. Similar to DART,[109] the only series observed for intact PEG oligomers by ASAP is the protonated ion series, which is a clear distinction from MALDI,[265] ESI[87] and DESI,[104] where PEG may be ionised simultaneously with a range of metal cations. Despite the high affinity of PEG to form alkali metal adducts in MALDI and ESI, doping a solution containing PEG with lithium bromide prior to ASAP analysis generated only protonated oligomers. Like PS, this result is justified through differences in energies required to vapourise the polymer and metal salt (747 kJ mol^{-1}). Despite $\mathbf{[PEG + H]^+}$ being the only intact molecular ion series present in the ASAP mass spectrum, additional ion series that result from in-source fragmentation add a degree of complexity, as shown in the expansion in Figure 8.4. This is highlighted by the second most intense distribution of peaks corresponding to **b** ions labelled as (△) in Figure 8.4. This assignment corresponds to cleavage at the ether oxygen atom, labelled as **b** in Figure 8.3. Cleavage at this C-O bond has the potential to generate two different chemical entities as the terminating group, which differ by 2 Da. ASAP provides evidence of both types, as shown inset in Figure 8.4. The ion series with an unsaturated $–CH=CH_2$ group $\mathbf{b_n}$, resulting from charge remote fragmentation, is commonly observed in CID tandem MS experiments.[87,88] $\mathbf{b_n}''$, the saturated counterpart ($-CH_2CH_3$) has been reported in pyrolysis studies, where thermal decomposition produced molecules that when ionised independently by MALDI MS formed $\mathbf{b_n}''$ and $\mathbf{a_n}''$ ions.[266] As ASAP MS analysis of PEG was performed at 600 °C, the probability that thermal decomposition contributes to the observed in-source dissociation is high, and was investigated further (see section 8.4). Further evidence for this can be seen in the third distribution, represented by (□) in Figure 8.4, which corresponds to cleavage of the C-C bond in the polymer backbone, yielding a series of peaks labelled $\mathbf{a_n}''$. Again, known to result from thermal decomposition, this species does not appear in DESI, ESI or MALDI tandem MS experiments, however cleavage of the C-C bond has been reported in high energy FAB-CID experiments when lithium adducted PEG was analysed with a laboratory frame collision energy of 50 eV.[131] GC-MS of low molecular weight PEGs also produced ions that resulted from cleavage of C-C bonds, where the authors proposed that these ions were formed by α-cleavage from a radical cation. Given the propensity for ASAP to generate both radical cations and protonated ions via the competing ionisation mechanisms, it is reasonable to suggest that some of these ions may also originate from a radical cation, and this proposal is explored further in section 8.4.

The molecular weight distribution observed in Figure 8.4 differs significantly from that observed for MALDI of the same sample (Figure 8.5), demonstrating that ASAP is not amenable to molecular weight determination or the calculation of polydispersity. It is worth considering that molecular weight determination by MALDI and ESI can be affected by matrix,[16,267] metal cation[38] and even metal anions[90], so caution should be taken when considering the reliability of any molecular weight distribution measurements by mass spectrometry.

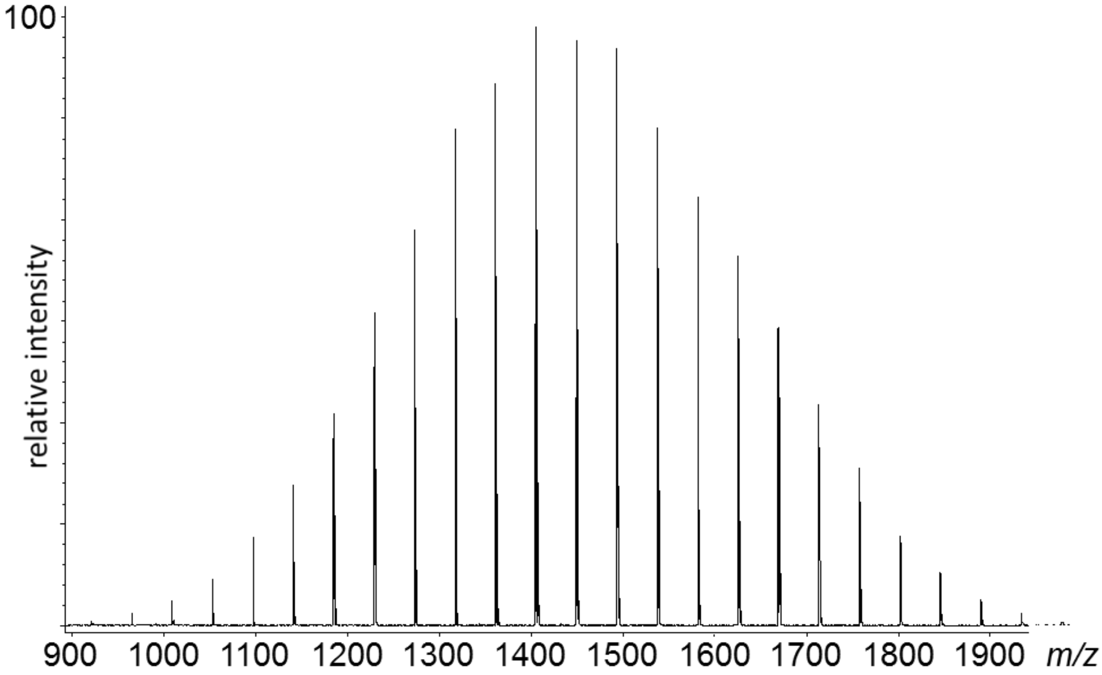

Figure 8.5 MALDI MS of PEG Mn = 1430 (Dried droplet method, using NaBr and DHB as a matrix).

.

8.2.3. ASAP MS of poly(methyl methacrylate)

PMMA, like PEG, is an example of an oxygen rich polymer containing carbon, hydrogen and oxygen atoms. The structure of PMMA (inset in Figure 8.6 differs) from PEG as the oxygen atoms are located on the side chains, where the backbone contains only carbon-carbon bonds similar to PS. ASAP MS analysis of the PMMA M_n = 1000 generated the spectrum given in Figure 8.6; it can be seen that four series of peaks are present, separated by 100.1 Da corresponding to the methyl methacrylate monomer unit ($C_5H_8O_2$).

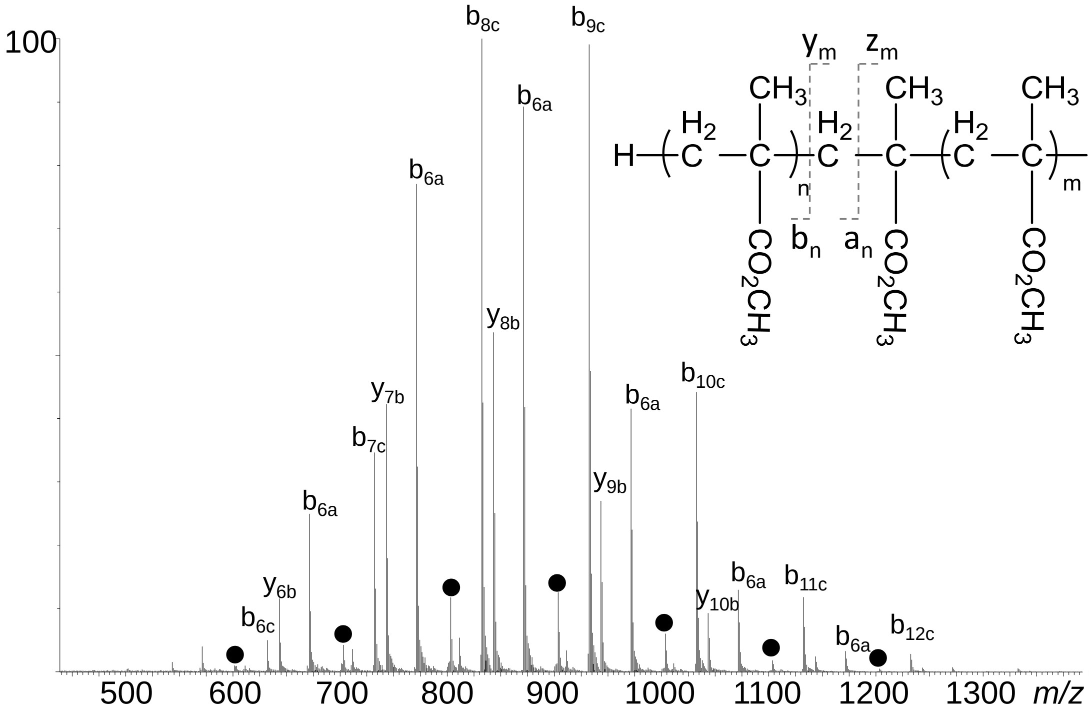

Figure 8.6 ASAP MS of PMMA M_n = 1000, inset (structure of Poly(methyl methacrylate), annotated to indicate cleavage sites and nomenclature used to differentiate between resulting product ions).

Table 8.1 Structural assignments for series of peaks from Figure 8.6.

m/z	Empirical formula	Structure	Label
703.3 ± 100.1	$C_{35}H_{59}O_{14} \pm C_5H_8O_2$	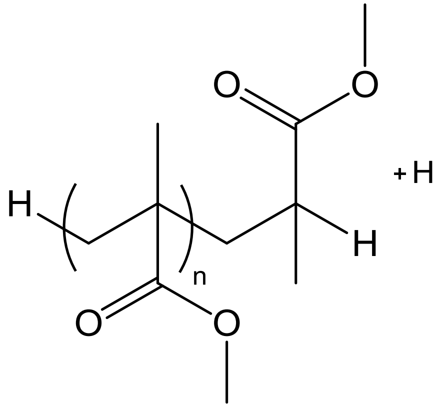	●
732.3 ± 100.1	$C_{37}H_{64}O_{14} \pm C_5H_8O_2$	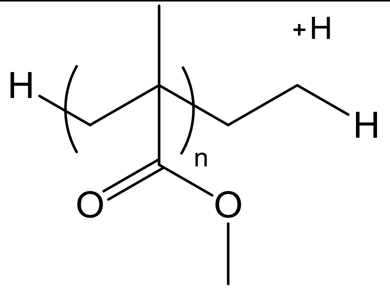	b_{nc}
743.3 ± 100.1	$C_{38}H_{63}O_{14} \pm C_5H_8O_2$	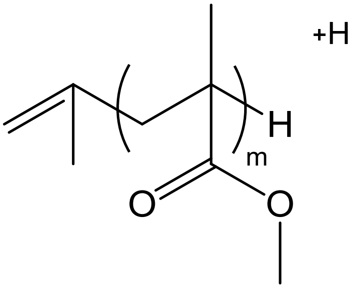	y_{mb}
771.3 ± 100.1	$C_{39}H_{63}O_{15} \pm C_5H_8O_2$	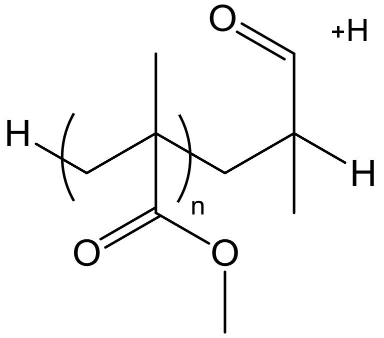	b_{na}

The series of peaks (●) correspond to **[PMMA + H]**$^+$, as PMMA is a polar polymer containing oxygen atoms, the presence of a protonated molecular ion is the expected result based on the observation for ASAP of PEG. The other series of peaks observed in Figure 8.6 do not correspond to intact molecular ions. Accurate mass analysis of ($\mathbf{b_{nc}}$), ($\mathbf{y_{mb}}$) and ($\mathbf{b_{na}}$) series of peaks provide empirical formula which are consistent with small neutral losses from the pendant methacrylate chains, as shown by the structures presented in Table 8.1. The series labelled ($\mathbf{y_{mb}}$) is a product ion series common to MALDI - CID experiments.[120]. Fragmentation within the methacrylate group is not typically observed in MALDI – CID, where fragmentation typically involves homolytic backbone cleavage followed by subsequent complete side chain loss. This demonstrates that differences may exist in the mechanisms of fragmentation between ASAP MS and MALDI CID tandem MS. These differences are supported by the (b_{nc}) series of peaks with the highest S/N ratio, where the empirical formula suggests that formation involves loss of both methacrylate and methyl groups of a monomer unit, as summarised in Table 8.1.

MALDI MS of PMMA M_n = 1000 generated the spectrum shown in Figure 8.7; it is noted that the spectra generated by ASAP and MALDI are in closer agreement for the molecular weight of PMMA than previously observed for PS and PEG.

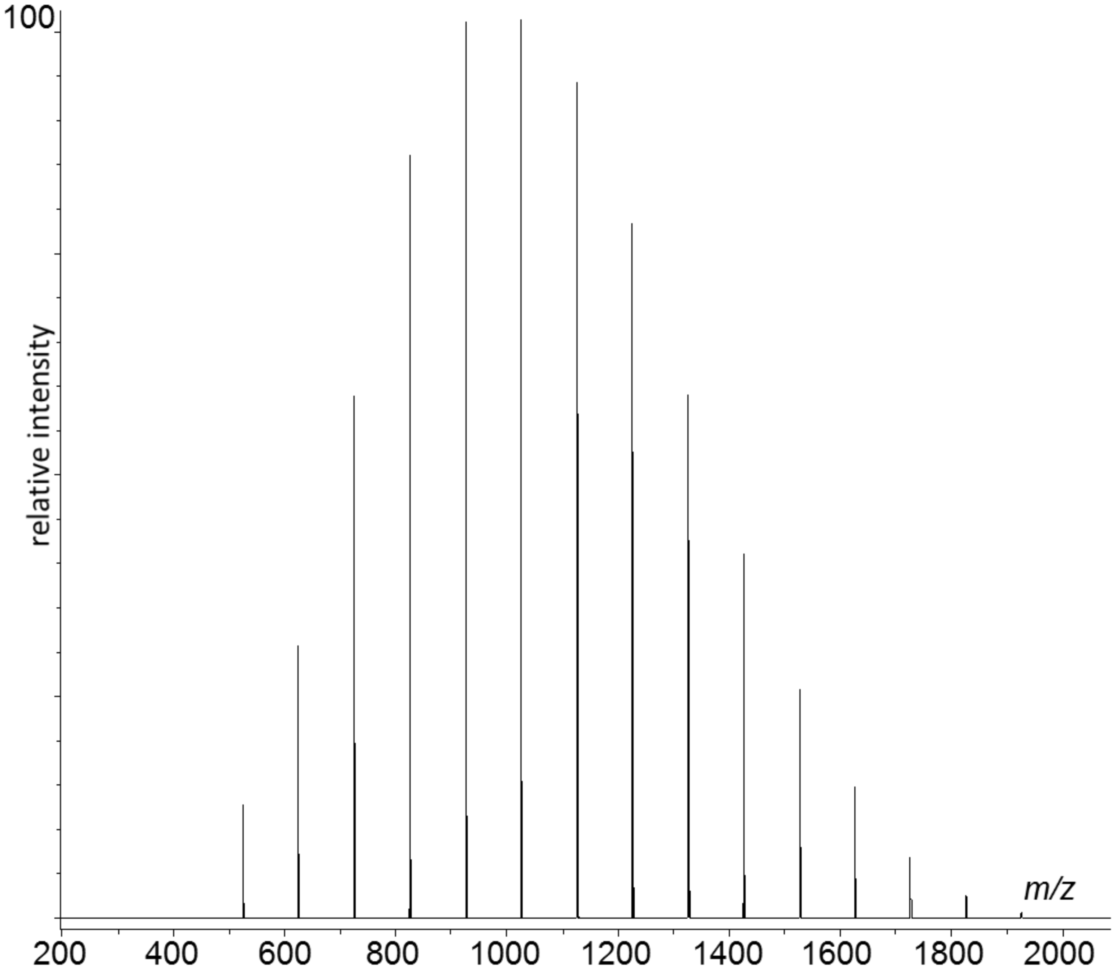

Figure 8.7 MALDI MS of PMMA M_n = 1000 (dried droplet method, using NaI and DHB as a matrix).

8.2.4. ASAP MS of Poly(ethylene)

Poly(ethylene) (PE), is a synthetic polymer containing only carbon and hydrogen atoms in a linear aliphatic chain. PE is rarely characterised using solvent-based analytical techniques due to issues regarding solubility.

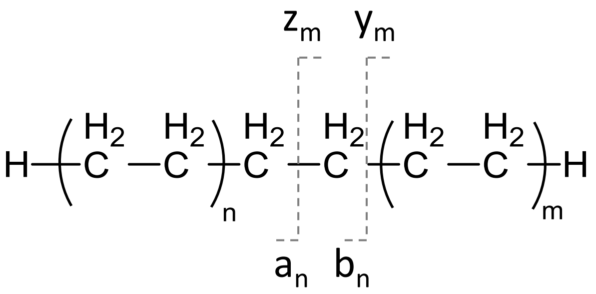

Figure 8.8 Structure of Poly(ethylene), annotated to indicate cleavage sites and nomenclature used to differentiate between resulting product ions.

PE is soluble in only a select number of solvents, and typically requires elevated temperatures.[268] This has significantly limited the application of mass spectrometry to the analysis of this polymer, where only MALDI and DART have been able to provide a mass spectrum for low molecular weight samples.[31,40,109] As a means to investigate the potential of ASAP, solid PE was applied to the ASAP capillary and inserted into the ion source at a desolvation gas temperature of 600 °C, with the resultant spectrum shown in Figure 8.9.

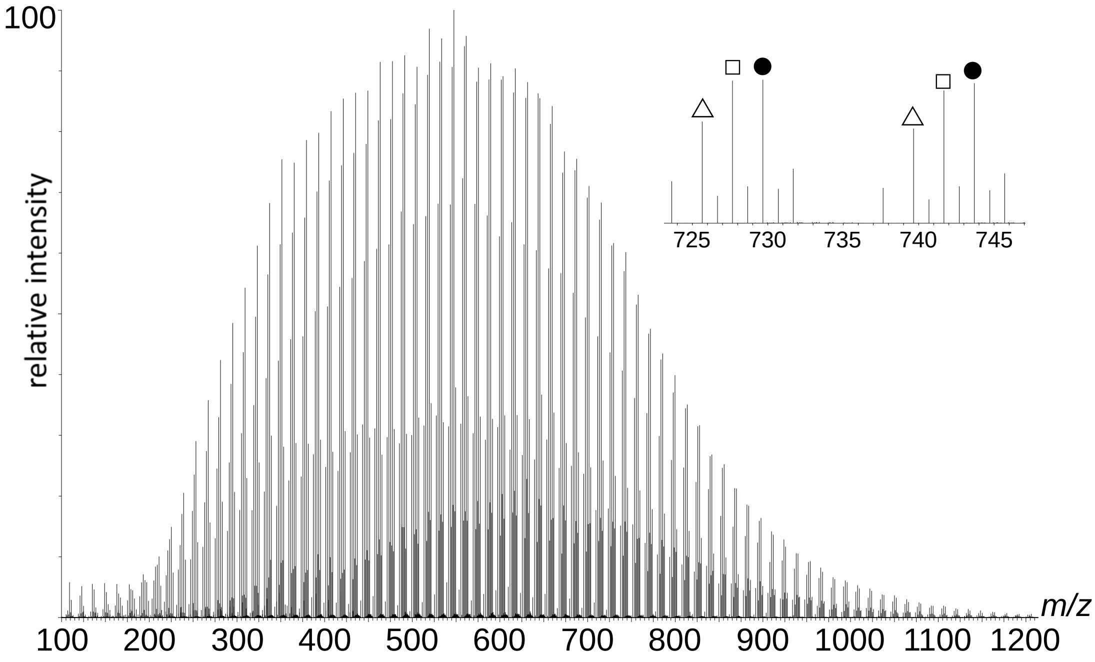

Figure 8.9 ASAP MS of poly(ethylene).

There are series of peaks that correspond to ions differing by 14 Da, the CH_2 repeat sub-unit of PE. PE is synthesised from monomers of ethylene with the molecular formula of C_2H_4, thus a series of peaks corresponding to intact PE would be separated by 28 Da. Therefore, the presence of peaks separated by 14 Da would suggest that in-source fragmentation is occurring.

Table 8.2 Product ion structures corresponding to the series of peaks observed in Figure 4.11.

label	Series formula	Structure	Assignment
●	$C_XH_{2X+1} \pm CH_2$	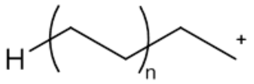	**b_n"/a_n"**
□	$C_XH_{2X-1} \pm CH_2$	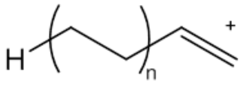	**b_n/a_n**
△	$C_XH_{2X-3} \pm CH_2$	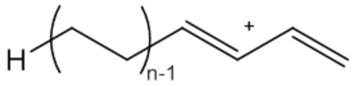	

Calculation of the empirical formula for the observed series highlighted inset in Figure 8.9 allows the generation of potential structures, as shown in Table 8.2. The series of peaks with the highest S/N ration, labelled (●), has a series molecular formula of C_XH_{2X+1}, which corresponds to a linear PE chain present as an even electron hydride abstracted species **$[M - H]^+$**, as shown in Table 8.2. Based on the nomenclature in Figure 8.8, the (●) series of peaks can be assigned as both **a_n"** and **b_n",** dependent upon the number of carbon atoms present in a given ion. Those containing an odd number of carbon atoms are assigned as **a_n"**, while those with an even number are denoted **b_n"**.

The presence of a hydride abstracted species is unusual based on previous work on the ASAP of polymers, however there are two potential methods that can justify the formation of hydride abstracted species. Firstly, Hourani *et al.* suggested that the presence of **$[M - H]^+$** in APCI analysis of linear hydrocarbons involved gas phase ion-molecule reactions with the general mechanism outlined for Analyte (M) in **Equations 8.1 – 8.2**.[269]

$$N_2 + e^- \rightarrow N_2^{\cdot+} + 2e^- \qquad \textbf{(8.1)}$$

$$M^{\cdot+} + N_2^{\cdot+} \rightarrow [M - H]^+ + N_2H^+ \qquad \textbf{(8.2)}$$

This mechanism can be applied to the formation of the PE ions in ASAP, where the generation of the analyte radical cation indicated in **Equation 8.2** is formed by the charge transfer mechanism (Section 2.1.4). Secondly, a proposal adapted from the analysis of hydrocarbons by EI again involves formation of an odd electron radical cation ion species, where the radical is stabilised through backbiting to a more stable secondary radical site, as shown in Figure 8.10. The presence of a radical within the backbone results in sigma bond cleavage, forming an even electron charged species and a radical with a neutral charge. Both of these methods of ionisation are theoretically possible, and consequently neither can be ruled out based on the experiments performed thus far.

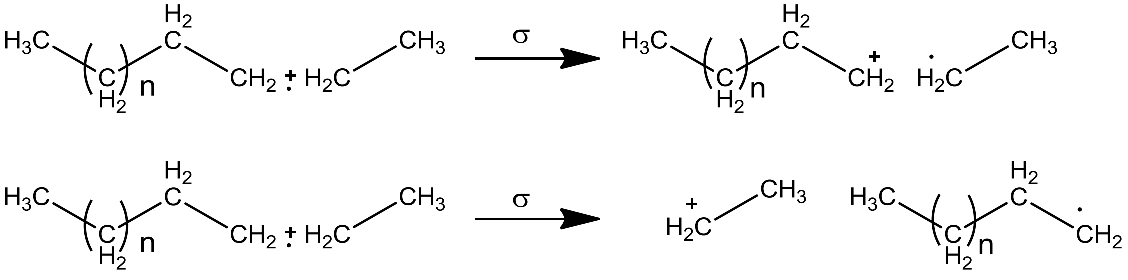

Figure 8.10 Formation of hydride abstracted species by EI.

The second most intense series of peaks that is observed in Figure 8.9, labelled (☐), was found 2 Da below (●), and had a general series molecular formula of C_xH_{2X-1}. This molecular formula corresponds to an alkene structure ionised as a hydride abstracted species, as shown in Table 8.2. This series can again be labelled using the standard nomenclature, where assignment is dependent upon the ion containing odd (**a_n**) or even (**b_n**) numbers of carbon atoms. The third ion series present, labelled (△), is 4 Da lower than (●), and has a general series formula consistent with a dialkene ionised as a hydride abstracted species, as shown in Table 8.2. It is noted that the general structure provided in Table 8.2 accounts for the molecular formula, however the location of the double bonds cannot be determined. Evidence for the formation of unsaturated ions (☐) and (△), can be obtained through investigation of ion series generated by MS analysis of low molecular weight hydrocarbons, which have an identical general molecular formulas to PE. Alkenes were detected in small quantities by APCI, where formation was believed to follow loss of H_2 from the hydride abstracted species.[270] The generation of unsaturated hydrocarbon chains from a saturated polymeric material could also involve a radical driven mechanism. It is important to consider the source of these radicals. Ionisation by ASAP has already demonstrated a capability to ionise polymers as radical cations (Section 4.2.1), however at the elevated temperatures used in ASAP it is important to consider thermal decomposition involving homolytic carbon-carbon bond cleavage. No matter the source of the radical species, the process is likely to involve stabilisation of the radical through backbiting and subsequent loss of a hydrogen radical that generates the alkene double bond, as shown in Figure 8.11.

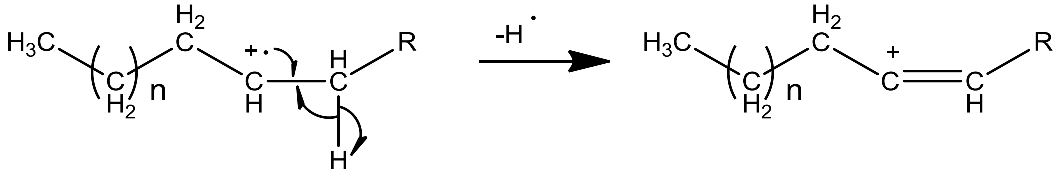

Figure 8.11 Formation of alkene like PE products.

Evidence for the formation of alkenes and dialkenes by thermal decomposition is found in the analysis of low molecular weight hydrocarbons by pyrolysis mass spectrometry.[271] Dialkenes (☐) are believed to result from sequential generation of unsaturated bonds (Figure 8.11). It would therefore appear that ASAP can generate molecules that are consistent with those formed during pyrolysis of related species. Ionisation of these molecules involves hydride abstraction, forming molecular ions consistent with those achieved by APCI and EI.

8.2.5. Influence of chain entanglement upon the observed molecular weight by ASAP MS

Table 8.3 Entanglement properties of polymers analysed by ASAP.

Polymer	Proposed M_n	ASAP spectral base peak	MALDI spectral base peak	Entanglement Molecular Weight (M_e)[272]
PMMA	1000	903.4	925.6	10013
PS	1770	1410.9	1725.5	13309
PEG	1470	811.4	1405.4	1624
PE	N/A	549	-	828

One potential reason for the significant difference in the observed and expected molecular weights may be due to the entanglement properties of the polymers when analysed from the solid state. As polymers approach the proposed entanglement molecular weight values (M_e), the entanglement properties begin to restrict the movement of the polymer chains within the material. For PEG, the spectral base peak observed in ASAP is 570 Da below that observed by MALDI. As the proposed M_n is in close proximity to the experimentally calculated M_e from Fetters *et al.*[272] it could be postulated that the influence of the entanglement properties is restricting the movement particularly of the higher molecular weight polymer chains, especially those above the M_e value. This would demonstrate a preference for the lower molecular weight species, accounting for the observed spectrum. When PS is analysed by ASAP, the observed spectral base peak is 200 Da below that observed in MALDI MS of the same polymer sample, accounting for the charge carriers present. As the M_n of this sample is significantly below the M_e value calculated by Fetters *et al.* it would be expected that the entanglement properties would have little to no influence upon the observed mass spectrum.[272] PMMA, which has the lowest proposed M_n of any polymer examined in this study, generated spectral base peaks in closer agreement when ionised by ASAP and MALDI. Like PS, the M_n of this sample is significantly below the calculated M_e, therefore the entanglement properties are not influencing the movement of the polymer chains, demonstrating good agreement between the techniques. Although there is no molecular weight information available for the PE sample analysed, it is believed to have an M_n value above the calculated M_e. The entanglement properties of the PE sample may be contributing to the number of ions resulting from in-source fragmentation that are observed in the ASAP mass spectrum for PE. However, PMMA demonstrates significant in-source fragmentation, which based on the M_n and M_e properties of the polymer are unlikely to be contributed by the entanglement properties, therefore it may be considered a source of fragmentation in certain situations, but is by no means the only source of in-source fragmentation.

8.3. Optimising ion source parameters for ASAP of synthetic polymers

The intention of this mass spectrometric analysis is to develop a methodology to optimise the S/N ratio of intact positively charged polymer ions, in order to further investigate the aspects of the mass spectrometer that affect those observations, and to ultimately understand the consequences of the mass spectrometer's parameters and how they affect the results. This will allow the development of experimental protocols to maximise the amount of analytical data for a given polymer, and allow the data to be interpreted accurately, correctly and with confidence. To assess the application of ASAP for the analysis of synthetic polymers, numerous variables were evaluated independently to establish their impact upon the molecular ion generated and the observed mass spectrum, these include:

- APCI Corona Current.
- Sampling Cone Voltage.
- Extraction Cone Voltage.
- Source Temperature.
- Desolvation Gas Temperature.
- Desolvation Gas Flow.

These parameters, or close equivalents, are common to many API oaToF mass spectrometers, and thus the developments made here could be easily extended to other systems. The majority of API systems are configured to supply a high pressure flow of nitrogen to facilitate API, therefore optimisation of ASAP with only adjustments to software settings is preferable to modifying hardware parameters. Ion transmission and mass analyser parameters were validated initially using an ESI source with each polymer to produce optimal signals. The interchangeable source housing of the Xevo makes this a facile process.

The role of the desolvation gas is to provide a temperature controlled means of vapourising the analyte, and to act as a source of charge to induce sample ionisation through ion-molecule reactions. Nitrogen has been utilised extensively in this role, as it is an inert gas that is stable at high temperatures. Nitrogen is capable of accessing vibronic excited states, permitting ionisation in the presence of a corona discharge, forming $N_2^{+\bullet}$ radicals. These radical species are formed even in the presence of analytes with lower ionisation energies, due to the significant excess of nitrogen molecules present in the ionisation process akin to APCI.[221] However, the desirable gas properties for ASAP are not restricted to nitrogen, inert gases such as helium, argon and neon provide potential alternatives. DART makes use of the fact that helium can access suitable electronic excitation states to provide metastable ions that can successfully ionise non-polar and polar analytes.[96] The larger noble gases argon and neon also have characteristics suitable for a desolvation gas with excitation states of lower energy than helium,[225] however excited argon atoms have been shown to be rapidly quenched in the presence of water vapour,[273] a less than ideal quality for use in an atmospheric pressure source. Further considerations when determining the suitability of a gas for a role as a desolvation gas are the relative ionisation energies of the gas, and the cost and availability of the gas at sufficient purity for the desired application.

8.3.1. Desolvation gas temperature

Initial experiments demonstrated that the temperature of the desolvation gas had the greatest influence upon the molecular weight distribution. To demonstrate the impact of the temperature of the desolvation gas, all other parameters were fixed at constant values and spectra were acquired at 100 °C intervals. The resultant data are presented in Figure 8.12.

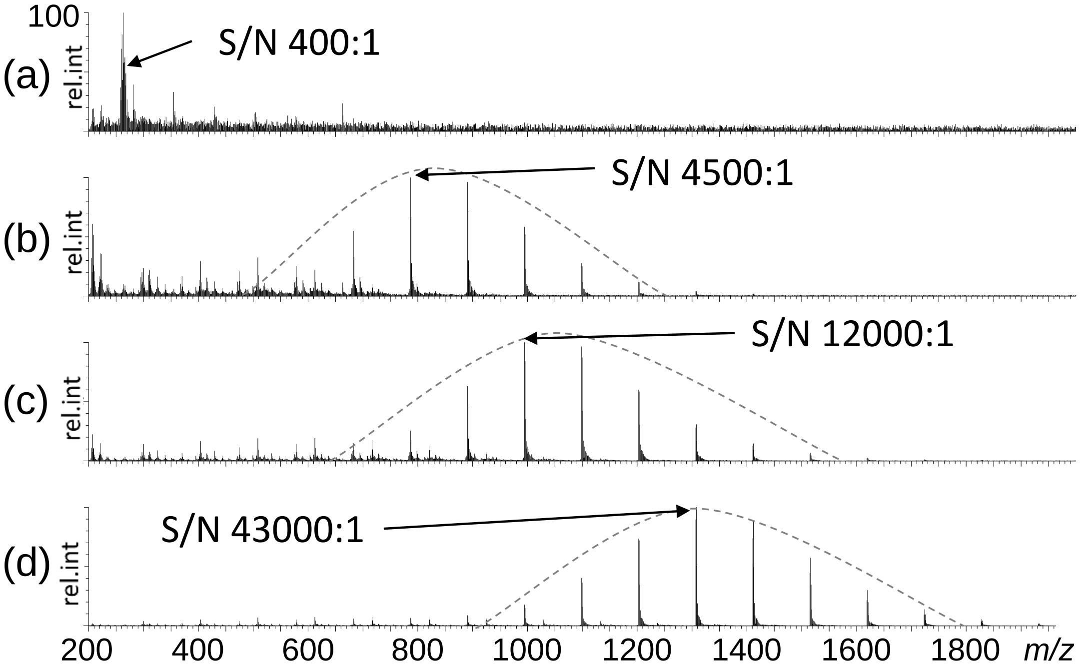

Figure 8.12 The effect of desolvation gas temperature upon ASAP of Poly(styrene) at (a) 300°C, (b) 400°C, (c) 500°C and (d) 600°C (all spectra represent 50 ToF scans).

From the data displayed in Figure 8.12, there is a clear correlation between the desolvation gas temperature and the mass spectrum that is observed. In Figure 8.12(a) at 300 °C, the desolvation gas temperature is only sufficient to volatilise molecules in the lowest *m/z* region of the spectrum. The little ionisation that has occurred generates signals with low S/N ratios, where the ions that are separated by 104 Da are only just visible above the background noise when the chromatogram is summed over 50 scans. An increase in the desolvation gas temperature to 400 °C (Figure 8.12(b)) demonstrates a notable improvement in the amount of information that can be obtained, and represents the minimum temperature from which a molecular weight distribution can be generated for this sample of PS. At 400 °C (Figure 8.12(b)) higher mass molecules are being ionised compared to 300 °C, as the molecular weight distribution spans the mass range from *m/z* 682.4 to *m/z* 1410.9. In the subsequent spectra (c) and (d), where the desolvation gas is further heated to 500 °C and 600 °C respectively, the spectral base peak in the distribution increases with final value for (d) at *m/z* 1410.9. Despite the highest achievable gas temperature being utilised, the centre of the distribution falls some way below the M_n = 1770 Da. However, it is a reasonable to put forward the hypothesis that increasing the temperature of the desolvation gas results in vapourisation of larger polymer chains that are invariably detected by the mass spectrometer, providing a trend consistent with that observed here.

A second correlation is shown in Figure 8.12, where the S/N of the base peak in each spectrum increases with desolvation gas temperature. Initially, at 300 °C, the S/N ratio of the base peak at *m/z* 262.8 is 400:1 (Figure 8.12(a)). This increases significantly to a ratio of 43000:1 for *m/z* 1410.9 at 600 °C (Figure 8.12(d)). As the *m/z* of the spectral base peak approaches the expected M_n of the sample (1770 Da), the peaks are expected to have a larger S/N ratio, as they represent a greater proportion of the sample than peaks more distant from the M_n. To establish whether this change in S/N was influenced by the higher proportion of molecules with a molecular weight closer to the polymer M_n, a single degree of polymerisation was monitored at the different temperatures. The peak at *m/z* 1098.7 corresponds to PS_{10}, which contains ten styrene units, and both terminal groups was observed at 400 °C with a S/N ratio is 600:1 (Figure 8.12(b)). Increasing the desolvation gas to temperature to 600 °C resulted in an increase in the S/N ratio to 12500:1 (Figure 8.12(d)). It was therefore decided that 600 °C, the maximum desolvation gas temperature investigated, would be used in the tandem MS experiments as it allowed the highest weight molecular ions to be observed, and generated the spectrum with the best S/N ratio.

Given the use of solid PS in Figure 8.12, it is important to eliminate sample loading variability as a factor in the increase in S/N ratio with desolvation gas temperatures. Therefore, PS was dissolved in acetone to a concentration of 10 mg mL^{-1}, whereupon 2 µl of the solution was pipetted onto the probe tip, thus minimising the error in sample loading. The resultant spectra are presented in Figure 8.13.

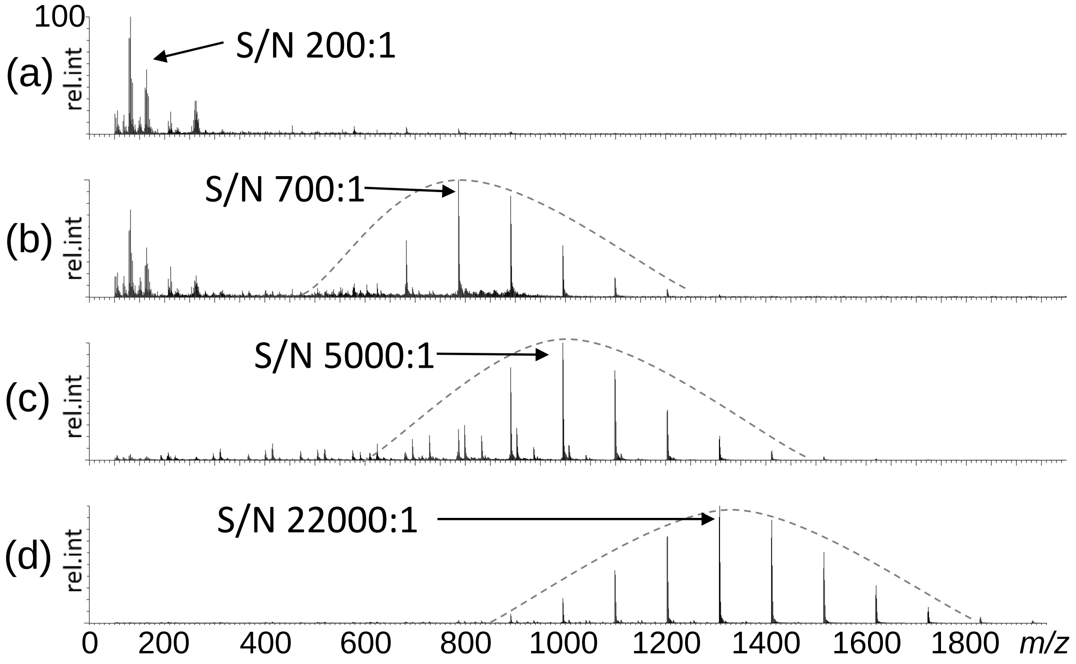

Figure 8.13 ASAP MS of PS (10 mg/ml in Acetone) (a) 300 °C, (b) 400 °C, (c) 500 °C and (d) 600 °C.

It is clear from the data in Figure 8.13 that the S/N ratio of the spectral base peak increases with desolvation gas temperature. The observation of an identical trend to the solid phase PS experiments confirms that the desolvation gas temperature is a major contributor to the S/N ratio of the molecular weight distribution, and that the previously observed trends are not dependent on sample loading.

When PEG is analysed using ASAP at the different desolvation gas temperatures, the resultant spectra reinforced the correlations previously observed for PS, as shown in Figure 8.14. An increase in the desolvation gas temperature results in a shift in the molecular weight distribution to the higher mass range. At 300 °C (Figure 8.14(a)), the molecular weight distribution has a spectrum base peak at *m/z* 399.2, and upon heating to 600 °C the spectrum base peak increases to *m/z* 811.4 (Figure 8.14(d)). The correlation of S/N ratio with desolvation gas temperature confirms the observation made for PS, with the spectrum base peak increasing from 25000:1 in Figure 8.14(a), to 310000:1 in Figure 8.14(d). From inspection of Figure 8.14, it is clear that increasing the desolvation gas temperature from 300 °C (Figure 8.14(b)) to 400 °C (Figure 8.14(c)) has led to a dramatic change in the spectrum observed, where the S/N ratio of the protonated molecular ion increases significantly relative to the ions formed by in-source fragmentation. As seen in all of the experiments, the molecular weight distribution varies significantly depending on the temperature. A desolvation gas temperature of 600 °C was selected for tandem MS experiments, as it was shown to generate the highest molecular weight intact ion with the greatest S/N ratio.

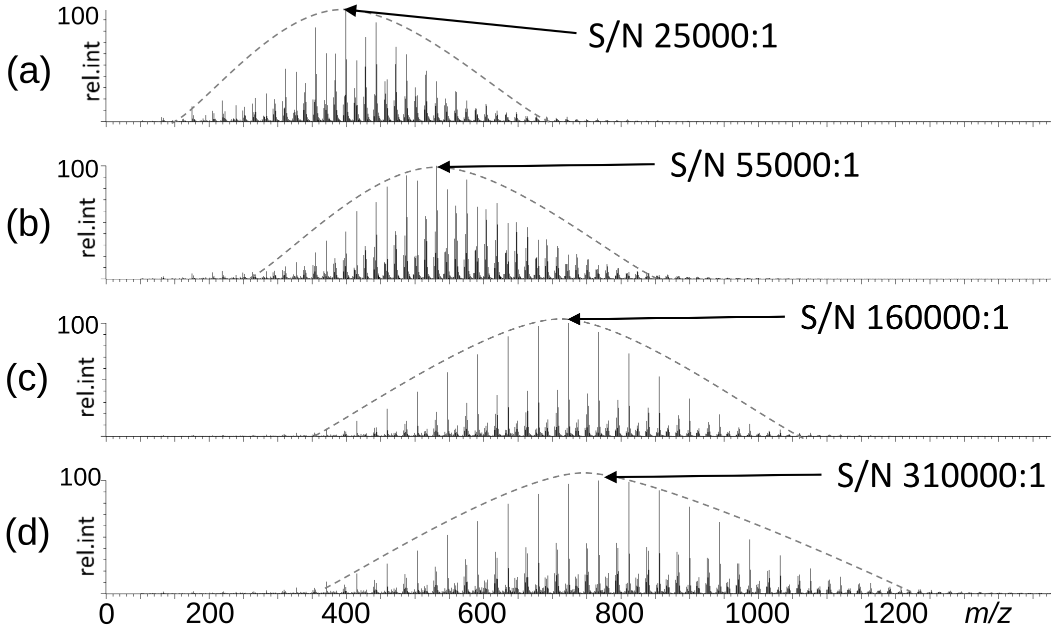

Figure 8.14 The effect of desolvation gas temperature upon ASAP of Poly(ethylene glycol) at (a) 300°C, (b) 400°C, (c) 500°C and (d) 600°C (all spectra represent 50 ToF scans).

8.3.2. Sample Cone Voltage

The maximum desolvation gas temperature examined (600 °C) was found to generate a molecular weight distribution with a value of M_n closest to the value measured by MALDI (Figure 8.2), and the greatest S/N ratio for the intact oligomers. Initial analysis of PS indicated the presence of additional series of peaks formed by in-source dissociation (Figure 8.1). It was found that in-source fragmentation could be influenced through manipulation of ion source parameters. The first parameter to be investigated was the voltage of the sample cone. In this series of experiments, the desolvation gas temperature was fixed to 600 °C and the sample cone voltage was recorded at 10 eV intervals. The resultant mass spectra for solid PS are provided in Figure 8.15.

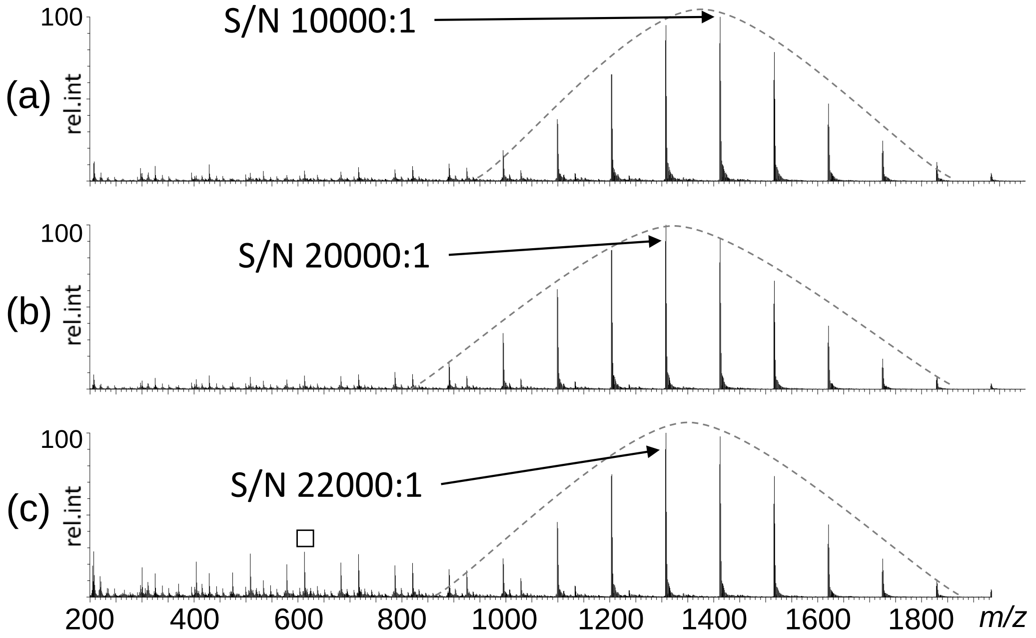

Figure 8.15 The effect of sample cone voltage upon ASAP of solid PS at (a) 20eV, (b) 30 eV and (c) 40 eV. ■ = *m/z* 612.4, the most intense ion formed by in-source dissociation.

It can be seen from all of the spectra featured in Figure 8.15 that varying the sample cone voltage has little visible effect on the observed molecular weight distribution, compared with the desolvation gas temperature. The two effects that a change in sample cone voltage has on the ASAP mass spectrum of PS are variance in the S/N ratio of the spectrum base peak and the degree of in-source fragmentation observed. The spectral base peak is observed to fluctuate between *m/z* 1410.9, which corresponds to PS_{13}, and *m/z* 1306.9, which corresponds to PS_{12}. One correlation that is apparent is the increasing S/N ratio of the spectral base peak as the sample cone voltage increases. Increasing the sampling cone voltage from 20 eV in Figure 8.15(a) to 30 eV in Figure 8.15(b) has in effect doubled the S/N ratio of the ions of interest; this is attributed to the higher potential difference being able to draw ions into the mass spectrometer more effectively. A further increase in sample cone voltage to 40 eV produces a marginal increase in the S/N ratio of the base peak, however this is not as significant as the change from 20 eV to 30 eV. Figure 8.15 also shows that varying the sampling cone voltage has a degree of influence upon the degree of in-source fragmentation that is observed. In Figure 8.15 (a), where the sample cone voltage is 20 eV, there is minimal in-source fragmentation; on increasing the sampling cone voltage the intensity of the peaks generated by in-source fragmentation increases significantly relative to the spectral base peak. Indeed, at 40 eV the most intense peak generated by in-source fragmentation (*m/z* 612.4 labelled (☐) in Figure 8.15 (c)) has an S/N ratio that is 30% of the spectral base peak (*m/z* 1410.9). Given that in-source fragmentation is likely to diminish the S/N ratio of the intact PS ions, but the S/N ratio of the intact ions increases with sample cone voltage, it appears that two competing mechanisms present. It is noted, however, that the S/N ratio of the peaks for ions formed by in-source fragmentation become more pronounced at higher sample cone voltages, where the trend is likely to increase if higher sample cone voltages were investigated.

It was therefore decided that the optimal level for the sample cone voltage was viewed to be 30 eV, as this level represented a compromise between significant improvement in the S/N ratio of the spectrum base peak, whilst minimising the impact of ions generated by in-source fragmentation.

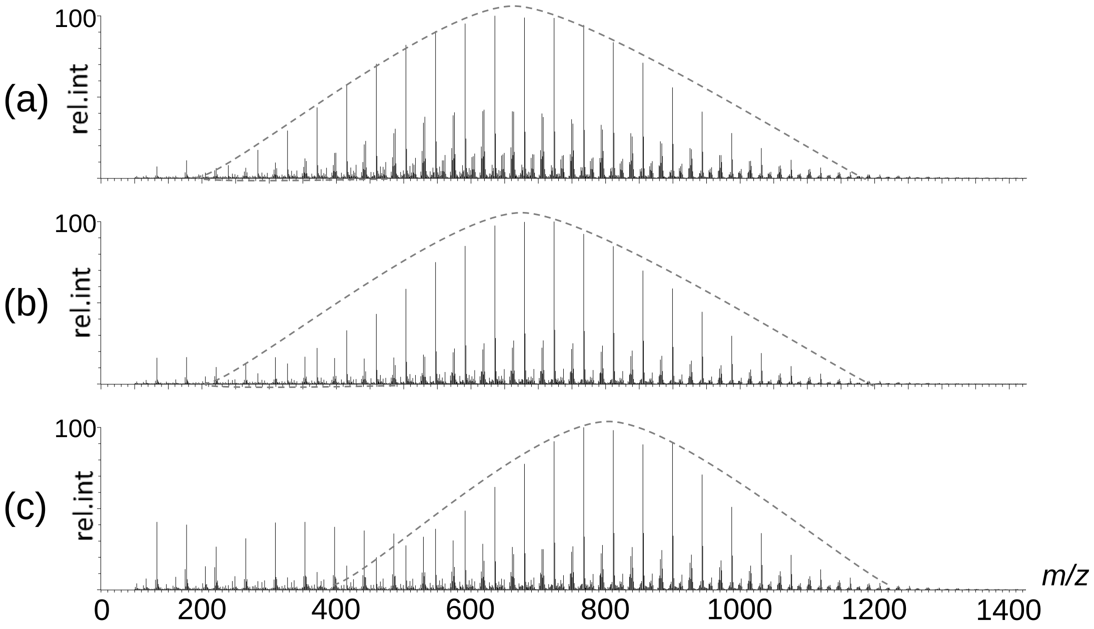

Figure 8.16 The effect of sample cone voltage upon ASAP of solid PEG at (a) 20eV, (b) 30 eV and (c) 40 eV.

In a corresponding experiment using PEG, a similar trend was identified, where increasing the sampling cone voltage led to little change in the molecular weight distribution, with the spectral base peak increasing from *m/z* 635.3 in Figure 8.16(a) to *m/z* 767.4 in Figure 8.16(d). The S/N ratio of the spectral base peak increased with sampling cone voltage from 80000:1 to 260000:1. However, the amount of in-source dissociation increases significantly with sample cone voltage. At a sample cone voltage of 40 eV, the most intense peak generated by in-source dissociation (*m/z* 133.1) has a S/N ratio that is 40% that of the [PEG + H] peak at *m/z* 767.4. The sample cone voltage that was selected for tandem MS experiments was 30 eV, as again there was notable improvement in the S/N ratio of the intact ion, with minimal change in the amount of in-source fragmentation observed.

8.3.3. Extraction Cone Voltage

During evaluation of the ion source, the voltage of the extraction cone was found to be a significant contributor to in-source fragmentation. The role of the extraction cone is to use electrostatic forces to extract ions from the atmospheric pressure region to the intermediate vacuum region, thus increasing the number of ions entering the mass spectrometer.

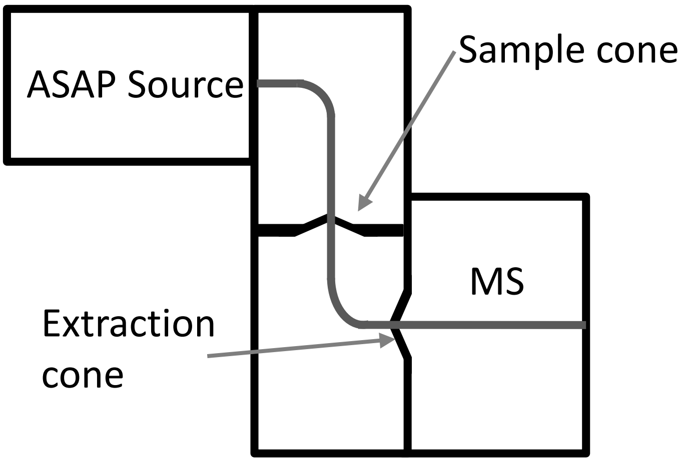

Figure 8.17 Schematic of ASAP ion source highlighting the sample cone and extraction cone.

As shown in the schematic of the source in Figure 8.17, the sample cone and extraction cone are in close proximity where the voltages applied to each are related. The sample cone which determines the voltage difference between the sample and extraction cones typically utilises voltages in the region of 10 V-100 V, where high voltages can cause in-source fragmentation, as shown in Section 8.3.2. The extraction cone voltage determines the voltage difference between the extraction cone and the next stage of ion transfer, where the voltage range is lower than that of the sample cone and is used to enhance ion transmission.

When high potential differences are used, ions are accelerated more quickly through a region of intermediate vacuum, which results in collisions that can induce fragmentation. With all other variables retained at constant values (600 °C, desolvation gas temperature and 30 eV sampling cone voltage), the voltage applied to the extraction cone was increased by incremental values, as shown in Figure 8.18. When the extraction cone voltage is increased from 0 V to 3 V there is little change in the observed molecular weight distribution, with the spectral base peak once again only fluctuating between PS_{12} and PS_{13}. At the lower extraction cone voltages there is no evidence of in-source fragmentation; however an extraction cone voltage of 3 V demonstrates the presence of in-source fragment ions. Despite the observed in-source fragmentation, the extraction cone performs its role; leading to an improved S/N ratio for the intact PS molecular ions with minimal change in the molecular weight distribution. It was therefore decided that an extraction cone voltage of 2 V would be utilised in tandem MS experiments, as it represented a high S/N ratio for the intact molecular ion with minimal fragmentation.

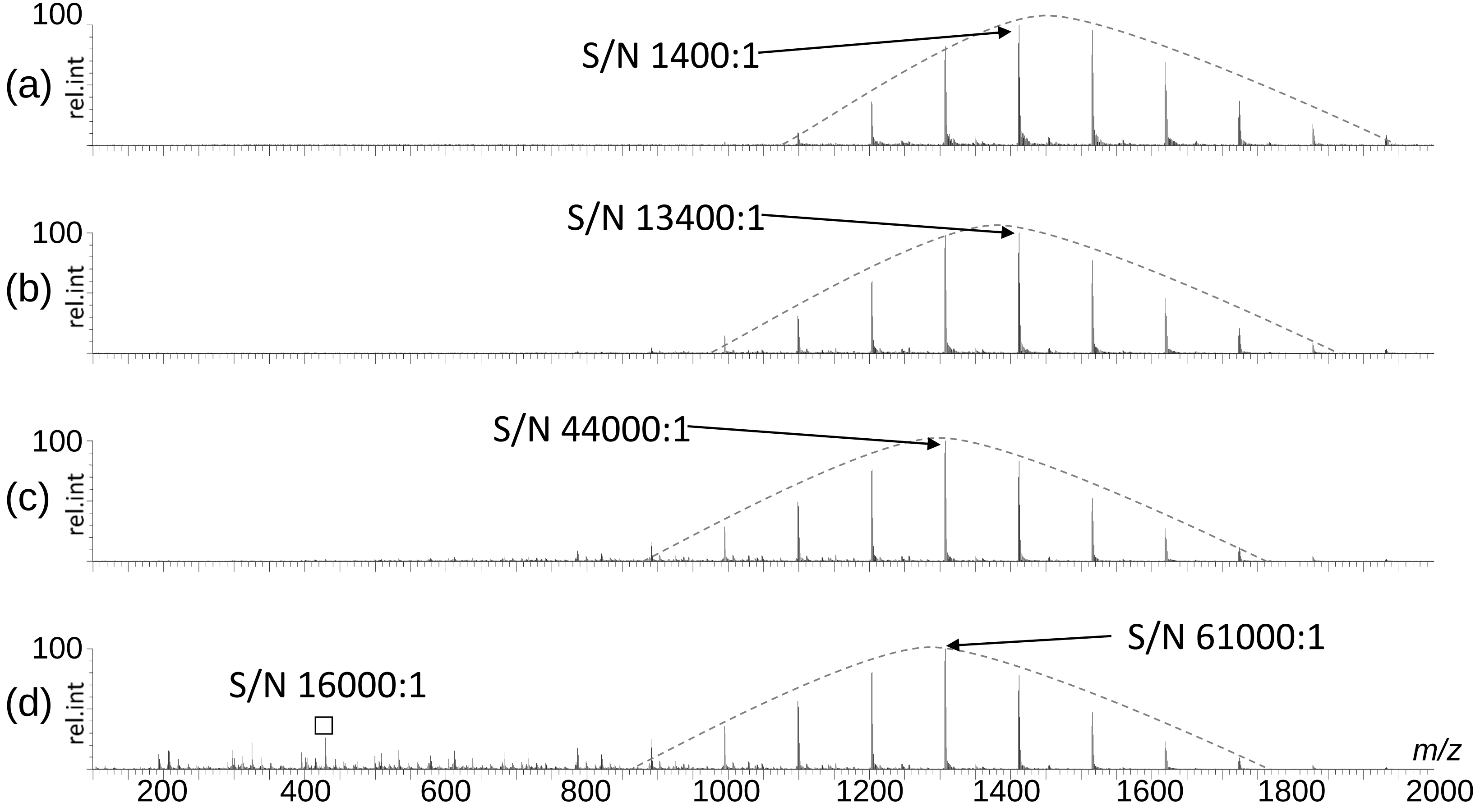

Figure 8.18 The effect of extraction cone voltage upon ASAP of solid PS at (a) 0 V, (b) 1 V, (c) 2 V and (d) 3 V, (spectra acquired through summation of 50 ToF scans).

8.4. Investigating the observed in-source dissociation of PEG

Optimisation of source parameters was shown to be an effective method with which to minimise fragmentation of PS, however evidence of in-source fragmentation could not be eliminated from ASAP analysis of PEG. Based on the ions generated by in-source fragmentation and the presence of these product ions in previous citations,[266,274] two major theories were investigated.

Firstly, using an ASAP ion source where the desolvation gas temperature can achieve 600°C raises the issue of thermal decomposition for the analysis of PEG.[275] Work by Lattimer demonstrated the formation of $\mathbf{a_n}''$ and $\mathbf{b_n}''$ ions when MALDI MS analysis was performed on a PEG sample that had been thermally degraded.[266] An investigation into the effect of temperature on the dissociation of PEG was performed, where (11.41 mg) of PEG M_n = 1430 was placed inside a gas chromatography oven at a temperature of 150 °C. MALDI ToF MS analysis of the resultant thermally decomposed PEG was performed by dissolving the sample in tetrahydrofuran (THF) and applying this solution to the ground steel MALDI target plate using the dried droplet method. A sample of PEG that was not thermally decomposed was prepared using an identical sample preparation, the MALDI spectra generated are provided in Figure 8.19. Thermal decomposition at 150 °C preserves the molecular weight distribution as shown in Figure 8.19(b), however there is evidence of other series of peaks present. The expansion in Figure 8.19(b) allows the full assignment of the three series of peaks, with the most intense series of peaks, as expected, corresponding to the intact polymer molecular ion present with a sodium cation. The two subsequent series of peaks correspond to the ions $\mathbf{a_n}''$ and $\mathbf{b_n}''$, both of which were observed in the ASAP full MS spectrum of PEG (Figure 8.4). Despite the thermal decompositions occurring on different time scales, minutes in this pyrolysis experiment and seconds in ASAP and different temperatures, the presence of $\mathbf{a_n}''$ and $\mathbf{b_n}''$ ions confirms that thermal decomposition can yield molecules that generate ions with identical *m/z* values to those observed in ASAP MS of PEG. As ASAP analysis was performed at a much higher temperature, reaching 600 °C, it is highly likely that analysis by ASAP resulted in thermal decomposition. The results observed here are supported by the previous work of Lattimer, who proposed that thermal decomposition of PEG was free radical in nature with preferential homolytic cleavage of the C-O bond.[266] The results observed in the inset in Figure 8.19(b) are in line with this proposition, as demonstrated by the superior S/N ratio of the $\mathbf{b_n}''$ ion generated through C-O bond cleavage when compared with the $\mathbf{a_n}''$ ion, which involved homolytic cleavage of the stronger C-C bond.

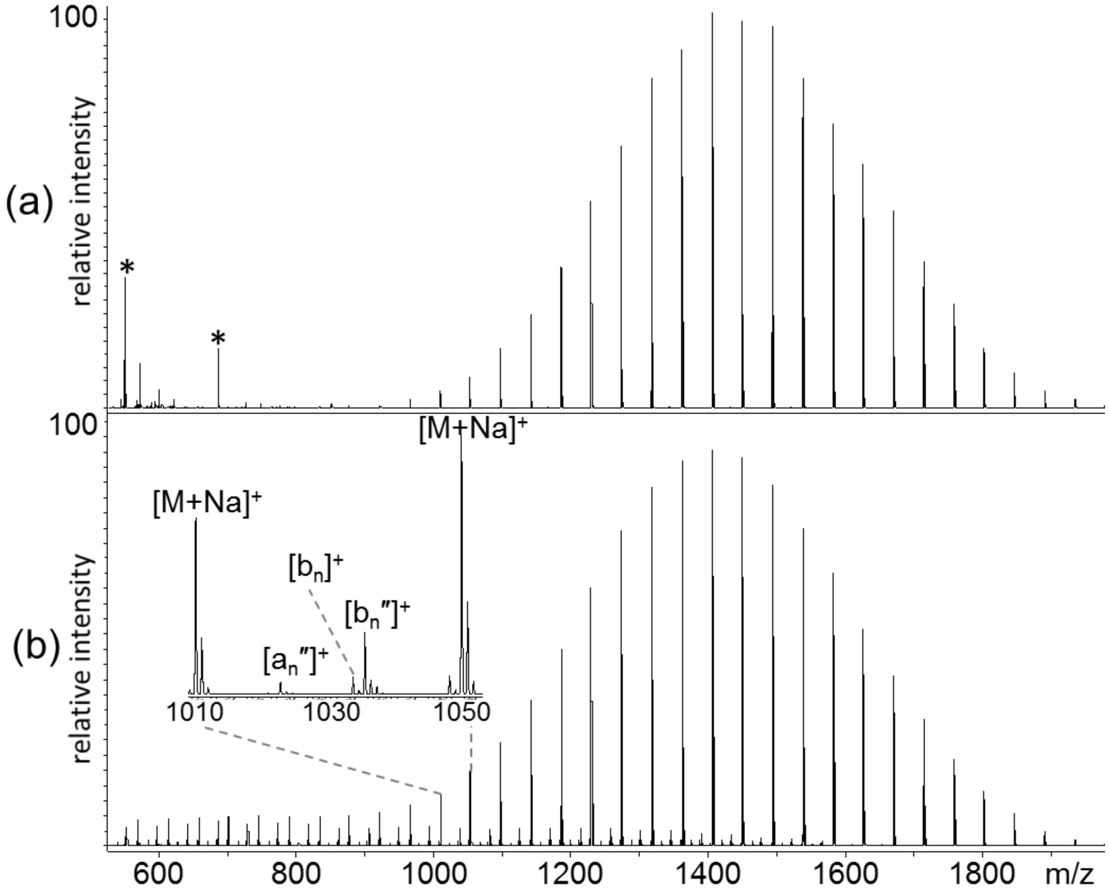

Figure 8.19 MALDI MS of PEG using DHB and NaI (a) untreated sample and (b) thermally decomposed for 30 minutes at 150 °C (* indicates NaI clusters).

Secondly, the work of Onigbinde *et al.* who performed GC-EI-MS on low molecular weight PEGs, proposed that $\mathbf{a_n}''$ and $\mathbf{b_n}''$ ions observed during in-source fragmentation may result from the decomposition of unstable PEG radical cations at a GC injection temperature of 250 °C.[274] ASAP has the capability to generate both radical cation and protonated molecular ions formed simultaneously.[226] Therefore, the decomposition of a PEG radical cation to form in-source fragmentation ions is theoretically possible. The method of ionisation is not only dependent on the chemistry of the analyte (such as proton affinity and polarity) but also on the conditions within the ion source. Ray *et al.* demonstrated that one ionisation mechanism could be favoured by altering the source conditions. It was discovered that flooding the source with a protic solvent mixture, such as methanol: water (50:50), created a 'wet' source that favoured the proton transfer mechanism.[226] As there was no $[\mathrm{PEG}]^{+\bullet}$ observed under full MS conditions, it was of interest to determine the effect of the source conditions upon the mass spectrum.

In this work, source conditions referred to as 'dry' involve a desolvation gas temperature of 600 °C which heated the source for 20 minutes prior to analysis. This process created a source that is as dry as can be reasonably achieved, where this method has been shown to limit the amount of water present.[276] Wet source conditions were created by infusing methanol: water (50:50) into the ASAP ion source using the auxiliary lockspray port. The source was flooded with the solvent mixture at 100 µL/min prior to analysis, and spectra were acquired with this infusion rate maintained throughout the measurement. In order to provide data that could be compared for both ion source conditions, the intensities of all ion peaks were measured for ten degrees of polymerisation, from n = 7 to n = 17. The intensities of each ion type were summed and then converted to percentage of the total ion intensity. The resultant data is displayed graphically in Figure 8.20.

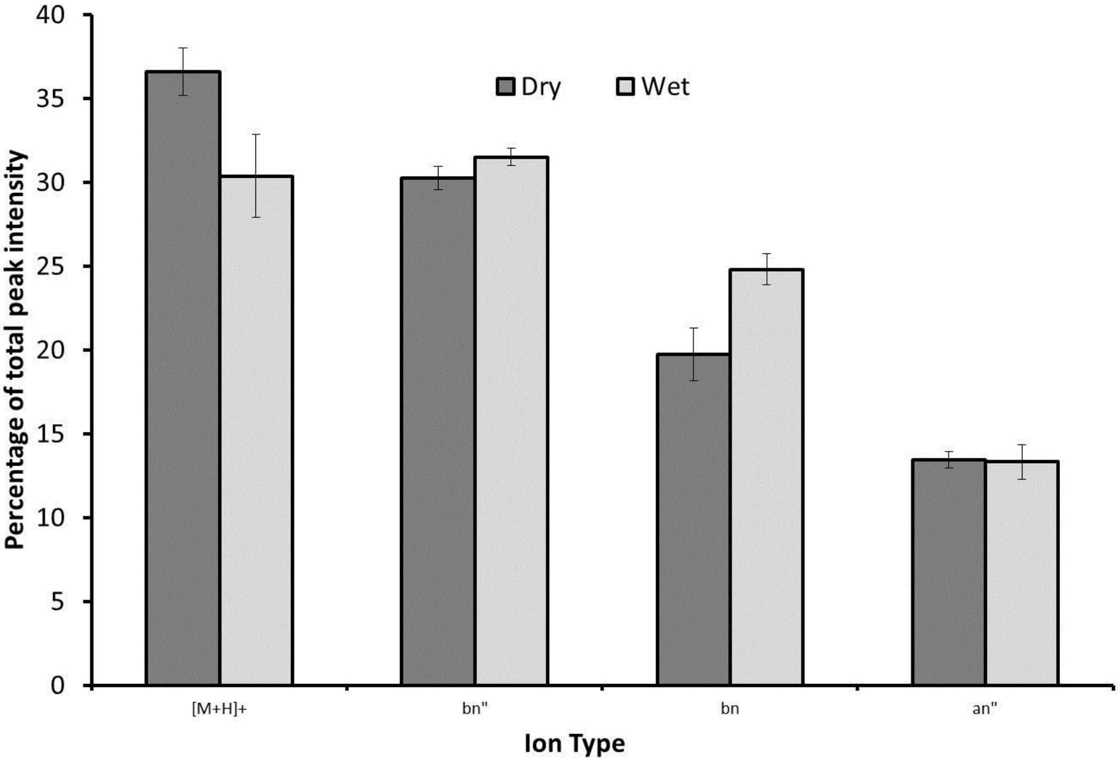

Figure 8.20 Change in peak intensities for PEG ions recorded using ASAP under different source conditions.

The results of Figure 8.20 demonstrate that changes in the source conditions did not affect all of the observed ion series. The percentage of the total peak intensities for $\mathbf{b_n}''$ and $\mathbf{a_n}''$ ions, which were previously identified as ions formed by thermal decomposition of PEG, demonstrate minimal variance under the different source conditions where the change is within the experimental error. This observation suggests that these ions do not form *via* a radical cation intermediate, providing additional support for the formation of these ions by thermal decomposition. It can be seen that the addition of solvent to the ion source, creating a 'wet' source, leads to a reduction in the percentage of total peak intensity of $\mathbf{[PEG+H]^+}$ and an increase in the percentage represented by the $\mathbf{b_n}$ ions. As $\mathbf{b_n}$ is the major ion series that results from CID tandem MS of PEG,[87] the observed change would suggest that the addition of solvent molecules creates a hostile environment within the source, which leads to in-source fragmentation of the polymer generating the $\mathbf{b_n}$ ions.

8.5. CID Tandem Mass Spectrometry

8.5.1. Tandem MS of PS

Using ion source parameters to give the highest S/N ratio with minimal in-source fragmentation, CID was performed on $[PS]^{+\bullet}$ to gain additional information regarding the polymeric structure. The precursor ion selected for tandem mass spectrometry experiments was $\mathbf{[PS_{14}]^{+\bullet}}$, which is an intact radical cation containing 14 styrene monomer units. CID of $\mathbf{[PS_{14}]^{+\bullet}}$ using argon as the collision gas generated the spectrum shown in Figure 8.21.

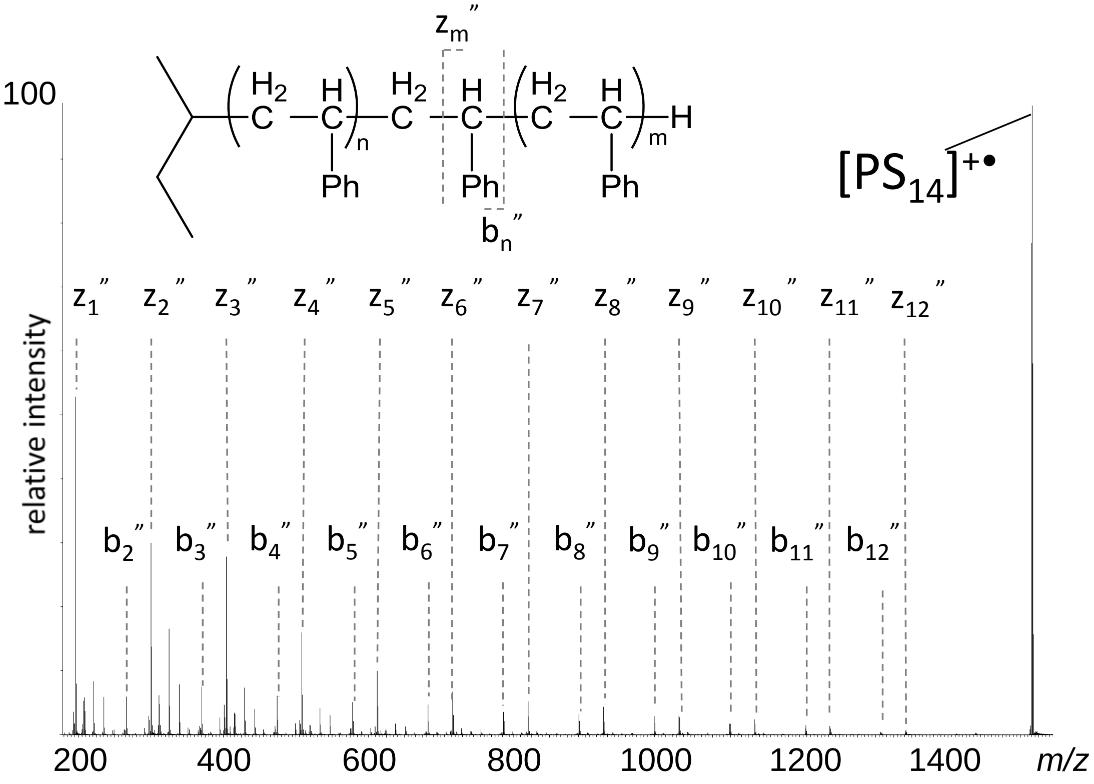

Figure 8.21 CID tandem MS of PS_{14} ($[C_4H_9(C_8H_8)_{14}H]^{+\bullet}$), inset structure of Poly(styrene), annotated to indicate cleavage sites and nomenclature used to differentiate between resulting product ions.

The product ions observed are labelled as $\mathbf{b_n''}$ and $\mathbf{z_m''}$, which correspond to specific backbone bond cleavages that include initiating and terminating end groups respectively, as shown inset in Figure 8.21. Figure 8.21 demonstrates that significant fragmentation has occurred during CID of the radical cation, generating product ions that provide structural information for 12 of the 14 monomer units present in the precursor ion. The two distinct product ion series originate in the low *m/z* region from the terminal groups, where $\mathbf{b_n}''$ contains the C_4H_9 initiating group and $\mathbf{z_m}''$ contains the H terminating group, and the *m/z* difference between the peaks corresponds to the mass of the styrene monomer unit of 104 Da (C_8H_8). The extent of fragmentation, as characterised by the number and type of product ion, in ASAP CID MS/MS is comparable to the MALDI CID MS/MS of the silver adducted species, as shown in Figure 8.22.

As shown inset in Figure 8.21, both product ion series are generated through fragmentation adjacent to the CH(Ph) group, which forms the basis of the new saturated CH_2(Ph) terminal group. As fragmentation of the C-C bond is likely to be via homolytic bond cleavage, fragmentation at the secondary carbon centre of CH(Ph) is preferable, as it is a more stable radical site than the primary CH_2, thus permitting hydrogen transfer to form the chain end. Closer inspection of the tandem MS spectrum in Figure 8.21 reveals that the product ions in the lower *m/z* region of the spectrum have the greatest S/N ratio, with the maximum at $\mathbf{z_1}''$. This would suggest that formation of the lower *m/z* product ions is preferential to the higher *m/z* species, and that fragmentation is more prevalent close to the polymer chain ends. The S/N ratio of the $\mathbf{z_m}''$ product ions compared to the $\mathbf{b_n}''$ ions below *m/z* 400 would suggest that backbone bond cleavage in the proximity of the C_4H_9 initiating group is preferential to the H terminating group. The product ions generated here by tandem mass spectrometry are similar to those generated previously by in-source fragmentation (Figure 8.1). In contrast, MALDI-CID (Figure 8.22) generates predominantly unsaturated $\mathbf{a_n}$ and $\mathbf{y_m}$ product ions, indicating that different fragmentation mechanisms exist for the different precursor ions. The mechanistic differences may be due to the precursor ions, where an odd-electron radical cation generates predominantly unsaturated **b** and **z** type ions, whereas an even-electron silver adducted species produce **a** and **y** type ions.

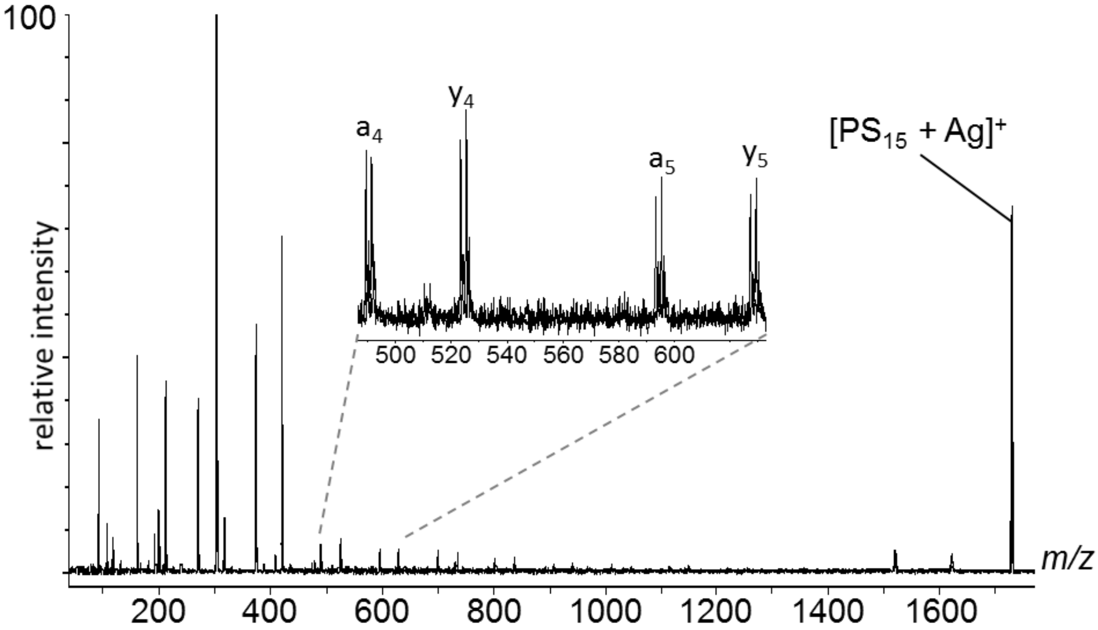

Figure 8.22 MALDI CID tandem MS of PS_{15} ($[C_4H_9(C_8H_8)_{15}H + Ag]^+$).

Mechanistic studies by Polce *et al.* proposed that the MALDI-CID of $\mathbf{[PS+Ag]^+}$ involved homolytic cleavage of the CH_2-CH(Ph) bond, as suggested for ASAP, where the radical is initially more stable at the secondary carbon centre. To generate the observed $\mathbf{a_n}$ and $\mathbf{y_m}$ ions, (pathway **i** in Scheme 8.1) the intermediate undergoes a (1,5 – H rearrangement) and subsequent β C-C bond cleavage.[143] Pathway **ii** in Scheme 8.1 generates the $\mathbf{b_n}^\bullet$ and $\mathbf{z_m}^\bullet$ radical species, which undergoes a hydrogen shift to generate the observed $\mathbf{b_n}''$ and $\mathbf{z_m}''$ product ions.

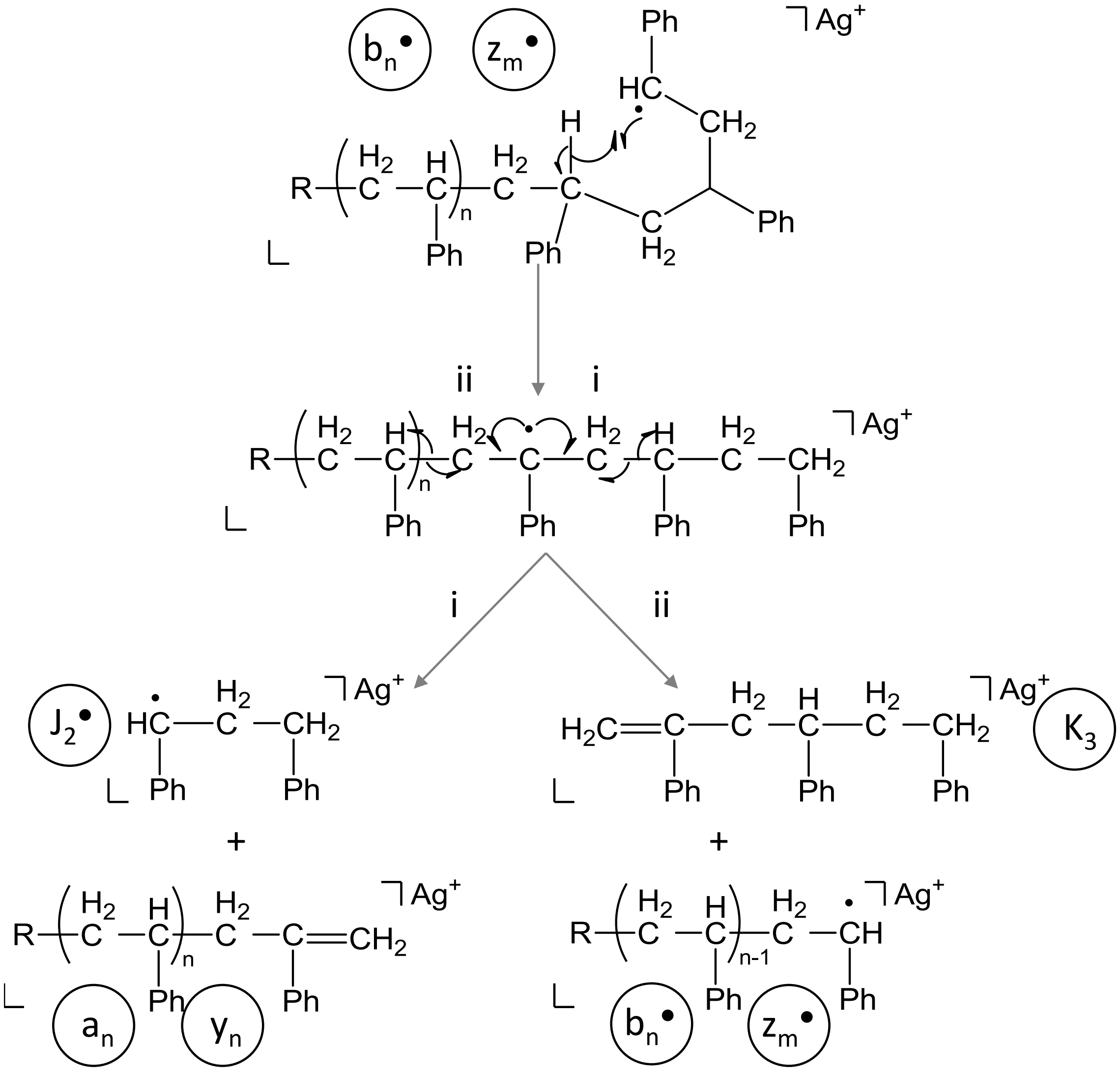

Scheme 8.1 Backbiting (1,5 H rearrangement) and subsequent C-C Bond scission in the benzylic radical ion. Reproduced from Polce *et al.*[20]

PS radical cations have been observed previously in EI MS, where the precursor ions fragmented readily under activated conditions to generate $\mathbf{b_n}''$ and $\mathbf{z_m}''$ as the dominant product ion series.[264] Jones *et al.* proposed that these product ions were generated through homolytic backbone cleavage, generating the secondary radical, where the addition of a hydrogen radical leads to the formation of the saturated chain end.[264] ASAP provides a method of accessing higher *m/z* $[PS]^{+\bullet}$ species that are sufficiently unstable that they readily fragment under low energy CID conditions, to yield comparable information to that obtained from EI MS.

8.5.2. Tandem MS of PEG

In a parallel experiment, **[PEG$_{22}$ + H]$^+$** selected for CID tandem mass spectrometry experiments. The resultant spectrum is included in Figure 8.23.

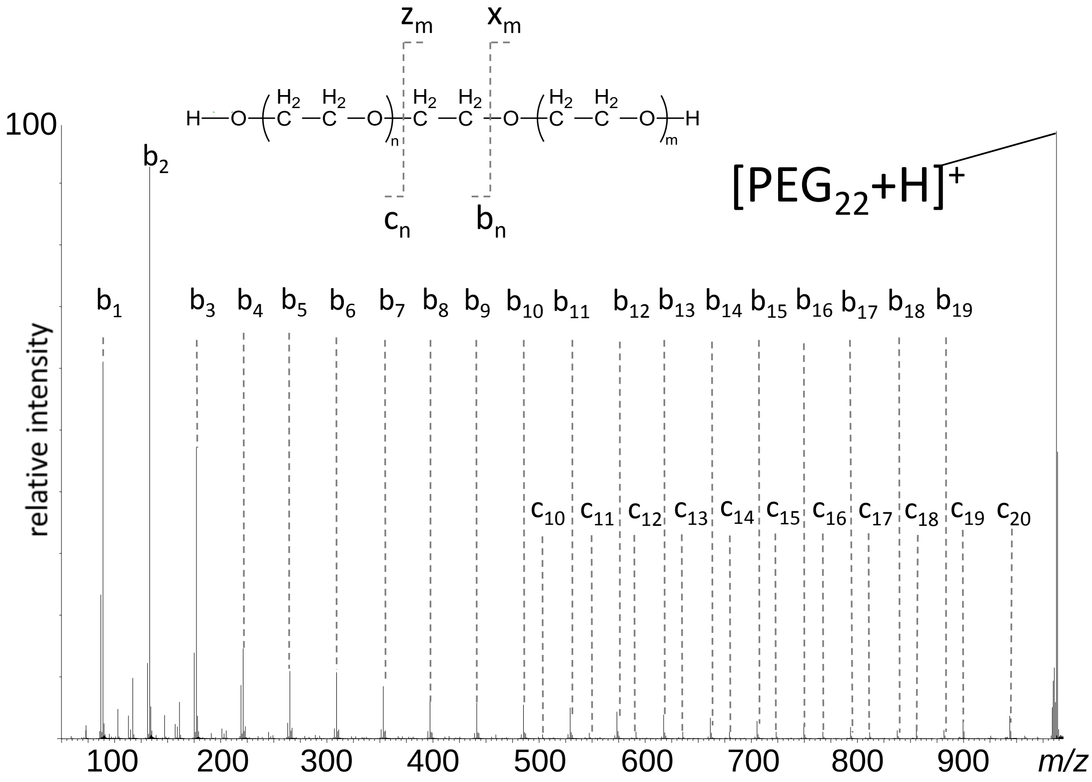

Figure 8.23 ASAP CID tandem MS of PEG$_{22}$ ([HO(C$_2$H$_4$O)$_{22}$H + H]$^+$) (c$_n$ = z$_m$ and b$_n$ = x$_m$), inset Structure of Poly(ethylene glycol), annotated to indicate cleavage sites and nomenclature used to differentiate between resulting product ions.

The fragmentation of **[PEG$_{22}$ + H]$^+$** ion generates a significant number of product ions that represent 20 of the 22 monomers present in the parent ion. The amount of structural information that can be obtained from ASAP CID of **[PEG$_{22}$ + H]$^+$** is comparable to what can be achieved using MALDI CID of the **[PEG + Na]$^+$** , as shown in Figure 8.24.

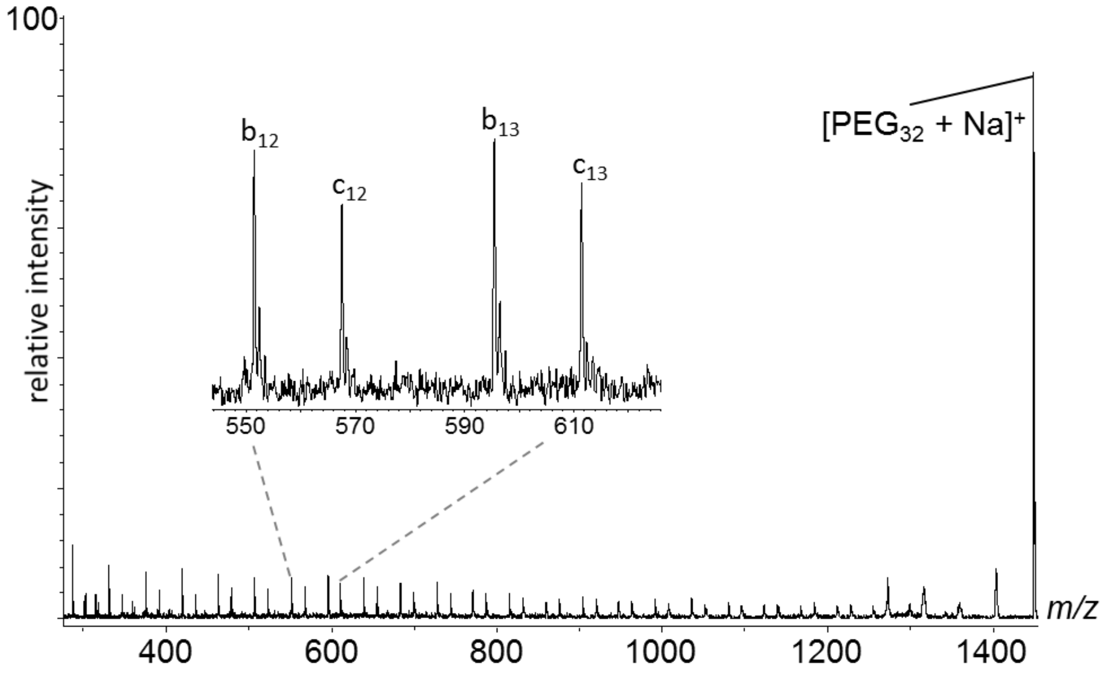

Figure 8.24 MALDI CID tandem MS of PEG_{32} ($[HO(C_2H_4O)_{32}H + Na]^+$) ($c_n = z_m$ and $b_n = x_m$).

In Figure 8.23, there are two major product ion series observed where the *m/z* value between each peak in a series corresponds to 44 Da, the mass of the ethylene glycol monomer unit. It is noted that only **b_n** and **c_n** product ions are labelled in the spectrum; as symmetrical end groups are present in this polymer as shown inset in Figure 8.23, the product ions **b_n** and **z_m** would have identical *m/z* values, assuming n = m. It is the same situation for **c_n** and **x_m** product ions, where the ions are indistinguishable due to the symmetrical chain ends. As it is not possible to distinguish from which end of the polymer product ions are generated, no directional sequencing information can be obtained, and consequently, for simplicity, only one set of product ion labels are required.

The most intense product ion series of peaks, labelled **b_n**, is generated through cleavage of the C-O bond in the polymer backbone, leading to the formation of an unsaturated vinyl terminal group. The intensity of this ion series of peaks reaches a maximum at **b_2**, where intensity then decreases with increasing *m/z*. This would suggest that fragmentation is favoured close to the polymer chain ends. One alternative explanation for the intensities of the product ion peaks in the low *m/z* region of the spectrum is that there are preferred sites for proton attachment in PEG. As the charge carrier must be retained in order for the product ions to be observed, the intensities of the peaks representing the ions **b_1** to **b_4** would suggest that during backbone fragmentation the proton is more likely to be bound to one of the first four monomer units from a chain end.

As stabilisation of the proton is likely to involve solvation by multiple oxygen atoms,[45] the chain terminus represents an ideal location, as the hydroxyl oxygen atoms can reorient themselves to more effectively solvate the charge carrier than backbone ether oxygen atoms.[202] This would suggest protonation is likely to occur directly on the chain end, however this is not reflected in the S/N ratio of the $\mathbf{b_1}$ ion peak, which is lower than the peak of the $\mathbf{b_2}$ ion. This observation is due to differences in the proton affinity of the hydroxyl and ether oxygen atoms, where the electron donating nature of the alkyl units increases the proton affinity of the ether oxygen atoms.[201] The S/N ratio of the $\mathbf{b_2}$ ion can be justified as the most favourable, as the proton can remain close to the oxygen with the highest proton affinity, but in a location where it can also benefit from effective solvation by the terminal hydroxyl oxygen.

The second product ion series of peaks, labelled $\mathbf{c_n}$, once again is generated through cleavage of the carbon-ether oxygen bond, generating an aldehyde -CH=O terminal group. It is of interest that the intensity of the peaks in the $\mathbf{c_n}$ series increases with *m/z* value; the reverse of what is observed for the $\mathbf{b_n}$ series. As these ions are only observed in the higher *m/z* region of the spectrum, and with ions assigned up to $\mathbf{c_{20}}$, formation of such ions may result from charge remote fragmentation with small chain neutral losses (similar to **b** ions but with no charge). For a precursor ion containing twenty two repeat units, the formation of $\mathbf{c_{20}}$ and $\mathbf{b_2}$ product ions, which represent the most intense peaks in each series, appears to demonstrate a favoured cleavage point in the molecule, where the location of the proton dictates which product ion is observed with the resultant neutral losses not observed. In the case of Figure 8.23, where $\mathbf{b_n}$ and $\mathbf{c_n}$ are the only product ion series observed and the charge carrier present is a proton, one mechanism which can account for the observed ions is charge-remote homolytic bond cleavage with subsequent β-$H^\bullet$ loss from the radical intermediate, as shown in Scheme 8.2.

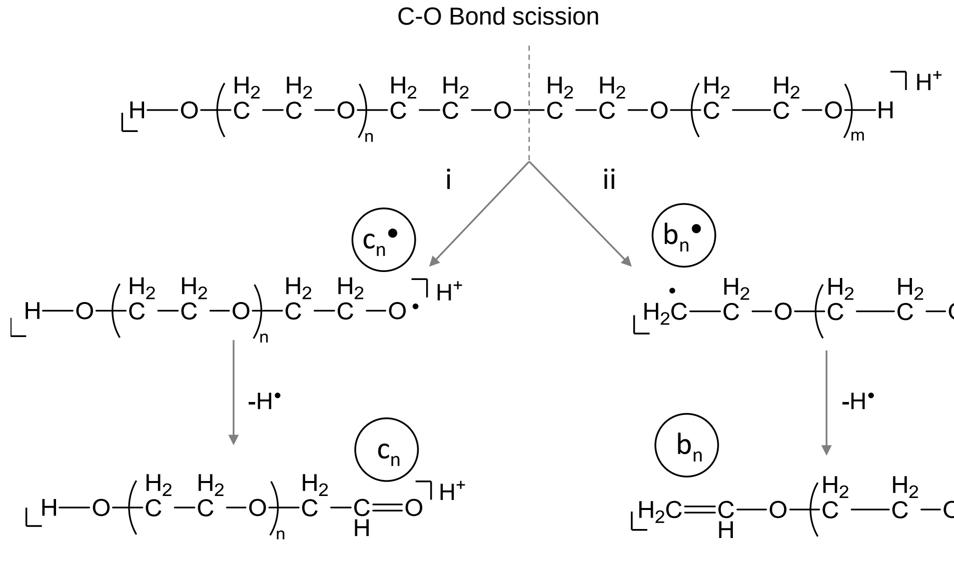

Scheme 8.2 Charge remote mechanism for homolytic cleavage of C-O bond.

8.6. MS analysis of an insoluble sugar functionalised block copolymer

8.6.1. Introduction

ASAP MS of synthetic polymers thus far has investigated well defined polymers that have been characterised by other mass spectrometry and analytical techniques. The term synthetic polymer can refer to a wide variety of materials that exhibit difficult and challenging chemistries for the analytical chemist. The design of a polymeric material for a specific application may require physical or chemical properties that are desired in the application, but hinder the characterisation of such materials. One specific example of this is the application of synthetic copolymers as synthetic cell mimics. This class of copolymers contain both hydrophilic and hydrophobic blocks that can form macromolecular structures, such as giant unilamellar vesicles, under the correct conditions. These copolymers are found to be insoluble in all solvents. Therefore, characterisation of these copolymers is a significant challenge, as solution phase NMR, conventional MALDI and ESI MS would not be possible due to solubility issues.

In this work, four block copolymers, kindly supplied by Dr Ahmed Eissa at Durham University, were analysed by ASAP MS. All compounds originate from a block copolymer of poly(ethylene-b-ethylene glycol) (**A**, Table 8.4). This block copolymer is an interesting target for ASAP as it contains polar, oxygen containing PEG and the purely hydrocarbon non-polar PE blocks, which were studied as homopolymers in Sections in 4.2.2 and 4.2.4. The block copolymer was functionalised with two different protected sugar moieties via a two-step synthesis involving the Copper-Catalysed Azide-Alkyne Cycloaddition click reaction (CuAAC), to generate compounds that correspond to the structures proposed in Table 8.4. The sugars selected in this study were α-L-fucose and β-D-glucose, which are both six membered cyclic sugars. Fucose is a hexose deoxy sugar and is interesting that it is only found in the L-configuration and it lacks a hydroxyl group at the 6 position, as shown in Figure 8.25. Glucose is an important carbohydrate in cell biology and can have numerous cyclic conformations, however the sample selected in this analysis has the D configuration, as shown in Figure 8.25. Solubility tests confirmed that all compounds tested were insoluble in solvents suitable for mass spectrometry.

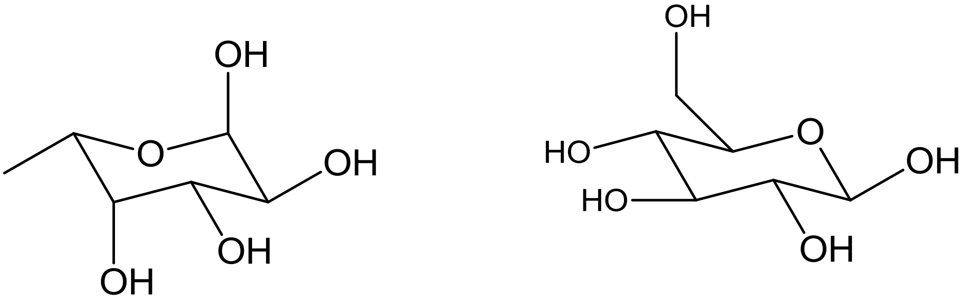

α-L-fucose β-D-glucose

Figure 8.25 Monosaccharide structures.

Table 8.4 Target structures and assignments for insoluble block copolymers.

Structure	Label
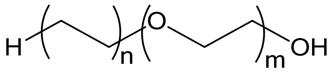	A
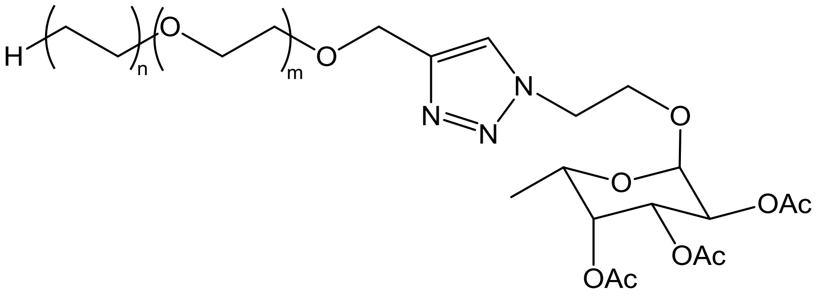	B
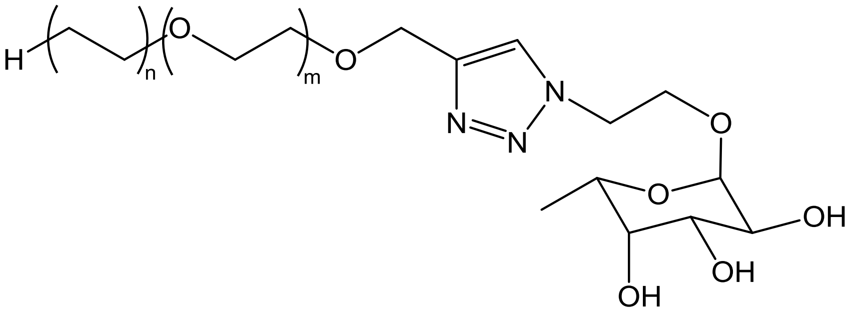	C
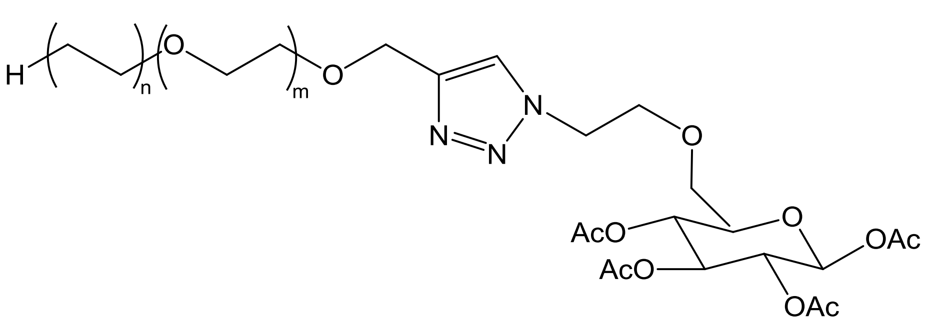	D

8.6.2. ASAP MS of copolymer A

The starting material, labelled A in Table 8.4, corresponds to a block copolymer comprised of ethylene and ethylene glycol monomers. An M_n = 875 Da for copolymer A was proposed by the manufacturer, placing it within the mass range of polymers previously studied by ASAP. It was found that this compound required a lower desolvation gas temperature of 400°C to successfully generate ions. However, the sample cone (20 eV) and extraction cone (2 V) voltage were similar to those validated in Section 8.2.

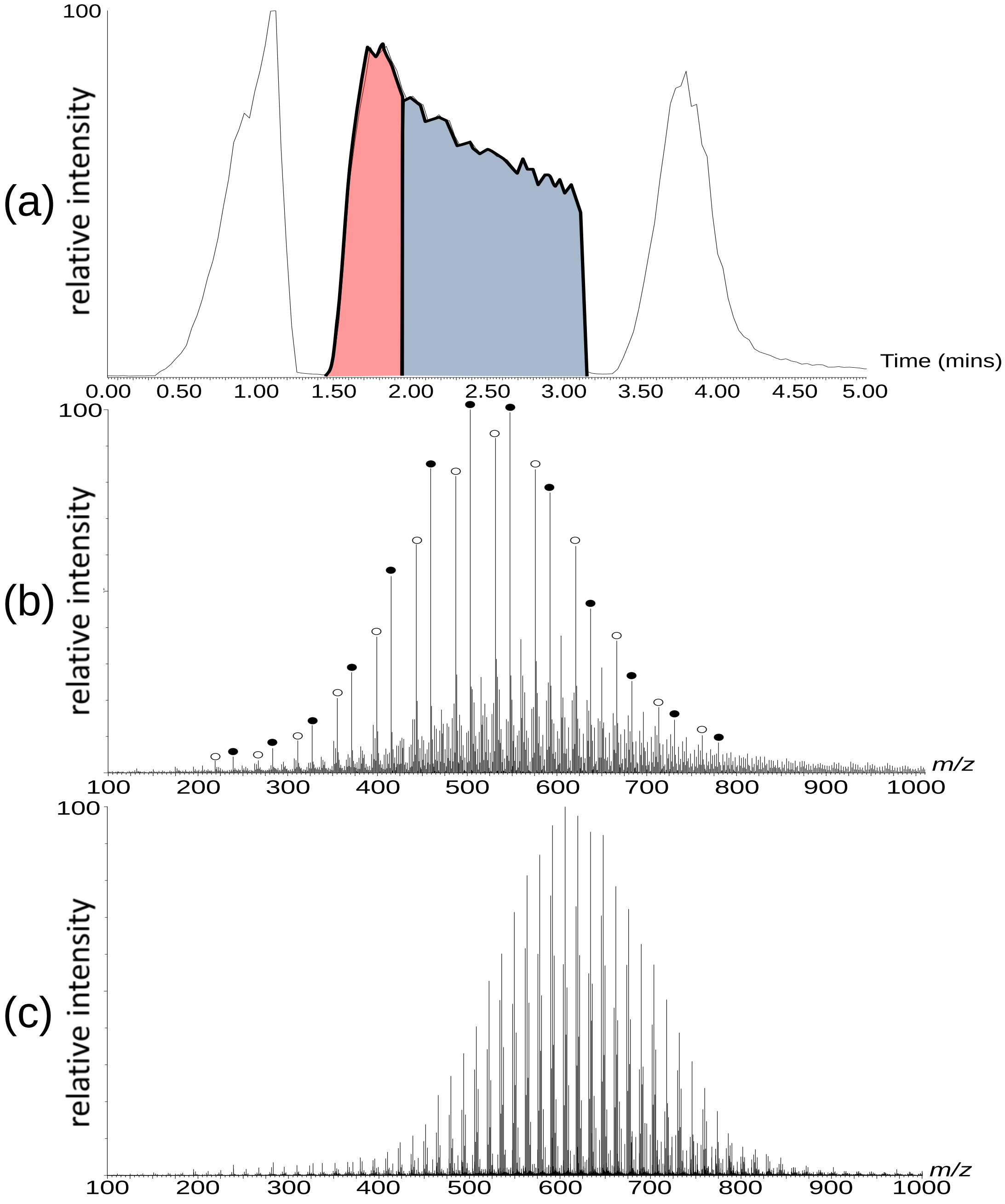

Figure 8.26 (a) Chromatogram generated for poly(ethylene-b-ethylene glycol) copolymer (b) MS spectrum 1.40-2.00 minutes and (c) MS spectrum 2.00- 3.20 minutes.

The sample was applied directly to the glass capillary through stirring in the reagent container; this not only limited contamination but also reduced sample preparation and facilitated real time reaction monitoring. On inspection of the chromatogram, (red/blue section, Figure 8.26(a)) it was found that two different polymeric series were observed at different times during the acquisition. Immediately following probe insertion into a 'dry' ion source at 1.40 minutes, the molecular weight distribution in Figure 8.26(b) was observed during the time highlighted in red in the chromatogram (Figure 8.26(a)).

The mass spectrum reveals two major series of peaks, where the *m/z* difference between the peaks labelled (•) corresponds to 44 Da, as does the second series, labelled (○). This observation was unexpected, as this value corresponds to the monomer unit of ethylene glycol (C_2H_4O), given to be present as a minor component of the block copolymer. To provide an accurate and precise mass measurement and to maintain chemical isolation of polymer and calibrant, an internal standard of PEG M_n = 200 was inserted prior to and post sample acquisition (as shown in Figure 8.26), and was used to apply a post-acquisition calibration to the mass spectrum. Following calibration *m/z* 503.3, a peak in the series labelled (•), generated an empirical formula of $C_{22}H_{47}O_{12}$, which corresponds to **[PEG + H]$^+$**. When *m/z* 487.3, a peak in the series labelled (○), was analysed it generated an empirical formula of $C_{22}H_{47}O_{11}$, which corresponds to **b_{10}''** ion series that was previously observed in Figure 8.4. This suggested that PEG oligomers were present as contaminants in the reagent container, and that the sample was a mixture of block copolymers and homopolymers.

Continued monitoring of the experiment allows the sample to reach thermal equilibrium, where the blue region of the chromatogram (2.00 – 3.20 min, Figure 8.26) presents a very different mass spectrum, as shown in Figure 8.26(c). Initial inspection identified that numerous ion series were present, which differ by 14 Da, and are likely to correspond to differences of CH_2 similar to that observed for PE in Figure 8.9. As the block copolymer can have a large number of block length combinations, the observation of a complex spectrum is not surprising. When an expanded view of the molecular weight distribution is examined, three series of peaks can be identified, as shown in Figure 8.27.

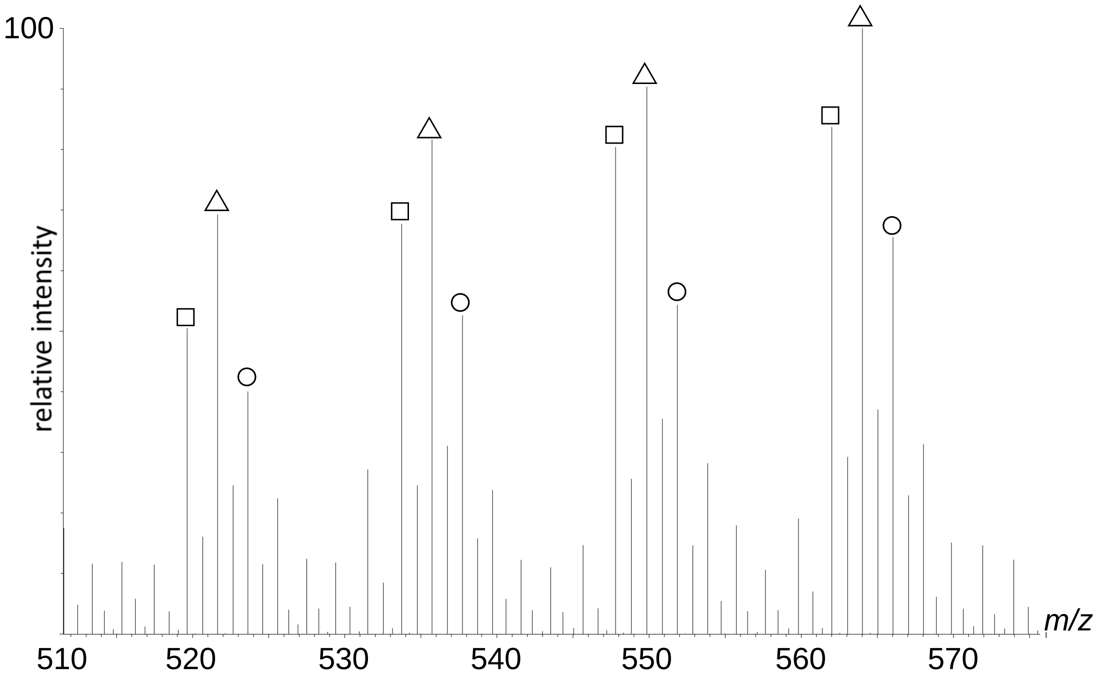

Figure 8.27 Expansion of the molecular weight distribution from *m/z* 510 to 580 in Figure 8.26(c).

The three series of peaks that have been labelled in Figure 8.27 are separated from each other by 2 Da. This adds a degree of complexity to the assignment of the ions, as the isotopic envelopes for each ion overlap. The assignments are further complicated by the presence of only carbon, hydrogen and oxygen atoms in the copolymer, which provide numerous potential empirical formulae for each *m/z* value. From the literature supplied by the manufacturer, the copolymer was given to be linear, and therefore to restrict the number of potential molecules, the double bond equivalence was limited to a value of 10. Using these conditions one empirical formula was proposed for each peak, as summarised in Table 8.5.

Table 8.5 Summary of empirical formulae for repeat series of peaks observed in Figure 4.31.

m/z	Empirical Formula	Proposed structure	Label
519.5	$C_{36}H_{71}O$	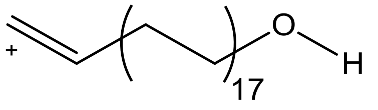	□
521.5	$C_{35}H_{69}O_2$	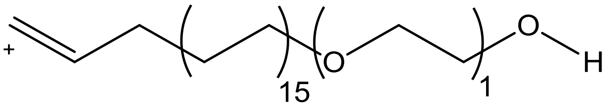	△
523.5	$C_{34}H_{67}O_3$	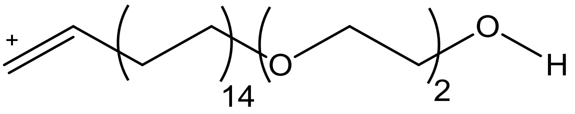	○

The presence of ions containing an odd number of carbon atoms from a copolymer made entirely of monomers with even numbers of carbon atoms would suggest that dissociation of the polymer is occurring. Further support for polymer fragmentation is found for the proposed ring double bond equivalence of 1.5. Utilising the empirical formulae and the double bond equivalence values, proposed structures that account for this data are provided in Table 8.5. It is noted that the empirical formula are all related, where the 2 Da difference is due to the replacement of CH_2 with an oxygen atom. Like PE, the block copolymer is believed to be present as a hydride abstracted molecular ion, which given the high PE content of the copolymer is expected. A double bond equivalence of 1.5 can be accounted for by the abstracted hydride and the presence of a double bond, as shown in the proposed structures in Table 8.5. Ions that contain an odd number of carbon atoms, such as *m/z* 521.5 in Table 8.5, can be rationalised through fragmentation in the poly(ethylene) block akin to that observed in Section 8.2.4, where ASAP MS of PE generated a methylene series of ions. The presence of a double bond suggests an alkene-like structure that was observed previously for PE in Section 8.2.2. The formation of the double bond is likely to involve thermal decomposition of the copolymer, leading to homolytic bond cleavage where loss of a hydrogen radical allows the formation of the double bond, as shown in Figure 8.11. This assignment is supported by work by Beyler *et al.* who demonstrated that poly(ethylene) homopolymers decompose by a radical driven mechanism, where intra and intermolecular chain transfer led to the formation of double bonds in the ethylene chain.[277]

8.6.3. ASAP MS of Copolymer B

Copolymer A was utilised in a multi-step synthesis following the reaction scheme in Figure 8.28. The experiment proceeds via initial functionalisation of the copolymer with an alkyne moiety (reaction **a**, Figure 8.28), where the product is utilised in a Copper-Catalysed Azide-Alkyne Cycloaddition click reaction (CuAAC) using a protected azidoethyl fucoside (reaction **b**, Figure 8.28).

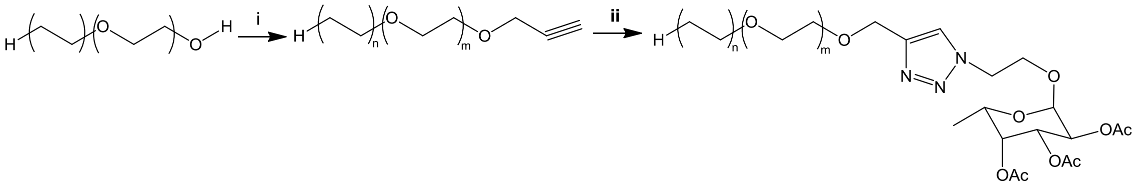

Figure 8.28 Synthesis of copolymer B (i:HC≡CCH$_2$Br, NaH,THF) (ii: $C_8H_{16}O_5N_3$,CuSO4,THF,H_2O).

MS was performed on the solid product, with the resultant spectrum shown in Figure 8.29. It was found that there are no peaks that correspond to the intact copolymer B. Despite this, there are a number of peaks that provide structurally useful information that permits characterisation of the sample. Firstly, a polymeric molecular weight distribution (♦) is observed in the *m/z* 450 – 900 region of the spectrum. In this instance, the mass difference between the peaks is 28 Da, which corresponds to the C_2H_4; the expected monomer unit of the poly(ethylene) block of the copolymer. This pattern was not observed for PE or copolymer A, which suggests that the click derived terminal group strongly influences the observed dissociation. Accurate mass analysis of *m/z* 477.5, a peak in the series labelled (♦), generated an empirical formula of $C_{34}H_{69}$. Given that all ions observed in this sequence correspond to even numbers of carbon atoms, this implies that fragmentation is occurring only at whole monomer units. As this alkyl chain contains identical C-C backbone bonds it is surprising, if fragmentation is occurring along the backbone, that sequential cleavage at each carbon atom is not observed. As demonstrated in Section 8.5.2, tandem mass spectrometry experiments involving polyethers generate the major product ions through cleavage of the carbon-oxygen bond, rather than the carbon-carbon bond.[87] Therefore, the carbon-ether oxygen bond which links the blocks of the copolymer is a likely cleavage site. Fragmentation at this position would account for the (♦) series observed here.

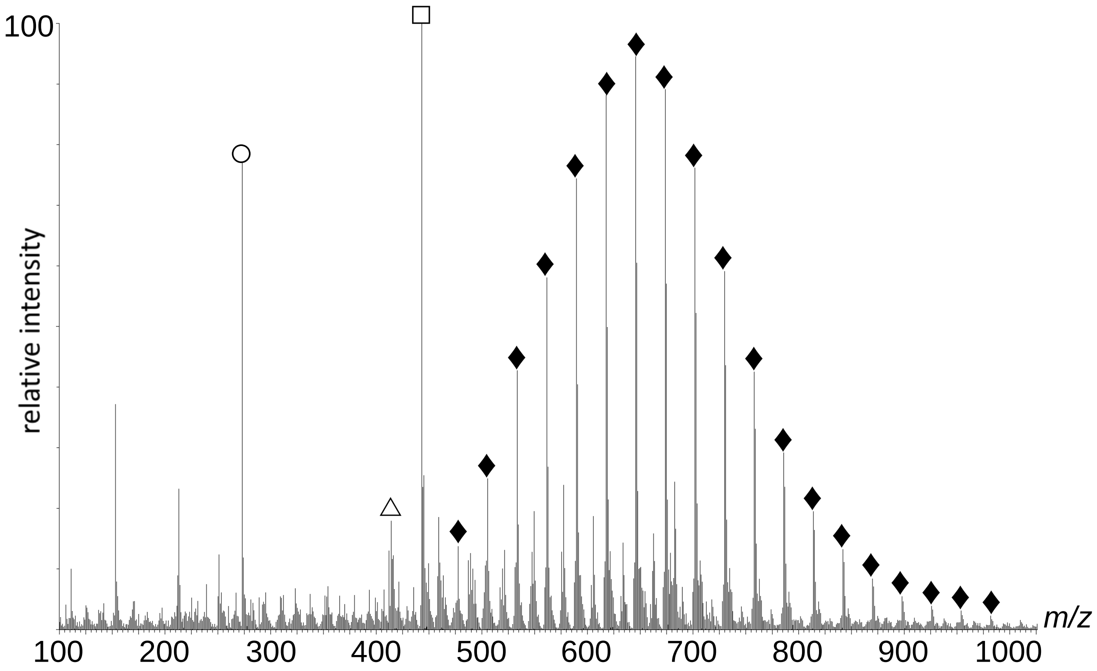

Figure 8.29 ASAP MS of copolymer B.

Table 8.6 Summary of ion assignments for ASAP of Copolymer B.

m/z	Empirical formula	Structure	Assignment
477.5	$C_{34}H_{69}$	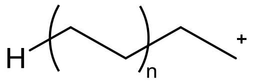	♦
605.6	$C_{42}H_{85}O$	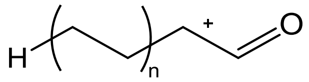	◊
443.1	$C_{19}H_{29}N_3O_9$	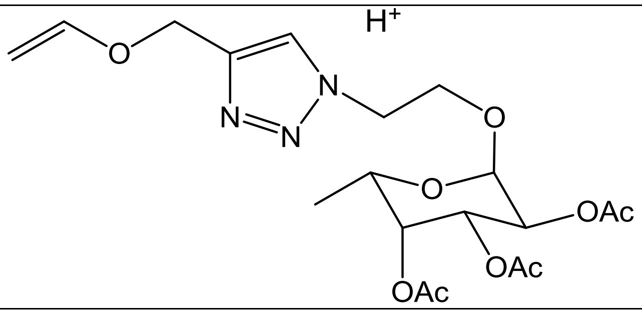	□
414.5	$C_{17}H_{25}N_3O_9$	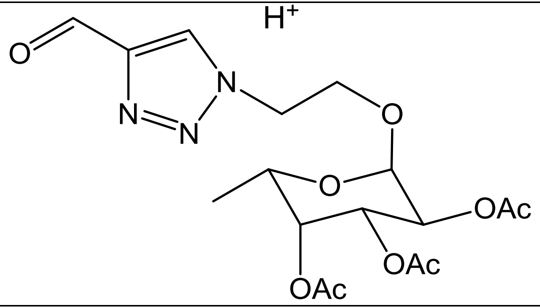	△
273.0	$C_{12}H_{17}O_7$	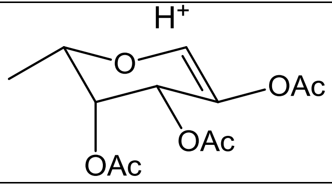	○

Further evidence for cleavage at the C-O bond of the copolymer is found through the presence of a second series of peaks, labelled (◊). As shown in Figure 8.30, the (◊) series is present *m/z* 16 above the (♦), where accurate mass analysis of *m/z* 605.6 yields an empirical formula of $C_{42}H_{85}O$, which corresponds to a straight chain polyethylene chain terminated with an unsaturated aldehyde CH=O end group, as shown in Table 8.6.

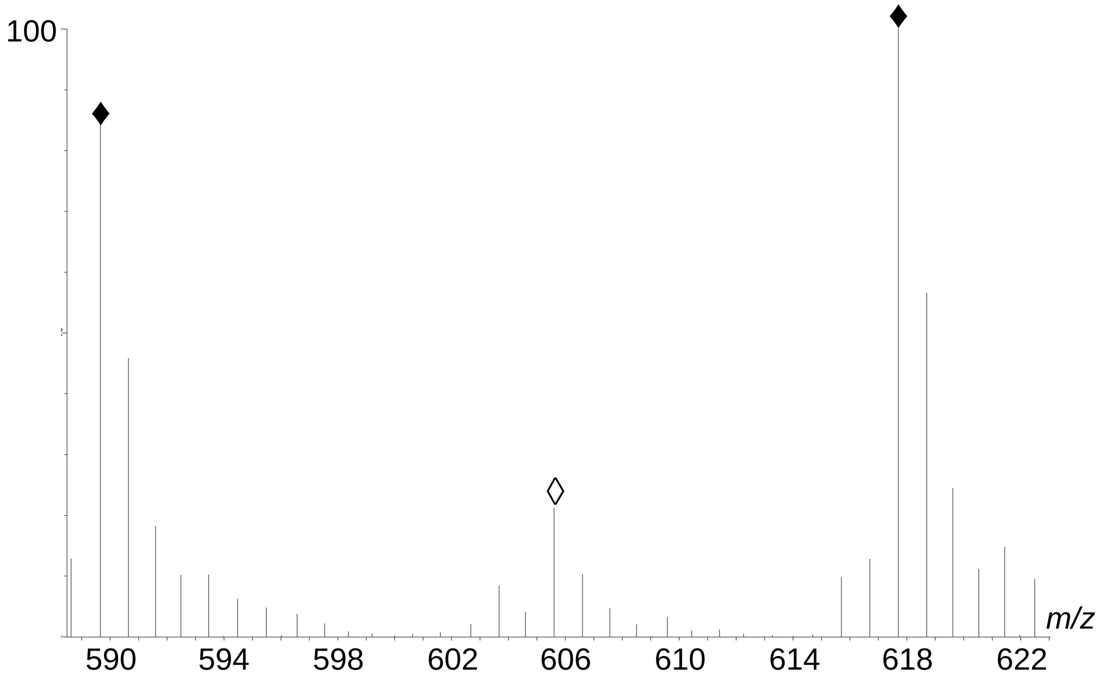

Figure 8.30 Expansion of *m/z* 590 -622 molecular weight distribution of copolymer B Figure 8.29.

In addition to the molecular weight distribution, there are a number of structurally significant ions that allow for characterisation of the hydrophilic part of the molecule. The spectral base peak at *m/z* 443.1, labelled (☐) in Figure 8.29, was found to have an empirical formula of $C_{19}H_{29}N_3O_9$, which is consistent with the proposed structure in Table 8.6. This structure results from fragmentation at the ether bond of the monomer linking the copolymer and the click derived end group. Additional confidence in this assignment is provided by the presence of the related peak at *m/z* 414.5, labelled (△). This peak is 28 Da below the spectral based peak, suggesting loss of C_2H_4 where cleavage in the copolymer now generates an aldehyde terminal group. The protected fucose moiety is also detected at *m/z* 273.0 (○), and like all other ions in this spectrum results from cleavage of a carbon-ether oxygen bond. The charge carrier present in ions at *m/z* 443, 414 and 273 was found to be a proton, which is not the same type of ion found for the polymeric portion of this molecule (**$[M\text{-}H^-]^+$**). The presence of multiple heteroatoms in this region of the molecule can aid in the stabilisation of a proton whereas the copolymer, which is hydrocarbon based, could not stabilise such a charge carrier. The structures of these ions would suggest that one possible site for the proton charge carrier is the fucose ring. This provides a high density of heteroatoms capable of stabilising the charge, and is present in all of the non-polymeric ions observed in Figure 8.29. This result is supported by work on monosaccharides, where species were capable of stabilising a charge carrier by the related APCI technique.[278]

8.6.4. ASAP MS of copolymer C

To utilise the sugar functionalised block copolymers in the formation of macromolecular structures such as synthetic vesicles, it is important that the sugar is present without any protecting groups. As copolymer B was analysed with acetyl groups protecting hydroxyl functionalities on the ring, it was of interest to establish the effect that de-protection may have upon the observed ASAP mass spectrum. Copolymer C was formed through de-protection of the hydroxyl groups on copolymer B using an exchange resin. ASAP MS of this compound generated the spectrum shown in Figure 8.31. This spectrum is noticeably more complex than that obtained for copolymer B, however the polymeric series of peaks (♦) corresponds to the linear PE sequence assigned previously in Section 8.6.3, where the mass difference between the ions corresponded to the C_2H_4. However, there are few ions present that correspond to the click derived terminal group. Indeed, the ions present < 300 Da involve multiple bond cleavage with losses of H_2O from the fucose ring, demonstrating that dehydration can occur during ASAP ionisation when the hydroxyl units are not protected. This result demonstrates that ASAP provides a less complex mass spectrum for the protected sugar copolymer B than can be achieved here for the de-protected copolymer C, where the structurally relevant peaks of copolymer B have a superior S/N ratio. Therefore, the conclusion of this work was to perform all future structural analysis of related copolymers with the sugar group protected.

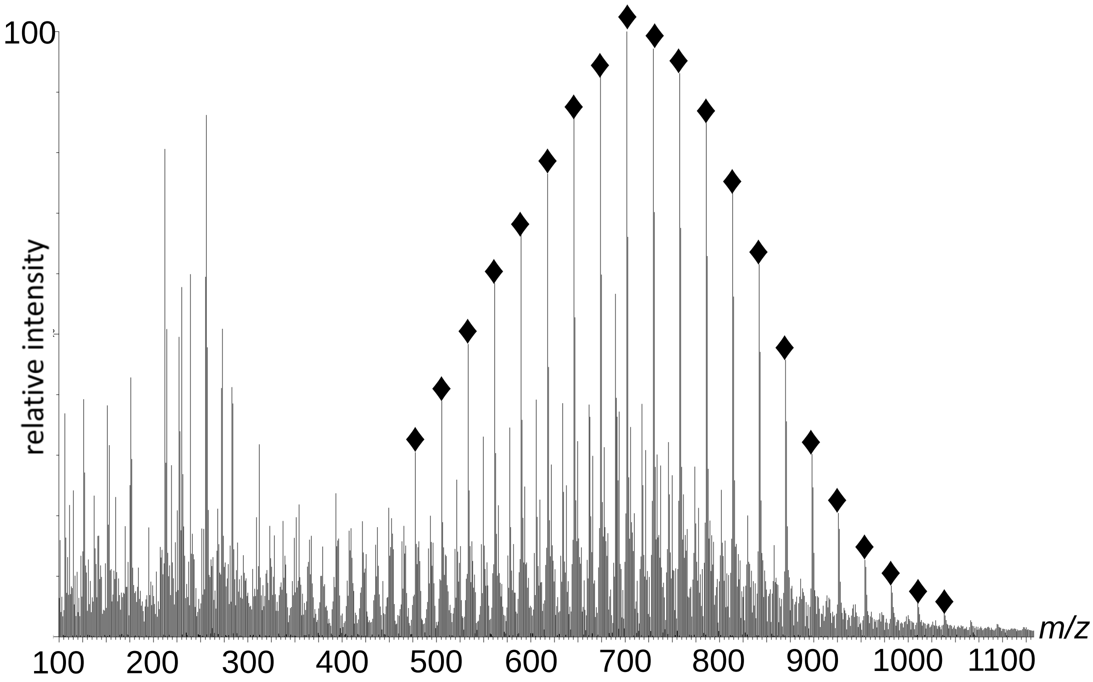

Figure 8.31 ASAP MS of copolymer C.

8.6.5. ASAP MS of copolymer D

In a related experiment, copolymer A was functionalised using the same process as in Figure 8.28, however a protected azidoethyl glucoside unit replaced azidoethyl fucoside to form copolymer D. This provided the opportunity to investigate the influence of the sugar moiety upon the mass spectrum. When ASAP mass spectrometry was performed on copolymer D, it generated a spectrum similar to that observed for copolymer B, as shown in Figure 8.32.

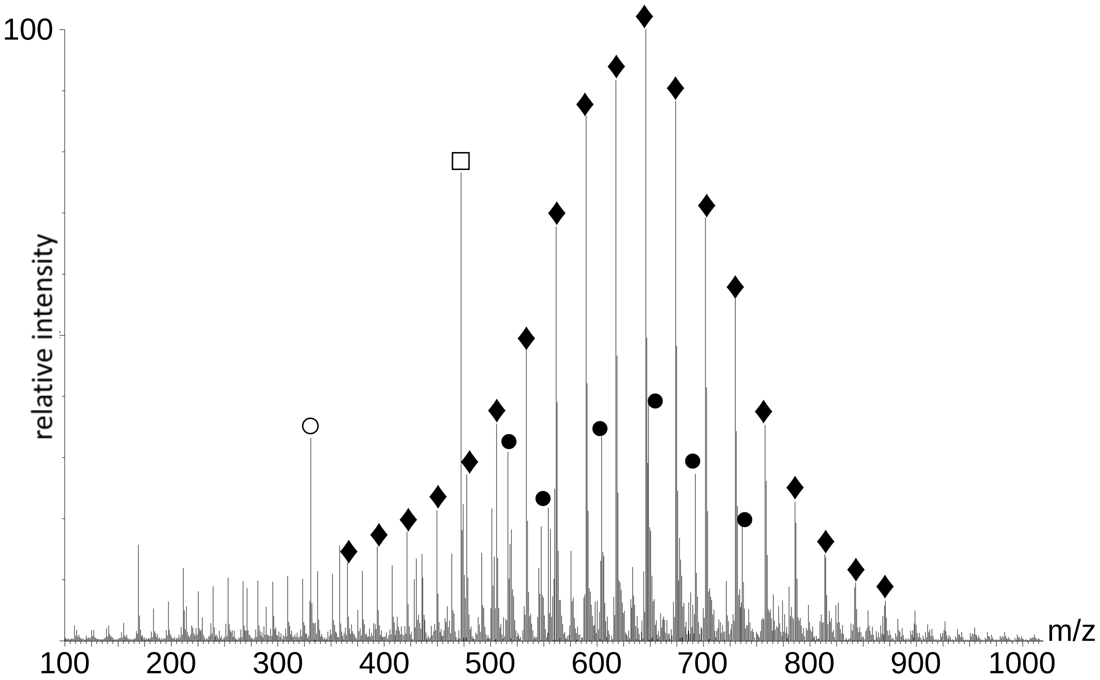

Figure 8.32 ASAP MS of copolymer D.

Once again, there is no presence of a series corresponding to intact copolymer D, however this spectrum does provide structurally significant ions that allude to the structure of the intact species. The series of peaks labelled (♦) is identical to that previously observed in the mass spectra of copolymer's B and C, where once again accurate and precise mass analysis indicate the presence of a purely hydrocarbon based species, as shown in Table 8.7. This result demonstrates that formation of the (♦) series of peaks is not influenced through changing the sugar group present.

Table 8.7 Ion Assignments for ASAP MS of copolymer D.

m/z	Empirical formula	Structure	Label
393.4 ± 28	$C_{28}H_{57} \pm C_2H_4$	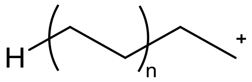	♦
331.1	$C_{14}H_{19}O_9$	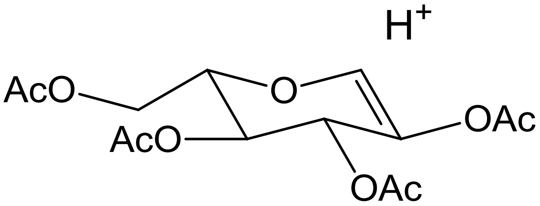	○
472.1	$C_{19}H_{26}N_3O_{11}$	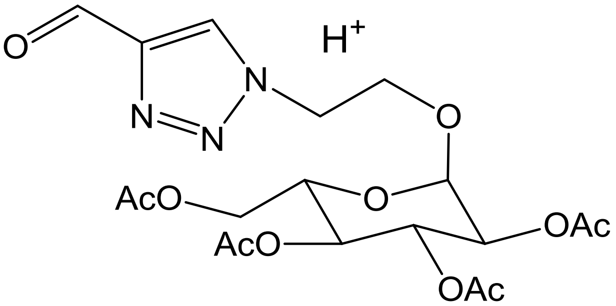	□
516.1	$C_{21}H_{30}N_3O_{12}$	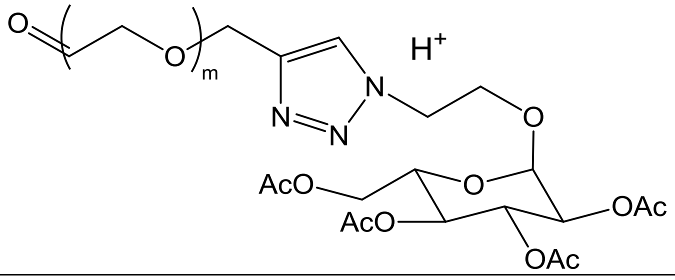	●

The ions in the lower mass region of the spectrum provide complementary information to that gained from the molecular weight distribution. At *m/z* 472.1 the peak labelled (□) represents an ion with an empirical formula of $C_{19}H_{26}N_3O_{11}$ that corresponds to the structure given in Table 8.7. Further evidence for the location of the charge carrier upon the sugar ring can be seen from the presence of the protected glucose unit at *m/z* 331.1, labelled with (○). There is one major difference observed in the comparison of the spectra generated for copolymer B and copolymer D, and that is the presence of the series of peaks (●) for the glucose derivative in Figure 8.32. The mass difference between the peaks in this series is 44 Da and can be related to the ethylene glycol units of the copolymer. The *m/z* of the (●) series corresponds to the click derived terminal group with sequential numbers of ethylene glycol units, thus proving for the first time that the copolymer contains up to six ethylene glycol units. It is currently unclear how the chemistry of the sugar group can influence the observed mass spectrum, and will require further investigation.

8.7. Conclusions of ASAP

The ASAP ion source has demonstrated significant benefits for the analysis of synthetic polymers, generating reproducible mass spectra for samples prepared as both solids and solutions. Direct analysis of synthetic polymers as solids not only reduces sample preparation but removes the issue of sample solubility, potentially increasing the number of synthetic polymers amenable to mass spectrometry analysis, as demonstrated with the sugar functionalised copolymers used in the formation of macromolecular structures in Section 8.6. It was also found that ionisation of the polymeric materials occurs via charge transfer, hydride abstraction and proton transfer forming radical cations, hydride abstracted ions and protonated molecular ions respectively. Ionisation of synthetic polymers without the addition of metal salts simplifies sample preparation, making this technique a simple and efficient method of polymer analysis.

Evaluation and optimisation of the ion source parameters identified a number of influential factors that affected the observed mass spectrum. The temperature of the desolvation gas was shown to have the most significant influence upon the observed molecular weight distribution. Increasing the desolvation gas temperature led to a dramatic shift in the distribution; demonstrating that calculating molecular weight values by this technique would be a significant challenge. As expected, the voltages of the sampling and extraction cone were shown to be major sources of in-source fragmentation, where increasing the voltages resulted in extensive in-source fragmentation ions. Despite this, the S/N intensity of the intact ions also increased, therefore a compromise on values between high S/N ratio of intact species and minimal in-source fragmentation was required. Identification of the major parameters affecting the polymer mass spectra will limit the amount of method development required to analyse new polymers by this technique.

Optimisation of the source parameters effectively limited the in-source fragmentation for PS, however it was still apparent in PEG. The addition of methanol: water to the ion source led to the formation of a ‘wet’ ion source, which improved the S/N ratio of the protonated molecular ions for PEG - a polymer with a greater proton affinity than water. The ions formed by in-source fragmentation in ASAP mass spectra were identified as products resulting from the thermal decomposition of PEG using MALDI MS. It is therefore important to validate the desolvation gas temperature for each new polymer. However, this result demonstrates that both intact molecules and pyrolysis information can be achieved in one run using ASAP.

Ionisation by ASAP generates radical cation and protonated molecular ions, species that are not preferentially formed by MALDI or ESI. These molecular ions fragmented readily under activated conditions, providing structural information relating to the terminal groups present and monomer sequence. For PS, CID of the odd electron radical cation generated complementary ions to those observed for the even electron silver adducted PS molecular ion, demonstrating differences in the fragmentation mechanisms based on the precursor ion.

Following evaluation of the ASAP ion source, ASAP was utilised in the analysis of an insoluble block copolymer and related functionalised species. Analysis of the starting material identified that the sample was a mixture of homopolymers and block copolymers, which could not be deduced from solid state NMR or FT-IR. The mass spectrum for copolymer A generated a methylene series which was consistent with previous analysis of poly(ethylene)s, confirming that this is the major constituent of the block copolymer. Functionalisation of the block copolymer with two different protected sugars generated mass spectra that did not contain the molecule of interest as an intact ion. However, ASAP was able to generate ions that corresponded to reciprocal portions of the molecule which, when used in tandem with FT-IR data, could be used to confirm the presence of the intact species. ASAP MS generated unique structural information that allowed successful identification of the copolymer species. It was also found that analysis of copolymers including a protected sugar group provided superior results compared to copolymers that included a de-protected sugar.

8.8. Future Work for ASAP

- As shown in the work, ASAP can be applied to a range of synthetic polymers; however the scope of the technique can be explored further through the analysis of other polymer materials. It would be of interest to analyse branched synthetic polymers in the solid state, as the degree of entanglement would be more complex than for linear samples. It is important to expand the types of polymer analysed by ASAP beyond those commonly associated with MS analysis. This work has shown that poly(ethylene)s can be ionised successfully as solids, and therefore other classes of insoluble polymers such as poly(amide)s and cyclo-poly(butadiene terephthalate)s may be amenable to this technique.
- Employ ASAP in tandem with ion mobility to probe the gas phase structures of these polymers that are present without metal cations. Information regarding gas phase structure could aid in identification of likely position of charge, and allow for a more refined fragmentation mechanism to be proposed.
- The flexibility of ASAP for direct field sampling makes this technique amenable to direct sampling from reaction vessels. This would be of interest as it allows the monitoring of a polymerisation in real time, providing information relating to the extent of reaction. This could be compared with the conventional method of removing an aliquot and performing NMR on the sample.
- Utilise ASAP to probe the induction period for RAFT polymerisation. It was originally proposed that dithiocarbonyl based RAFT agents have induction periods prior to polymerisation, due to the slow re-initiation rate of the leaving group radical.[279] However, it has been suggested that the induction period may be due to irreversible termination reactions involving intermediate and terminating radicals.[280] Direct sampling followed by immediate analysis using ASAP may provide evidence supporting one of these proposals.

9. References

(1) Peacock, A. *Polymer Chemistry: properties and applications*; Hanser, 2006.

(2) Wiegand, S. *Molecular characterisation and analysis of synthetic polymers*; Elsevier: Amsterdam, Netherlands, 2008.

(3) Stevens, M. P. *Polymer Chemistry: An Introduction*, 1999.

(4) Guaita, M.; Chiantore, O.; Munari, A.; Manaresi, P.; Pilati, F.; Toselli, M. *Eur Polym J* **1991**, *27*, 385.

(5) Pasch, H. *MALDI-TOF Mass Spectrometry of Synthetic Polymers*, 2003.

(6) Lorenz, S. A.; Maziarz, E. P.; Wood, T. D. *Appl Spectrosc* **1999**, *53*, 18a.

(7) Ibbett, R. N. *NMR Spectroscopy of Polymers*; Chapman and Hall: Glasgow, United Kingdom, 1993.

(8) Grubisic, Z.; Rempp, P.; Benoit, H. *Journal of Polymer Science Part B-Polymer Letters* **1967**, *5*, 753.

(9) Striegel, A. M. *Anal Chem* **2005**, *77*, 104A.

(10) Kostanski, L. K.; Keller, D. M.; Hamielec, A. E. *J Biochem Biophys Methods* **2004**, *58*, 159.

(11) Striegel, A. M. *Anal Bioanal Chem* **2008**, *390*, 303.

(12) Siewing, A.; Lahn, B.; Braun, D.; Pasch, H. *J Polym Sci Pol Chem* **2003**, *41*, 3143.

(13) Karas, M.; Hillenkamp, F. *Anal Chem* **1988**, *60*, 2299.

(14) Fenn, J. B.; Mann, M.; Meng, C. K.; Wong, S. F.; Whitehouse, C. M. *Science* **1989**, *246*, 64.

(15) Schriemer, D. C.; Li, L. *Anal Chem* **1996**, *68*, 2721.

(16) Nielen, M. W. F. *Mass Spectrom Rev* **1999**, *18*, 309.

(17) Murgasova, R.; Hercules, D. M. *Int J Mass Spectrom* **2003**, *226*, 151.

(18) Rader, H. J.; Schrepp, W. *Acta Polymerica* **1998**, *49*, 272.

(19) Weidner, S. M.; Trimpin, S. *Anal Chem* **2010**, *82*, 4811.

(20) Weidner, S. M.; Trimpin, S. *Anal Chem* **2008**, *80*, 4349.

(21) Vergne, M. J.; Hercules, D. M.; Lattimer, R. P. *Journal of Chemical Education* **2007**, *84*, 81.

(22) Peacock, P. M.; McEwen, C. N. *Anal Chem* **2006**, *78*, 3957.

(23) Peacock, P. M.; McEwen, C. N. *Anal Chem* **2004**, *76*, 3417.

(24) Gruendling, T.; Weidner, S.; Falkenhagen, J.; Barner-Kowollik, C. *Polymer Chemistry* **2010**, *1*, 599.

(25) Wetzel, S. J.; Guttman, C. M.; Girard, J. E. *Abstr Pap Am Chem S* **2003**, *225*, U666.

(26) Hanton, S. D.; Owens, K. G. *J Am Soc Mass Spectrom* **2005**, *16*, 1172.

(27) Hoteling, A. J.; Mourey, T. H.; Owens, K. G. *Anal Chem* **2005**, *77*, 750.

(28) Meier, M. A. R.; Adams, N.; Schubert, U. S. *Anal Chem* **2007**, *79*, 863.

(29) Gopferich, A. *Biomaterials* **1996**, *17*, 103.

(30) Berthod, A.; Crank, J. A.; Rundlett, K. L.; Armstrong, D. W. *Rapid Commun Mass Spectrom* **2009**, *23*, 3409.

(31) Wallace, W. E. *Chem Commun* **2007**, 4525.

(32) Ma, Z.; Qiang, L. L.; Fan, Q. L.; Wang, Y. Y.; Pu, K. Y.; Yin, R.; Huang, W. *J Mass Spectrom* **2007**, *42*, 20.

(33) Watanabe, T.; Kawasaki, H.; Yonezawa, T.; Arakawa, R. *J Mass Spectrom* **2008**, *43*, 1063.

(34) Gorman, C. B.; Petrie, R. J.; Genzer, J. *Macromolecules* **2008**, *41*, 4856.

(35) Seino, T.; Sato, H.; Yamamoto, A.; Nemoto, A.; Torimura, M.; Tao, H. *Anal Chem* **2007**, *79*, 4827.

(36) Chen, Y.; Vertes, A. *Anal Chem* **2006**, *78*, 5835.

(37) Mowat, I. A.; Donovan, R. J. *Rapid Commun Mass Spectrom* **1995**, *9*, 82.

(38) Burgers, P. C.; Terlouw, J. K. *Rapid Commun Mass Spectrom* **1998**, *12*, 801.

(39) Keki, S.; Deak, G.; Zsuga, M. *Rapid Commun Mass Spectrom* **2001**, *15*, 675.

(40) Chen, R.; Yalcin, T.; Wallace, W. E.; Guttman, C. M.; Li, L. *J Am Soc Mass Spectrom* **2001**, *12*, 1186.

(41) Chen, H.; He, M. Y.; Wan, X. H.; Yang, L. F.; He, H. F. *Rapid Commun Mass Spectrom* **2003**, *17*, 177.

(42) Shimada, K.; Matsuyama, S.; Saito, T.; Kinugasa, S.; Nagahata, R.; Kawabata, S. *Int J Mass Spectrom* **2005**, *247*, 85.

(43) Gidden, J.; Bowers, M. T.; Jackson, A. T.; Scrivens, J. H. *J Am Soc Mass Spectrom* **2002**, *13*, 499.

(44) Gidden, J.; Jackson, A. T.; Scrivens, J. H.; Bowers, M. T. *Int J Mass Spectrom* **1999**, *188*, 121.

(45) Gidden, J.; Wyttenbach, T.; Jackson, A. T.; Scrivens, J. H.; Bowers, M. T. *J Am Chem Soc* **2000**, *122*, 4692.

(46) Rashidzadeh, H.; Wang, Y.; Guo, B. *Rapid Commun Mass Spectrom* **2000**, *14*, 439.

(47) Hoberg, A. M.; Haddleton, D. M.; Derrick, P. J.; Jackson, A. T.; Scrivens, J. H. *Eur Mass Spectrom* **1998**, *4*, 435.

(48) Wetzel, S. J.; Guttman, C. M.; Flynn, K. M. *Rapid Commun Mass Spectrom* **2004**, *18*, 1139.

(49) Brandt, H.; Ehmann, T.; Otto, M. *J Am Soc Mass Spectrom* **2010**, *21*, 1870.

(50) Haddleton, D. M.; Waterson, C.; Derrick, P. J. *Eur Mass Spectrom* **1998**, *4*, 203.

(51) Yalcin, T.; Dai, Y. Q.; Li, L. *J Am Soc Mass Spectrom* **1998**, *9*, 1303.

(52) Hoberg, A. M.; Haddleton, D. M.; Derrick, P. J. *Eur Mass Spectrom* **1997**, *3*, 471.

(53) Vorm, O.; Roepstorff, P.; Mann, M. *Anal Chem* **1994**, *66*, 3281.

(54) Hanton, S. D.; Hyder, I. Z.; Stets, J. R.; Owens, K. G.; Blair, W. R.; Guttman, C. M.; Giuseppetti, A. A. *J Am Soc Mass Spectrom* **2004**, *15*, 168.

(55) Chen, H. R.; Guo, B. C. *Anal Chem* **1997**, *69*, 4399.

(56) Marie, A.; Fournier, F.; Tabet, J. C. *Anal Chem* **2000**, *72*, 5106.

(57) Skelton, R.; Dubois, F.; Zenobi, R. *Anal Chem* **2000**, *72*, 1707.

(58) Trimpin, S.; Rouhanipour, A.; Az, R.; Rader, H. J.; Mullen, K. *Rapid Commun Mass Spectrom* **2001**, *15*, 1364.

(59) Trimpin, S.; Keune, S.; Rader, H. J.; Mullen, K. *J Am Soc Mass Spectrom* **2006**, *17*, 661.

(60) Trimpin, S.; McEwen, C. N. *J Am Soc Mass Spectrom* **2007**, *18*, 377.

(61) Trimpin, S.; Weidner, S. M.; Falkenhagen, J.; McEwen, C. N. *Anal Chem* **2007**, *79*, 7565.

(62) Hanton, S. D.; Parees, D. M. *J Am Soc Mass Spectrom* **2005**, *16*, 90.

(63) Trimpin, S.; Grimsdale, A. C.; Rader, H. J.; Mullen, K. *Anal Chem* **2002**, *74*, 3777.

(64) Trimpin, S.; Wijerathne, K.; McEwen, C. N. *Analytica Chimica Acta* **2009**, *654*, 20.

(65) Barrere, C.; Hubert-Roux, M.; Lange, C. M.; Rejaibi, M.; Kebir, N.; Desilles, N.; Lecamp, L.; Burel, F.; Loutelier-Bourhis, C. *Rapid Commun Mass Spectrom* **2012**, *26*, 1347.

(66) Gies, A. P.; Nonidez, W. K.; Anthamatten, M.; Cook, R. C.; Mays, J. W. *Rapid Commun Mass Spectrom* **2002**, *16*, 1903.

(67) Hortal, A. R.; Hurtado, P.; Martinez-Haya, B.; Arregui, A.; Banares, L. *Applied Physics a-Materials Science & Processing* **2008**, *92*, 859.

(68) Hortal, A. R.; Hurtado, P.; Martinez-Haya, B.; Arregui, A.; Banares, L. *J Phys Chem B* **2008**, *112*, 8530.

(69) Jackson, C. A.; Simonsick, W. J. *Current Opinion in Solid State & Materials Science* **1997**, *2*, 661.

(70) McEwen, C. N.; Peacock, P. M. *Anal Chem* **2002**, *74*, 2743.

(71) OConnor, P. B.; McLafferty, F. W. *J Am Chem Soc* **1995**, *117*, 12826.

(72) Latourte, L.; Blais, J. C.; Tabet, J. C.; Cole, R. B. *Anal Chem* **1997**, *69*, 2742.

(73) Jackson, A. T.; Slade, S. E.; Scrivens, J. H. *Int J Mass Spectrom* **2004**, *238*, 265.

(74) Prokai, L.; Simonsick, W. J. *Rapid Commun Mass Spectrom* **1993**, *7*, 853.

(75) Gruendling, T.; Guilhaus, M.; Barner-Kowollik, C. *Anal Chem* **2008**, *80*, 6915.

(76) Gruendling, T.; Guilhaus, M.; Barner-Kowollik, C. *Macromolecules* **2009**, *42*, 6366.

(77) Aaserud, D. J.; Prokai, L.; Simonsick, W. J. *Anal Chem* **1999**, *71*, 4793.

(78) Nielen, M. W. F. *Rapid Commun Mass Spectrom* **1996**, *10*, 1652.

(79) Nielen, M. W. F.; Malucha, S. *Rapid Commun Mass Spectrom* **1997**, *11*, 1194.

(80) Montaudo, M. S.; Puglisi, C.; Samperi, F.; Montaudo, G. *Rapid Commun Mass Spectrom* **1998**, *12*, 519.

(81) Hanton, S. D. *Chem Rev* **2001**, *101*, 527.

(82) Fei, X.; Murray, K. K. *Anal Chem* **1996**, *68*, 3555.

(83) Fei, X.; Wei, G.; Murray, K. K. *Anal Chem* **1996**, *68*, 1143.

(84) Liu, X. M.; Maziarz, E. P.; Heiler, D. J.; Grobe, G. L. *J Am Soc Mass Spectrom* **2003**, *14*, 195.

(85) Feldermann, A.; Toy, A. A.; Davis, T. P.; Stenzel, M. H.; Bamer-Kowollik, C. *Polymer* **2005**, *46*, 8448.

(86) Toy, A. A.; Vana, P.; Davis, T. P.; Barner-Kowollik, C. *Macromolecules* **2004**, *37*, 744.

(87) Chen, R.; Li, L. *J Am Soc Mass Spectrom* **2001**, *12*, 832.

(88) Girod, M.; Carissan, Y.; Humbel, S.; Charles, L. *Int J Mass Spectrom* **2008**, *272*, 1.

(89) Deery, M. J.; Jennings, K. R.; Jasieczek, C. B.; Haddleton, D. M.; Jackson, A. T.; Yates, H. T.; Scrivens, J. H. *Rapid Commun Mass Spectrom* **1997**, *11*, 57.

(90) Gruendling, T.; Hart-Smith, G.; Davis, T. P.; Stenzel, M. H.; Barner-Kowollik, C. *Macromolecules* **2008**, *41*, 1966.

(91) Bogan, M. J.; Agnes, G. R. *J Am Soc Mass Spectrom* **2002**, *13*, 177.

(92) Bagal, D.; Zhang, H.; Schnier, P. D. *Anal Chem* **2008**, *80*, 2408.

(93) Maziarz, E. P.; Baker, G. A.; Wood, T. D. *Macromolecules* **1999**, *32*, 4411.

(94) Nasioudis, A.; Joyce, W. F.; van Velde, J. W.; Heeren, R. M. A.; van den Brink, O. F. *Anal Chem* **2010**, *82*, 5735.

(95) Takats, Z.; Wiseman, J. M.; Gologan, B.; Cooks, R. G. *Science* **2004**, *306*, 471.

(96) Cody, R. B.; Laramee, J. A.; Durst, H. D. *Anal Chem* **2005**, *77*, 2297.

(97) McEwen, C. N.; McKay, R. G.; Larsen, B. S. *Anal Chem* **2005**, *77*, 7826.

(98) Takats, Z.; Wiseman, J. M.; Cooks, R. G. *J Mass Spectrom* **2005**, *40*, 1261.

(99) Cooks, R. G.; Gologan, B.; Wiseman, J.; Talaty, N.; Chen, H.; Cotte-Rodriguez, I. *Abstr Pap Am Chem S* **2005**, *230*, U298.

(100) Wiseman, J. M.; Puolitaival, S. M.; Takats, Z.; Cooks, R. G.; Caprioli, R. M. *Angew Chem Int Edit* **2005**, *44*, 7094.

(101) Weston, D. J.; Bateman, R.; Wilson, I. D.; Wood, T. R.; Creaser, C. S. *Anal Chem* **2005**, *77*, 7572.

(102) Rodriguez-Cruz, S. E. *Rapid Commun Mass Spectrom* **2006**, *20*, 53.

(103) Nefliu, M.; Venter, A.; Cooks, R. G. *Chem Commun* **2006**, 888.

(104) Jackson, A. T.; Williams, J. P.; Scrivens, J. H. *Rapid Commun Mass Spectrom* **2006**, *20*, 2717.

(105) Harris, G. A.; Galhena, A. S.; Fernandez, F. M. *Anal Chem* **2011**, *83*, 4508.

(106) Nilles, J. M.; Connell, T. R.; Durst, H. D. *Anal Chem* **2009**, *81*, 6744.

(107) Ackerman, L. K.; Noonan, G. O.; Begley, T. H. *Food Addit Contam A* **2009**, *26*, 1611.

(108) Nyadong, L.; Harris, G. A.; Balayssac, S.; Galhena, A. S.; Malet-Martino, M.; Martino, R.; Parry, R. M.; Wang, M. D. M.; Fernandez, F. M.; Gilard, V. *Anal Chem* **2009**, *81*, 4803.

(109) Laramée, J. A.; Cody, R. B.; Nilles, J. M.; Durst, H. D. In *Forensic Analysis on the Cutting Edge*; John Wiley & Sons, Inc.: 2007, p 175.

(110) Petucci, C.; Diffendal, J. *J Mass Spectrom* **2008**, *43*, 1565.

(111) Bruns, E. A.; Perraud, V.; Greaves, J.; Finlayson-Pitts, B. J. *Anal Chem* **2010**, *82*, 5922.

(112) Rozenski, J. *Int J Mass Spectrom* **2011**, *304*, 204.

(113) Smith, M. J. P.; Cameron, N. R.; Mosely, J. A. *Analyst* **2012**, *137*, 4524.

(114) Aebersold, R.; Goodlett, D. R. *Chem Rev* **2001**, *101*, 269.

(115) Crecelius, A. C.; Baumgaertel, A.; Schubert, U. S. *J Mass Spectrom* **2009**, *44*, 1277.

(116) Hager, J. W.; Le Blanc, J. C. Y. *Rapid Commun Mass Spectrom* **2003**, *17*, 1056.

(117) Sleno, L.; Volmer, D. A. *J Mass Spectrom* **2004**, *39*, 1091.

(118) Biemann, K. *Biomed Environ Mass* **1988**, *16*, 99.

(119) Domon, B.; Costello, C. E. *Glycoconjugate J* **1988**, *5*, 397.

(120) Wesdemiotis, C.; Solak, N.; Polce, M. J.; Dabney, D. E.; Chaicharoen, K.; Katzenmeyer, B. C. *Mass Spectrom Rev* **2011**, *30*, 523.

(121) Shukla, A. K.; Futrell, J. H. *J Mass Spectrom* **2000**, *35*, 1069.

(122) Jackson, A. T.; Yates, H. T.; Scrivens, J. H.; Critchley, G.; Brown, J.; Green, M. R.; Bateman, R. H. *Rapid Commun Mass Spectrom* **1996**, *10*, 1668.

(123) Bottrill, A. R.; Giannakopulos, A. E.; Waterson, C.; Haddleton, D. M.; Lee, K. S.; Derrick, P. J. *Anal Chem* **1999**, *71*, 3637.

(124) Chen, R.; Yu, X. L.; Li, L. *J Am Soc Mass Spectrom* **2002**, *13*, 888.

(125) Williams, J. P.; Hilton, G. R.; Thalassinos, K.; Jackson, A. T.; Scrivens, J. H. *Rapid Commun Mass Spectrom* **2007**, *21*, 1693.

(126) Hilton, G. R.; Jackson, A. T.; Thalassinos, K.; Scrivens, J. H. *Anal Chem* **2008**, *80*, 9720.

(127) Knop, K.; Jahn, B. O.; Hager, M. D.; Crecelius, A.; Gottschaldt, M.; Schubert, U. S. *Macromol Chem Physic* **2010**, *211*, 677.

(128) Nasioudis, A.; Heeren, R. M. A.; van Doormalen, I.; de Wijs-Rot, N.; van den Brink, O. F. *J Am Soc Mass Spectrom* **2011**, *22*, 837.

(129) Jackson, A. T.; Green, M. R.; Bateman, R. H. *Rapid Commun Mass Spectrom* **2006**, *20*, 3542.

(130) Okuno, S.; Kiuchi, M.; Arakawa, R. *Eur J Mass Spectrom* **2006**, *12*, 181.

(131) Lattimer, R. P. *J Am Soc Mass Spectrom* **1994**, *5*, 1072.

(132) Lattimer, R. P. *J Am Soc Mass Spectrom* **1992**, *3*, 225.

(133) Scrivens, J. H.; Jackson, A. T.; Yates, H. T.; Green, M. R.; Critchley, G.; Brown, J.; Bateman, R. H.; Bowers, M. T.; Gidden, J. *Int J Mass Spectrom* **1997**, *165*, 363.

(134) Jackson, A. T.; Bunn, A.; Priestnall, I. M.; Borman, C. D.; Irvine, D. J. *Polymer* **2006**, *47*, 1044.

(135) Baumgaertel, A.; Becer, C. R.; Gottschaldt, M.; Schubert, U. S. *Macromol Rapid Comm* **2008**, *29*, 1309.

(136) Alhazmi, A. M.; Mayer, P. M. *J Am Soc Mass Spectrom* **2009**, *20*, 60.

(137) Jackson, A. T.; Yates, H. T.; Scrivens, J. H.; Green, M. R.; Bateman, R. H. *J Am Soc Mass Spectrom* **1997**, *8*, 1206.

(138) Chaicharoen, K.; Polce, M. J.; Singh, A.; Pugh, C.; Wesdemiotis, C. *Anal Bioanal Chem* **2008**, *392*, 595.

(139) Hart-Smith, G.; Lammens, M.; Du Prez, F. E.; Guilhaus, M.; Barner-Kowollik, C. *Polymer* **2009**, *50*, 1986.

(140) Jackson, A. T.; Yates, H. T.; Scrivens, J. H.; Green, M. R.; Bateman, R. H. *J Am Soc Mass Spectrom* **1998**, *9*, 269.

(141) Jackson, A. T.; Bunn, A.; Hutchings, L. R.; Kiff, F. T.; Richards, R. W.; Williams, J.; Green, M. R.; Bateman, R. H. *Polymer* **2000**, *41*, 7437.

(142) Polce, M. J.; Ocampo, M.; Quirk, R. P.; Leigh, A. M.; Wesdemiotis, C. *Anal Chem* **2008**, *80*, 355.

(143) Polce, M. J.; Ocampo, M.; Quirk, R. P.; Wesdemiotis, C. *Anal Chem* **2008**, *80*, 347.

(144) Gies, A. P.; Vergne, M. J.; Orndorff, R. L.; Hercules, D. M. *Macromolecules* **2007**, *40*, 7493.

(145) Jackson, A. T.; Slade, S. E.; Thalassinos, K.; Scrivens, J. H. *Anal Bioanal Chem* **2008**, *392*, 643.

(146) Arnould, M. A.; Vargas, R.; Buehner, R. W.; Wesdemiotis, C. *Eur J Mass Spectrom* **2005**, *11*, 243.

(147) De Winter, J.; Coulembier, O.; Dubois, P.; Gerbaux, P. *Int J Mass Spectrom* **2011**, *308*, 11.

(148) Altuntas, E.; Knop, K.; Tauhardt, L.; Kempe, K.; Crecelius, A. C.; Jager, M.; Hager, M. D.; Schubert, U. S. *J Mass Spectrom* **2012**, *47*, 105.

(149) Ellison, S. T.; Gies, A. P.; Hercules, D. M.; Morgan, S. L. *Macromolecules* **2009**, *42*, 3005.

(150) Memboeuf, A.; Drahos, L.; Vekey, K.; Lendvay, G. *Rapid Commun Mass Spectrom* **2010**, *24*, 2471.

(151) Collins, S.; Rimmer, S. *Rapid Commun Mass Spectrom* **2004**, *18*, 3075.

(152) Scrivens, J. H.; Jackson, A. T. *Int J Mass Spectrom* **2000**, *200*, 261.

(153) Jackson, A. T.; Scrivens, J. H.; Williams, J. P.; Baker, E. S.; Gidden, J.; Bowers, M. T. *Int J Mass Spectrom* **2004**, *238*, 287.

(154) Terrier, P.; Buchmann, W.; Desmazieres, B.; Tortajada, J. *Anal Chem* **2006**, *78*, 1801.

(155) Wesdemiotis, C.; Pingitore, F.; Polce, M. J.; Russell, V. M.; Kim, Y.; Kausch, C. M.; Connors, T. H.; Medsker, R. E.; Thomas, R. R. *Macromolecules* **2006**, *39*, 8369.

(156) Weidner, S. M.; Falkenhagen, J.; Maltsev, S.; Sauerland, V.; Rinken, M. *Rapid Commun Mass Spectrom* **2007**, *21*, 2750.

(157) Girod, M.; Phan, T. N. T.; Charles, L. *Rapid Commun Mass Spectrom* **2008**, *22*, 3767.

(158) Girod, M.; Phan, T. N. T.; Charles, L. *Rapid Commun Mass Spectrom* **2009**, *23*, 1476.

(159) Crecelius, A. C.; Becer, C. R.; Knop, K.; Schubert, U. S. *J Polym Sci Pol Chem* **2010**, *48*, 4375.

(160) Miladinovic, S. M.; Kaeser, C. J.; Knust, M. M.; Wilkins, C. L. *Int J Mass Spectrom* **2011**, *301*, 184.

(161) Zubarev, R. A.; Kelleher, N. L.; McLafferty, F. W. *J Am Chem Soc* **1998**, *120*, 3265.

(162) Savitski, M. M.; Kjeldsen, F.; Nielsen, M. L.; Zubarev, R. A. *Angew Chem Int Edit* **2006**, *45*, 5301.

(163) Heeren, R. M. A.; Kleinnijenhuis, A. J.; McDonnell, L. A.; Mize, T. H. *Anal Bioanal Chem* **2004**, *378*, 1048.

(164) McLafferty, F. W.; Kelleher, R. L.; Zubarev, R. A.; Bush, K.; Furie, B.; Furie, B. C.; Walsh, C. T. *Anal Chem* **1999**, *71*, 4250.

(165) Bakhtiar, R.; Guan, Z. Q. *Biochem Bioph Res Co* **2005**, *334*, 1.

(166) Zubarev, R. A.; Haselmann, K. F.; Budnik, B.; Kjeldsen, F.; Jensen, F. *Eur J Mass Spectrom* **2002**, *8*, 337.

(167) Zubarev, R. A.; Horn, D. M.; Fridriksson, E. K.; Kelleher, N. L.; Kruger, N. A.; Lewis, M. A.; Carpenter, B. K.; McLafferty, F. W. *Anal Chem* **2000**, *72*, 563.

(168) Simons, J. *Chem Phys Lett* **2010**, *484*, 81.

(169) Uggerud, E. *Int J Mass Spectrom* **2004**, *234*, 45.

(170) McLafferty, F. W.; Ge, Y.; Lawhorn, B. G.; ElNaggar, M.; Strauss, E.; Park, J. H.; Begley, T. P. *J Am Chem Soc* **2002**, *124*, 672.

(171) McLafferty, F. W.; Zubarev, R. A.; Kruger, N. A.; Fridriksson, E. K.; Lewis, M. A.; Horn, D. M.; Carpenter, B. K. *J Am Chem Soc* **1999**, *121*, 2857.

(172) Syrstad, E. A.; Turecek, F. *J Am Soc Mass Spectrom* **2005**, *16*, 208.

(173) Swierszcz, I.; Skurski, P.; Simons, J. *J Phys Chem A* **2012**, *116*, 1828.

(174) Leymarie, N.; Costello, C. E.; O'Connor, P. B. *J Am Chem Soc* **2003**, *125*, 8949.

(175) O'Connor, P. B.; Lin, C.; Cournoyer, J. J.; Pittman, J. L.; Belyayev, M.; Budnik, B. A. *J Am Soc Mass Spectrom* **2006**, *17*, 576.

(176) Lin, C.; O'Connor, P. B.; Cournoyer, J. J. *J Am Soc Mass Spectrom* **2006**, *17*, 1605.

(177) Chakraborty, T.; Holm, A. I. S.; Hvelplund, P.; Nielsen, S. B.; Poully, J. C.; Worm, E. S.; Williams, E. R. *J Am Soc Mass Spectrom* **2006**, *17*, 1675.

(178) Mihalca, R.; Kleinnijenhuis, A. J.; McDonnell, L. A.; Heck, A. J. R.; Heeren, R. M. A. *J Am Soc Mass Spectrom* **2004**, *15*, 1869.

(179) Kjeldsen, F.; Haselmann, K. F.; Budnik, B. A.; Jensen, F.; Zubarev, R. A. *Chem Phys Lett* **2002**, *356*, 201.

(180) Williams, J. P.; Creese, A. J.; Roper, D. R.; Green, B. N.; Cooper, H. J. *J Am Soc Mass Spectrom* **2009**, *20*, 1707.

(181) Cody, R. B.; Freiser, B. S. *Anal Chem* **1979**, *51*, 547.

(182) Lioe, H.; O'Hair, R. A. J. *Anal Bioanal Chem* **2007**, *389*, 1429.

(183) Yoo, H. J.; Liu, H. C.; Hakansson, K. *Anal Chem* **2007**, *79*, 7858.

(184) Feketeova, L.; O'Hair, R. A. J. *Rapid Commun Mass Spectrom* **2009**, *23*, 60.

(185) Feketeova, L.; O'Hair, R. A. J. *Rapid Commun Mass Spectrom* **2009**, *23*, 3259.

(186) Feketeova, L.; Ryzhov, V.; O'Hair, R. A. J. *Rapid Commun Mass Spectrom* **2009**, *23*, 3133.

(187) Mosely, J. A.; Smith, M. J. P.; Prakash, A. S.; Sims, M.; Bristow, A. W. T. *Anal Chem* **2011**, *83*, 4068.

(188) Feketeova, L.; Wong, M. W.; O'Hair, R. A. J. *European Physical Journal D* **2010**, *60*, 11.

(189) Prakash, A. S.; Smith, M. J. P.; Kaabia, Z.; Hurst, G.; Yan, C.; Sims, M.; Bristow, A. W. T.; Stokes, P.; Parker, D.; Mosely, J. A. *J Am Soc Mass Spectrom* **2012**, *23*, 850.

(190) Budnik, B. A.; Haselmann, K. F.; Zubarev, R. A. *Chem Phys Lett* **2001**, *342*, 299.

(191) Kornacki, J. R.; Adamson, J. T.; Hakansson, K. *J Am Soc Mass Spectrom* **2012**, *23*, 2031.

(192) Adamson, J. T.; Hakansson, K. *J Am Soc Mass Spectrom* **2007**, *18*, 2162.

(193) Mo, J. J.; Hakansson, K. *Anal Bioanal Chem* **2006**, *386*, 675.

(194) McFarland, M. A.; Marshall, A. G.; Hendrickson, C. L.; Nilsson, C. L.; Fredman, P.; Mansson, J. E. *J Am Soc Mass Spectrom* **2005**, *16*, 752.

(195) Yoo, H. J.; Wang, N.; Zhuang, S. Y.; Song, H. T.; Hakansson, K. *J Am Chem Soc* **2011**, *133*, 16790.

(196) Syka, J. E. P.; Coon, J. J.; Schroeder, M. J.; Shabanowitz, J.; Hunt, D. F. *Proc Natl Acad Sci U S A* **2004**, *101*, 9528.

(197) McLuckey, S. A.; Mentinova, M. *J Am Soc Mass Spectrom* **2011**, *22*, 3.

(198) Li, X. J.; Lin, C.; Han, L.; Costello, C. E.; O'Connor, P. B. *J Am Soc Mass Spectrom* **2010**, *21*, 646.

(199) Jones, A. W.; Cooper, H. J. *Analyst* **2011**, *136*, 3419.

(200) Mikesh, L. M.; Ueberheide, B.; Chi, A.; Coon, J. J.; Syka, J. E. P.; Shabanowitz, J.; Hunt, D. F. *Bba-Proteins Proteom* **2006**, *1764*, 1811.

(201) Cerda, B. *Eur J Mass Spectrom* **1999**, *5*, 335.

(202) Cerda, B. A.; Breuker, K.; Horn, D. M.; McLafferty, F. W. *J Am Soc Mass Spectrom* **2001**, *12*, 565.

(203) Cerda, B. A.; Horn, D. M.; Breuker, K.; McLafferty, F. W. *J Am Chem Soc* **2002**, *124*, 9287.

(204) Jackson, A. T. In *57th ASMS Conference on Mass Spectrometry and Allied Topics* Philadelphia, Pennsylvania, USA, 2009.

(205) Scionti, B. In *58th ASMS Conference on Mass Spectrometry and Allied Topics* Salt Lake City, Utah, USA, 2010.

(206) Little, D. P.; Speir, J. P.; Senko, M. W.; Oconnor, P. B.; Mclafferty, F. W. *Anal Chem* **1994**, *66*, 2809.

(207) McGrath, S. C.; University of North Carolina: http://www.unc.edu/~smcgrath/SaraMcGrath.PDF.

(208) Trimpin, S.; Plasencia, M.; Isailovic, D.; Clemmer, D. E. *Anal Chem* **2007**, *79*, 7965.

(209) Trimpin, S.; Clemmer, D. E. *Anal Chem* **2008**, *80*, 9073.

(210) De Winter, J.; Lemaur, V.; Ballivian, R.; Chirot, F.; Coulembier, O.; Antoine, R.; Lemoine, J.; Cornil, J.; Dubois, P.; Dugourd, P.; Gerbaux, P. *Chemistry-a European Journal* **2011**, *17*, 9738.

(211) Cole, R. B. *Electrospray and MALDI mass spectrometry: fundementals, instrumentation, practicalities and biological applications*; Second edition ed.; Wiley: Hoboken, NJ, USA, 2010.

(212) Tanaka, K. *Rapid Commun Mass Spectrom* **1988**, *12*, 151.

(213) Itina, T. E.; Zhigilei, L. V.; Garrison, B. J. *Nucl Instrum Methods Phys Res Sect B-Beam Interact Mater Atoms* **2001**, *180*, 238.

(214) Itina, T. E.; Zhigilei, L. V.; Garrison, B. J. *J Phys Chem B* **2002**, *106*, 303.

(215) Hillenkamp, P.-K. *MALDI MS: A practical guide to Instrumentation, Methods and Applications*, 2007.

(216) *Bruker Autoflex operators manual* 2004.

(217) Dole, M.; Mack, L. L.; Hines, R. L. *J Chem Phys* **1968**, *49*, 2240.

(218) Thomson, B. A.; Iribarne, J. V.; Dziedzic, P. J. *Anal Chem* **1982**, *54*, 2219.

(219) Thermo *LTQ FT Ultra Manual*.

(220) *Waters Xevo QToF MS operators overview and maintenance guide*; Waters, 2008.

(221) Terrier, P.; Desmazieres, B.; Tortajada, J.; Buchmann, W. *Mass Spectrom Rev* **2011**, *30*, 854.

(222) Cody, R. B. *Anal Chem* **2009**, *81*, 1101.

(223) Covey, T. R.; Thomson, B. A.; Schneider, B. B. *Mass Spectrom Rev* **2009**, *28*, 870.

(224) Horning, E. C.; Carroll, D. I.; Dzidic, I.; Haegele, K. D.; Horning, M. G.; Stillwel.Rn *J Chromatogr Sci* **1974**, *12*, 725.

(225) Faubert, D.; Paul, G. J. C.; Giroux, J.; Bertrand, M. J. *International Journal of Mass Spectrometry and Ion Processes* **1993**, *124*, 69.

(226) Ray, A. D.; Hammond, J.; Major, H. *Eur J Mass Spectrom* **2010**, *16*, 169.

(227) Ifa, D. R.; Wu, C. P.; Ouyang, Z.; Cooks, R. G. *Analyst* **2010**, *135*, 669.

(228) Kertesz, V.; Van Berkel, G. J. *Rapid Commun Mass Spectrom* **2008**, *22*, 2639.

(229) Green, F. M.; Stokes, P.; Hopley, C.; Seah, M. P.; Gilmore, I. S.; O'Connor, G. *Anal Chem* **2009**, *81*, 2286.

(230) Green, F. M.; Salter, T. L.; Gilmore, I. S.; Stokes, P.; O'Connor, G. *Analyst* **2010**, *135*, 731.

(231) A.I, M. *Dictionary of Mass Spectrometry*; Wiley, 2009.

(232) Douglas, D. J.; Frank, A. J.; Mao, D. M. *Mass Spectrom Rev* **2005**, *24*, 1.

(233) Perry, R. H.; Cooks, R. G.; Noll, R. J. *Mass Spectrom Rev* **2008**, *27*, 661.

(234) Hu, Q. Z.; Noll, R. J.; Li, H. Y.; Makarov, A.; Hardman, M.; Cooks, R. G. *J Mass Spectrom* **2005**, *40*, 430.

(235) Nikolaev, E. N.; Boldin, I. A.; Jertz, R.; Baykut, G. *J Am Soc Mass Spectrom* **2011**, *22*, 1125.

(236) Schaub, T. M.; Hendrickson, C. L.; Horning, S.; Quinn, J. P.; Senko, M. W.; Marshall, A. G. *Anal Chem* **2008**, *80*, 3985.

(237) Karabacak, N. M.; Easterling, M. L.; Agar, N. Y. R.; Agar, J. N. *J Am Soc Mass Spectrom* **2010**, *21*, 1218.

(238) Marshall, A. G.; Guan, S. H. *Rapid Commun Mass Spectrom* **1996**, *10*, 1819.

(239) Caravatti, P.; Allemann, M. *Org Mass Spectrom* **1991**, *26*, 514.

(240) Marshall, A. G.; Hendrickson, C. L. *Int J Mass Spectrom* **2002**, *215*, 59.

(241) Amster, I. J. *J Mass Spectrom* **1996**, *31*, 1325.

(242) Marshall, A. G. *Int J Mass Spectrom* **2000**, *200*, 331.

(243) Marshall, A. G.; Hendrickson, C. L.; Emmett, M. R. *Abstr Pap Am Chem S* **2000**, *220*, U98.

(244) Wollyung, K. M.; Xu, K. T.; Cochran, M.; Kasko, A. M.; Mattice, W. L.; Wesdemiotis, C.; Pugh, C. *Macromolecules* **2005**, *38*, 2574.

(245) Barner-Kowollik, C. *Mass Spectrometry in Polymer Chemistry*; Wiley, 2011.

(246) Lattimer, R. P. *International Journal of Mass Spectrometry and Ion Processes* **1992**, *116*, 23.

(247) Selby, T. L.; Wesdemiotis, C.; Lattimer, R. P. *J Am Soc Mass Spectrom* **1994**, *5*, 1081.

(248) Kruger, N. A.; Zubarev, R. A.; Horn, D. M.; McLafferty, F. W. *Int J Mass Spectrom* **1999**, *185*, 787.

(249) Ude, S.; de la Mora, J. F.; Thomson, B. A. *J Am Chem Soc* **2004**, *126*, 12184.

(250) Atkins, P. W. *Physical Chemistry*; Oxford University Press, 1999.

(251) Mosely, J. A.; Murray, B. S.; Parker, D. *Eur J Mass Spectrom* **2009**, *15*, 145.

(252) Sugar, J.; Musgrove, A. *J Phys Chem Ref Data* **1990**, *19*, 527.

(253) Cowie, J. M. G. *Polymers: Chemistry and Physics of modern materials*; CRC Press, 2008.

(254) Barner-Kowollik, C. *Handbook of RAFT polymerisation*; Wiley, 2008.

(255) Hart-Smith, G.; Lovestead, T. M.; Davis, T. P.; Stenzel, M. H.; Barner-Kowollik, C. *Biomacromolecules* **2007**, *8*, 2404.

(256) Lovestead, T. M.; Hart-Smith, G.; Davis, T. P.; Stenzel, M. H.; Barner-Kowollik, C. *Macromolecules* **2007**, *40*, 4142.

(257) Vana, P.; Albertin, L.; Barner, L.; Davis, T. P.; Barner-Kowollik, C. *J Polym Sci Pol Chem* **2002**, *40*, 4032.

(258) Clarke, M. B.; Bezabeh, D. Z.; Howard, C. T. *J Agr Food Chem* **2006**, *54*, 1975.

(259) Murgasova, R.; Hercules, D. M. *Anal Bioanal Chem* **2002**, *373*, 481.

(260) Twohig, M.; Shockcor, J. P.; Wilson, I. D.; Nicholson, J. K.; Plumb, R. S. *J Proteome Res* **2010**, *9*, 3590.

(261) McEwen, C.; Gutteridge, S. *J Am Soc Mass Spectrom* **2007**, *18*, 1274.

(262) Knochenmuss, R.; Zenobi, R. *Chem Rev* **2003**, *103*, 441.

(263) Fussell, R. J.; Chan, D.; Sharman, M. *Trac-Trends in Analytical Chemistry* **2010**, *29*, 1326.

(264) Jones, G. G.; Pauls, R. E.; Willoughby, R. C. *Anal Chem* **1991**, *63*, 460.

(265) Montaudo, G.; Montaudo, M. S.; Puglisi, C.; Samperi, F. *Macromolecules* **1995**, *28*, 4562.

(266) Lattimer, R. P. *J Anal Appl Pyrol* **2000**, *56*, 61.

(267) Wetzel, S. J.; Guttman, C. M.; Girard, J. E. *Int J Mass Spectrom* **2004**, *238*, 215.

(268) Mark, J. E. *Polymer Data Handbook*; Second Edition ed.; Oxford University Press: USA, 2009.

(269) Hourani, N.; Kuhnert, N. *Rapid Commun Mass Spectrom* **2012**, *26*, 2365.

(270) Bell, S. E.; Ewing, R. G.; Eiceman, G. A.; Karpas, Z. *J Am Soc Mass Spectrom* **1994**, *5*, 177.

(271) Lattimer, R. P. *J Anal Appl Pyrol* **1995**, *31*, 203.

(272) Fetters, L. J.; Lohse, D. J.; Richter, D.; Witten, T. A.; Zirkel, A. *Macromolecules* **1994**, *27*, 4639.

(273) Hiraoka, K.; Fujimaki, S.; Kambara, S.; Furuya, H.; Okazaki, S. *Rapid Commun Mass Spectrom* **2004**, *18*, 2323.

(274) Onigbinde, A.; Nicol, G.; Munson, B. *Eur J Mass Spectrom* **2001**, *7*, 279.

(275) Voorhees, K. J.; Baugh, S. F.; Stevenson, D. N. *J Anal Appl Pyrol* **1994**, *30*, 47.

(276) Mosely, J. A. In *British Mass Spectrometry Society Annual Meeting* Cardiff, UK, 2010.

(277) Beyler, C. L. In *The SPFE Handbook of Fire Safety Engineering*; DiNenno, P. J., Ed.; NPFA: Quincy, MA, USA, 1988.

(278) Zhu, Z. Q.; Song, L. G.; Bartmess, J. E. *Rapid Commun Mass Spectrom* **2012**, *26*, 1320.

(279) Barner-Kowollik, C.; Buback, M.; Charleux, B.; Coote, M. L.; Drache, M.; Fukuda, T.; Goto, A.; Klumperman, B.; Lowe, A. B.; McLeary, J. B.; Moad, G.; Monteiro, M. J.; Sanderson, R. D.; Tonge, M. P.; Vana, P. *J Polym Sci Pol Chem* **2006**, *44*, 5809.

(280) Monteiro, M. J.; de Brouwer, H. *Macromolecules* **2001**, *34*, 349.

10. Appendix

10.1. Supplementary information for ESI MS and tandem MS of PEG

Table 10.1 Ion assignments for MS and tandem MS of [PEG$_{31}$ + Li]$^+$.

Figure 3.1				
MJPS_PEG_CHCA_LiBr_FullMS				
m/z	empirical formula	structure	accuracy /ppm	assignment
1389.4	$C_{62}H_{126}O_{32}Li$	$HO(C_2H_4O)_{31}H$ + Li		[M + Li]+
1405.3	$C_{62}H_{126}O_{32}Na$	$HO(C_2H_4O)_{31}H$ + Na		[M + Na]+
MJPS_PEG_Li_fullMS				
m/z	empirical formula	structure	accuracy /ppm	assignment
1389.83529	$C_{62}H_{126}O_{32}Li$	$HO(C_2H_4O)_{31}H$ + Li	-2.4	[M + Li]+
698.42675	$C_{62}H_{126}O_{32}Li_2$	$HO(C_2H_4O)_{31}H$ + 2Li	-0.5	[M + 2Li]2+
1405.81003	$C_{62}H_{126}O_{32}Na$	$HO(C_2H_4O)_{31}H$ + Na	-1.7	[M + Na]+
Figure 3.2				
MJPS_PEG_Li_ACHA_iso1389_LIFT				
m/z	empirical formula	structure	accuracy /ppm	assignment
1389.449	$C_{62}H_{126}O_{32}Li$	$HO(C_2H_4O)_{31}H$ + Li		[M + Li]+
887.658	$C_{40}H_{80}O_{20}Li$	$HO(C_2H_4O)_{19}CH=CH_2$ + Li		b_{19}
861.617	$C_{38}H_{78}O_{20}Li$	$HO(C_2H_4O)_{19}H$ + Li		c_{19}''
859.613	$C_{38}H_{76}O_{20}Li$	$HO(C_2H_4O)_{19}CH_2CH=O$ + Li		c_{19}
843.604	$C_{38}H_{76}O_{19}Li$	$HO(C_2H_4O)_{18}CH=CH_2$ + Li		b_{18}
MJPS_PEG_LIBR_CID12				
m/z	empirical formula	structure	accuracy	assignment
1389.8511	$C_{62}H_{126}O_{32}Li$	$HO(C_2H_4O)_{31}H$ + Li	8.6	[M + Li]+
887.5612	$C_{40}H_{80}O_{20}Li$	$HO(C_2H_4O)_{19}CH=CH_2$ + Li	5.2	b_{19}
861.4955	$C_{38}H_{78}O_{20}Li$	$HO(C_2H_4O)_{19}H$ + Li	5.5	c_{19}''
859.5024	$C_{38}H_{76}O_{20}Li$	$HO(C_2H_4O)_{19}CH_2CH=O$ + Li	-7.7	c_{19}
843.5128	$C_{38}H_{76}O_{19}Li$	$HO(C_2H_4O)_{18}CH=CH_2$ + Li	-1.5	b_{18}
MJPS_PEG_Li_iso1389_CID40				
1389.83784	$C_{62}H_{126}O_{32}Li$	$HO(C_2H_4O)_{31}H$ + Li	-0.6	[M + Li]+

887.54017	$C_{40}H_{80}O_{20}Li$	$HO(C_2H_4O)_{19}CH=CH_2 + Li$	0.5	b_{19}
861.52511	$C_{38}H_{78}O_{20}Li$	$HO(C_2H_4O)_{19}H + Li$	1.2	$c_{19}^{''}$
859.50897	$C_{38}H_{76}O_{20}Li$	$HO(C_2H_4O)_{19}CH_2CH=O + Li$	0.6	c_{19}
843.51392	$C_{38}H_{76}O_{19}Li$	$HO(C_2H_4O)_{18}CH=CH_2 + Li$	0.5	b_{18}
Figure 3.3				
MJPS_PEG_Li_iso1389_EID22				
m/z	empirical	structure	accuracy	assignment
1389.89058	$C_{62}H_{126}O_{32}Li$	$HO(C_2H_4O)_{31}H + Li$	7.6	[M + Li]+
887.56421	$C_{40}H_{80}O_{20}Li$	$HO(C_2H_4O)_{19}CH=CH_2 + Li$	7.6	b_{19}
873.54642	$C_{39}H_{79}O_{20}Li$	$CH_2=CHO(C_2H_4O)_{19}CH=CH_2 +$	5.6	J^{VV}
861.54779	$C_{38}H_{78}O_{20}Li$	$HO(C_2H_4O)_{19}H + Li$	5.1	$c_{19}^{''}$
859.53158	$C_{38}H_{76}O_{20}Li$	$HO(C_2H_4O)_{19}CH_2CH=O + Li$	6.9	c_{19}
857.55222	$C_{39}H_{78}O_{19}Li$	$CH_3O(C_2H_4O)_{19}CH_2CH=O + Li$	8.2	J^{MV}
843.53622	$C_{38}H_{76}O_{19}Li$	$HO(C_2H_4O)_{18}CH=CH_2 + Li$	6.9	b_{18}
Figure 3.4				
MJPS_PEG_LIBR_CID6				
m/z	empirical formula	structure	accuracy /ppm	assignment
698.4578	$C_{62}H_{126}O_{32}Li_2$	$HO(C_2H_4O)_{31}H + 2Li$	-2.5	[M + 2Li]2+
271.1823	$C_{12}H_{24}O_6Li$	$HO(C_2H_4O)_5CH=CH_2 + Li$	3.3	b_5
255.1926	$C_{12}H_{24}O_5Li$	$CH_2=CHO(C_2H_4O)_4CH_2CH_3 +$	5.6	J^{EV}
245.1725	$C_{10}H_{22}O_6Li$	$HO(C_2H_4O)_5H + Li$	6.8	$c_5^{''}$
243.1582	$C_{10}H_{20}O_6Li$	$HO(C_2H_4O)_4CH_2CH=O + Li$	6.6	c_{19}
241.175	$C_{11}H_{21}O_5Li$	$CH_3O(C_2H_4O)_4CH=CH_2 + Li$	8.2	J^{MV}
227.1602	$C_{10}H_{20}O_5Li$	$HO(C_2H_4O)_4CH=CH_2 + Li$	7.7	b_4
MJPS_PEG_Li_iso698_CID30				
698.92926	$C_{62}H_{126}O_{32}Li_2$	$HO(C_2H_4O)_{31}H + 2Li$	-2.5	[M + 2Li]2+
799.48804	$C_{36}H_{72}O_{18}Li$	$HO(C_2H_4O)_{17}CH=CH_2 + Li$	0.9	b_{17}
815.48264	$C_{36}H_{72}O_{19}Li$	$HO(C_2H_4O)_{17}CH_2CH=O + Li$	0.5	c_{17}
817.49835	$C_{36}H_{74}O_{19}Li$	$HO(C_2H_4O)_{18}H + Li$	0.6	$c_{17}^{''}$
843.51385	$C_{38}H_{76}O_{19}Li$	$HO(C_2H_4O)_{18}CH=CH_2 + Li$	0.4	b_{18}
676.4148	$C_{60}H_{122}O_{31}Li_2$	$HO(C_2H_4O)_{30}H + 2Li$	1.2	$c_{29}^{2+''}$
667.40927	$C_{60}H_{120}O_{30}Li_2$	$HO(C_2H_4O)_{29}CH=CH_2 + 2Li$	0.9	$b_{29}^{2+''}$
654.40174	$C_{58}H_{118}O_{30}Li_2$	$HO(C_2H_4O)_{29}H + 2Li$	1.4	$c_{28}^{2+''}$
645.39627	$C_{58}H_{116}O_{29}Li_2$	$HO(C_2H_4O)_{28}CH=CH_2 + 2Li$	1.1	$b_{28}^{2+''}$
632.38854	$C_{56}H_{114}O_{29}Li_2$	$HO(C_2H_4O)_{28}H + 2Li$	1.3	$c_{27}^{2+''}$
MJPS_PEG_Li_iso698_ECD5				
698.42904	$C_{62}H_{126}O_{32}Li_2$	$HO(C_2H_4O)_{31}H + 2Li$	2.8	[M + 2Li]2+
1395.86271	$C_{62}H_{125}O_{32}Li_2$	$HO(C_2H_4O)_{31}Li + Li$	11.4	[M + 2Li - H]+
MJPS_PEG_Li_iso698_ECD20				

m/z	empirical	structure	accuracy	assignment
698.43368	$C_{62}H_{126}O_{32}Li_2$	$HO(C_2H_4O)_{31}H + 2Li$	9.5	[M + 2Li]2+
1395.87745	$C_{62}H_{125}O_{32}Li_2$	$HO(C_2H_4O)_{31}Li + Li$	21.9	[M + 2Li - H]+
271.17464	$C_{12}H_{24}O_6Li$	$HO(C_2H_4O)_5CH{=}CH_2 + Li$	7.0	b_5
255.17945	$C_{12}H_{24}O_5Li$	$CH_2{=}CHO(C_2H_4O)_4CH_2CH_3$ +	6.5	J^{EV}
245.15855	$C_{10}H_{22}O_6Li$	$HO(C_2H_4O)_5H + Li$	5.9	$c_5^{''}$
243.14286	$C_{10}H_{20}O_6Li$	$HO(C_2H_4O)_4CH_2CH{=}O + Li$	5.8	c_{19}
241.16358	$C_{11}H_{21}O_5Li$	$CH_3O(C_2H_4O)_4CH{=}CH_2 + Li$	5.8	J^{MV}
227.14774	$C_{10}H_{20}O_5Li$	$HO(C_2H_4O)_4CH{=}CH_2 + Li$	5.3	b_4
Figure 3.6				
MJPS_PEG_LIBR_CID7				
m/z	empirical formula	structure	accuracy /ppm	assignment
467.9694	$C_{62}H_{126}O_{32}Li_3$	$HO(C_2H_4O)_{31}H + 3Li$	-2.5	[M + 3Li]3+
698.4578	$C_{62}H_{126}O_{32}Li_2$	$HO(C_2H_4O)_{31}H + 2Li$	-2.5	[M + 2Li]2+
271.1883	$C_{12}H_{24}O_6Li$	$HO(C_2H_4O)_5CH{=}CH_2 + Li$	3.3	b_5
255.1926	$C_{12}H_{24}O_5Li$	$CH_2{=}CHO(C_2H_4O)_4CH_2CH_3$ +	5.6	J^{EV}
245.1725	$C_{10}H_{22}O_6Li$	$HO(C_2H_4O)_5H + Li$	6.8	$c_5^{''}$
243.1525	$C_{10}H_{20}O_6Li$	$HO(C_2H_4O)_4CH_2CH{=}O + Li$	6.6	c_{19}
241.175	$C_{11}H_{21}O_5Li$	$CH_3O(C_2H_4O)_4CH{=}CH_2 + Li$	8.2	J^{MV}
227.1602	$C_{10}H_{20}O_5Li$	$HO(C_2H_4O)_4CH{=}CH_2 + Li$	7.7	b_4
MJPS_PEG_LiBR_CID32				
468.29094	$C_{62}H_{126}O_{32}Li_3$	$HO(C_2H_4O)_{31}H + 3Li$	-3.3	[M + 3Li]3+
698.42697	$C_{62}H_{126}O_{32}Li_2$	$HO(C_2H_4O)_{31}H + 2Li$	-0.1	[M + 2Li]2+
453.28108	$C_{60}H_{122}O_{31}Li_3$	$HO(C_2H_4O)_{30}H + 3Li$	-0.1	$c_{30}^{2+''}$
438.60567	$C_{58}H_{118}O_{30}Li_3$	$HO(C_2H_4O)_{29}H + 3Li$	-0.1	$c_{29}^{2+''}$
623.38228	$C_{28}H_{56}O_{14}Li$	$HO(C_2H_4O)_{13}CH{=}CH_2 + Li$	-0.3	b_{13}
579.35639	$C_{26}H_{52}O_{13}Li$	$HO(C_2H_4O)_{13}CH{=}CH_2 + Li$	0.2	b_{12}
535.33023	$C_{24}H_{48}O_{12}Li$	$HO(C_2H_4O)_{12}CH{=}CH_2 + Li$	0.4	b_{12}
MJPS_PEG_LiBr_iso467_ECD5				
467.95602	$C_{62}H_{126}O_{32}Li_3$	$HO(C_2H_4O)_{31}H + 3Li$	-1.0	[M + 3Li]3+
701.4303	$C_{62}H_{125}O_{32}Li_3$	$HO(C_2H_4O)_{31}Li + 2Li$	-1.2	[M-H +
1401.854	$C_{62}H_{124}O_{32}Li_3$	$LiO(C_2H_4O)_{31}Li + Li$	-0.7	[M-2H +
MJPS_PEG_LiBr_iso467_EID24				
467.95708	$C_{62}H_{126}O_{32}Li_3$	$HO(C_2H_4O)_{31}H + 3Li$	-0.5	[M + 3Li]3+
701.43267	$C_{62}H_{125}O_{32}Li_3$	$HO(C_2H_4O)_{31}Li + 2Li$	0.5	[M-H +
1401.86122	$C_{62}H_{124}O_{32}Li_3$	$LiO(C_2H_4O)_{31}Li + Li$	2.7	[M-2H +
271.17286	$C_{12}H_{24}O_6Li$	$HO(C_2H_4O)_5CH{=}CH_2 + Li$	0.4	b_5
258.16501	$C_{11}H_{23}O_6Li$	$HO(C_2H_4O)_5{=}CH_2 + Li$	0.4	J^{MH}
255.17793	$C_{12}H_{24}O_5Li$	$CH_2{=}CHO(C_2H_4O)_4CH_2CH_3$ +	0.4	J^{EV}
251.16541	$C_{10}H_{21}O_6Li_2$	$HO(C_2H_4O)_5Li + Li$	0.5	$c_5^{\wedge}$

243.14151	$C_{10}H_{20}O_6Li$	$HO(C_2H_4O)_4CH_2CH{=}O + Li$	0.3	c_{19}
241.16226	$C_{11}H_{21}O_5Li$	$CH_3O(C_2H_4O)_4CH{=}CH_2 + Li$	0.3	J^{MV}
227.14658	$C_{10}H_{20}O_5Li$	$HO(C_2H_4O)_4CH{=}CH_2 + Li$	0.2	b_4

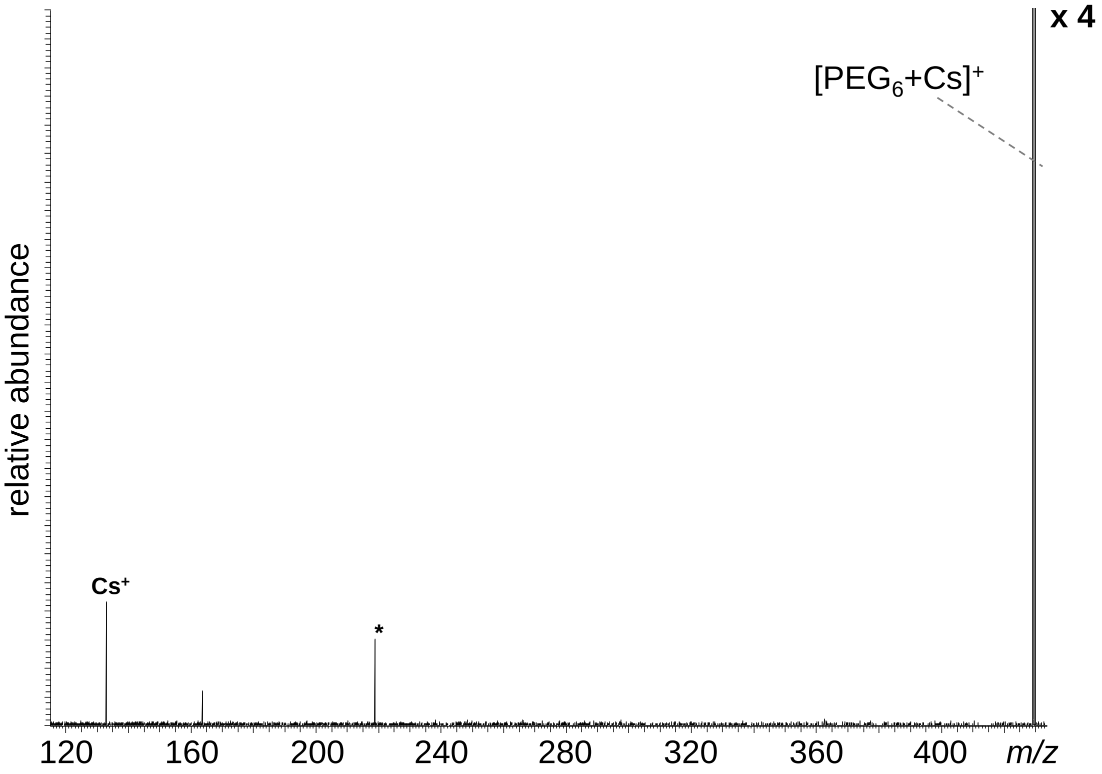

Figure 10.1 CID Tandem MS of $[CH_3O(C_2H_4O)_6H + Cs]$+ demonstrating cation detachment.(* = electronic noise at *m/z* 218.9).

Table 10.2 Summary of ion assignments for tandem MS of $[PEG_{31} + nLi]^{n+}$, where n =2 or 3.

Figure 3.8				
PEG_FT_POS_iso624_CID15				
m/z	empirical formula	structure	accuracy /ppm	assignment
623.40505	$C_{27}H_{61}O_{14}N$	$CH_3O(C_2H_4O)_{13}H + NH_4$	-6.7	$[M + NH_4]$+
605.37462	$C_{27}H_{57}O_{14}$	$CH_3O(C_2H_4O)_{13}H + H$	-0.3	[M + H]+
561.3491	$C_{25}H_{53}O_{13}$	$CH_3O(C_2H_4O)_{12}H + H$	0.9	$c_{12}^{''+}$
499.31199	$C_{23}H_{47}O_{11}$	$CH_3O(C_2H_4O)_{10}CH{=}CH_2 + H$	0.4	b_{10+}
485.29621	$C_{22}H_{45}O_{11}$	$CH_2{=}CHO(C_2H_4O)_{10}H + Na$	0.5	z_{10+}
473.29622	$C_{21}H_{45}O_{11}$	$CH_3O(C_2H_4O)_{10}H + H$	0.1	$c_{10}^{''+}$
PEG_FT_POS_iso61_CID25				
611.38279	$C_{27}H_{56}O_{14}Li$	$CH_3O(C_2H_4O)_{13}H + Li$	-0.4	[M + Li]+
567.35718	$C_{25}H_{52}O_{13}Li$	$CH_3O(C_2H_4O)_{12}H + Li$	0.9	$c_{12}^{''}$

553.34142	$C_{24}H_{50}O_{13}Li$	$HO-CH_2-CH_2O(C_2H_4O)_{11}H + H$	0.5	x_{11}''
549.34652	$C_{25}H_{50}O_{12}Li$	$CH_3O(C_2H_4O)_{11}CH=CH_2 + H$	0.5	b_{11}
535.33083	$C_{24}H_{48}O_{12}Li$	$CH_2=CHO(C_2H_4O)_{11}H + Na$	0.5	z_{11}
PEG_FT_POS_iso627_CID25				
627.36012	$C_{27}H_{56}O_{14}Na$	$CH_3O(C_2H_4O)_{13}H + Na$	-7.1	[M + Na]+
583.33112	$C_{25}H_{52}O_{12}Na$	$CH_3O(C_2H_4O)_{12}H + Na$	1.0	c_{12}''
PEG_FT_POS_iso643_CID20				
643.33118	$C_{27}H_{56}O_{14}K$	$CH_3O(C_2H_4O)_{13}H + K$	0.7	[M + K]+
MJPS_PEG_AgTFA_iso711_CID32				
713.26943	$C_{27}H_{56}O_{14}Ag$	$CH_3O(C_2H_4O)_{13}H + Ag$	-2.7	[M + Ag]+
667.24429	$C_{25}H_{52}O_{13}Ag$	$CH_3O(C_2H_4O)_{12}H + Ag$	-2.4	c_{12}''
653.22893	$C_{24}H_{50}O_{13}Ag$	$HO-CH_2-CH_2O(C_2H_4O)_{11}H +$	-2.0	x_{11}''
649.23395	$C_{25}H_{50}O_{12}Ag$	$CH_3O(C_2H_4O)_{11}CH=CH_2 + Ag$	-2.1	b_{11}
635.21824	$C_{24}H_{48}O_{12}Ag$	$CH_2=CHO(C_2H_4O)_{11}H + Ag$	-2.3	z_{11}
623.21813	$C_{23}H_{48}O_{12}Ag$	$CH_3O(C_2H_4O)_{11}H + Ag$	-2.5	c_{11}''
MJPS_PEG_CuMeSal_iso667_CID30				
667.29434	$C_{27}H_{56}O_{14}Cu$	$CH_3O(C_2H_4O)_{13}H + Cu$	-2.8	[M + Cu]+
447.16382	$C_{17}H_{36}O_9Cu$	$CH_3O(C_2H_4O)_8H + Cu$	-2.6	c_8''
433.1482	$C_{16}H_{34}O_9Cu$	$HO-CH_2-CH_2O(C_2H_4O)_8H +$	-2.6	x_7''
429.15337	$C_{17}H_{34}O_8Cu$	$CH_3O(C_2H_4O)_7CH=CH_2 + Cu$	-2.5	b_7
415.13778	$C_{16}H_{32}O_8Cu$	$CH_2=CHO(C_2H_4O)_7H + Cu$	-2.3	z_7
Figure 3.9				
PEG_FT_POS_iso624_EID23				
m/z	empirical formula	structure	accuracy /ppm	assignment
622.40517	$C_{27}H_{60}O_{14}N$	$CH_3O(C_2H_4O)_{13}H + NH_4$	7.0	[M + NH_4]+
340.23452	$C_{15}H_{37}O_7Na$	$CH_3O(C_2H_4O)_6CH=CH_2 + Na$	4.5	b_6
327.22654	$C_{14}H_{33}O_7N$	$CH_2=CHO(C_2H_4O)_6H + Na$	-2.3	z_6
PEG_OMe_FT_iso627_ECD21				
627.36041	$C_{27}H_{56}O_{14}Na$	$CH_3O(C_2H_4O)_{13}H + Na$	6.7	[M + Na]+
495.28386	$C_{21}H_{44}O_{11}Na$	$CH_3O(C_2H_4O)_9CH_2-CH_2-OH +$	11.6	c_9''
493.2685	$C_{21}H_{42}O_{11}Na$	$CH_3O(C_2H_4O)_9CH_2-CH=O +$	12.2	c_9
481.26807	$C_{20}H_{42}O_{11}Na$	$HO-CH_2-CH_2O(C_2H_4O)_9H +$	11.6	x_9''
479.25236	$C_{20}H_{40}O_{11}Na$	$O=CH-CH_2O(C_2H_4O)_9H + Na$	11.5	x_9
477.27305	$C_{21}H_{42}O_{10}Na$	$CH_3O(C_2H_4O)_9CH=CH_2 + Na$	11.5	b_9
463.25702	$C_{20}H_{40}O_{10}Na$	$CH_2=CHO(C_2H_4O)_9H + Na$	11.0	z_9
PEG_OMe_FT_iso643_ECD21				
643.33746	$C_{27}H_{56}O_{14}K$	$CH_3O(C_2H_4O)_{13}H + K$	11.3	[M + K]+
303.12379	$C_{12}H_{24}O_6K$	$CH_2=CHO(C_2H_4O)_5H + K$	11.0	z_5
317.13974	$C_{13}H_{26}O_6K$	$CH_3O(C_2H_4O)_5CH=CH_2 + K$	11.5	b_5
319.11901	$C_{12}H_{24}O_7K$	$O=CH-CH_2O(C_2H_4O)_5H + K$	11.4	x_5

331.15575	$C_{14}H_{28}O_6K$	$CH_2=CHO(C_2H_4O)_5CH_2CH_3$ +	12.1	J_5^{EV}
334.1429	$C_{13}H_{27}O_7K$	$CH_3O(C_2H_4O)_5CH_2$-CH=O + K	12.2	c_5
347.15114	$C_{14}H_{28}O_7K$	$CH_2=CHO(C_2H_4O)_6H$ + K	13.0	z_6
MJPS_PEG_AgTFA_iso711_EID23				
711.27283	$C_{27}H_{56}O_{14}Ag$	$CH_3O(C_2H_4O)_{13}H$ +Ag	1.8	[M + Ag]+
341.05139	$C_{11}H_{22}O_5Ag$	$CH_3O(C_2H_4O)_5CH=CH_2$ + Ag	0.4	b_5
328.04351	$C_{10}H_{21}O_5Ag$	$CH_2=CHO(C_2H_4O)_4H$ + Ag	0.2	z_4
314.02783	$C_9H_{19}O_5Ag$	$CH_3O(C_2H_4O)_3CH_2$-CH=O +	0.1	c_3
311.04081	$C_{10}H_{20}O_4Ag$	$CH_2=CHO(C_2H_4O)_3CH_2CH_3$ +	12.0	J_5^{EV}
MJPS_PEG_CuMeSal_iso667_EID25				
667.29657	$C_{27}H_{56}O_{14}Cu$	$CH_3O(C_2H_4O)_{13}H$ +Cu	0.8	[M + Cu]+
446.157968	$C_{17}H_{35}O_9Cu$	$CH_3O(C_2H_4O)_8$+ Cu(II)	1.2	$c_7^{\wedge}$
432.14021	$C_{16}H_{33}O_9Cu$	Cu(II)-O-CH_2-$CH_2O(C_2H_4O)_7H$	1.2	$x_7^{\wedge}$
429.15472	$C_{17}H_{34}O_8Cu$	$CH_3O(C_2H_4O)_7CH=CH_2$ + Cu	0.7	b_7
415.13914	$C_{16}H_{32}O_8Cu$	$CH_2=CHO(C_2H_4O)_7H$ + Cu	1.0	z_7
Figure 3.10				
MJPS_PEG_CuCl2_iso666_CID19				
m/z	empirical formula	structure	accuracy	assignment
666.28877	$C_{27}H_{55}O_{14}Cu$	$CH_3O(C_2H_4O)_{13}$ +Cu(II)	0.8	[M-H+Cu(II)]+
446.15742	$C_{17}H_{35}O_9Cu$	$CH_3O(C_2H_4O)_8$ + Cu(II)	0.6	$c_8^{\wedge}$
432.14224	$C_{16}H_{33}O_9Cu$	Cu(II)-O-CH_2-$CH_2O(C_2H_4O)_8H$	1.7	$x_7^{\wedge}$
416.14683	$C_{16}H_{33}O_8Cu$	$CH_2=CHO(C_2H_4O)_7$ + Cu(II)	0.5	$z_7^{\wedge}$
402.13314	$C_{15}H_{31}O_8Cu$	$CH_3O(C_2H_4O)_7$ + Cu(II)	0.5	$c_8^{\wedge}$
MJPS_PEG_ZnCl2_iso667_CID24				
667.28882	$C_{27}H_{55}O_{14}Zn$	$CH_3O(C_2H_4O)_{13}$ +Zn(II)	1.6	[M-H+Zn(II)]+
623.2676	$C_{25}H_{51}O_{13}Zn$	$CH_3O(C_2H_4O)_{12}$+ Zn(II)	1.9	$c_{11}^{\wedge}$
579.23602	$C_{23}H_{47}O_{12}Zn$	$CH_3O(C_2H_4O)_{11}$+ Zn(II)	1.2	$c_{10}^{\wedge}$
447.1573	$C_{17}H_{35}O_9Zn$	$CH_3O(C_2H_4O)_9$+ Zn(II)	1.4	$c_7^{\wedge}$
433.14224	$C_{16}H_{33}O_9Zn$	Cu(II)-O-CH_2-$CH_2O(C_2H_4O)_7H$	2.7	$x_7^{\wedge}$
MJPS_PEG_CaCl2_iso643_CID23				
643.32805	$C_{27}H_{55}O_{14}Ca$	$CH_3O(C_2H_4O)_{13}$ +Ca(II)	10.6	[M + Ca - H]+
599.29352	$C_{25}H_{51}O_{13}Ca$	$CH_3O(C_2H_4O)_{12}$ + Ca (II)	-2.5	$c_{12}^{\wedge}$
479.21553	$C_{20}H_{39}O_{10}Ca$	Ca(II)-O-CH_2-	-1.7	$x_{19}^{\wedge}$
MJPS_PEG_CaCl2_iso322_CID23				
322.16407	$C_{27}H_{55}O_{14}Ca$	$CH_3O(C_2H_4O)_{13}H$ +Ca(II)	-0.6	[M + Ca(II)]2+
629.30499	$C_{26}H_{53}O_{14}Ca$	Ca(II)-O-CH_2-	-0.9	$x_{12}^{\wedge}$
585.27885	$C_{24}H_{49}O_{13}Ca$	Ca(II)-O-CH_2-	-0.8	$x_{11}^{\wedge}$
555.26805	$C_{23}H_{47}O_{13}Ca$	$CH_3O(C_2H_4O)_{11}$+ Ca(II)	-1.3	$c_{10}^{\wedge}$
MJPS_PEG_MgCl2_CID_iso314_CID20				
314.17529	$C_{27}H_{55}O_{14}Mg$	$CH_3O(C_2H_4O)_{13}H$ +Mg(II)	-0.6	[M + Mg(II)]2+
569.30017	$C_{24}H_{49}O_{13}Mg$	Mg(II)-O-CH_2-	-1.1	$x_{11}^{\wedge}$

495.26437	$C_{21}H_{43}O_{11}Ca$	$CH_3O(C_2H_4O)_{10}$+ Ca(II)	-1.3	$c_9^{\wedge}$
254.13601	$C_{22}H_{44}O_{11}Ca$	CH_2=CHO$(C_2H_4O)_{7H}$ + Mg(II)	-0.6	$z_7^{''2+}$
241.12821	$C_{20}H_{42}O_{11}Mg$	H-O-CH_2-$CH_2O(C_2H_4O)_9H$ +	-1.1	$x_9^{''2+}$
Figure3.13				
MJPS_PEG_CuCl2_iso666_EID25				
m/z	empirical formula	structure	accuracy /ppm	assignment
666.29163	$C_{27}H_{55}O_{14}Cu$	$CH_3O(C_2H_4O)_{13}$ +Cu(II)	5.1	[M-H+Cu(II)]+
446.15875	$C_{17}H_{35}O_9Cu$	$CH_3O(C_2H_4O)_8$+ Cu(II)	3.4	$c_7^{\wedge}$
MJPS_PEG_ZnCl2_iso667_EID25				
667.29144	$C_{27}H_{55}O_{14}Zn$	$CH_3O(C_2H_4O)_{13}$ +Zn(II)	5.5	[M-H + Zn(II)]+
301.06322	$C_{10}H_{21}O_6Zn$	$CH_3O(C_2H_4O)_4$+ Zn(II)	2.7	$c_4^{\wedge}$
315.07902	$C_{11}H_{23}O_6Zn$	Zn(II)-CH2-$CH_2O(C_2H_4O)_7H$	3.0	$z_5^{\wedge}$
329.09479	$C_{12}H_{25}O_6Zn$	Zn(II)-O-CH_2-$CH_2O(C_2H_4O)_4H$	3.3	$x_5^{\wedge}$
345.08972	$C_{12}H_{25}O_7Zn$	$CH_3O(C_2H_4O)_5$+ Zn(II)	3.17	$c_5^{\wedge}$
MJPS_PEG_CaCl2_iso642_EID23				
643.32205	$C_{27}H_{55}O_{14}Ca$	$CH_3O(C_2H_4O)_{13}$ +Ca(II)	1.284	[M-H +
277.09572	$C_{10}H_{21}O_6Ca$	Ca(II)-O-CH_2-$CH_2O(C_2H_4O)_4H$	-0.491	$x_4^{\wedge}$
259.08515	$C_{10}H_{19}O_5Ca$	Ca(II)-CH2-$CH_2O(C_2H_4O)_4H$	-0.546	$z_4^{\wedge}$
247.08512	$C_9H_{19}O_5Ca$	$CH_3O(C_2H_4O)_4$+ Ca(II)	-0.694	$c_4^{\wedge}$
233.06947	$C_8H_{17}O_5Ca$	Ca(II)-O-CH_2-$CH_2O(C_2H_4O)_3H$	-0.735	$x_3^{\wedge}$
Figure 3.14				
MJPS_PEG_CaCl2_iso322_ECD20				
m/z	empirical formula	structure	accuracy /ppm	assignment
322.1637	$C_{27}H_{56}O_{14}Ca$	$CH_3O(C_2H_4O)_{13}H$ +Ca(II)	-0.559	[M +
335.13734	$C_{13}H_{27}O_7Ca$	$CH_3O(C_2H_4O)_6$+ Ca(II)	-1.136	$c_5^{\wedge}$
347.1373	$C_{14}H_{27}O_7Ca$		-1.212	
349.15295	$C_{14}H_{29}O_7Ca$		-1.205	
365.14789	$C_{14}H_{29}O_8Ca$	Ca(II)-O-CH_2-$CH_2O(C_2H_4O)_4H$	-1.083	$x_5^{\wedge}$
379.16353	$C_{15}H_{31}O_8Ca$	$CH_3O(C_2H_4O)_7$+ Ca(II)	-1.07	$c_6^{\wedge}$
MJPS_PEG_MgCl2_iso314_ECD23				
314.17557	$C_{27}H_{56}O_{14}Mg$	$CH_3O(C_2H_4O)_{13}H$ +Mg(II)	-0.559	[M + Mg(II)]2+
363.18657	$C_{15}H_{31}O_8Mg$	$CH_3O(C_2H_4O)_7$+ Mg(II)	0.506	$c_6^{\wedge}$
393.19712	$C_{16}H_{33}O_9Mg$	Mg(II)-O-CH_2-	0.43	$x_6^{\wedge}$
407.21286	$C_{17}H_{35}O_9Mg$	$CH_3O(C_2H_4O)_8$+ Mg(II)	0.636	$c_7^{\wedge}$

Table 10.3 Ion assignments for Tandem MS of [PEG + X^1 + X^2]$^{2+}$.

Figure 3.17				
PEG_FT_POS_iso728_CID25				
m/z	empirical formula	structure	accuracy /ppm	assignment
728.92798	$C_{64}H_{131}O_{33}LiNa$	$HO(C_2H_4O)_{32}H$ + Li + Na	-4.1	[M+Na+Li]2+
1433.8645	$C_{64}H_{130}O_{33}Li$	$HO(C_2H_4O)_{32}H$ + Li	-0.3	[M+Li]+
PEG_FT_POS_iso736_CID20				
736.91449	$C_{64}H_{131}O_{33}LiK$	$HO(C_2H_4O)_{32}H$ + Li + K	-3.0	[M+K+Li]2+
1433.86389	$C_{64}H_{130}O_{33}Li$	$HO(C_2H_4O)_{32}H$ + Li	-0.7	[M + Li]+
PEG_FT_POS_iso744_CID20				
744.45679	$C_{64}H_{131}O_{33}NaK$	$HO(C_2H_4O)_{32}H$ +Na + K	7.5	[M+K+Na]2+
1449.8385	$C_{64}H_{130}O_{33}Na$	$HO(C_2H_4O)_{32}H$ + Na	-0.1	[M+Na]+
Figure 3.18				
PEG_FT_POS_iso728_ECD5				
m/z	empirical formula	structure	accuracy /ppm	assignment
728.42705	$C_{64}H_{131}O_{33}LiNa$	$HO(C_2H_4O)_{32}H$ + Li + Na	-0.1	[M+Na+Li]2+
1433.87369	$C_{64}H_{130}O_{33}Li$	$HO(C_2H_4O)_{32}H$ + Li	6.1	[M+Li]+
1455.856	$C_{64}H_{129}O_{33}LiNa$	$HO(C_2H_4O)_{32}$ Li + Na	-6.3	[M-H+Na+Li]+
PEG_FT_POS_iso736_ECD5				
736.41231	$C_{64}H_{131}O_{33}LiK$	$HO(C_2H_4O)_{32}H$ + Li + K	-0.7	[M+K+Li]2+
1433.86639	$C_{64}H_{130}O_{33}Li$	$HO(C_2H_4O)_{32}H$ + Li	1.0	[M+Li]+
1471.82184	$C_{64}H_{129}O_{33}LiK$	$HO(C_2H_4O)_{32}Li$ + K	0.7	[M-H+K+Li]+
PEG_FT_POS_iso744_ECD5				
744.39868	$C_{64}H_{131}O_{33}NaK$	$HO(C_2H_4O)_{32}H$ +Na + K	-3.0	[M+K+Na]2+
1465.81121	$C_{64}H_{130}O_{33}K$	$HO(C_2H_4O)_{32}H$ + K	0.7	[M+K]+
1484.90131	$C_{64}H_{129}O_{33\mathrm{Na}}K$	$HO(C_2H_4O)_{32}Na$ + K	0.7	[M-H+K+Na]+
Figure 3.19				
PEG_FT_POS_iso728_ECD20				
m/z	empirical formula	structure	accuracy /ppm	assignment
728.4343	$C_{64}H_{131}O_{33}LiNa$	$HO(C_2H_4O)_{32}H$ + Li + Na	10.0	[M+Na+Li]2+
1433.90985	$C_{64}H_{130}O_{33}Li$	$HO(C_2H_4O)_{32}H$ + Li	31.4	[M+Li]+
1455.89123	$C_{64}H_{129}O_{33}LiNa$	$HO(C_2H_4O)_{32}$ Li + Na	30.5	[M-H+Na+Li]+
463.25511	$C_{20}H_{40}O_{10}Na$	$HO(C_2H_4O)_9CH=CH_2$ + Na	8.1	b_9^{Na}
447.28103	$C_{20}H_{40}O_{10}Li$	$HO(C_2H_4O)_9CH=CH_2$ + Li	7.7	b_9^{Li}
419.22813	$C_{18}H_{36}O_9Na$	$HO(C_2H_4O)_8CH=CH_2$ + Na	7.1	b_8^{Na}
403.25397	$C_{18}H_{36}O_9Li$	$HO(C_2H_4O)_8CH=CH_2$ + Li	6.1	b_8^{Li}

PEG_FT_POS_iso736_ECD20				
736.42053	$C_{64}H_{131}O_{33}LiK$	$HO(C_2H_4O)_{32}H$ + Li + K	8.9	[M+K+Li]2+
1433.89621	$C_{64}H_{130}O_{33}Li$	$HO(C_2H_4O)_{32}H$ + Li	21.9	[M +Li]+
1471.84424	$C_{64}H_{129}O_{33}LiK$	$HO(C_2H_4O)_{32}Li$ + K	16.0	[M-H+K+Li]+
491.30564	$C_{22}H_{44}O_{11}Li$	$HO(C_2H_4O)_{10}CH{=}CH_2$ + Li	3.7	b_{10}^{Li}
479.22773	$C_{20}H_{40}O_{10}K$	$HO(C_2H_4O)_9CH{=}CH_2$ + K	5.1	b_9^{K}
447.2795	$C_{20}H_{40}O_{10}Li$	$HO(C_2H_4O)_9CH{=}CH_2$ + Li	4.2	b_9^{Li}
435.20059	$C_{18}H_{36}O_9K$	$HO(C_2H_4O)_8CH{=}CH_2$ + K	3.4	b_9^{K}
PEG_FT_POS_iso744_ECD23				
744.40923	$C_{64}H_{131}O_{33}NaK$	$HO(C_2H_4O)_{32}H$ +Na + K	11.2	[M+K+Na]2+
1465.84591	$C_{64}H_{130}O_{33}K$	$HO(C_2H_4O)_{32}H$ + K	22.7	[M+K]+
479.22803	$C_{20}H_{40}O_{10}K$	$HO(C_2H_4O)_9CH{=}CH_2$ + K	5.7	b_9^{K}
463.25396	$C_{20}H_{40}O_{10}Na$	$HO(C_2H_4O)_9CH{=}CH_2$ + Na	5.6	b_9^{Na}
435.20128	$C_{18}H_{36}O_9K$	$HO(C_2H_4O)_8CH{=}CH_2$ + K	5.0	b_9^{K}
419.2272	$C_{18}H_{36}O_9Na$	$HO(C_2H_4O)_8CH{=}CH_2$ + Na	4.9	b_8^{Na}

Table 10.4 Ion assignments for H/D exchange experiments.

Figure 3.20				
PEG_FT_POS_iso1449_ECD20		MeOH		
m/z	empirical formula	structure	accuracy /ppm	assignment
947.5437	$C_{42}H_{84}O_{21}Na$	$HO(C_2H_4O)_{20}CH{=}CH_2$ + Na	4.2	b_{20}
919.5144	$C_{40}H_{80}O_{21}Na$	$HO(C_2H_4O)_{19}CH_2CH{=}O$ +	6.5	c_{19}
903.51642	$C_{40}H_{80}O_{20}Na$	$HO(C_2H_4O)_{19}CH{=}CH_2$ + Na	5.2	b_{19}
PEG_FT_POS_iso1451_ECD20		MeOD		
948.55856	$C_{42}H_{83}DO_{21}Na$	$DO(C_2H_4O)_{20}CH{=}CH_2$ + Na	11.6	b_{20}
920.5262	$C_{40}H_{79}DO_{21}Na$	$DO(C_2H_4O)_{19}CH_2CH{=}O$ +	10.8	c_{19}
904.5314	$C_{42}H_{83}DO_{21}Na$	$DO(C_2H_4O)_{19}CH{=}CH_2$ + Na	-3.1	b_{19}^{D}
Figure 3.21				
PEG_OMe_FT_iso627_ECD21		MeOH		
m/z	empirical formula	structure	accuracy /ppm	assignment
507.2844	$C_{22}H_{44}O_{11}Na$	$CH_2{=}CHO(C_2H_4O)_{10}H$ + Na	12.4	z_{10}
495.28386	$C_{21}H_{44}O_{11}Na$	$CH_3O(C_2H_4O)_9CH_2\text{-}CH_2\text{-}OH$	11.6	c_9''
493.2685	$C_{21}H_{42}O_{11}Na$	$CH_3O(C_2H_4O)_9CH_2\text{-}CH\text{-}O$ +	12.2	c_9
481.26807	$C_{20}H_{42}O_{11}Na$	$HO\text{-}CH_2\text{-}CH_2O(C_2H_4O)_9H$ +	11.6	x_9''
479.25236	$C_{20}H_{40}O_{11}Na$	$O{=}CH\text{-}CH_2O(C_2H_4O)_9H$ +	11.5	x_9
477.27305	$C_{21}H_{42}O_{10}Na$	$CH_3O(C_2H_4O)_9CH{=}CH_2$ +	11.5	b_9
463.25702	$C_{20}H_{40}O_{10}Na$	$CH_2{=}CHO(C_2H_4O)_9H$ + Na	11.0	z_9

PEG_OMe_FT_EID21		MeOD		
508.29327	$C_{22}H_{43}O_{11}DNa$	$CH_2=CHO(C_2H_4O)_{10}D$ + Na	14.4	z_{10}^{D}
495.28609	$C_{21}H_{44}O_{11}Na$	$CH_3O(C_2H_4O)_9CH_2$-CH_2-OH	16.1	$c_9^{''}$
493.27083	$C_{21}H_{42}O_{11}Na$	$CH_3O(C_2H_4O)_9CH_2$-CH-O +	16.9	c_9
482.27624	$C_{20}H_{41}O_{11}DNa$	HO-CH_2-$CH_2O(C_2H_4O)_9D$ +	12.3	$x_9^{''D}$
480.26112	$C_{20}H_{39}O_{11}DNa$	O=CH-$CH_2O(C_2H_4O)_9H$ +	13.5	x_9^{D}
477.27526	$C_{21}H_{42}O_{10}Na$	$CH_3O(C_2H_4O)_9CH=CH_2$ +	16.1	b_9
464.26548	$C_{20}H_{39}O_{10}DNa$	$CH_2=CHO(C_2H_4O)_9D$ + Na	12.4	z_9^{D}

10.2. Supplementary information for ESI MS of homopolymers and copolymers

Table 10.5 Ion assignments for MS and tandem MS of PMMA and PS.

Figure 4.1				
PMMA_FT_fullms2				
m/z	empirical formula	structure	accuracy /ppm	assignment
1425.73965	$C_{70}H_{114}O_{28}Na$	$[H(C_5H_8O_2)_{14}H + Na]$	0.2	$[M+Na]^+$
1441.71484	$C_{70}H_{114}O_{28}K$	$[H(C_5H_8O_2)_{14}H + K]$	1.0	$[M+K]^+$
1474.75845	$C_{145}H_{238}O_{58}Na_2$	$[H(C_5H_8O_2)_{29}H + 2Na]$	0.8	$[M+2Na]^{2+}$
Figure 4.2				
PMMA_FT_iso1425_CID16a				
m/z	empirical formula	structure	accuracy /ppm	assignment
1425.74878	$C_{70}H_{114}O_{28}Na$	$[H(C_5H_8O_2)_{14}H + Na]$	6.9	$[M+Na]^+$
923.46439	$C_{45}H_{72}O_{18}Na$	$[H(C_5H_8O_2)_9CH_2$-	3.6	b_9
909.44874	$C_{44}H_{70}O_{18}Na$	$[CH_2=C(CO_2CH_3)$-	3.6	z_9
879.47331	$C_{44}H_{72}O_{16}Na$	$[H(C_5H_8O_2)_8CH_2$-	2.3	a_{9b}
865.4586	$C_{43}H_{70}O_{16}Na$	$[CH_2=C(CH_3)$-$(C_5H_8O_2)_8H$ +	3.5	y_{8b}
PMMA_FT_iso1425_EID20				
1425.75287	$C_{70}H_{114}O_{28}Na$	$[H(C_5H_8O_2)_{14}H + Na]$	9.8	$[M+Na]^+$
923.47484	$C_{45}H_{72}O_{18}Na$	$[H(C_5H_8O_2)_9CH_2$-	6.4	b_9
909.45893	$C_{44}H_{70}O_{18}Na$	$[CH_2=C(CO_2CH_3)$-	6.2	z_9
879.47717	$C_{44}H_{72}O_{16}Na$	$[H(C_5H_8O_2)_8CH_2$-	6.7	a_{9b}
865.46104	$C_{43}H_{70}O_{16}Na$	$[CH_2=C(CH_3)$-$(C_5H_8O_2)_8H$ +	6.3	y_{8b}
Figure 4.3				
MJPS_PMMA_DHB_NaBr_MS_MS_1				

m/z	empirical formula	structure	accuracy /ppm	assignment
925.597	$C_{45}H_{74}O_{18}Na$	$[H(C_5H_8O_2)_9H + Na]$		$[M+Na]^+$
479.46	$C_{24}H_{40}O_8Na$	$[H(C_5H_8O_2)_4CH_2$-		a_{3b}
465.433	$C_{23}H_{38}O_8Na$	$[CH_2=C(CH_3)$-$(C_5H_8O_2)_4H$ +		y_{3b}
423.385	$C_{20}H_{32}O_8Na$	$[H(C_5H_8O_2)_3CH_2$-		b_3
409.362	$C_{19}H_{30}O_8Na$	$[CH_2=C(CO_2CH_3)$-		z_3
Figure 4.4				
PS_FT_fullms7				
m/z	empirical formula	structure	accuracy /ppm	assignment
1413.7364	$C_{100}H_{106}Ag$	$[C_4H_9(C_8H_8)_{12}H + Ag]$	1.3	$[M+Ag]^+$
1621.86021	$C_{116}H_{124}Ag$	$[C_4H_9(C_8H_8)_{14}H + Ag]$	0.3	$[M+Ag]^+$
Figure 4.5				
MJPS_PS_FT_POS_iso1415_CID20				
m/z	empirical formula	structure	accuracy /ppm	assignment
1413.74852	$C_{100}H_{106}Ag$	$[C_4H_9(C_8H_8)_{12}H + Ag]$	10.0	$[M+Ag]^+$
MJPS_PS_FT_POS_iso1415_ECD23				
1413.76738	$C_{100}H_{106}Ag$	$[C_4H_9(C_8H_8)_{12}H + Ag]$	23.2	$[M+Ag]^+$
419.09572	$C_{24}H_{24}Ag$	$[CH_2=C(Ph)(C_8H_8)_2H + Ag]$	6.7	y_1
302.02365	$C_{15}H_{15}Ag$	[CH(Ph)=CH.CH(Ph)-H +	3.9	z_1
196.12531	$C_{15}H_{16}$	[CH(Ph)=CH.CH(Ph)-H + H]	0.6	z_1-Ag
117.07006	C_9H_9	$[CH_2$=CH.CH(Ph)-H + H]	-3.2	J_1-Ag
Figure 4.6				
MJPS_PS_FT_POS_iso1643_CID15				
m/z	empirical formula	structure	accuracy /ppm	assignment
1642.00725	$C_{124}H_{130}Na$	$[C_4H_9(C_8H_8)_{15}H + Na]$	0.1	$[M+Na]^+$
MJPS_PS_FT_POS_iso1643_EID23				
1641.99285	$C_{124}H_{130}Na$	$[C_4H_9(C_8H_8)_{15}H + Na]$	-8.6	$[M+Na]^+$
855.5099	$C_{64}H_{64}Na$	$[CH_2=C(Ph)(C_8H_8)_7H + Na]$	23.0	y_7
821.53589	$C_{61}H_{66}Na$	$[C_4H_9(C_8H_8)_7=CH_2 + Na]$	36.1	a_7
751.44199	$C_{56}H_{56}Na$	$[CH_2=C(Ph)(C_8H_8)_6H + Na]$	23.0	y_6
717.45692	$C_{53}H_{58}Na$	$[C_4H_9(C_8H_8)_6=CH_2 + Na]$	18.5	a_6

Figure 4.7				
MJPS_PS_DITH_AgTFA_MS_MS5				
m/z	empirical formula	structure	accuracy /ppm	assignment
1727.913	$C_{124}H_{140}Ag$	$[C_4H_9(C_8H_8)_{15}H + Ag]$		$[M+Ag]^+$
629.441	$C_{48}H_{48}Ag$	$[CH_2{=}C(Ph)(C_8H_8)_5H + Ag]$		y_5
595.421	$C_{45}H_{50}Ag$	$[C_4H_9(C_8H_8)_5{=}CH_2 + Ag]$		a_5
525.335	$C_{40}H_{40}Ag$	$[CH_2{=}C(Ph)(C_8H_8)_4H + Ag]$		y_4
489.36	$C_{37}H_{42}Ag$	$[C_4H_9(C_8H_8)_4{=}CH_2 + Ag]$		a_4

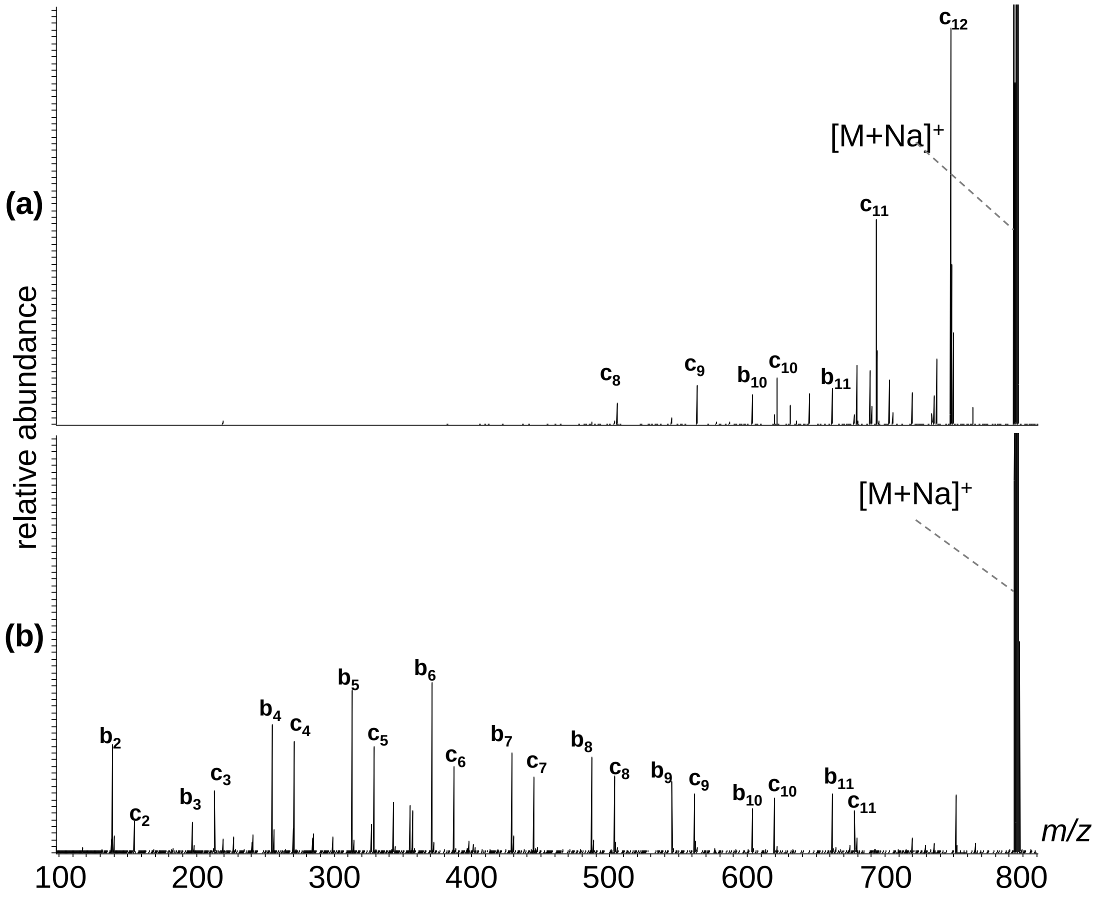

Figure 10.2 Tandem MS of $[HO(C_3H_6O)_{13}H + Na]^+$: (a) LTQ-CID and (b) EID (20.1 eV).

Table 10.6 Summary of ion assignments for ESI of Copolymers.

Figure 4.11				
PEG_PPG_iso779_CID17				
m/z	empirical	structure	accurac	assignmen

	formula		y /ppm	t
779.51442	$C_{38}H_{76}O_{14}Na$	$[HO(C_3H_6O)_{12}(C_2H_4O)_1H + Na]$	2.2	$[M+Na]^+$
735.48825	$C_{36}H_{72}O_{13}Na$	$[HO(C_3H_6O)_{11}CH_2C(CH_3){=}O + Na]$	2.4	c^{PG12}
719.49317	$C_{36}H_{72}O_{12}Na$	$[HO(C_3H_6O)_{11}CH_2C{=}CH_2 + Na]$	2.2	b^{PG12}
661.45083	$C_{33}H_{76}O_{11}Na$	$[HO(C_3H_6O)_{10}CH_2C{=}CH_2 + Na]$	1.7	b^{PG11}
PEG_PPG_iso779_EID21				
779.52062	$C_{38}H_{76}O_{14}Na$	$[HO(C_3H_6O)_{12}(C_2H_4O)_1H + Na]$	10.1	$[M+Na]^+$
503.32263	$C_{24}H_{48}O_9Na$	$[HO(C_3H_6O)_7CH_2C(CH_3){=}O + Na]$	7.1	c^{PG7}
487.3278	$C_{24}H_{48}O_8Na$	$[HO(C_3H_6O)_7CH_2C{=}CH_2 + Na]$	7.5	b^{PG7}
Figure 4.12				
PEG_PPG_iso765_CID16				
m/z	empirical formula	structure	accuracy /ppm	assignment
765.49827	$C_{37}H_{74}O_{14}Na$	$[HO(C_3H_6O)_{11}(C_2H_4O)_2H + Na]$	1.6	$[M+Na]^+$
719.49345	$C_{35}H_{68}O_{13}Na$	$[HO(C_3H_6O)_{11}CH_2CH_2{=}O + Na]$	1.8	$c^{PG11EG1}$
661.451	$C_{33}H_{66}O_{11}Na$	$[HO(C_3H_6O)_{10}CH_2C{=}CH_2 + Na]$	1.1	b^{PG11}
PEG_PPG_iso765_EID21				
765.50461	$C_{37}H_{74}O_{14}Na$	$[HO(C_3H_6O)_{11}(C_2H_4O)_2H + Na]$	9.1	$[M+Na]^+$
445.28055	$C_{21}H_{42}O_8Na$	$[HO(C_3H_6O)_6CH_2C(CH_3){=}O+ Na]$	6.3	c^{PG7}
429.28549	$C_{21}H_{42}O_7Na$	$[HO(C_3H_6O)_6CH_2C{=}CH_2 + Na]$	6.2	b^{PG7}
415.23316	$C_{19}H_{36}O_8Na$	$[O{=}CH_{-} CH(CH_3)O(C_3H_6O)_4(C2H4O)_2H + Na]$	5.7	x^{PG4EG2}
Figure 4.13				
PEG_PPG_iso751_CID15				
m/z	empirical	structure	accurac	assignmen
751.48287	$C_{36}H_{72}O_{14}Na$	$[HO(C_3H_6O)_{10}(C_2H_4O)_3H + Na]$	1.2	$[M+Na]^+$
703.46164	$C_{34}H_{64}O_{13}Na$	$[HO(C_3H_6O)_{10}(C_2H_4O)CH_2CH_2{=}O + Na]$	1.1	$c^{PG10EG2}$
689.44615	$C_{34}H_{664}O_{12}Na$	$[HO(C_3H_6O)_{10}(C_2H_4O)CH{=}CH_2 + Na]$	1.4	$b^{PG10EG2}$
677.44583	$C_{33}H_{66}O_{12}Na$	$[O{=}CH\text{-}CH(CH_3)O(C_3H_6O)_8(C_2H_4O)_3H + Na]$	0.9	x^{PG9EG3}
603.40888	$C_{30}H_{60}O_{10}Na$	$[HO(C_3H_6O)_9CH_2C{=}CH_2 + Na]$	0.8	b^{PG10}
PEG_PPG_iso751_CID15				
751.48608	$C_{36}H_{72}O_{14}Na$	$[HO(C_3H_6O)_{10}(C_2H_4O)_3H + Na]$	5.5	$[M+Na]^+$
387.23668	$C_{18}H_{36}O_7Na$	$[HO(C_3H_6O)_5CH_2C(CH_3){=}O+ Na]$	2.1	c^{PG6}

371.24169	$C_{18}H_{36}O_6Na$	$[HO(C_3H_6O)_5CH_2C{=}CH_2 + Na]$	2.0	b^{PG6}
355.24668	$C_{18}H_{36}O_5Na$	$[HO(C_2H_4O)(C_3H_6O)_3CH_2C{=}CH_2 + Na]$	1.8	b^{PG4EG1}
343.21013	$C_{16}H_{32}O_6Na$	$[CH_2{=}C(CH_3)O(C_3H_6O)_3(C_2H_4O)_2H+Na]$	1.4	x^{PG3EG2}
Figure 4.16				
MJPS_FT_POS_JEFF_H_CID25				
m/z	empirical	structure	accurac	assignmen
910.59566	$C_{42}H_{88}O_{19}N$	$[NH_2(C_3H_6O)_3(C_2H_4O)_{16}CH_3 + H]$	0.1	$[M+H]^+$
MJPS_FT_POS_JEFF_H_EID20a				
910.60431	$C_{42}H_{88}O_{19}N$	$[NH_2(C_3H_6O)_3(C_2H_4O)_{16}CH_3 + H]$	10.2	$[M+H]^+$
394.2825	$C_{19}H_{40}O_7N$	$[NH_2(C_3H_6O)_3(C_2H_4O)_4CH{=}CH_2 + H]$	5.1	b^{PG3EG4}
381.27452	$C_{18}H_{39}O_7N$	$[NH_2(C_3H_6O)_2(C_2H_4O)_5CH{=}CH_2 + H]$	4.9	b^{PG2EG5}
368.26653	$C_{17}H_{36}O_7N$	$[NH_2(C_3H_6O)_3(C_2H_4O)_3CH_2CH_2\text{-}OH+H]$	4.6	$c^{''PG3EG3}$
366.25084	$C_{17}H_{36}O_7N$	$[NH_2(C_3H_6O)_3(C_2H_4O)_3CH_2CH{=}O+ H]$	4.5	c^{PG3EG3}
364.27161	$C_{18}H_{36}O_6N$	$[NH_2(C_3H_6O)_4(C_2H_4O)_2CH{=}CH_2 + H]$	4.7	b^{PG4EG2}
350.25578	$C_{17}H_{36}O_6N$	$[NH_2(C_3H_6O)_3(C_2H_4O)_3CH{=}CH_2 + H]$	4.3	b^{PG3EG3}
Figure 4.18				
MJPS_PEGranPPG_iso1210_EID2				
m/z	empirical	structure	accurac	assignmen
1209.76733	$C_{56}H_{114}O_{25}Na$	$[HO(C_3H_6O)_8(C_2H_4O)_{16}H + Na]$	10.5	$[M+Na]^+$
301.16411	$C_{13}H_{26}O_6Na$		4.7	b^{PG1EG4}
287.14834	$C_{12}H_{24}O_6Na$		4.5	c^{PG2EG2}
285.16903	$C_{13}H_{26}O_5Na$		4.3	b^{PG3EG1}
273.13252	$C_{11}H_{22}O_5Na$		4.1	c^{PG1EG3}
271.15322	$C_{12}H_{24}O_5Na$		4.0	b^{PG2EG2}
257.13736	$C_{11}H_{22}O_5Na$		3.4	b^{PG1EG3}
Figure 4.21				
MJPSa_PB_DPE_iso1281_CID20				
m/z	empirical	structure	accurac	assignmen
1284.64551	$C_{90}H_{94}Ag$	$[C_4H_9(C_{14}H_{12})_5(C_4H_6)_4H + Ag]$	14.5	$[M+Ag]^+$
1043.46912	$C_{72}H_{72}Ag$		0.6	
989.42215	$C_{68}H_{66}Ag$		0.6	
975.4064	$C_{67}H_{64}Ag$		0.5	
953.42123	$C_{65}H_{66}Ag$		-0.3	
877.3904	$C_{59}H_{62}Ag$		0.2	
823.34368	$C_{55}H_{56}Ag$		0.5	

809.32765	$C_{54}H_{54}Ag$		0.0	
755.28103	$C_{50}H_{48}Ag$		0.4	
741.26529	$C_{49}H_{46}Ag$		0.3	
643.24965	$C_{41}H_{44}Ag$		0.4	
629.23398	$C_{40}H_{42}Ag$		0.4	
589.20288	$C_{37}H_{38}Ag$		0.7	
575.18692	$C_{36}H_{36}Ag$		0.2	
Figure 4.22				
MJPSa_PB_DPE_iso1281_EID20				
m/z	empirical	structure	accurac	assignmen
1281.66586	$C_{90}H_{94}Ag$	$[C_4H_9(C_{14}H_{12})_5(C_4H_6)_4H + Ag]$	19.7	$[M+Ag]^+$
589.20688	$C_{37}H_{38}Ag$		7.5	
575.191	$C_{36}H_{36}Ag$		7.3	
395.09477	$C_{22}H_{27}Ag$		4.8	
344.07064	$C_{18}H_{21}Ag$		3.6	
328.03914	$C_{17}H_{17}Ag$		3.1	
286.9996	$C_{14}H_{12}Ag$		2.1	
273.9917	$C_{13}H_{11}Ag$		2.0	
106.90461	Ag		-4.5	
Figure 4.23				
MJPSa_PB_DPE_iso1335_CID20				
m/z	empirical	structure	accurac	assignmen
1335.69294	$C_{94}H_{100}Ag$	$[C_4H_9(C_{14}H_{12})_5(C_4H_6)_5H + Ag]$	-7.9	[M+Ag]+
1043.46916	$C_{72}H_{72}Ag$		1.2	
989.42195	$C_{68}H_{66}Ag$		1.0	
953.42151	$C_{65}H_{66}Ag$		0.5	
877.39104	$C_{59}H_{62}Ag$		1.5	
823.34367	$C_{55}H_{56}Ag$		1.1	
809.32773	$C_{54}H_{54}Ag$		0.8	
755.28124	$C_{50}H_{48}Ag$		1.4	
741.26531	$C_{49}H_{46}Ag$		1.1	
643.24981	$C_{41}H_{44}Ag$		1.5	
629.23433	$C_{40}H_{42}Ag$		1.8	
589.203	$C_{37}H_{38}Ag$		1.9	
575.18688	$C_{36}H_{36}Ag$		1.1	
MJPSa_PB_DPE_iso1335_EID20				
m/z	empirical	structure	accurac	assignmen
1335.71316	$C_{94}H_{100}Ag$	$[C_4H_9(C_{14}H_{12})_5(C_4H_6)_5H + Ag]$	19.5	[M+Ag]+
755.28604	$C_{50}H_{48}Ag$		7.8	

589.20697	$C_{37}H_{38}Ag$		8.6	
575.19119	$C_{36}H_{36}Ag$		8.6	
341.04701	$C_{18}H_{18}Ag$		4.7	
328.03907	$C_{17}H_{17}Ag$		4.6	
398.11814	$C_{22}H_{27}Ag$		5.8	
286.99962	$C_{14}H_{12}Ag$		4.1	

10.3. Supplementary information for RAFT polymerisation

DFT Calculation Parameters.

Electronic structure calculations were performed using Density Functional Theory (DFT). Initial molecule creation in GaussView 4.1.2 was followed by a simple clean function that gave the optimised bond angles. Optimisation and frequency calculations were set-up with a ground state-restricted B3LYP method using a 6-31G(d) basis set. The first calculation established the optimum form of the CPADB molecule as a neutral, where the addition of charge carriers to the optimised CPADB formed the basis for all further optimisation and frequency calculations for the charged ions.

Monitoring fragmentation as a function of electron irradiation time.

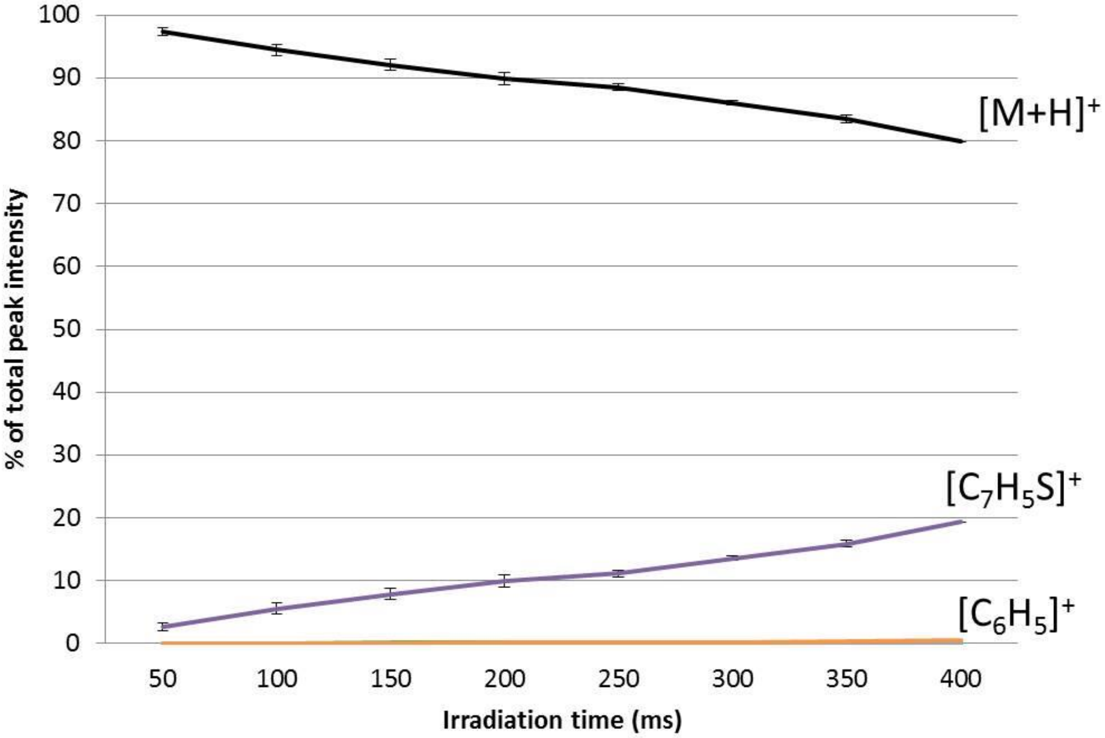

Figure 10.3 Fragmentation as a function of irradiation time for [CPADB + H]$^+$ at 9.1 eV (product ions [$C_7H_5S_2$]$^+$, [$C_7H_6S_2$]$^+$, [$C_7H_5S_2$]$^+$ and [C_6H_5ON]$^+$ represent < 1 % of total peak intensity and consequently have not been labelled).

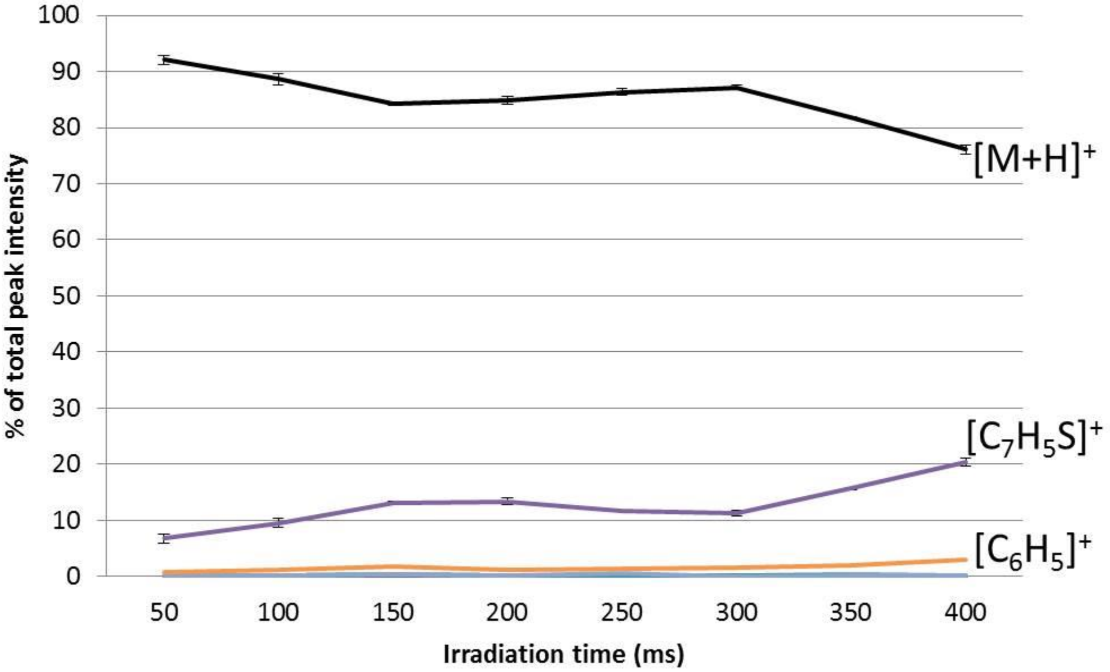

Figure 10.4 Fragmentation as a function of irradiation time for [CPADB + H]$^+$ at 19.1 eV (product ions [$C_7H_5S_2$]$^+$, [$C_7H_6S_2$]$^+$, [$C_7H_5S_2$]$^+$ and [C_6H_5ON]$^+$ represent < 1 % of total peak intensity and consequently have not been labelled).

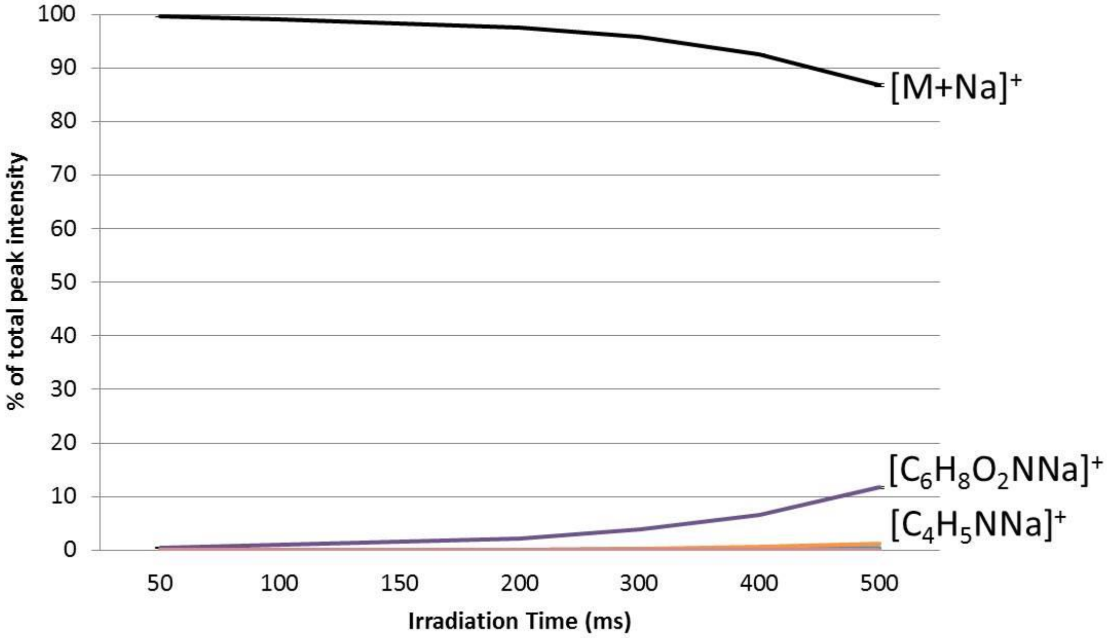

Figure 10.5 Fragmentation as a function of irradiation time for [CPADB + Na]$^+$ at 9.1 eV (product ions [C_7H_5S]$^+$, [C_3H_4NSNa]$^+$ and [$C_2H_3O_2Na$]$^+$ represent < 1 % of total peak intensity and consequently have not been labelled.)

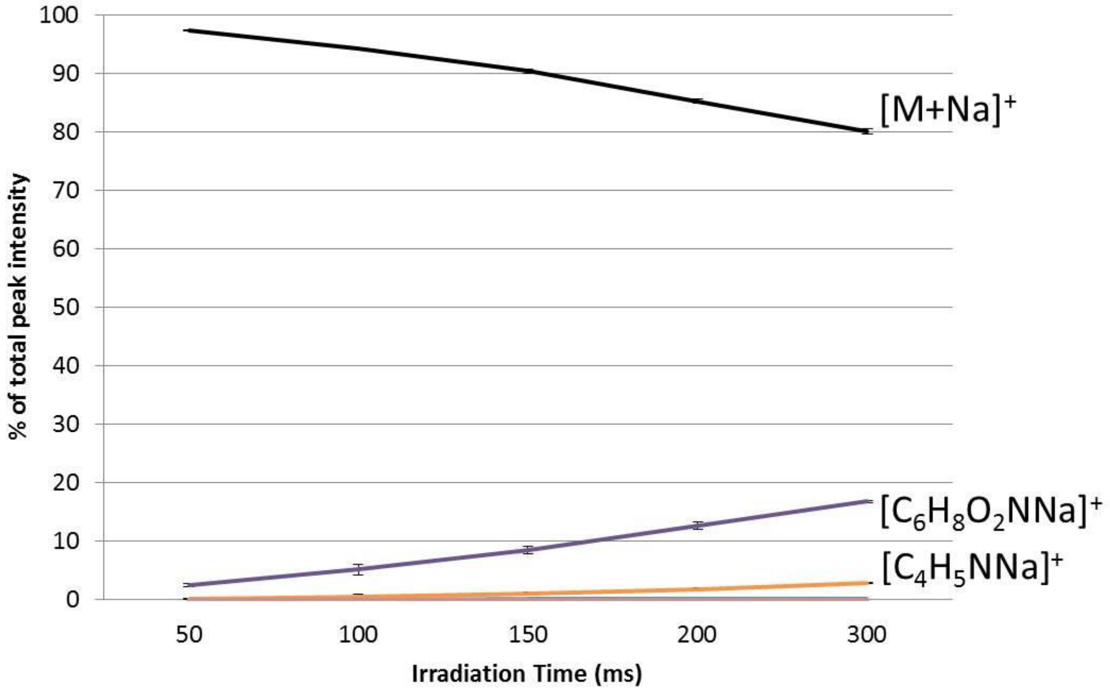

Figure 10.6 Fragmentation as a function of irradiation time for [CPADB + Na]$^+$ at 19.1 eV (product ions [C_7H_5S]$^+$, [C_3H_4NSNa]$^+$ and [$C_2H_3O_2Na$]$^+$ represent < 1 % of total peak intensity and consequently have not been labelled.)

EID of $[4CDSPA + H]^+$.

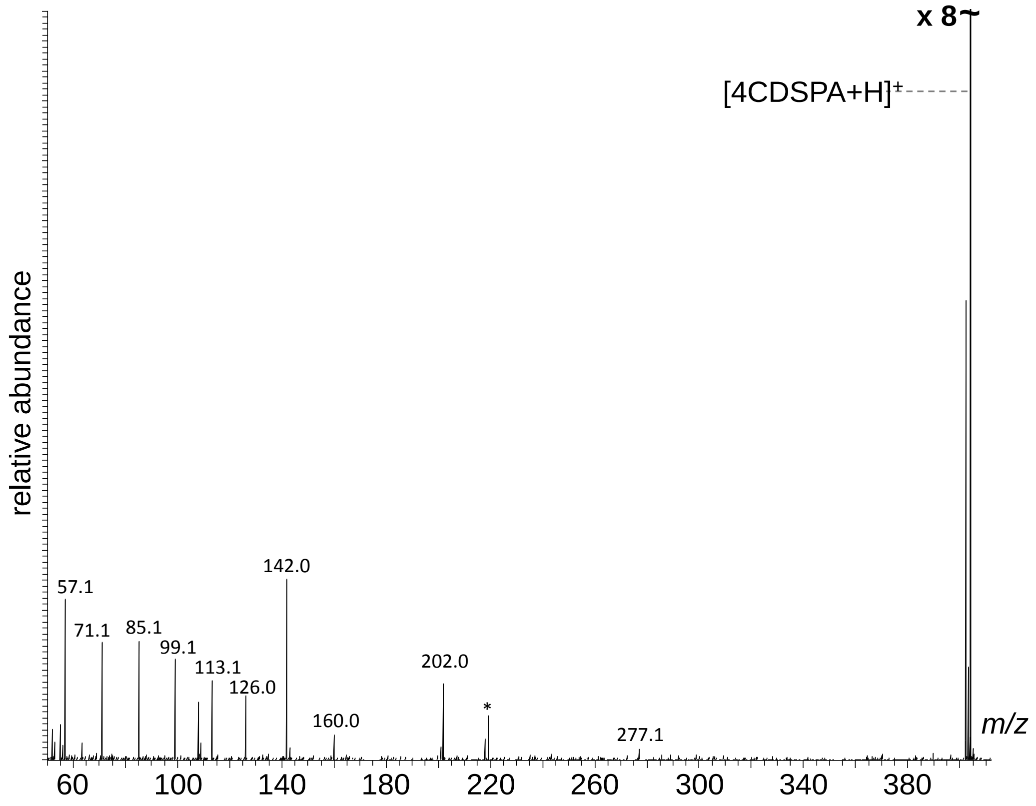

Figure 10.7 EID of $[4CDSPA + H]^+$.

Table 10.7 Summary of product ions observed in EID of $[4CDSPA + H]^+$.

<table>
<tr><td colspan="4">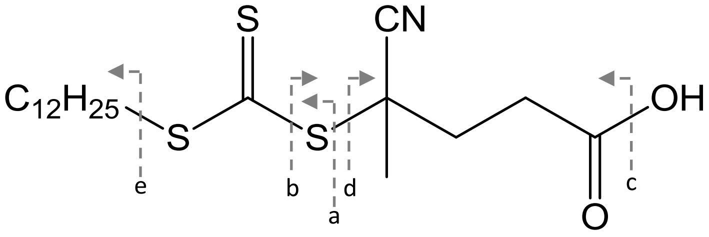 </td></tr>
<tr><td><i>m/z</i></td><td>Empirical Formula</td><td>Accuracy/ppm</td><td>Proposed Bond Cleavage</td></tr>
<tr><td>404.17864</td><td>$C_{19}H_{34}NO_2S_3$</td><td>9.9</td><td></td></tr>
<tr><td>277.11371</td><td>$C_{13}H_{25}S_3$</td><td>8.7</td><td>a</td></tr>
<tr><td>160.04390</td><td>$C_6H_{10}NO_2S$</td><td>7.6</td><td>b</td></tr>
<tr><td>142.03314</td><td>C_6H_8NOS</td><td>7.2</td><td>bc</td></tr>
<tr><td>126.05586</td><td>$C_6H_8NO_2$</td><td>7.1</td><td>d</td></tr>
<tr><td>113.13324</td><td>C_8H_{17}</td><td>6.7</td><td>e</td></tr>
<tr><td>99.11749</td><td>C_7H_{15}</td><td>6.6</td><td>e</td></tr>
<tr><td>85.10173</td><td>C_6H_{13}</td><td>6.4</td><td>e</td></tr>
<tr><td>71.08597</td><td>C_5H_{11}</td><td>6.2</td><td>e</td></tr>
<tr><td>57.07020</td><td>C_4H_9</td><td>5.6</td><td>e</td></tr>
</table>

EID of [4CDSPA + Na]$^+$

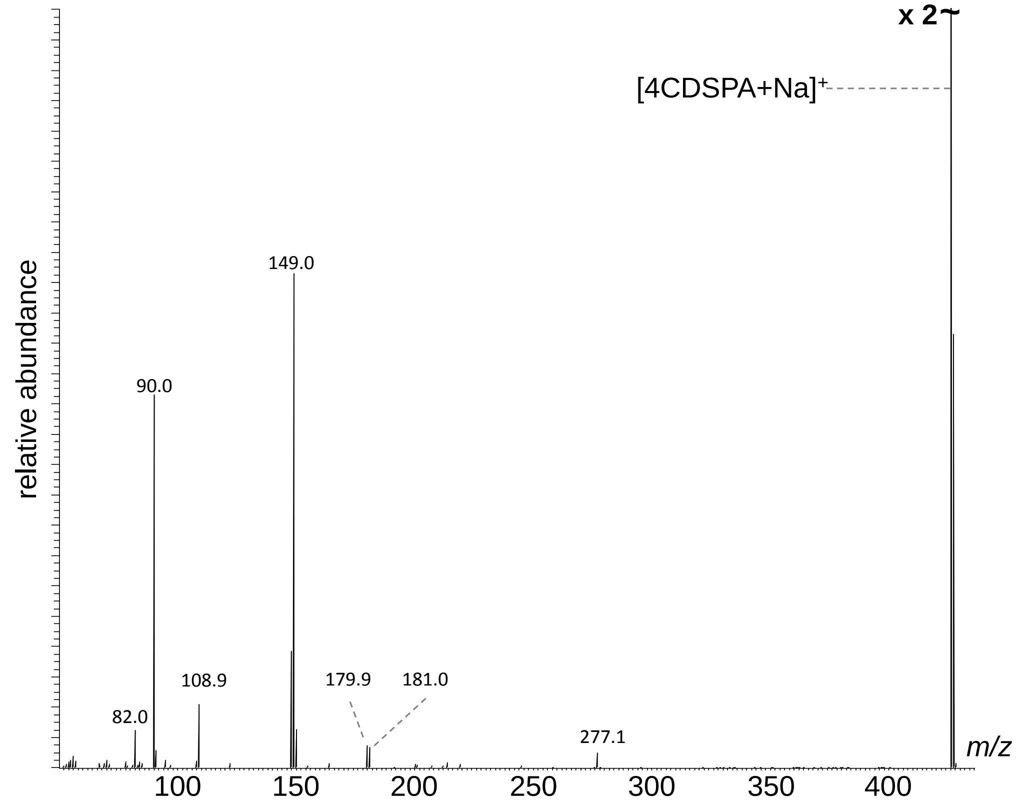

Figure 10.8 EID of [4CDSPA + Na]$^+$.

Table 10.8 Summary of product ions observed in EID of [4CDSPA + Na]$^+$.

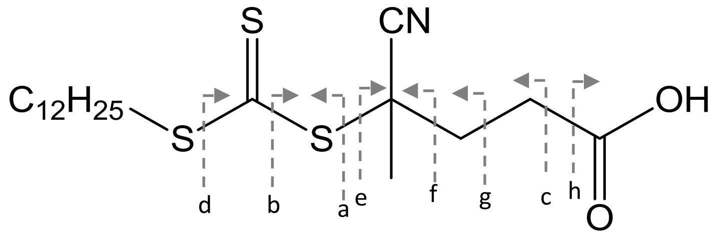

m/z	Empirical Formula	Accuracy/ppm	Proposed Bond Cleavage
426.16043	$C_{19}H_{33}NO_2S_3Na$	17.5	
277.11554	$C_{13}H_{25}S_3$	15.3	a
181.01873	$C_6H_8NO_2SNa$	10.7	b
179.99313	$C_6H_7NS_2Na$	10.7	cd
150.04945	$C_6H_9NO_2Na$	-20.6	e
149.04610	$C_6H_8NO_2Na$	9.2	e
148.03825	$C_6H_7NO_2Na$	9.1	e
108.99648	C_3H_4NSNa	7.5	bf
90.03205	C_4H_5NNa	7.0	eg
82.00308	$C_2H_3O_2Na$	6.8	H

EID of CMDTC + H

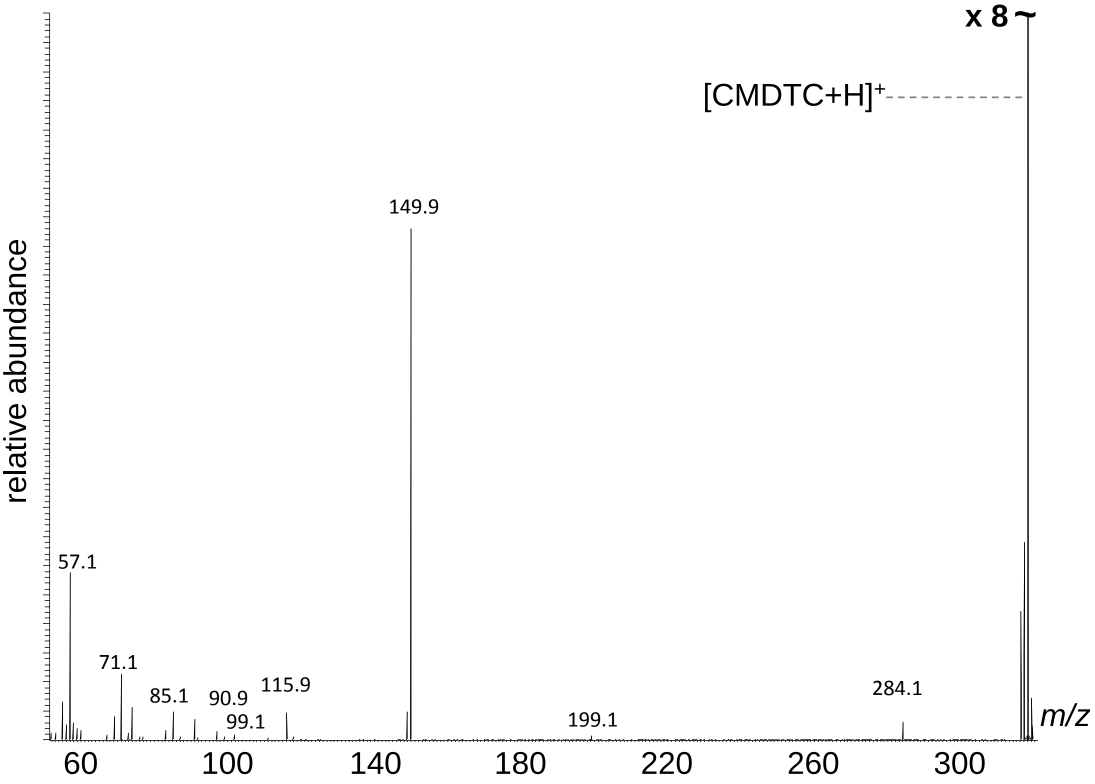

Figure 10.9 EID of [CMDTC+ H]$^+$.

Table 10.9 Summary of product ions observed in EID of [CMDTC + H]$^+$.

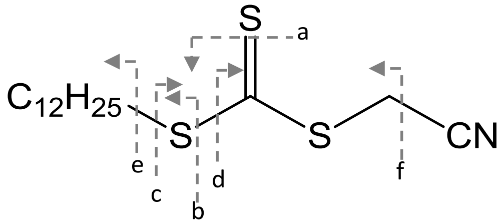

m/z	Empirical Formula	Accuracy/ppm	Proposed Bond Cleavage
318.13890	$C_{15}H_{28}NS_3$	3.3	N/A
284.15101	$C_{15}H_{26}NS_2$	3.1	a
199.15203	$C_{12}H_{23}S$	2.7	b
149.95039	$C_3H_4NS_3$	2.3	c
115.96254	$C_3H_2NS_2$	1.9	d
99.11697	C_7H_{15}	1.4	e
90.96719	$C_2H_3S_2$	1.3	df

85.10129	C_6H_{13}	1.3	e
71.08652	C_5H_{11}	1.3	e
57.06999	C_4H_9	2.0	e

EID of [CMDTC + Na]$^+$

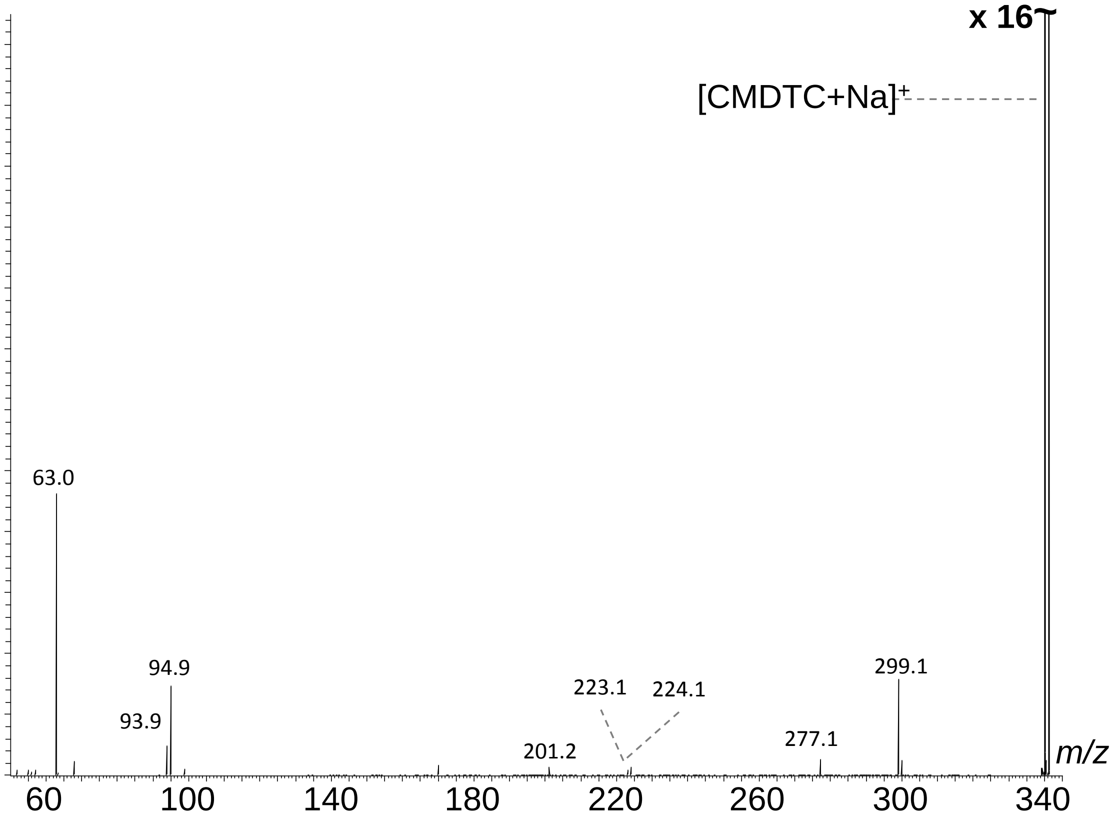

Figure 10.10 EID of [CMDTC + Na]$^+$.

Table 10.10 Summary of product ions observed in EID of [CMDTC + Na]$^+$.

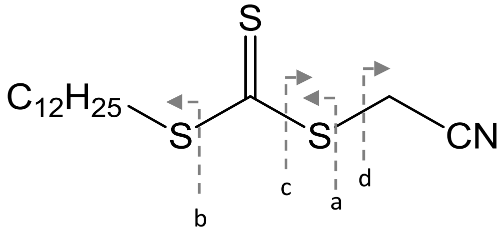			
m/z	Empirical Formula	Accuracy/ppm	Proposed Bond Cleavage
340.12099	$C_{15}H_{27}NS_3Na$	3.5	N/A
299.09509	$C_{15}H_{23}S_3$	2.0	(-NH_2Na)
277.11275	$C_{13}H_{25}S_3$	5.2	a

224.15802	$C_{12}H_{25}SNa$	4.9	b
223.15005	$C_{12}H_{24}SNa$	4.3	b
201.16794	$C_{12}H_{25}S$	3.9	b
94.98021	C_2H_2NSNa	2.0	c
93.97238	C_2H_1NSNa	2.0	c
63.00810	C_2H_2NNa	2.5	d

EID of [DDMAT + Na]$^+$

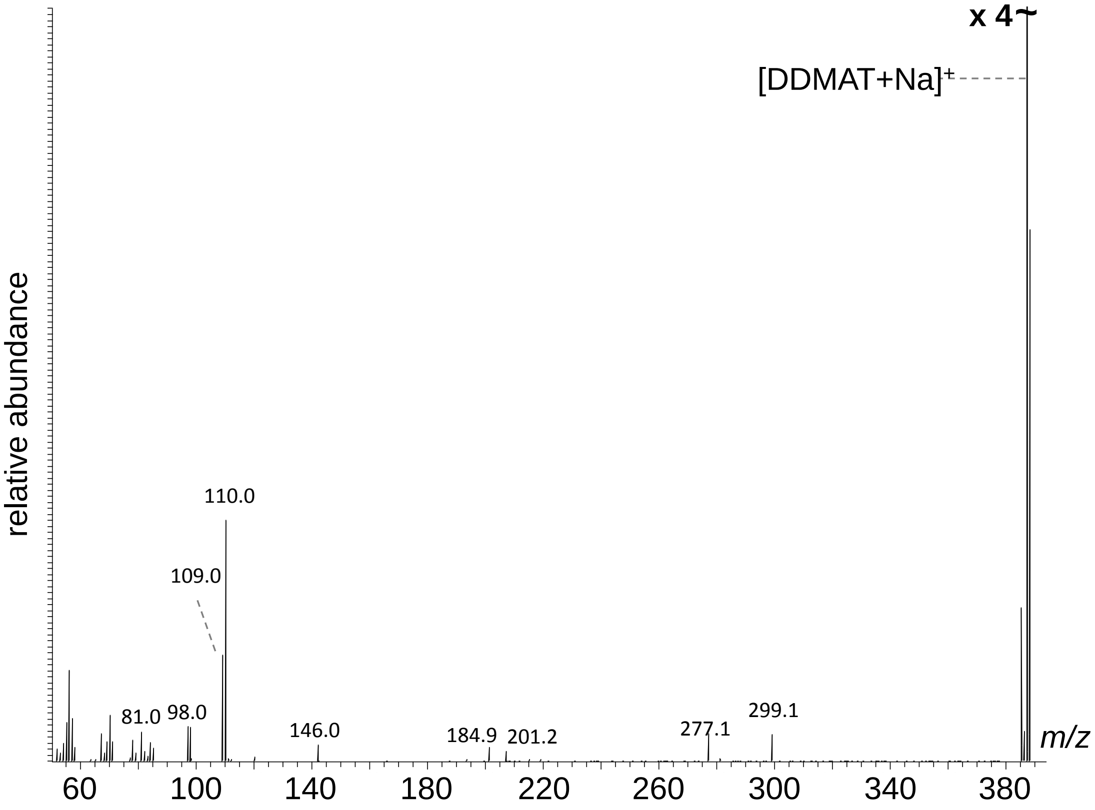

Figure 10.11 EID of [DDMAT + Na]$^+$.

Table 10.11 Summary of product ions observed in EID of [DDMAT + Na]$^+$.

<table>
<tr><td colspan="4">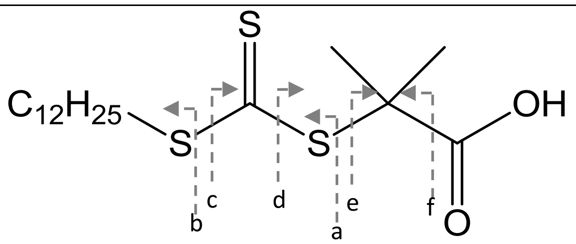
</td></tr>
<tr><td>*m/z*</td><td>Empirical Formula</td><td>Accuracy/ppm</td><td>Proposed Bond</td></tr>
</table>

			Cleavage
387.14930	$C_{17}H_{32}O_2S_3Na$	9.4	
299.09584	$C_{13}H_{24}S_3Na$	8.7	a
277.11370	$C_{13}H_{25}S_3$	8.6	a
201.16877	$C_{12}H_{25}S$	8.1	b
184.97513	$C_5H_6O_2S_2Na$	7.5	c
146.00685	$C_4H_7O_2SNa$	6.7	d
110.03449	$C_4H_7O_2Na$	6.3	e
109.02666	$C_4H_6O_2Na$	6.0	e
98.01663	C_3H_7SNa	5.7	ef
81.03153	C_3H_6ONa	5.5	n/a

EID of [PPDB + Na]$^+$

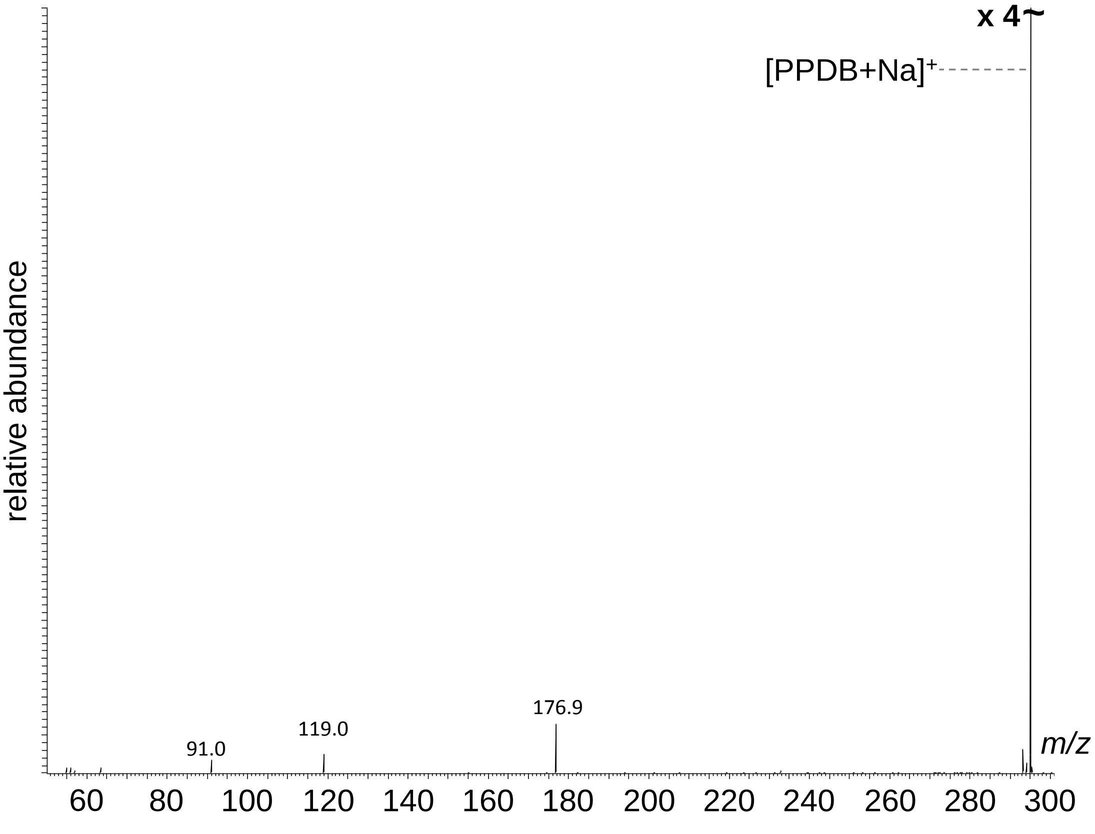

Figure 10.12 EID of [PPDB + Na]$^+$.

Table 10.12 Summary of product ions observed in EID of $[PPDB + Na]^+$.

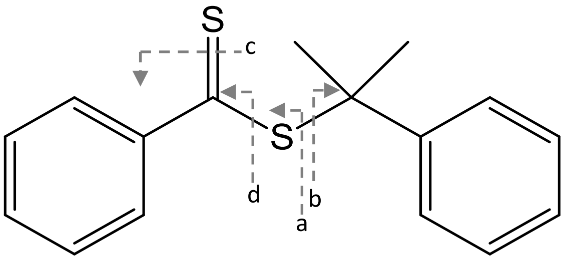 			
m/z	Empirical Formula	Accuracy/ppm	Proposed Bond Cleavage
295.06027	$C_{16}H_{16}S_2Na$	5.9	N/A
176.98093	$C_7H_6S_2Na$	3.5	a
119.08579	C_9H_{11}	2.2	b
91.05439	C_7H_7	1.8	cd

10.4. Supplementary information for ASAP of Polymers

Table 10.13 Summary of ion assignments for ASAP of polymers.

Figure 8.1			
MJPS_PS_600oC(65)			
m/z	empirical formula	degree of polymerisation	assignment
786.5387	$C_{60}H_{66}$	7	•
1931.5198	$C_{148}H_{152}$	18	•
300.1964	$C_{23}H_{24}$	2	z_2
1132.7306	$C_{87}H_{88}$	10	z_{10}
474.3435	$C_{36}H_{42}$	4	b_3
578.4063	$C_{44}H_{50}$	5	b_4
682.7543	$C_{52}H_{58}$	6	b_5
Figure 8.2			
MJPS_PS_DITH_AgTFA_MS3			
m/z	empirical formula	degree of polymerisation	assignment
1101.1000	$C_{76}H_{82}Ag$	9	
2456.2000	$C_{180}H_{186}Ag$	22	
Figure 8.4			
MikeS_PEG_600oC(44)			

m/z	empirical formula	degree of polymerisation	assignment
503.2784	$C_{22}H_{47}O_{12}$	11	•
1207.6702	$C_{52}H_{107}O_{27}$	26	•
529.2922	$C_{24}H_{49}O_{12}$	11	△
1279.7158	$C_{58}H_{121}O_{29}$	28	△
517.2953	$C_{23}H_{49}O_{12}$	11	□
1177.6549	$C_{53}H_{109}O_{27}$	26	□
Figure 8.5			
MJPS_PEG1500_DHB_Na3			
m/z	empirical formula	degree of polymerisation	assignment
965.3000	$C_{42}H_{84}O_{22}Na$	21	
1933.9000	$C_{86}H_{72}O_{44}Na$	43	
Figure 8.6			
m/z	empirical formula	degree of polymerisation	assignment
703.3205	$C_{35}H_{59}O_{14}$	7	•
1103.4934	$C_{55}H_{91}O_{22}$	11	•
632.2635	$C_{32}H_{62}O_{12}$	5	b_{5c}
1132.4839	$C_{57}H_{85}O_{20}$	10	b_{10c}
643.3057	$C_{33}H_{55}O_{12}$	5	y_{5b}
1043.4842	$C_{53}H_{87}O_{20}$	9	y_{9b}□
1071.4738	$C_{54}H_{87}O_{21}$	9	b_{9a}
Figure 8.7			
MJPS_PMMA1K_NaI_DHB2			
m/z	empirical formula	degree of polymerisation	assignment
525.2	$C_{25}H_{42}O_{10}Na$	5	
1725.8	$C_{85}H_{138}O_{34}Na$	17	
Figure 8.9			
m/z	empirical formula	degree of polymerisation	assignment
517.4445	$C_{37}H_{73}$	18	□
519.4581	$C_{37}H_{75}$	18	•
531.4589	$C_{38}H_{75}$	18	□
533.4715	$C_{38}H_{77}$	18	•
Figure 8.19			

MJPS_PEGdeg_THF_DHB_NaI_success			
m/z	empirical formula	degree of polymerisation	assignment
1053.2000	$C_{46}H_{92}O_{24}Na$	23	[M+Na]
1037.6000	$C_{46}H_{92}O_{23}Na$	22	b_n''
1035.6000	$C_{46}H_{90}O_{23}Na$	22	b_n
1023.6000	$C_{45}H_{90}O_{23}Na$	22	a_n''
Figure 8.21			
MikeS_PS600oC(11)			
m/z	empirical formula	degree of polymerisation	assignment
1515.9865	$C_{116}H_{122}$	14	M+●
300.1781	$C_{23}H_{24}$	2	z_n''
370.2568	$C_{28}H_{34}$	3	b_n''
Figure 8.22			
MJPS_PS_DITH_AgTFA_MS_MS5			
m/z	empirical formula	degree of polymerisation	assignment
1727.9100	$C_{124}H_{130}Ag$	15	[M+Ag]
489.3600			a_4
523.3400			y_4
Figure 8.23			
MikeS_PEG1500_600oC(23)			
m/z	empirical formula	degree of polymerisation	assignment
987.5630	$C_{44}H_{91}O_{23}$	22	[M+H]
133.0833	$C_6H_{13}O_3$	2	b_2
547.3233	$C_{24}H_{49}O_{13}$	12	c_{11}
Figure 8.24			
MJPS_PEG1500_LIFTCID1405			
m/z	empirical formula	degree of polymerisation	assignment
1450.0090	$C_{64}H_{130}O_{33}Na$	32	[M+Na]
595.4730	$C_{26}H_{52}O_{13}Na$	12	b_{12}
611.4470	$C_{26}H_{52}O_{14}Na$	12	c_{12}
Figure 8.26			
m/z	empirical formula	degree of polymerisation	assignment

503.3000	$C_{22}H_{47}O_{12}$	11	[M+H]+
487.3100	$C_{22}H_{45}O_{11}$	10	b_{10}''
519.5373	$C_{36}H_{71}O$		□
521.5316	$C_{35}H_{59}O_2$		△
523.5132	$34H_{67}O_3$		○
Figure 8.29			
m/z	empirical formula	degree of polymerisation	assignment
477.5	$C_{34}H_{69}$		♦
605.6	$C_{42}H_{85}O$		○
443.1	$C_{19}H_{29}N_3O_9$		□
414.5	$C_{17}H_{25}N_3O_9$		△
Figure 8.32			
m/z	empirical formula	degree of polymerisation	assignment
393.4453	$C_{28}H_{57}$	13	♦
785.8973	$C_{56}H_{113}$	27	♦
331.1016	$C_{14}H_{19}O_9$		○
472.1507	$C_{19}H_{26}N_3O_{11}$		□
516.1786	$C_{21}H_{30}N_3O_{12}$		•
648.2631	$C_{29}H_{40}O_{15}$		•

11. Papers.

11.1. Electron-Induced Dissociation of Singly Charge Organic Cations as a Tool for Structural Characterization of Pharmaceutical Type Molecules

J. A. Mosely, M. J. P. Smith, A. S. Prakash, M. Sims and A. W. T. Bristow, *Anal Chem*, 2011, **83**, 4068-4075.

11.2. Using Electron Induced Dissociation on an LC Time-Scale to Characterize a mixture of Analogous Small Organic Molecules

A. S. Prakash, M. J. P. Smith, Z. Kaabia, G. Hurst, C. Yan, M. Sims, A. W. T. Bristow, P. Stokes, D. Parker and J. A. Mosely, *J Am Soc Mass Spectrom*, 2012, **23**, 850-857.

11.3. Evaluating Atmospheric pressure Solids Analysis Probe (ASAP) mass spectrometry for the analysis of low molecular weight synthetic polymers

M. J. P. Smith, N. R. Cameron and J. A. Mosely, *Analyst*, 2012, **137**, 4524-4530.